Development of novel sorber bed heat and mass exchangers for sorption cooling systems

by

Seyedhesam Bahrehmand

M.Sc., Amirkabir University of Technology (Tehran Polytechnic), 2013

B.Sc., Amirkabir University of Technology (Tehran Polytechnic), 2011

Thesis Submitted in Partial Fulfillment of the
Requirements for the Degree of
Doctor of Philosophy

in the
School of Mechatronic Systems Engineering
Faculty of Applied Sciences

Simon Fraser University

Fall 2020

Declaration of Committee

Name:	**Seyedhesam Bahrehmand**
Degree:	**Doctor of Philosophy**
Title:	**Development of novel sorber bed heat and mass exchangers for sorption cooling systems**
Committee:	**Chair: Amr Marzouk** Lecturer, Mechatronics
	Majid Bahrami Supervisor Professor, Mechatronics
	Michael Eikerling Committee member Professor, Chemistry
	Woo Soo Kim Committee member Associate Professor, Mechatronics
	Gordon McTaggart-Cowan Examiner Associate Professor, Sustainable Energy Engineering
	Belal Dawoud External Examiner Professor, Faculty of Mechanical Engineering Ostbayerische Technische Hochschule Regensburg

Abstract

The current cooling systems mainly employ vapor compression refrigeration technology, which increases the electricity peak load significantly and has a high carbon footprint. One alternative solution is sorption systems, run by low-grade thermal energy, i.e. heat sources with temperature less than 100 ºC, such as waste heat, which is non-payable. Also, sorption systems have negligible carbon footprint. Despite all the promising features and benefits, current sorption systems are not ready for wide market adoption. A revolutionary approach to their design and development is needed to overcome their technical limitations such as low specific cooling power (SCP) and low coefficient of performance (COP). Graphite flakes were added to the sorbent to increase the sorbent thermal diffusivity; however, it reduces the active sorbent. The counteracting effect of graphite flake additives in the sorbent was studied using a custom-built gravimetric large pressure jump test bed. It was found that graphite flake additives can increase or decrease the sorption performance depending on the cycle time. Furthermore, 2-D analytical models were developed that consider the spatial and temporal variation of water uptake and temperature in sorber bed heat and mass exchangers (S-HMXs). Two designs of plate fin (P-HMX) and finned-tube (F-HMX) were considered because of the high SCP and COP. Using the analytical models, it was shown that the entire S-HMX components should be optimized simultaneously, and the objective functions of SCP and COP should be optimized together. Thus, an analysis of variance and simultaneous multi-objective optimization of the S-HMX components were performed using the developed analytical models. Based on the optimization study, the P-HMX and the F-HMX were specifically designed and built for sorption cooling systems. The experimental results showed that the present P-HMX achieved an SCP of 1,005 W/kg sorbent, and a COP of 0.60 for T_{des}=90 °C, T_{sorp}= T_{cond}=30 °C and T_{evap}=15 °C. Furthermore, the F-HMX yielded an SCP of 766 W/kg and COP of 0.55. It was shown that the P-HMX provided 4.3 times higher SCP, and 3 times higher COP compared to an off-the-shelf heat exchanger coated with a similar composite sorbent consisting of $CaCl_2$, silica gel B150 and PVA.

Keywords: optimized sorber bed heat and mass exchanger; sorption cooling systems; analytical modeling; optimization; specific cooling power; coefficient of performance

Dedication

To my beloved wife, Ghazaleh, my dear parents, Behzad and Narges, and my dear brother and best friend, Saeed for their love, support and encouragement.

Acknowledgement

I would like to express my sincere gratitude to many great people who made accomplishing this dissertation possible. First, I'd like to express my deepest appreciation to my senior supervisor at Simon Fraser University (SFU), Dr. Majid Bahrami, for his great support and guidance throughout my PhD studies. He has had a remarkable impact on my critical thinking, research and presentation skills. It was a privilege working with Dr. Bahrami and learning from him. I'd like to express my gratitude to my supervisory committee members, Dr. Woo Soo Kim and Dr. Michael Eikerling, for their discussions and comments on my research project. Also, I'd like to thank my examining committee members, Dr. Belal Dawoud and Dr. Gordon McTaggart-Cowan for their valuable time reading this thesis and comments. I am also grateful to Dr. Amr Marzouk for accepting to be the defense committee chairman.

Moreover, I'd like to express my gratitude to Maryam Khajehpour, Claire McCague and Wendell Huttema, Postdoctoral Fellows, and Khorshid Fayazmanesh, PhD graduate at Laboratory for Alternative Energy Conversion (LAEC), for the technical support and expert guidance, particularly in the experiments of G-LPJ, TGA, TPS, SEM imaging as well as coating the heat exchangers. Furthermore, I'd like to thank Mr G. Mustafa Sajid and Mr James Shoults at SFU machine shop for their help with manufacturing the sorber bed heat and mass exchangers.

I greatly appreciate the financial support provided by SFU through Multi-year Funding (MYF) scholarship consisting of Graduate Dean's Entrance Scholarship and Provost's Prize of Distinction.

I gratefully acknowledge the financial support of the Natural Sciences and Engineering Research Council of Canada (NSERC) through the Automotive Partnership Canada Grant No. APCPJ 401826-10 and Idea to Innovation Grant No. I2IPJ 530368-2018.

I am also thankful to SFU 4D LABS for providing access to scanning electron microscopy.

Finally, I would like to express my deepest gratitude to my lovely wife, parents and brother, for their unconditional love and support throughout my life.

Table of Contents

List of Tables

List of Figures

Nomenclature

A	Heat transfer area, m^2
b	Height of fin and sorbent (m)
Bi	Biot number (hl/k)
c	Specific heat capacity, J/kg K
Fo	Fourier number
h	Convective heat transfer coefficient (W/m^2K)
h_{ads}	Enthalpy of adsorption, J/kg
h_{fg}	Enthalpy of evaporation, J/kg
H	Height, m
J	Bessel function of the first kind
k	Thermal conductivity, W/m K
L	Characteristic length, m
m	Mass, kg
$m^{'}$	Slope of fitted line for uptake versus temperature (-0.0118 for sorption and -0.0123 for desorption) [1], [2]
p	Pressure, Pa
p_0	Saturation pressure, Pa
Pe	Peclet number
Pr	Prandtl number
$\dot{q}$	Heat flux, W
Q	Energy, J
r	Coordinate
r_1	Fluid tube radius, m
R	Thermal resistance, K m/W
Re	Reynolds number
T	Temperature, K
t	Time (s), thickness (m)
u	Velocity, m s^{-1}
$\dot{V}$	Volumetric flow rate, m^3 s^{-1}
W	Width of the tube cross-section (m)
X	Spatial Eigenfunction in x, η direction
x	Coordinate
y	Coordinate
Y	Bessel function of the second kind

Greek symbols

α	Thermal diffusivity, m^2/s
γ	Eigenvalue in η direction
Γ	Temporal Eigenfunction
η	Dimensionless coordinate of x
θ	Dimensionless temperature
η	Dimensionless coordinate
κ	Dimensionless thermal conductivity ratio
λ	Eigenvalue in ξ direction
Λ	Dimensionless thermal contact conductance
μ	Dimensionless thermal diffusivity ratio
ξ	Dimensionless coordinate of y

ρ	Density, kg/m^3
τ	Cycle time, s
φ	Graphite flake content in the sorbent (g graphite/g dry sorbent)
Φ	Spatial Eigenfunction in x, η direction
ψ	Spatial Eigenfunction in y, ξ direction
ω	Water uptake (g H_2O/g dry sorbent)

Subscripts

0	Initial condition
ads	Adsorption
base	Baseline case
c	Channel
cond	Condenser
des	Desorption
e	Electrical
evap	Evaporator/evaporative
eq	Equilibrium
f	Fin
fs	Fin spacing
g	Gas or vapor
HTF	Heat transfer fluid
s	Sorbent
sat	saturation
sorb	Sorbent
sorp	Sorption
t	Tube
th	Thermal
tot	Total
w	Water

Abbreviations

AC	Air conditioning
ACS	Absorption cooling systems
ANOVA	Analysis of variance
CEC	Combined evaporator and condenser
COP	Coefficient of performance
F-HMX	Finned-tube heat and mass exchanger
G-LPJ	Gravimetric large pressure jump
GWP	Global warming potential
HEX	Heat exchanger
HR	Heat recovery
HTF	Heat transfer fluid
LGTE	Low-grade thermal energy
ODP	Ozone depletion potential
P-HMX	Plate fin heat and mass exchanger
PVP	Polyvinylpyrrolidone
RSC	Reversed Stirling cycle
SEM	Scanning electron microscopy
SCP	Specific cooling power
SCS	Sorption cooling systems
S-HMX	Sorber bed heat and mass exchanger

TCR	Thermal contact resistance
TCS	Temperature control system
TGA	Thermogravimetric analyzer
TPS	Transient plane source
VCR	Vapor compression refrigeration
VSCP	Volumetric specific cooling power

Executive summary

On the global scale, air conditioning (AC) systems consume 15% of the total electricity [3]–[5]. Vapor compression refrigeration (VCR) systems are currently the most competitive technology meeting market requirements [6], and form 99% of space-cooling energy consumption in the US [7]. However, they are powered by electricity, which is produced predominantly from fossil fuels, up to 76% globally [8], and employ fluorocarbon refrigerants that contribute to global warming because of their greenhouse gas (GHG) emission effects. In addition to the building sector, VCR systems used in vehicle AC increase the fuel consumption of internal combustion engine (ICE) by up to 20% because of the extra load on the engine [9]. In ICE vehicles, up to 70% of total fuel energy is wasted to the ambient in the form of low-grade heat in the radiator and the flue gas in the exhaust system [10]. This available waste heat can be utilized to run sorption cooling systems (SCS) to produce cooling, which leaves the mechanical energy output for propulsion, increasing the overall vehicle efficiency substantially. Sorption systems can be driven by low-grade thermal energy, heat sources with temperature less than 100 °C, which is non-payable and abundant in transportation, building and industrial sectors. Furthermore, they employ zero-Global Warming Potential and zero-Ozone Depletion Potential materials, no moving parts, and consume a small amount of electrical power. In addition to AC, sorption systems have shown enormous potential for other applications, including heat pumping, heat upgrading, thermal energy storage, desalination, dehumidification and gas separation.

Nevertheless, sorption systems are not competitive with VCR systems. A revolutionary approach to their design and development is needed to overcome the technical limitations. This PhD program aims to address two major limitations of sorption systems, namely:

i. Low specific cooling power (SCP), resulting from low sorbent thermal diffusivity and the use of off-the-shelf heat and mass exchanger designs. High porosity of the sorbent materials, which is crucial for sorption mass transfer, results in low thermal conductivity that impedes their heat transfer. Furthermore, commonly used off-the-shelf heat exchangers as the sorber bed heat and mass exchanger (S-HMX), such as radiators and coolers, are not specifically designed and optimized for sorption systems and can limit their performance; and

ii. Low coefficient of performance (COP), in part due to high thermal inertia of the currently used off-the-shelf heat exchangers in sorption systems.

Objectives

The objective of this PhD dissertation is to establish a systematic method for specific design and optimization of sorber bed heat and mass exchangers (S-HMXs) for sorption cooling systems. This methodology can be applied to other sorption applications as well. This systematic method includes modeling, optimization, construction and testing a proof-of-concept demonstration of the S-HMXs with the cooling capacity > 0.5 kW, SCP > 700 W/kg and COP > 0.55. The proposed S-HMXs can reduce the heat source energy consumption as well as the mass and volume of the SCS. The compact and efficient S-HMX design would increase market readiness of SCS, helping to sustainably meet the additional demand on the global energy supply due to the increased use of air conditioning systems.

Research methodology

A systematic approach is undertaken to achieve the objectives of this PhD program, and summarized in the following milestones:

- Selection and characterization of suitable sorption pairs with thermal diffusivity of at least 1 mm^2/s and differential uptake of 0.4 g H_2O/g sorbent;
- Investigation of the transient behavior of sorbent materials by adding thermally conductive additives and their effect on sorption performance;
- Development of suitable models to be used for design and optimization of the S-HMX geometry, heat transfer characteristics and cycle time;
- Finding the key design and operating parameters of the S-HMXs that dominate the performance of SCS, namely the SCP and COP;
- Performing multi-objective optimization of the key parameters of the S-HMXs using the developed models to achieve optimum SCP and COP;
- Building proof-of-concept S-HMXs based on the optimization study for the targeted AC applications; and
- Testing the optimized S-HMXs to experimentally validate the performance targets – cooling capacity > 0.5 kW, SCP > 700 W/kg, and COP > 0.55.

Research Roadmap and Contributions

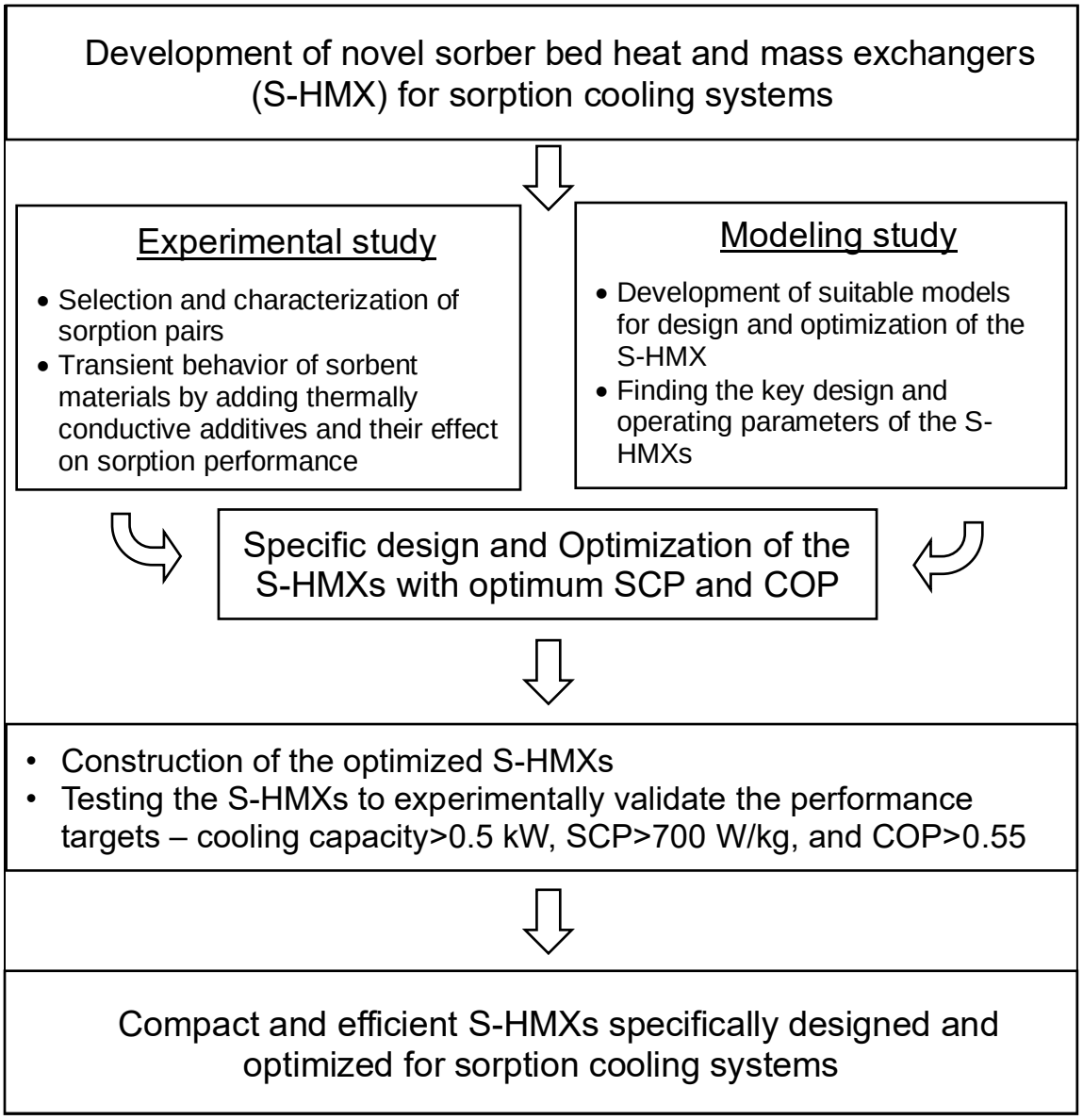

The contributions of this research project are highlighted below:

1. Low sorbent thermal diffusivity is one of the main reasons for the low performance of SCS. Graphite flakes were added to the sorbent to increase thermal diffusivity. However, it reduces the active material fraction. For the first time, the counteracting effects of graphite flake additives in the sorbent was studied using a custom-built gravimetric large pressure jump (G-LPJ) test bed [11]. It was found that depending on the cycle time, adding graphite flake additive could increase or decrease the sorption performance. Thus, a suitable model was imperative for optimization of these parameters in the S-HMX for these conflicting trends.

2. For the first time, 2-D analytical models were developed that consider the spatial and temporal variation of water uptake and temperature in the sorber bed heat and mass exchanger (S-HMX), and have low computation time, which is crucial for optimization and real-time control of the S-HMXs. Two designs of plate fin heat and mass exchangers (P-HMX) and finned-tube heat and mass exchangers (F-HMX) were considered because of the high SCP and COP. The analytical models were validated using the data collected from G-LPJ and the custom-built two-sorber bed sorption test bed [1], [2], [12]. The proposed models accurately predicted the performance of the S-HMXs and provided a reliable and easy-to-use design and optimization tool for the S-HMXs of SCS. Using the analytical model, it was shown that the entire S-HMX components should be optimized simultaneously; otherwise the performance would be limited. Moreover, it was indicated that the objective functions of SCP and COP should be optimized simultaneously due to the conflicting trend between SCP and COP.

3. Therefore, for the first time in the literature, an analysis of variance (ANOVA) and simultaneous multi-objective optimization of the S-HMX components were performed using the developed analytical model [13]. The design with SCP of 976 W/kg and COP of 0.60 was selected for the P-HMX and the design with SCP of 757 W/kg and COP of 0.55 was selected for the F-HMX because they satisfy the performance targets.

4. For the first time in the literature, the S-HMXs of the P-HMX and the F-HMX were specifically designed for sorption cooling systems based on the optimization study [13]. The experimental results showed that the present P-HMX achieved a cooling power of 0.59 kW, SCP of 1,005 W/kg sorbent, and a COP of 0.60. These were

notably higher than the previously published results in the literature. Furthermore, the F-HMX yielded a cooling power of 0.29 kW, SCP of 766 W/kg and COP of 0.55.

5. It was shown that the P-HMX provides 4.3 times higher SCP, and 3 times higher COP compared to a typical off-the-shelf heat exchanger, an engine oil cooler coated with a similar composite sorbent consisting of $CaCl_2$, silica gel B150 and PVA [13]. It clearly indicated the potential for specific design and optimization of the S-HMX to enhance the performance of sorption systems.
6. The P-HMX was tested under various operating conditions: i) desorption temperature, 60–90 °C; ii) sorption and condenser temperature, 20–40 °C; iii) evaporator temperature, 5–20 °C; and iv) cycle time, 10–20 min. SCP in the range of 320–1,230 W/kg and COP of 0.40–0.80 were measured in our testbed over the range of targeted operating conditions [13].

Scholarly contributions

1) H. Bahrehmand, M. Bahrami, Optimized sorber bed heat exchangers for sorption cooling systems, Submitted to *Applied Thermal Engineering*, 2020.
2) H. Bahrehmand, M. Bahrami, An analytical design tool for sorber bed heat and mass exchangers of sorption cooling systems, *International Journal of Refrigeration*, 100, 2019, 368-379.
3) H. Bahrehmand, M. Khajehpour, M. Bahrami, Finding optimal conductive additive content to enhance the performance of coated sorption beds: An experimental study, *Applied Thermal Engineering*, 143 (2018) 308-315.
4) H. Bahrehmand, M. Ahmadi, M. Bahrami, Oscillatory heat transfer in coated sorber beds: An analytical solution, *International Journal of Refrigeration* (2018), https://doi.org/10.1016/j.ijrefrig.2018.05.006.
5) H. Bahrehmand, M. Ahmadi, M. Bahrami, Analytical modeling of oscillatory heat transfer in coated sorption beds, *International Journal of Heat Mass and Transfer*, 121 (2018) 1–9.
6) H. Bahrehmand, M. Bahrami, Development of novel sorber bed heat exchangers for sorption cooling systems, *International Sorption Heat Pump Conference*, Berlin, Germany, August 2021.
7) H. Bahrehmand, M. Bahrami, Improved coefficient of performance in sorption systems, *International Sorption Heat Pump Conference*, Berlin, Germany, August 2021.
8) H. Bahrehmand, M. Bahrami, Optimal design of sorber beds for sorption systems, 5th *IEA Experts Meetings*, University of Ottawa, Canada, May 2019.
9) M. Bollwein, R. Abadi, H. Bahrehmand, Majid Bahrami, Potential integration of sorption cooling systems in PEM fuel cell buses, 5th *IEA Experts Meetings*, University of Ottawa, Canada, May 2019.
10) H. Bahrehmand, M. Bahrami, Analytical model for sorber bed heat and mass exchangers of sorption cooling systems, *International Conference on Polygeneration*, Fukuoka, Japan, 2019.
11) H. Bahrehmand, M. Khajehpour, W. Huttema, C. McCague, M. Bahrami, The impact of graphite flake on specific cooling power of sorption chillers, *Heat Power Cycles Conference*, Bayreuth, Germany, 2018.
12) S. Bahrehmand, K. Fayazmanesh, W. Huttema, M. Ahmadi, C. McCague, M. Bahrami, Analytical modeling of oscillatory heat transfer in coated sorption beds, *International Sorption Heat Pump Conference*, Tokyo, Japan, August 2017.

1. Introduction to cooling technologies, vapor compression versus sorption

Cooling is the fastest-growing use of energy in buildings but is also one of the most critical blind spots in today's energy debate [14]. Rising demand for space cooling is putting enormous strain on electricity systems in many countries, as well as driving up emissions [14]. The global stock of AC systems in buildings will grow to 5.6 billion by 2050, up from 1.6 billion today – which amounts to 10 new ACs sold every second for the next 30 years [15]. The global AC market was valued at USD $135.2 billion in 2018 and is expected to reach around USD $292.7 billion by 2025, at a compound annual growth rate (CAGR) of approximately 11.7% for the forecast period of 2019 to 2025 [16]. **Fig. 1** shows the space cooling energy demand growth from 2016 to 2050 [14]. It can be seen that global cooling energy demand is expected to triple by 2050, requiring new electricity capacity equivalent to the combined electricity capacity of the US, EU and Japan today [15]. **Fig. 1** also shows that with advancements of cooling technologies, the space cooling energy demand in 2050 can be reduced by 45%. Advancements of cooling technologies include (i) performance enhancement of the current cooling systems and (ii) development of cooling systems powered with energy sources other than electricity. **Fig. 2** shows the share of cooling in electricity system peak loads in selected countries/region. It can be seen that the cooling electricity peak load will increase more in the fast-growing nations, with the largest increase happening in hot countries like India – where the share of AC in peak electricity load could reach 45% in 2050, up from 10% today without action [14], [15]. Nonetheless, advancements in cooling technology can decrease this peak load; and thus the need for new power plants, and investments in utilities and electrical grid to meet peak power demand [14], [15]. **Fig. 3** shows that with technology advancements, the cumulative investments in power generation for space cooling to 2050 can be reduced by 38% from USD $3.183 trillion to USD $1.977 trillion [14].

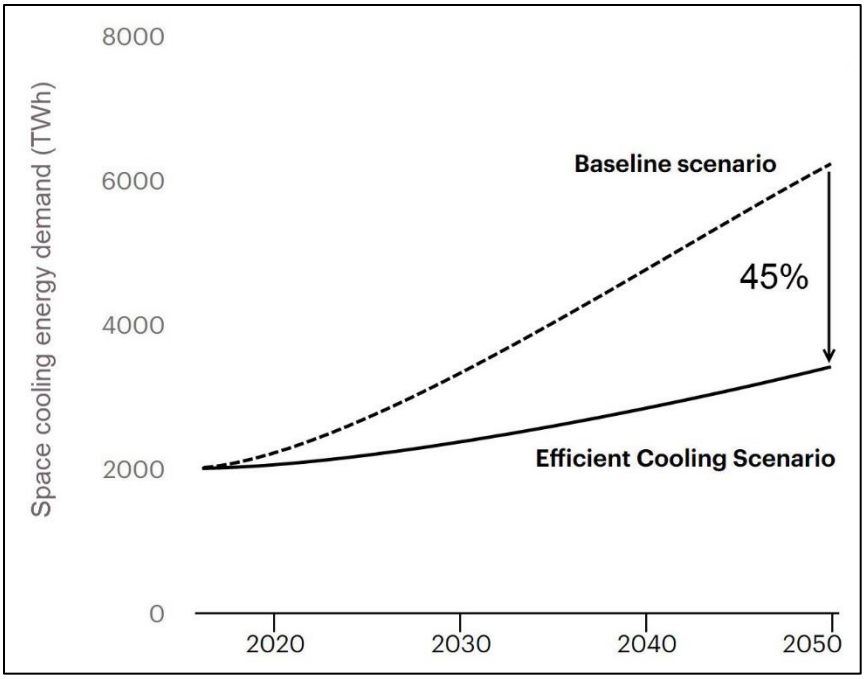

Fig. 1. Space cooling energy demand growth from 2016 to 2050, projections from International Energy Agency [14]

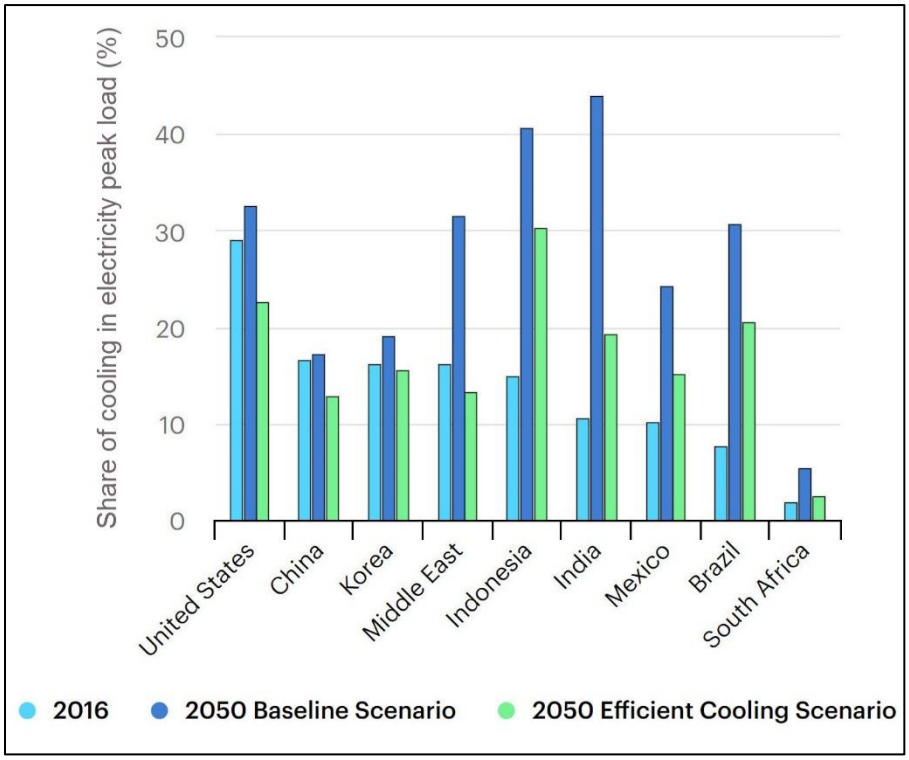

Fig. 2. Share of cooling in electricity system peak loads in selected countries/regions from 2016 to 2050, projections from International Energy Agency [14]

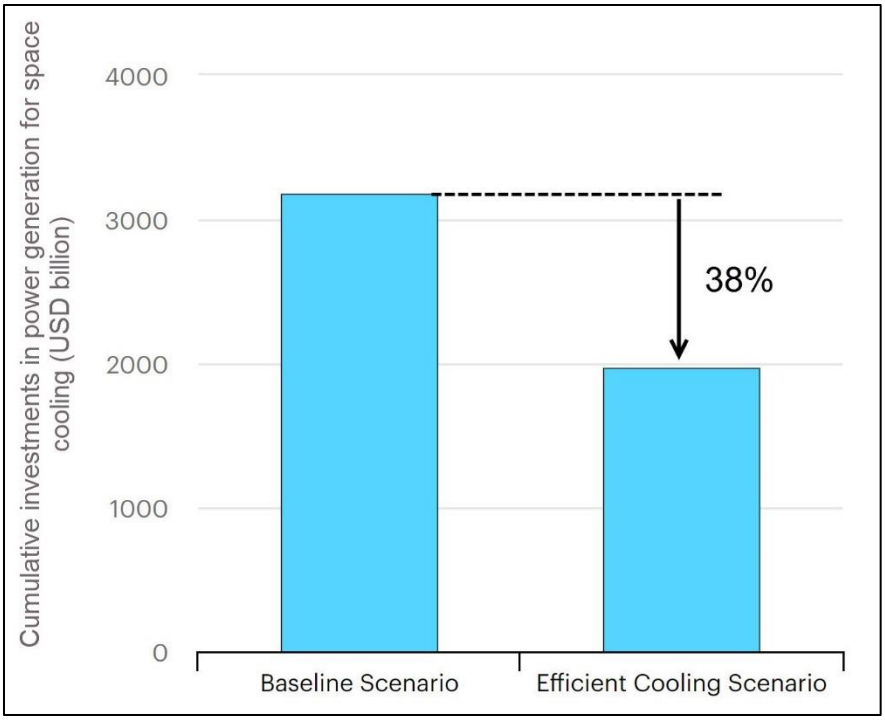

Fig. 3. Cumulative investments in power generation for space cooling to 2050, projections from International Energy Agency [14]

1.1. State-of-the-art of refrigeration systems

Refrigeration systems are used to produce cooling effects for air conditioning (AC) applications [17]–[20], ice-making industries [21], food industries [22], vaccine protection [23], etc. Vapor compression refrigeration technology is the dominant technology currently being used in the market [6]. Alternative cooling technologies are magnetic cooling, thermoacoustic cooling, thermoelectric cooling, reversed Stirling cooling, absorption cooling, and adsorption cooling [24]. In the following, these cooling technologies are briefly discussed and compared.

1.1.1. Vapor compression refrigeration (VCR) systems

Vapor compression refrigeration (VCR) systems are currently the most used technology [6] and form 99% of space-cooling energy consumption in the US [7]. **Fig. 4** shows the schematic diagram of a VCR system. In a VCR system, the low-pressure and low-temperature refrigerant enters the compressor in the state of saturated vapor and undergoes a compression process, which increases its pressure and temperature. Subsequently, the superheated vapor refrigerant is condensed in the condenser and releases heat to the ambient. Afterwards, the saturated liquid refrigerant passes through

an expansion valve or a capillary tube to reduce its pressure and become ready for the evaporation process at low temperature. Finally, the refrigerant, which is a mixture of liquid and vapor phases at this state, is evaporated in the evaporator and provides the cooling effect [25].

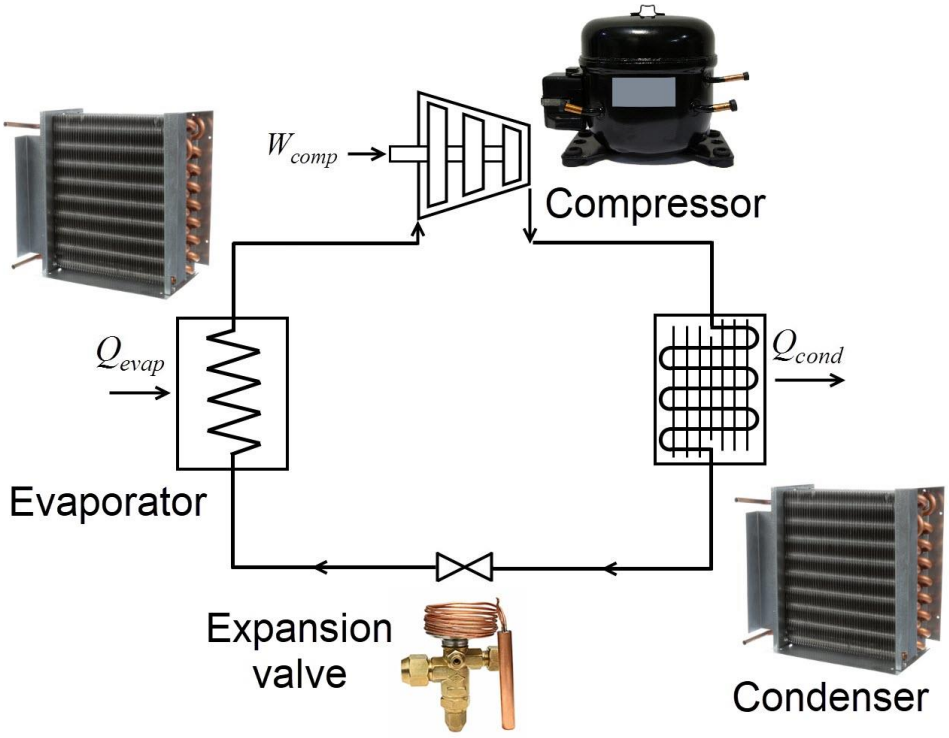

Fig. 4. Schematic diagram of vapor compression refrigeration (VCR) systems

This dominant position of VCR has been achieved due to its low capital cost, superior efficiency, low operating cost, and good personal safety record compared to the other cooling technologies [24], [26]. The coefficient of performance (COP) of efficient VCR AC products range 3.5–4.1 [27], which is higher than other cooling technologies. However, the main drawbacks of VCR are

- The increasing trend of the electricity consumption and peak power load for cooling, which would require significant investments in new power plants and electric grid. Therefore, developing cooling technologies powered by energy sources other than electricity could reduce the electricity consumption, peak power load, and hence, the investments substantially.
- The environmental impact; VCR systems contribute to about 10% of greenhouse gas (GHG) emissions globally [28].

In the transportation sector, VCR systems are run by engine mechanical power, which is generated by burning fossil fuels. According to Natural Resources Canada (NRCan), VCR systems in vehicle AC increases fuel consumption by up to 20% because of the extra load on the engine [9]; this number can reach 90% in the idling condition [29]. The US consumes approximately 27 billion liters of gasoline each year for vehicle AC systems [30]. This has placed vehicle AC as the second largest consumer of the fossil energy after vehicle propulsion [30]. The global market for automotive AC was estimated at USD $12 billion in 2015 and is anticipated to grow at a compound annual growth rate (CAGR) of over 8 % to 2024 [31].

Moreover, VCR systems in building and industrial sectors are powered by electricity, which is produced predominantly from fossil fuels, up to 76% globally [8]. On the global scale, AC systems consume 15% of the total electricity [3]–[5], and nearly 50% of the total electricity in the buildings [32]–[35].

In addition to the energy sources of VCR, their refrigerants also contribute to global warming because of their greenhouse gas (GHG) emission effects. In 2020, even though most common refrigerants such as R134a, R404A, and R410A possess zero ozone depletion potential (ODP), they still have global warming potential (GWP) of 1,300, 3,943 and 2,088, respectively [36]. Global warming increases the need for AC, which in turn, contributes to global warming, i.e. a vicious cycle that continues.

There exists refrigerants with low GWP of 0–125, such as halogenated alkenes, halogenated oxygenates, halogenated nitrogen compounds, halogenated sulfur compounds, and inorganic refrigerants, e.g. carbon dioxide and ammonia [37]. Nevertheless, their application has been limited due to one or more of the following properties: (i) poor thermodynamic properties; (ii) toxicity; (iii) chemical instability; (iv) low to moderate flammability; and (v) very high operating pressures [37].

1.1.2. Magnetic cooling systems

Magnetic cooling is based on the magnetocaloric effect (MCE) [24]. For normal magnetocaloric materials, magnetization will lead to heating of the material, and demagnetization will lead to cooling of the material. They can be coupled to heat transfer fluid circuits through heat exchangers to realize cooling effects. The COP of magnetic coolers ranges between 1.6–1.8 [38], [39], which is less than that of VCR. Other setbacks include low cooling capacities, low temperature lifts, large pressure drops through the

regenerator bed, expensive room temperature superconducting materials, and high electricity consumption [24], [40].

1.1.3. Thermoacoustic cooling systems

Thermoacoustic cooling is based on the conversion of acoustic energy to thermal energy [24]. The presence of an acoustic wave expands and contracts a working fluid (gas). As the gas expands, its pressure and temperature are reduced; likewise, as the gas contracts, its pressure and temperature are increased. To achieve cooling, the working gas must be coupled to an external heat transfer fluid through heat exchangers. The COP of thermoacoustic coolers is about 1.7 [41], which is less than that of VCR. The other downsides are the possibility of shock waves, low cooling capacities, large physical size, heat exchanger inefficiencies, high electricity consumption, and the parasitic heat conduction from the hot heat exchanger to the cold heat exchanger [24], [40].

1.1.4. Thermoelectric cooling systems

Thermoelectric cooling is based on the Peltier effect: when an electrical current is applied to two conductors of dissimilar metals, a temperature difference will develop across the two junctions, that is, one junction will become colder and the other one hotter [24]. To exploit the cooling, the materials should be coupled with heat transfer fluid through heat exchangers. The COP of thermoelectric cooling systems is about 0.3–0.6 [42], [43], which is much lower than that of VCR. The major drawbacks of thermoelectric coolers are low performance, lack of commercial materials, and high electricity consumption [24], [40].

1.1.5. Reversed Stirling cycle (RSC)

Reversed Stirling cycle (RSC) is comprised of two isothermal and two constant volume processes [20]. The main components of an RSC are two pistons located in a cylinder and a regenerator located between the two pistons. By reciprocating two pistons, one piston releases heat and the other one absorbs heat. The COP of RSC ranges between 0.8–1.6 [44]. The power density of RSC is less than 1 W/kg, which results in a heavy system [45], [46].

1.1.6. Absorption cooling systems (ACS)

In absorption cooling systems (ACS), the liquid absorbents such as LiBr, LiCl and $CaCl_2$, absorb the refrigerant such as water in the absorber when the absorbent is cooled

with a heat transfer fluid (HTF) through a heat exchanger (HEX). The refrigerant is evaporated from the evaporator and generates cooling. Afterwards, the weak solution of absorbent and refrigerant is pumped to the regenerator where it is heated with HTF through HEX. The refrigerant is desorbed from the regenerator to the condenser where it is condensed and then travels to the evaporator through an expansion valve. The rich solution returns to the absorber through an expansion valve to continue the cycle [47]. Replacing the compressor in VCR with a pump in ACS reduces the power consumption of the system dramatically [46]. The COP of ACS is below 0.8 when low-grade thermal energy (LGTE) is used, i.e. heat sources with temperature less than 100 ºC [48]. The COP of ACS can increase to 1.8 if higher temperature heat sources and multi-effect ACS are used [48]. Nonetheless, the system would become larger due to multi-stages of absorption and require higher levels of heating such as gas-fired regenerators. The main drawbacks of ACS are the large size, low COP, corrosive absorbents, low mass transfer, crystallization, swelling and agglomeration of salt [46], [47], [49], [50].

1.1.7. Adsorption cooling systems (SCS)

The operation of adsorption cooling systems is similar to that of ACS, i.e. based on two main processes, namely heating–desorption–condensation and cooling–sorption–evaporation. The main difference is that in SCS, the sorbent does not flow between the hot and cold absorbers, rather it is heated and cooled intermittently, for desorption and sorption processes, respectively. The advantages of SCS are non-corrosive, non-toxic and environmentally friendly sorption pairs with zero ozone depletion potential (ODP) and zero global warming potential (GWP), low desorption temperature, no moving parts, low noise level, low electricity consumption and low maintenance [46], [51], [52]. Nevertheless, the major disadvantages are low COP because of temperature swing between sorption and desorption and large size. COP of SCS ranges from 0.50 to 0.75, see Section 1.7 for more details. However, SCS can be powered with LGTE, such as waste heat and solar energy, which is non-payable and abundant in transportation, industrial and building sectors.

1.2. Available waste heat and utilization

Low-grade thermal energy (LGTE) such as waste heat and solar energy is abundant in transportation, building and industrial sectors. Waste heat is available in the form of steam, hot water, fume and exhaust discharged from engines, boilers, furnaces, refrigeration

systems, driers, air compressors, fuel cells, data centers, etc. [53]. **Fig. 5** shows the Canadian energy flow from the energy sources to the export energy, domestic useful energy and domestic waste energy. It can be observed in **Fig. 5** that in domestic energy consumption, 67% of the primary energy is wasted.

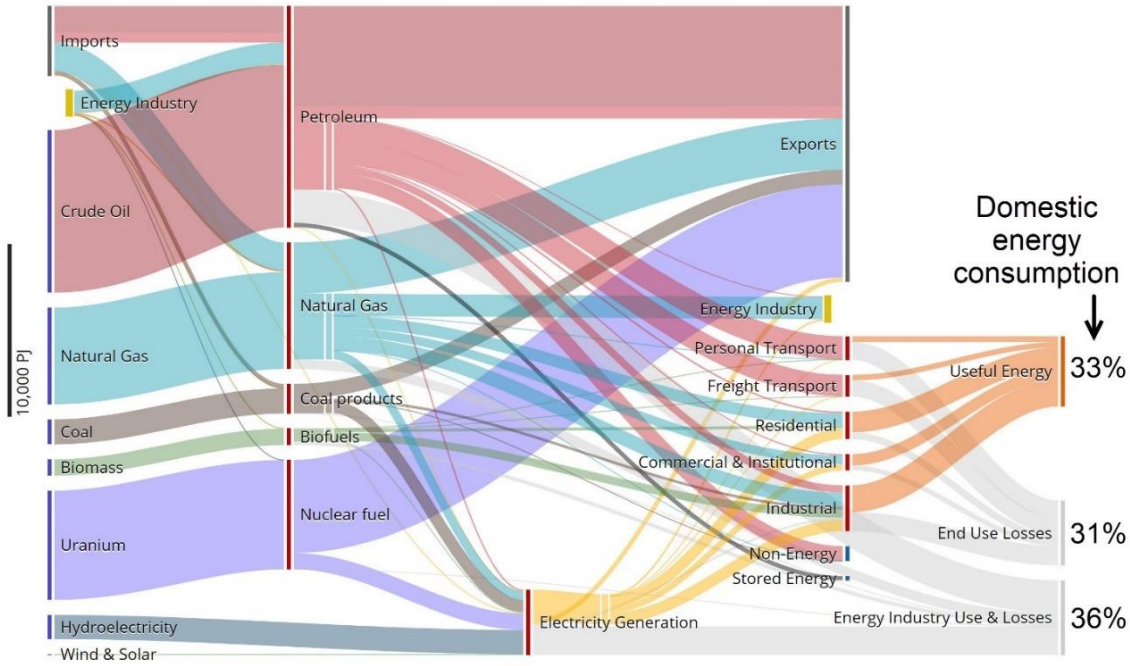

Fig. 5. Canadian energy flow from sources to useful and waste energy 2013, data from CESAR: Canadian Energy Systems Analysis Research [54]

Fig. 6 shows the global waste heat distribution in 2016 [8]. It can be seen that 52% of the global primary energy is wasted in the form of heat. **Fig. 6** also indicates that 63% of the global waste heat is low-grade, i.e. $T < 100\ ^{o}C$. Compared to high-grade ($T > 300\ ^{o}C$) and medium-grade ($100\ ^{o}C < T < 300\ ^{o}C$) waste heat, utilization and recovering low-grade waste heat is far more challenging and not commonly applied in practice [53]. The low-grade waste heat has the potential to be utilized by adsorption [55], absorption [56], organic Rankine cycles [57] and Kalina cycles [58] technologies to produce electricity, heating, cooling, fresh water and hydrogen [53]. Among these technologies, sorption technology has the advantages of simple configuration, no moving parts, environmentally friendly refrigerants and high energy density. Sorption systems can utilize the low-grade waste heat to (i) generate cooling for air-conditioning and refrigeration; (ii) store thermal energy; (iii) upgrade the heat to a higher temperature level (heat transformers); (iv) heat pumping; (v) dehumidification; (vi) desalination; and (vii) gas separation. However, the

main disadvantages of incumbent sorption systems include bulkiness, poor heat and mass transfer, and output intermittency [53]. The present study focuses on the sorption cooling systems (SCS) for air-conditioning applications. Nonetheless, the proposed methodology can be applied to other applications by changing the operating conditions and the objective functions.

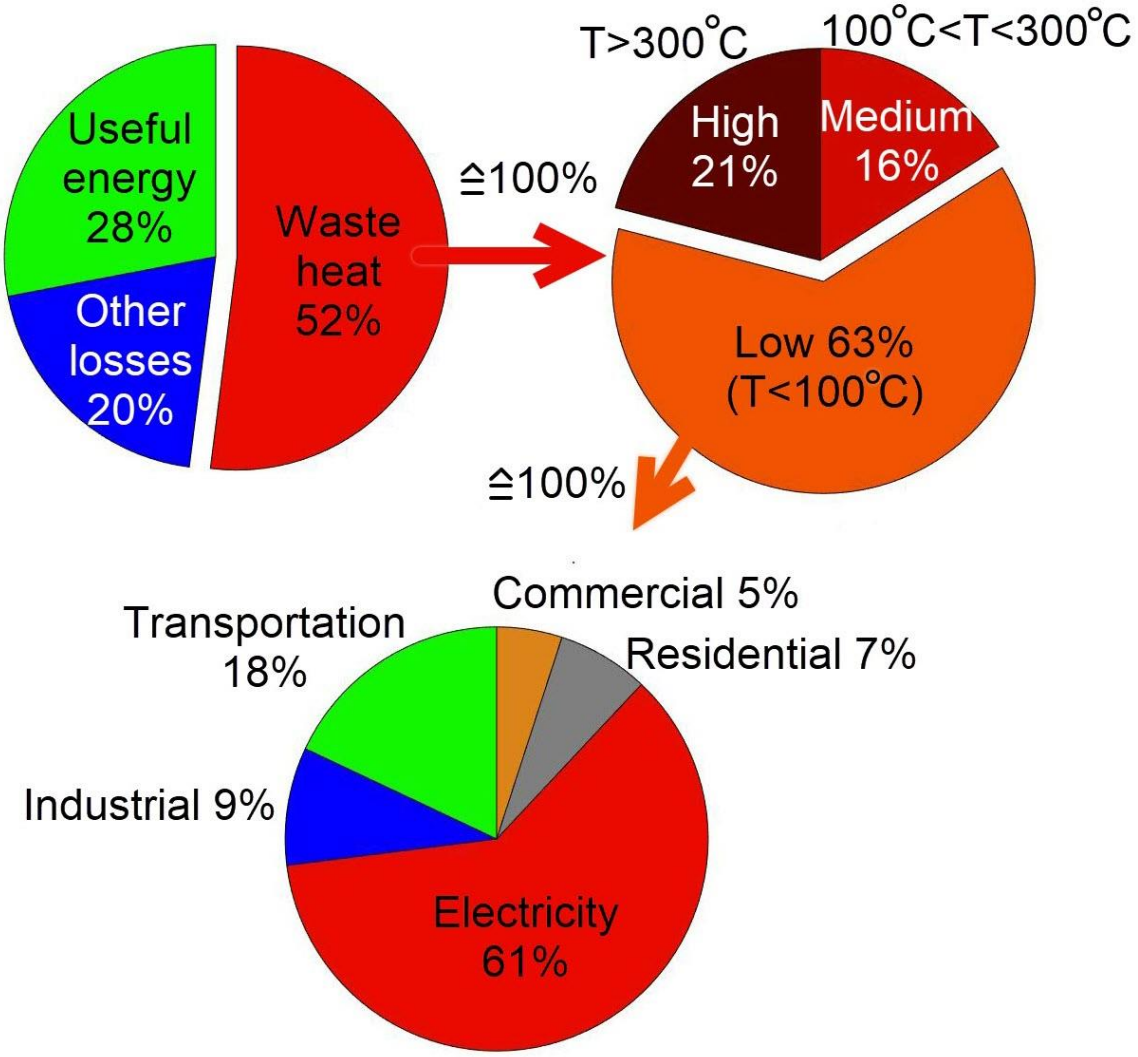

Fig. 6. Global waste heat distribution in 2016 with their temperature levels [8]

As an example, **Fig. 7** shows the energy consumption in internal combustion engines (ICE) in vehicles [10]. It can be seen that 70% of total fuel energy is wasted to the ambient in the form of heat and only 25% of the input energy is used for vehicle propulsion and accessories. In a more innovative and greener system such as in PEM fuel cell buses, the AC system draws 30–44% of the electric power generated by the fuel cell [59], and 50% of the input hydrogen energy in PEM fuel cells is wasted to the ambient in the form of heat

[60], more information about the integration of sorption cooling systems in PEM fuel cell buses can be found in Appendix H. The available waste heat can be utilized to run sorption cooling systems (SCS) to address the cooling need, which leaves the mechanical and electrical energy output for propulsion, increasing the efficiency substantially, as well as decreasing the GHG emissions.

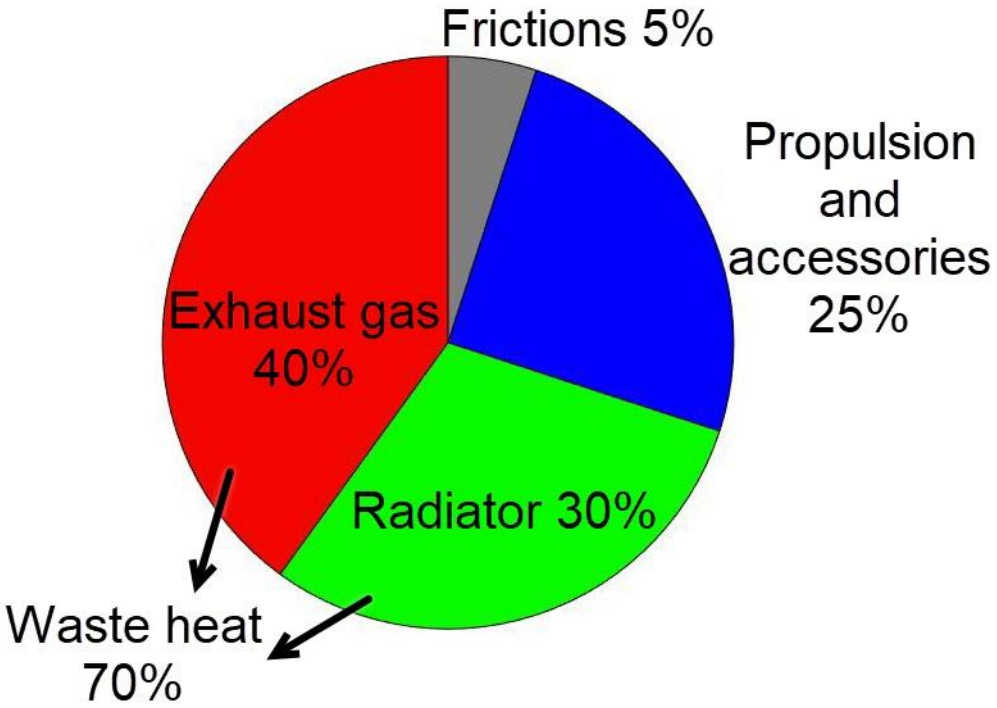

Fig. 7. Energy consumption of internal combustion engines (ICE) in vehicles [10]

As another example, in electric vehicles (EV), AC systems are the highest consumer of electric power among the auxiliary components [61]. AC systems reduce the driving range of EVs by about 30–40% depending on the size of the AC and the driving cycles [10], [62]. Sorption systems can be desorbed while electric vehicles (EV) are being charged using electric resistance heaters [63]. After the EV starts a trip, the sorption systems can start the sorption/evaporation process to generate AC without using the battery electricity, which can increase the battery range considerably [63].

1.3. Sorption phenomena

Adsorption is, in general, the adhesion of ions or molecules of gases, liquids or dissolved solids to a solid surface [64]. The adsorption phenomenon is an exothermic process in which molecules of a liquid or gas, called adsorbate, accumulate on a solid surface, called adsorbent. Adsorbents are porous materials with the ability to take up

several times of their volume of gases or liquids. **Fig. 8** shows the structure and scanning electron microscope (SEM) images of three common adsorbents, namely activated carbon, silica gel and zeolite. On the other hand, in absorption process, molecules of gas or liquid penetrate in the solid or liquid phase. Composite sorbents consist of salts impregnated into the pore structures of porous matrices. The porous matrix such as silica gel adsorbs the adsorbate and the salt absorbs the absorbate. Due to the simultaneous adsorption and absorption in composite sorbents, the phenomenon is called sorption, i.e. adsorption and absorption, and the material is called sorbent, i.e. adsorbent and absorbent.

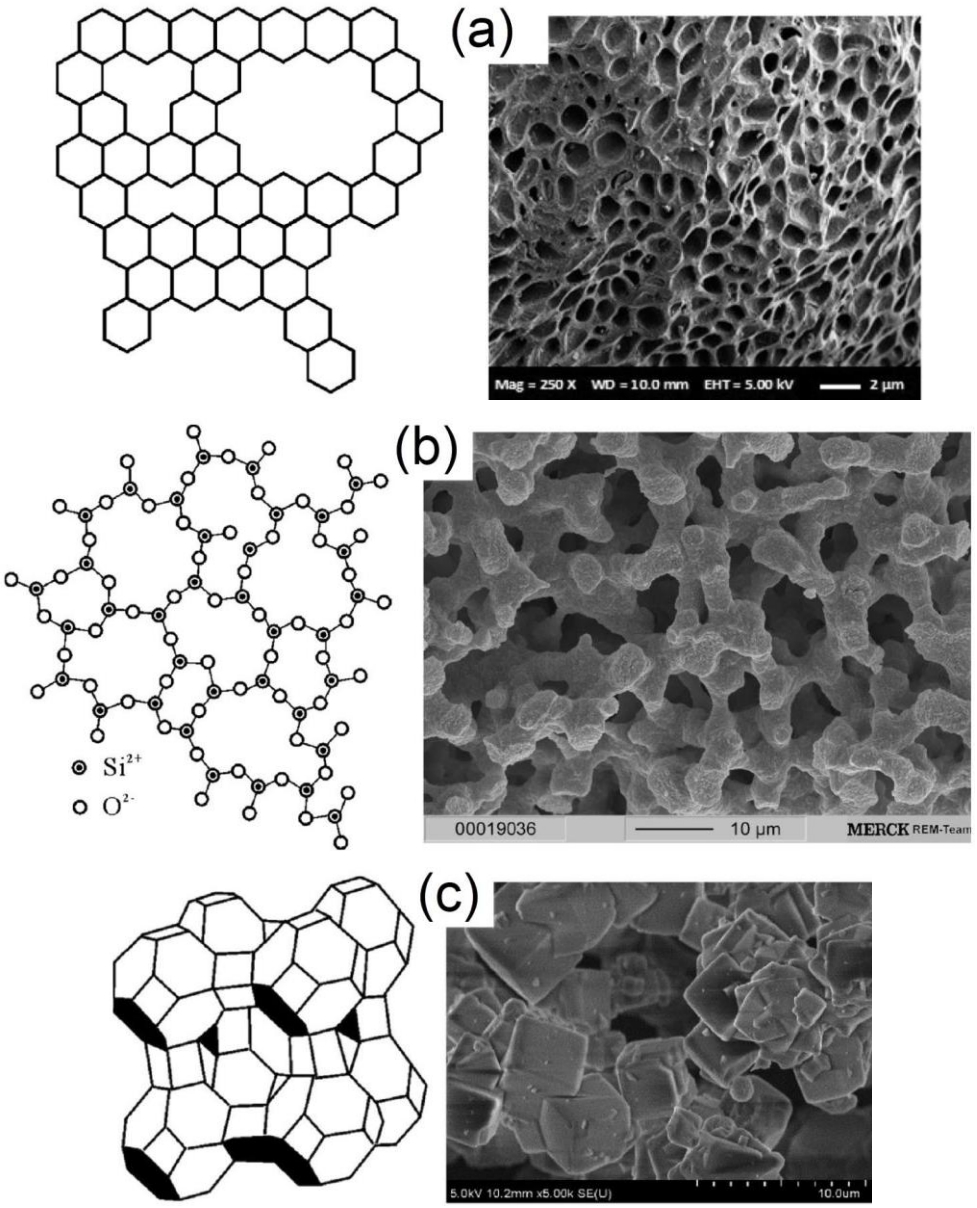

Fig. 8. Structure and SEM images of sorbent materials: (a) activated carbon; (b) silica gel; and (c) zeolite [65]–[70]

1.4. Selection of sorption pairs

1.4.1. Selection of sorbate (refrigerant)

Table 1 shows the comparison between the most commonly used sorbates (refrigerants) in sorption cooling systems. In the present study, water is selected as the sorbate due to the high enthalpy of evaporation, non-toxicity, non-flammability, compatibility with metals, zero ODP and zero GWP. However, the low operating pressure requires suitable sealing and vacuum chamber design. Also, **Table 1** shows that water

cannot operate below 4ºC, which is acceptable for AC applications as the common AC temperature is 6 ºC [71].

Table 1. The most commonly used sorbates in sorption cooling systems and their comparison [6]

	Water	**Ammonia**	**Methanol**	**Ethanol**
h_{fg} (kJ/kg) at 40ºC	2,406	1,333	1,195	905
Operating pressure (kPa) at 5–40ºC	0.5–5.5	500–2,000	5–50	2–20
Toxicity/flammability	No	Yes	Yes	Yes
Compatibility with metals	Compatible	Incompatible with copper	Incompatible with copper at high temperature	–
ODP	0	0	–	–
GWP	0	0	2.8	–
Minimum operating temperature (ºC)	4	-20	-20	-20

1.4.2. Selection of sorbent material

Table 2 shows three main categories of sorbent materials, namely (i) physical sorbents; (ii) chemical sorbents; and (iii) composite sorbents [67], [72]. Physical sorbents such as silica gel and zeolite have relatively low sorption capacity compared to chemical and composite sorbents. On the other hand, chemical sorbents such as $CaCl_2$ and CaO have relatively high sorption capacity; nonetheless, their application is limited due to the swelling and agglomeration of salt, and the low mass transfer resulting from their low specific surface area [50], [67]. Composite sorbents offer a high specific surface area due to the impregnation of salts into the pore structures of porous matrices, which increases the mass transfer significantly. Moreover, composite sorbents such as silica gel+$CaCl_2$ have relatively high sorption capacity and a wide range of relative pressure, p/p_0, over which their sorption occurs.

Table 2. Different categories of sorbent material, their bonds, advantages and disadvantages [67], [72]

Sorbent	**Physical**	**Chemical**	**Composite**
Bond	Van der Waals	Chemical	Combination of chemical and Van der Waals
Examples	Activated carbon, silica gel, zeolite, and MOFs	Metal chlorides, metal hydrides, and metal oxides	Combination of metal chlorides and activated carbon, or expanded graphite, or silica gel or zeolite
Advantage	Low mass transfer resistance	High sorption capacity	Low mass transfer resistance, high sorption capacity
Disadvantage	Low sorption capacity	High mass transfer resistance, swelling and agglomeration of salt	

Fig. 9 shows the water sorption isotherms of different sorbent materials at 25 °C. Sorption isotherms of composite sorbent of mesoporous silica gel B150/$CaCl_2$, microporous silica gel B40 and silica gel B60 (SiliaFlash, Silicycle, Inc., Quebec, Canada), FAM-Z02 (AQSOA Mitsubishi Plastics, Inc.) are obtained using an IGA-002 thermogravimetric sorption analyzer (TGA) (Hiden Isochema). Details of the TGA measurements are presented in Chapter 1. Water sorption isotherms of MOFs, MIL-101 (Cr) UoB, MIL-100 (Fe) UoB, Aluminum fumarate, CPO-27 (Ni)) are obtained from Ref. [73], and SAPO-34 from Ref. [74].

The commonly-used operating conditions of sorption cooling systems for air-conditioning (AC) applications, i.e. T_{des}=90 °C, T_{sorp}= T_{cond}=30 °C, T_{evap}=15 °C [75], correspond to p/p_0 of 0.06063 and 0.4017 for desorption and sorption, respectively. It can be seen in **Fig. 9** that the composite sorbent of silica gel B150/$CaCl_2$ has the highest sorption capacity compared to microporous silica gel, zeolite-based sorbents, i.e. FAM-Z02 and SAPO-34, and MOFs in the p/p_0 range of 0.06063 and 0.4017.

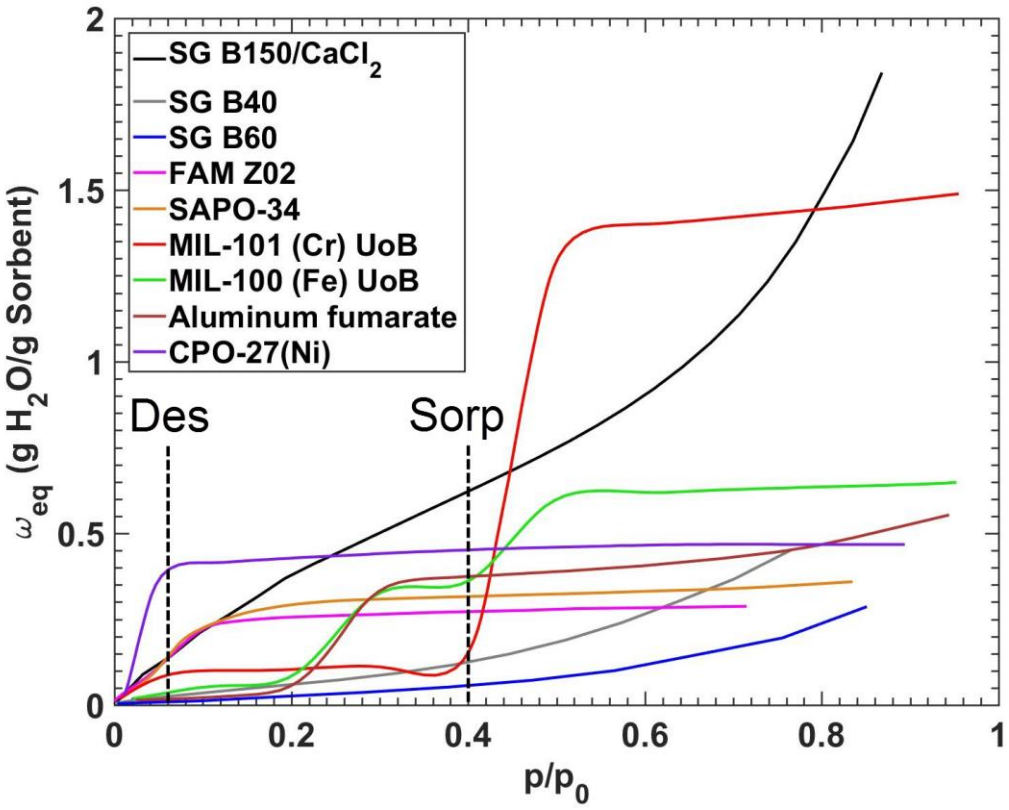

Fig. 9. Water sorption isotherms of different sorbent materials at 25 °C, silica gel B150/calcium chloride, silica gel B40, silica gel B60, zeolite-based sorbents of FAM Z02 and SAPO-34, Metal organic framework (MOF) of MIL-101 (Cr) UoB, MIL-100 (Fe) UoB, Aluminum fumarate, and CPO-27 (Ni)

Fig. 10–**Fig. 12** show the isotherms of silica gel/$CaCl_2$ composite sorbents versus zeolite-based sorbents of SAPO-34 and FAM-Z02 for different temperatures of (a) desorption, (b) sorption and condenser, and (c) evaporator. It can be seen in **Fig. 9** and **Fig. 11** that the sorption of zeolite-based sorbents occurs in a narrow range of p/p_0, which limits their application to high desorption temperatures and low condenser temperatures. For example, **Fig. 9** and **Fig. 11** show that the sorption of SAPO-34 and FAM-Z02 becomes negligible for desorption temperature less than 80 °C and condenser temperature more than 40 °C. However, **Fig. 9** shows that sorption of silica gel/$CaCl_2$ composite sorbents takes place in the entire range of p/p_0. Hence, silica gel/$CaCl_2$ composite sorbents are more suitable for applications with heat source temperature less than 80 °C and condenser temperature more than 40 °C. On the other hand, the main advantage of zeolite-based sorbents is their sorption at low evaporator temperature. **Fig. 12** indicates that by decreasing the evaporator temperature, sorption of silica gel/$CaCl_2$

composite sorbents reduce substantially more than that of zeolite-based sorbents. Consequently, zeolite-based sorbents may be more suitable for applications with low evaporator temperature.

In the present PhD thesis, composite sorbents of silica gel B150/$CaCl_2$ are used due to

- Higher sorption capacity compared to the other sorbents for the operating conditions of air-conditioning applications, **Fig. 9**.
- Higher sorption capacity at low desorption temperature and high condenser temperature, **Fig. 9** and **Fig. 11**.
- Lower cost and higher market availability [76].

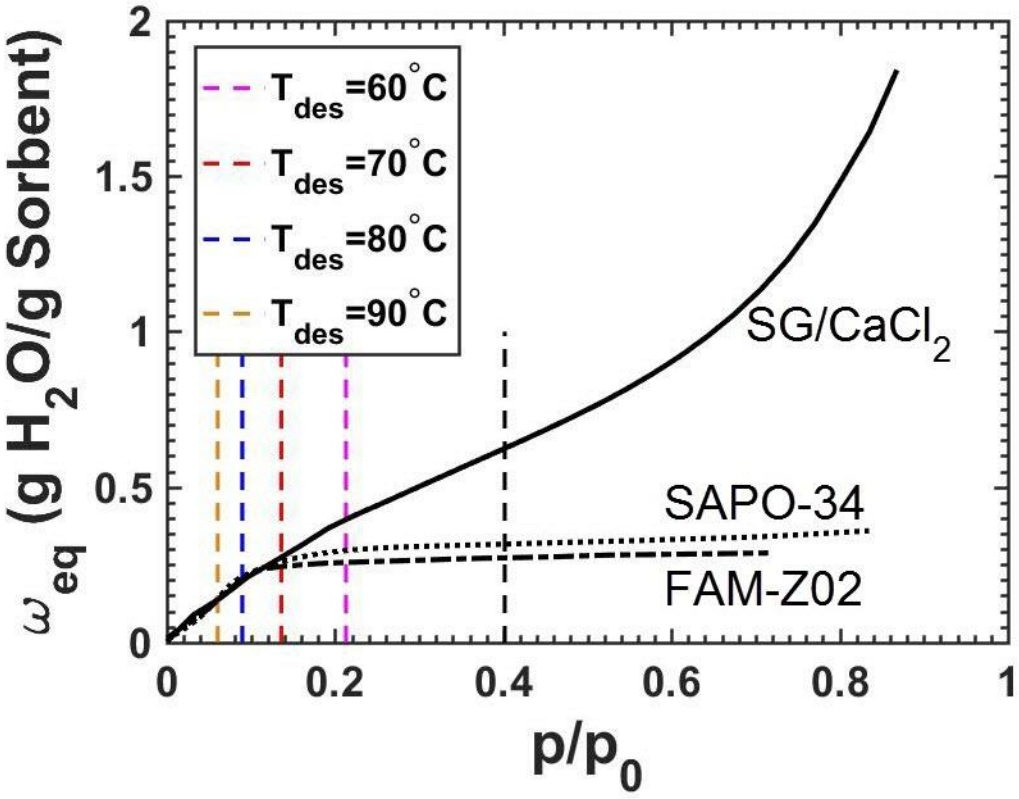

Fig. 10. Isotherms of silica gel/$CaCl_2$ composite sorbents versus zeolite-based sorbents of SAPO-34 and FAM-Z02 for different desorption temperatures, isotherms were obtained at 25 °C

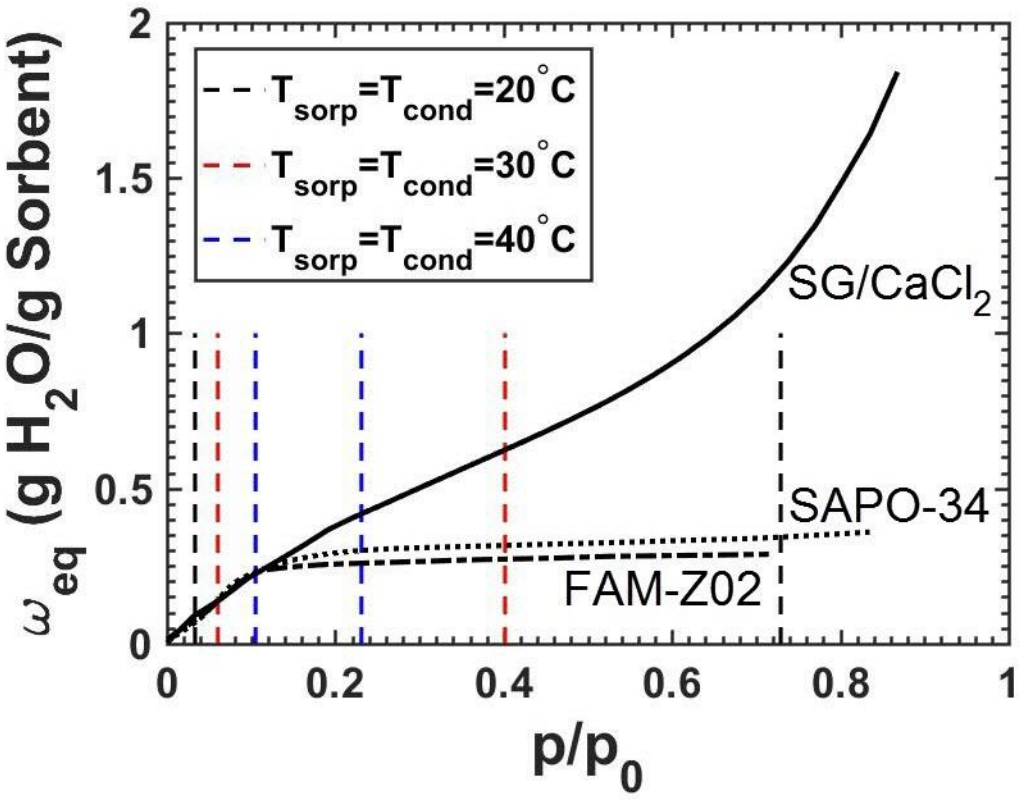

Fig. 11. Isotherms of silica gel/$CaCl_2$ composite sorbents versus zeolite-based sorbents of SAPO-34 and FAM-Z02 for different sorption and condenser temperatures, isotherms were obtained at 25 °C

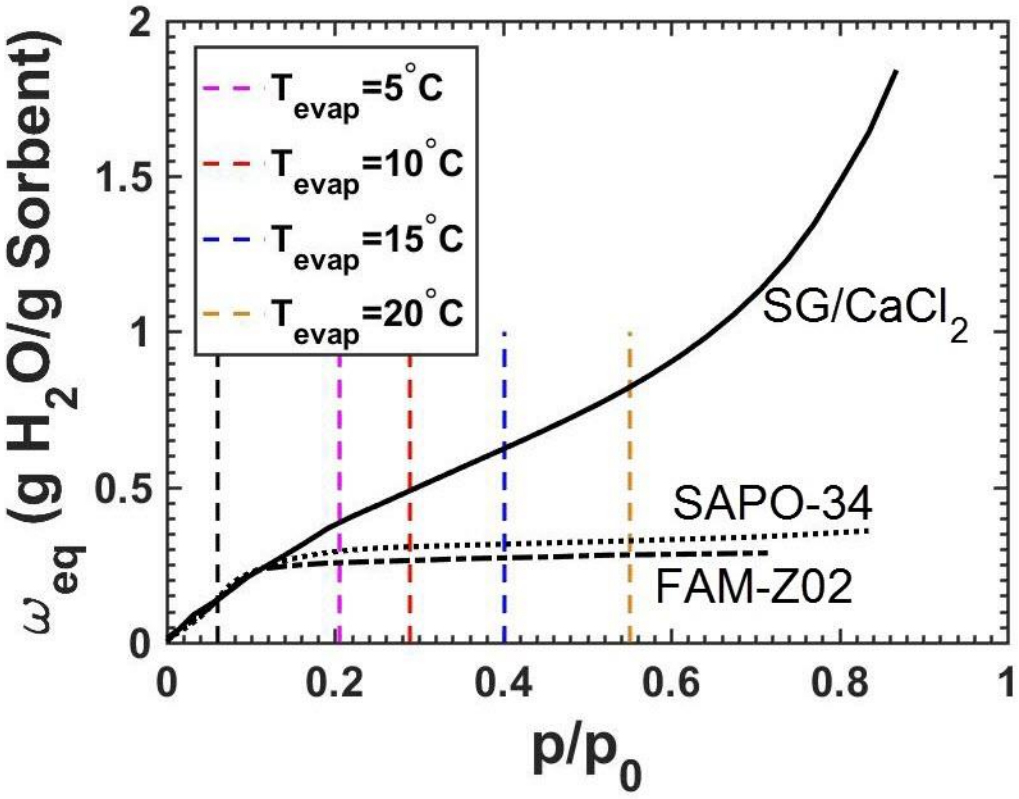

Fig. 12. Isotherms of silica gel/$CaCl_2$ composite sorbents versus zeolite-based sorbents of SAPO-34 and FAM-Z02 for different evaporator temperatures, isotherms were obtained at 25 °C

One important consideration in the composite sorbents of salt in porous matrix such as $CaCl_2$ in silica gel is the threshold where the pores of the porous matrix become filled with salt/water solution. After this threshold, the salt solution starts leaking from the pores and forming a film on the surface of the silica particles [77]. Tanashev et al. [78] measured the change in the thermal conductivity of salt in silica composites as a function of adsorbed water and observed a steep rise when the salt solution leaked from the pores, connecting the silica gel particles and enhancing the heat transfer. For example, for silica gel/$CaCl_2$ sorbents, the thermal conductivity jumped from 0.21 (W/m.K) to 0.31 (W/m.K) by leaking the salt solution from the pores. It was found that the threshold occurs when the pore volume fraction occupied with the salt solution reaches 0.60-0.64 [78]. The leakage of salt solution from the pores can decrease the mass transfer in sorption systems, and thus should be avoided by adjusting the ratio of $CaCl_2$ to silica gel depending on the operating conditions and the range of p/p_0 [77], [79].

1.5. Thermodynamic cycle of SCS

Sorption cooling systems (SCS) work based on two main steps: heating–desorption–condensation and cooling–sorption–evaporation [72], [76]. As can be seen in **Fig. 13**, compared to **Fig. 4**, the compressor in VCR is replaced with sorber bed heat and mass exchangers (S-HMXs) in SCS. The S-HMXs consist of three main components (i) sorbent material in the form of grains, pellets or coating; (ii) heat exchanger (HEX); and (iii) heat transfer fluid (HTF). Sorbent materials can ad/absorb the sorbate when cooled and connected to the evaporator; and can desorb the sorbate to the condenser at a higher pressure when heated. The sorbent is heated and cooled with HTF through HEX. As a result, the increase in pressure, or the compression of the refrigerant, which is the driving force in the refrigeration cycles, can be provided by the heat, rather than the compressor work. Hence, waste heat and solar energy can be utilized to run the refrigeration cycle instead of the mechanical work from the engines or electrical energy in VCR.

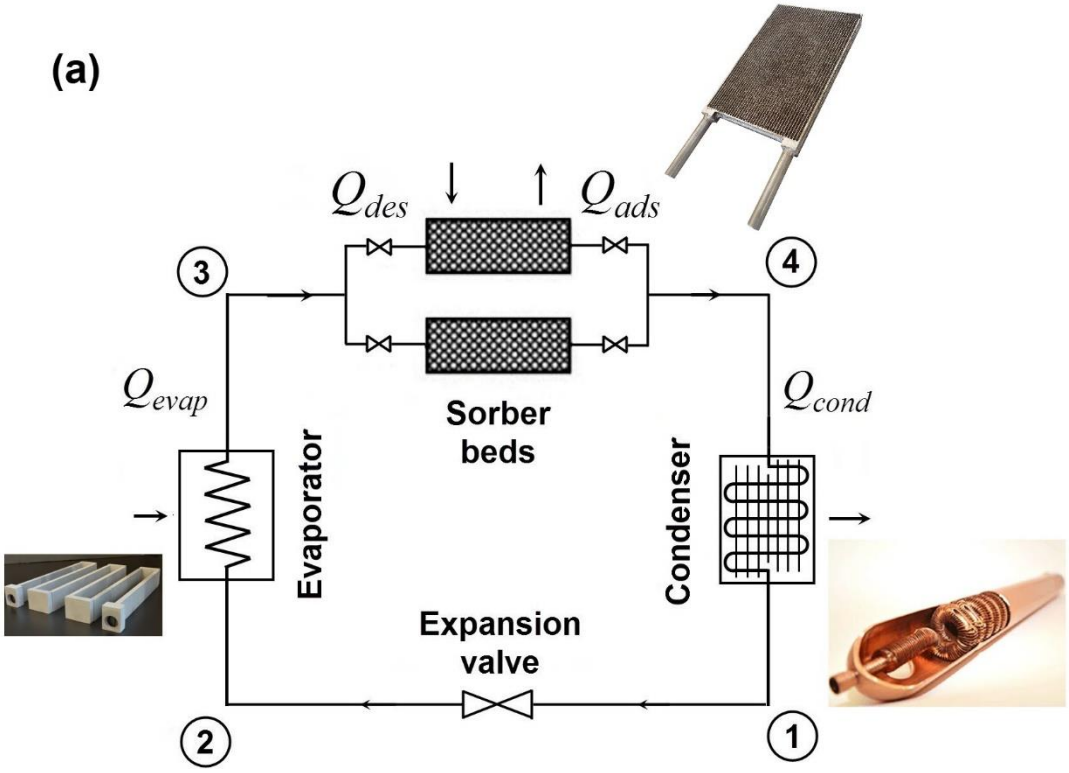

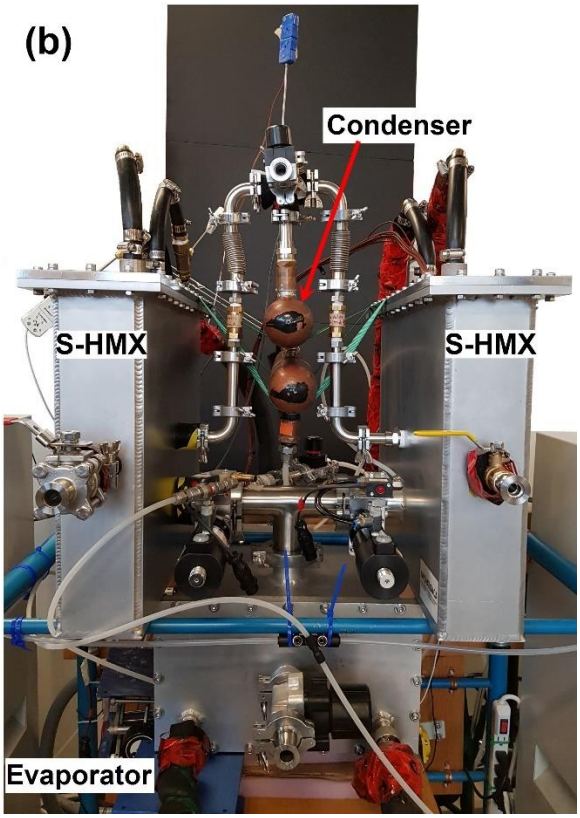

Fig. 13. (a) Schematic diagram; and (b) picture of sorption systems available in our laboratory consisting of sorber bed heat and mass exchangers (S-HMX), evaporator and condenser. More details can be found in Section 5.4

Fig. 14 presents the basic thermodynamic cycle of an SCS [72], [76]. More information about the advanced sorption cycles is presented in Appendix A. The first step is isosteric cooling, process 1'-2'. Both valves of the S-HMXs are closed and the bed is cooled at a constant uptake, 1'-2', to prepare for sorption process. At the same time, the refrigerant pressure is reduced at a constant enthalpy by passing through an expansion valve, Process 1-2. Then, the valve to the evaporator is opened and the sorbate is evaporated in the evaporator, Process 2-3, and ad/absorbed in the S-HMX at a constant pressure, i.e. isobaric sorption, Process 2'-3. Due to the exothermic nature of sorption, the S-HMX needs to be cooled during this process. Subsequently, both valves are closed, and the bed is heated at a constant uptake to prepare for the desorption process, i.e. isosteric heating, 3-4. Finally, the valve to the condenser is opened, and the refrigerant is desorbed in the S-HMX, i.e. isobaric desorption, Process 4-1', and condensed in the condenser, Process 4-1. Because of the endothermic desorption, the S-HMX needs to be heated in this process.

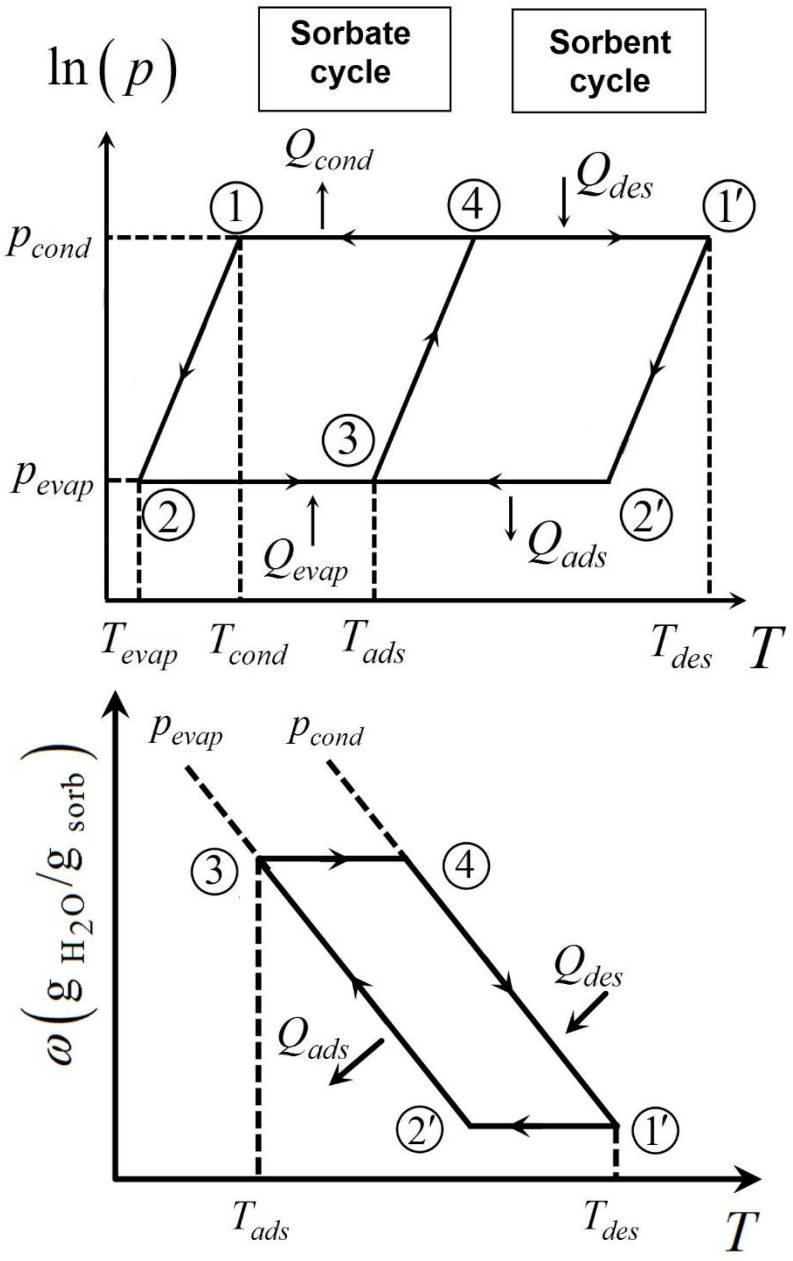

Fig. 14. Thermodynamic cycle of sorption cooling systems: isosteric cooling (1'-2'), isobaric sorption (2'-3), isosteric heating (3-4), and isobaric desorption (4-1')

1.6. Performance parameters

Specific cooling power (SCP) represents how fast the cooling energy can be delivered and how compact the system is. For a sorption cooling system with an ideal evaporator and condenser, SCP can be increased by enhancing the heat and mass transfer processes in the S-HMX. SCP can be defined in different ways depending on the system scale and the objective as follows:

- Cooling power per sorbent mass. This parameter is the most widely used parameter in the literature [6], [75] for the research prototypes. Thus, this parameter is used as the main SCP parameter in the present study to be compared against the literature.

$$SCP = \frac{Q_{evap}}{m_{sorb}\tau} = \frac{m_{sorb}\int_{ads}\frac{d\omega}{dt}h_{fg}dt}{m_{sorb}\tau} = \frac{\Delta\omega\, h_{fg@T_{evap}}}{\tau} \quad \text{[W/kg]} \quad (1)$$

  where, Q_{evap} is the evaporative cooling energy (J), m_{sorb} is the sorbent mass (kg), τ is the cycle time (s), h_{fg} is the sorbate enthalpy of evaporation (J/kg), and ω is the sorbate uptake (g sorbate/g sorbent).

- Cooling power per total mass of the sorber bed heat and mass exchanger (S-HMX) consisting of the sorbent, heat exchanger (HEX) and heat transfer fluid (HTF). This parameter provides a better representation of the sorption system as the sorbent material is not standalone, rather it is always used with HEX and HTF. This parameter is used in the present study and compared against the studies in the literature that report mass of HEX and HTF.

$$SCP_{S-HMX} = \frac{Q_{evap}}{\left(m_{sorb} + m_{HEX} + m_{HTF}\right)\tau} \quad \text{[W/kg]} \quad (2)$$

  where, Q_{evap} is the evaporative cooling energy (J), m_{sorb} is the sorbent mass (kg), m_{HEX} is the heat exchanger (HEX) mass (kg), m_{HTF} is the heat transfer fluid (HTF) mass (kg), and τ is the cycle time (s).

- Cooling power per total volume of the S-HMX consisting of the sorbent, HEX and HTF. This parameter is used in the present study.

$$VSCP_{S-HMX} = \frac{Q_{evap}}{\left(V_{sorb} + V_{HEX} + V_{HTF}\right)\tau} \quad \text{[W/m}^3\text{]} \quad (3)$$

where, Q_{evap} is the evaporative cooling energy (J), V_{sorb} is the sorbent volume (m^3), V_{HEX} is the HEX volume (m^3), V_{HTF} is the HTF volume (m^3), and τ is the cycle time (s).

- Cooling power per total mass or volume of the sorption cooling system consisting of (i) sorber bed heat and mass exchangers (S-HMXs) and their vacuum chambers; (ii) evaporator and its vacuum chamber; (iii) condenser and its vacuum chamber; (iv) liquid-to-air heat exchangers to cool the condenser and the S-HMX with the ambient; (v) liquid-to-air heat exchangers to provide the evaporative cooling to the cooling zone; (vi) vacuum connections, fittings and the valves; (vii) heat transfer fluid connections, fittings, valves, and hoses to the S-HMXs, evaporator, condenser, the liquid-to-air heat exchangers, and to the heat source; (viii) programmable logic controllers (PLC) and the sensors to control the operation of the sorption cooling system; (ix) the unit frame; and (x) the user interface panel. This parameter is the most suitable index for the entire system performance. However, most of the aforementioned components are not employed in research prototypes as the tests are conducted with temperature control systems to mimic the heat source, ambient cooling and evaporative cooling. Hence, this parameter is only used for the commercial sorption AC products.

$$SCP_{total} = \frac{Q_{evap}}{m_{tot}\tau} \quad [W/kg] \quad (4)$$

$$VSCP_{total} = \frac{Q_{evap}}{V_{tot}\tau} \quad [W/m^3] \quad (5)$$

where, Q_{evap} is the evaporative cooling energy (J), m_{tot} is the total system mass (kg), V_{tot} is the total system volume (m^3), and τ is the cycle time (s).

Thermal coefficient of performance (COP_{th}) is defined as the ratio of evaporative cooling energy to the input thermal energy, Eq. (6). COP can be increased by: i) enhancing the heat and mass transfer processes inside the S-HMX, which increases both the evaporative cooling energy and the desorption heat, which overall increases COP, and ii) decreasing the sensible energy required to overcome thermal inertia of the heat exchanger (HEX), sorbent material, refrigerant inside the sorbent and the heat transfer fluid (HTF). Since, sorption cooling systems (SCS) are thermally driven, this parameter is used for both sorption research prototypes and the commercial products.

$$COP_{th} = \frac{Q_{evap}}{Q_{th,input}} = \frac{Q_{evap}}{Q_{sens} + Q_{des}} =$$

$$\frac{m_{sorb} \int_{ads} \frac{d\omega}{dt} h_{fg} dt}{\int_{des} \left(\left(m_{HEX} c_{p,HEX} + m_{sorb} \left(c_{p,s} + \omega c_{p,w} \right) + m_{HTF} c_{p,HTF} \right) \frac{dT}{dt} - m_{sorb} \frac{d\omega}{dt} h_{ads} \right) dt} \quad [-] \quad (6)$$

where, Q_{evap} is the evaporative cooling energy (J), $Q_{th,input}$ is the input thermal energy (J), Q_{sens} is thermal energy required to overcome thermal inertia of the sorber bed heat and mass exchanger (J), Q_{des} is thermal energy consumed for desorption (J), m_{sorb} is the sorbent mass (kg), m_{HEX} is the heat exchanger (HEX) mass (kg), m_{HTF} is the heat transfer fluid (HTF) mass (kg), h_{fg} is the sorbate enthalpy of evaporation (J/kg), c_p is the specific heat (J/(kg K)), ω is the sorbate uptake (g sorbate/g sorbent), T is the sorbent temperature (K), and h_{fg} is the sorbate enthalpy of sorption (J/kg). COP_{th} is particularly important is applications where a limited amount of heat source is available. One is example is provided in Appendix H.

Electrical coefficient of performance (COP_e) is defined as the ratio of evaporative cooling energy to the input electrical energy, Eq. (7). This parameter is mainly used for VCR systems. Even though SCS are thermally driven and consume a small amount of electricity, this parameter is also calculated for SCS commercial products to compare their operation costs with VCR. For SCS, the reported COP_e includes the electrical energy used by the heat transfer fluid circulation pumps.

$$COP_e = \frac{Q_{evap}}{w_{elec,input}} \quad [-] \quad (7)$$

where, Q_{evap} is the evaporative cooling energy (J) and $Q_{elec,input}$ is the input electrical energy (J).

1.7. Need for research

The performance of sorption AC has been enhanced considerably over the past decade due to new sorbent materials, coating technologies, heat exchanger designs and advanced sorption cycles [6], which has led to commercial sorption AC products. **Table 3** presents the performance of the commercially available sorption AC products in 2020 and **Fig. 15** summarizes these performance parameters in comparison between sorption AC

and VCR systems. It can be seen that COP_{th} ranges between 0.50–0.75, COP_e ranges 7.5–69.9, SCP_{total} ranges 15.9–45.4 W/kg, and $VSCP_{total}$ ranges 3.5–18.5 kW/m^3. On the other hand, in 2020, COP_e of efficient VCR AC products range 3.5–4.1, SCP_{total} ranges 113–160 W/kg, and $VSCP_{total}$ ranges 17–23 kW/m^3 [27], [80], [81]. It should be noted that in SCS, the input thermal energy is non-payable as waste heat or solar energy can be used. Thus, COP_e is the parameter that shows the operation cost due to electricity consumption. It can be seen that COP_e of SCS is 1.8–20 times higher than VCR, which can reduce the operation cost and carbon footprint substantially. Nonetheless, SCP_{total} of VCR is 2.5–10 times higher than SCS and $VSCP_{total}$ of VCR is 0.9–6.5 times that of SCS, which is the main impediment against wide adoption of SCS, particularly for automotive AC.

Table 3. List of the commercially available sorption AC products with their cooling performance

Ref.	Commercial product	Q_{evap} (kW)	COP_{th}	COP_e	SCP_{total} (W/kg)	$VSCP_{total}$ (kW/m^3)
[82]	InvenSor LTC 10 e plus	10.0	0.70	25.3	22.7	8.8
[83]	InvenSor LTC 30 e plus	35.0	0.72	39.1	29.2	15.2
[84]	InvenSor LTC 90 e plus	105.0	0.75	39.1	23.3	10.2
[85]	Fahrenheit eCoo 10	16.7	0.65	64.2	45.1	12.5
[85]	Fahrenheit eCoo 10X	25.0	0.65	48.9	45.4	14.9
[85]	Fahrenheit eCoo 20	33.4	0.65	64.2	42.5	13.0
[85]	Fahrenheit eCoo 20 ST	33.4	0.65	31.2	39.6	13.0
[85]	Fahrenheit eCoo 20X	50.0	0.65	48.9	43.4	15.6
[85]	Fahrenheit eCoo 30	50.0	0.65	50.8	40.4	15.3
[85]	Fahrenheit eCoo 30X	75.0	0.65	48.6	43.4	15.8
[85]	Fahrenheit eCoo 40X	100.0	0.65	48.4	43.5	15.6
[85]	Fahrenheit eCoo S	8.4	0.65	45.4	32.3	7.8
[85]	Fahrenheit Zeo M 10	20.0	0.50	69.9	45.4	10.1
[85]	Fahrenheit Zeo M 20	40.0	0.50	69.9	41.3	15.5
[85]	Fahrenheit Zeo M 30	60.0	0.50	69.9	41.3	18.5
[86]	SolabCool SolabChiller	4.5	0.65	7.5	17.3	3.5
[87]	HIJC ADCM models	70–350	0.65	NR	NR	NR
[88]	Mitsubishi Plastics M-TYPE	10.0	NR	NR	NR	8.1
[89]	Mayekawa Z-3515	105.0	NR	10	15.9	6.7
[89]	Mayekawa Z-3525	215.0	NR	10	21.5	8.5
[89]	Mayekawa Z-6025	430.0	NR	10	28.7	10.3

"NR" means not reported.

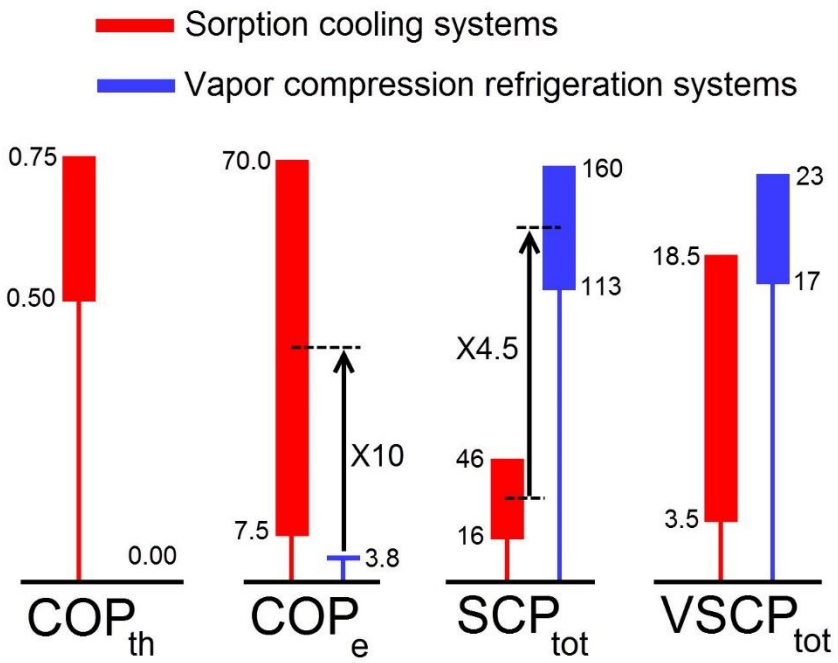

Fig. 15. Comparison of sorption cooling systems versus vapor compression refrigeration systems in terms of performance parameters of thermal coefficient of performance (COP_{th}), electrical coefficient of performance (COP_e), specific cooling power (SCP_{tot}), and volumetric specific cooling power ($VSCP_{tot}$)

Table 4 shows the commercially available hybrid VCR/SCS AC products. It can be seen that COP_e of the VCR systems increases by about 59% by adding SCS, due to less electricity consumption. **Table 4** also shows that SCP_{total} ranges 54.4–55.6 W/kg, which is between that of SCS and VCR. Furthermore, it can be observed that $VSCP_{total}$ ranges 18.06–27.97 kW/m^3, which, on average, is higher than both SCS and VCR. Therefore, in the applications where both LGTE, such as waste heat or solar energy, and electricity are available, hybrid VCR/SCS can achieve compact AC systems with low electricity consumption.

Table 4. List of the commercially available hybrid VCR/SCS AC products with their cooling performance

Ref.	Commercial product	Q_{evap} (kW)	COP_{SCS}	COP_{VCR}	COP_{th}	COP_e	SCP_{total} (W/kg)	$VSCP_{total}$ (kW/m^3)
[85]	Fahrenheit eCoo 10 HC 30	46.7	0.65	2.5	1.82	3.89	55.6	18.18
[85]	Fahrenheit eCoo 20 HC 60	91.4	0.65	1.6	1.78	2.54	54.4	27.97
[85]	Fahrenheit eCoo 20 HCN 60	92.8	0.65	NR	1.81	NR	54.6	18.06

1.8. Objective

The objective of this PhD study is to establish a systematic method to design and optimize sorber bed heat and mass exchangers for sorption systems. The next objective is to apply this method to develop sorber bed heat and mass exchangers with optimum SCP and COP (SCP > 700 W/kg and COP > 0.55), which can facilitate the adoption of SCS in AC applications. The methodology of this PhD thesis can be applied to other sorption applications, such as heat pump, heat transformer, heat storage, dehumidification, desalination and gas separation.

In the literature, it is suggested that the minimum reasonable SCP and COP of SCS are 354 W/kg and 0.55 [6], [90], [91]. The desired SCP for AC of light-duty vehicles is 350 W/kg [75]. Moreover, the maximum SCP achieved by 2016, i.e. beginning of this PhD program, was 675 W/kg [92]. Hence, the performance target for this PhD program was set to SCP > 700 W/kg, and COP > 0.55. As a proof-of-concept SCS, the cooling power was set to a cooling capacity > 0.5 kW to be tested in the lab; however, SCS are modular and can be scaled up for different applications.

The aforementioned performance targets will be achieved with the following milestones:

- Selection of suitable sorption pairs with a differential uptake of 0.4 g H_2O/g sorbent;
- Increasing the sorbent thermal diffusivity up to 1 mm^2/s by adding thermally conductive additives;
- Investigation of the transient behavior of sorbent materials by adding thermally conductive additives and their effect on sorption performance;
- Development of suitable models to be used for design and optimization of the S-HMX.
- Finding the key design and operating parameters of the S-HMXs that dominate the performance of SCS;
- Performing multi-objective optimization of the key parameters of the S-HMXs using the developed models to achieve optimum SCP and COP;
- Building proof-of-concept S-HMXs based on the optimization study for targeted AC applications; and
- Testing the optimized S-HMXs to experimentally validate the performance targets – SCP > 700 W/kg, and COP > 0.55, cooling capacity > 0.5 kW.

1.9. Organization of the Dissertation

This PhD dissertation is comprised of 6 chapters and 7 appendices organized as follows:

1.9.1. Introduction to cooling technologies, vapor compression versus sorption

Chapter 1 provides an introduction to cooling technologies for air conditioning (AC) and refrigeration. It was shown that vapor compression refrigeration (VCR) is the dominant technology currently used because of high performance, compactness, and low cost. Nonetheless, VCR systems have significant GHG emissions. Also, with the increasing trend of AC usage, the Grid and power plants would require significant investment to cope with the peak load by VCR. The substantial potential of sorption cooling systems (SCS) as an alternative to VCR was discussed due to environmentally friendly sorption pairs and utilization of low-grade thermal energy, such as waste heat and solar energy. Suitable sorption pairs were selected to achieve the target for the present PhD study. The need for research was shown by comparing SCS with VCR in terms of the performance parameters. The rationale behind the selection of the target performance parameters was elaborated.

1.9.2. Sorption performance enhancement with thermally conductive additives

In Chapter 2, the effect of graphite flakes as thermally conductive additives in the sorbent on the sorption performance are studied. First, a critical literature review is conducted to identify the suitable additives for sorption systems and the appropriate methods to experimentally investigate their effect on the sorption performance. It was found that there is no study in the literature that investigates the counteracting effects of heat and mass transfer by adding thermally conductive additives. Hence, for the first time, the conflicting effects of graphite flake additives in the sorbent was studied using a custom-built gravimetric large pressure jump (G-LPJ) test bed. G-LPJ test bed was custom-built in collaboration with Dr. Wendell Huttema, a former Postdoctoral Fellow, Dr. Claire McCague, a current Postdoctoral Fellow, and Khorshid Fayazmanesh, a PhD graduate at LAEC. Furthermore, the procedure to prepare the composite sorbents is discussed. Moreover, measurements of thermal diffusivity and sorption isotherm are presented, which were performed by Maryam Khajehpour, a former Postdoctoral Fellow at LAEC.

1.9.3. Analytical modeling of sorber bed heat and mass exchangers

In Chapter 3, for the first time, 2-D analytical models were developed that consider the spatial and temporal variation of water uptake and temperature in the sorber bed heat and mass exchanger (S-HMX), and have low computation time, which is crucial for optimization and real-time control of the S-HMXs. The assumptions and solution methodology of the analytical models are presented for the plate-fin sorber bed heat and mass exchangers (P-HMX) in Cartesian coordinate system and the finned-tube sorber bed heat and mass exchangers (F-HMX) in cylindrical coordinate system. In addition, an off-the-shelf engine oil cooler is used for validation of the model and as a benchmark for the optimized S-HMXs, which will be presented in Chapter 1. Finally, a parametric study is performed to investigate the effect of the S-HMX geometry, heat transfer characteristics and cycle time on the sorption performance.

1.9.4. Analysis of variance (ANOVA) and optimization of sorber bed heat and mass exchangers

In Chapter 4, first, a critical literature review is carried out to show the gap in the literature to perform a simultaneous optimization of the S-HMX design and operating parameters. To address this gap, for the first time, the 2-D analytical model developed in the previous chapter, is used to conduct analysis of variance (ANOVA) to pinpoint the key parameters affecting the sorption performance. Furthermore, for the first time in the literature, a multi-objective optimization on the S-HMX key parameters is conducted achieving the optimum sorption performance.

1.9.5. Development of optimized sorber bed heat and mass exchangers

In Chapter 5, For the first time in the literature, the S-HMXs of the P-HMX and the F-HMX were specifically designed for sorption cooling systems based on the optimization study. The manufacturing procedure and characteristics of the optimized S-HMXs of the plate fin sorber bed heat and mass exchanger (P-HMX) and the finned-tube sorber bed heat and mass exchanger (F-HMX) are presented. The two-sorber bed sorption test bed was initially custom-built by Dr. Amir Sharafian, a PhD graduate and Dr. Wendell Huttema, a former Postdoctoral Fellow at LAEC. The two-sorber bed sorption test bed was improved

and modified to test the optimized S-HMXs in the present study. Finally, the experimental results are presented and the optimized S-HMXs performance is evaluated.

1.9.6. Conclusions, contributions, limitations, potential for further development and broader implementation, and future research

In Chapter 6, the main conclusions, findings and contributions of this PhD study are discussed. Moreover, limitations and potential for further development and implementation of the developed methodology to other sorption applications, including, sorption pairs and thermally-conductive additives, analytical modeling, ANOVA, optimization, and development and testing of the sorber beds, are presented. Also, recommendations are presented for future research to approach the wide adoption of sorption cooling systems (SCS) for air conditioning systems and other applications of sorption systems, such as heat pump, heat transformer, heat storage, dehumidification, desalination and gas separation.

1.9.7. Enhancement of coefficient of performance (COP)

In Appendix A, methods are presented to increase COP of SCS, while keeping the system compact with high SCP. Detailed share of desorption heat and sensible energy of each component of the S-HMX, i.e. heat exchanger (HEX), sorbent material, refrigerant inside the sorbent and the heat transfer fluid (HTF) is discussed. The impact of HEX thermal conductivity and heat capacity on the COP is shown. The rationale behind the selection of aluminum as the HEX material is elaborated. Different methods of heat recovery are shown to eliminate thermal inertia of HTF.

1.9.8. Uncertainty analysis of the measurements in chapter 2 and 5

In Appendix B, the uncertainty analysis in the measurements of this PhD study are presented.

1.9.9. Gravimetric large pressure jump (G-LPJ) data

In Appendix C, the gravimetric large pressure jump (G-LPJ) data, discussed in chapter 2, is presented.

1.9.10. Optimized sorber bed heat and mass exchangers data

In Appendix D, the data obtained from two-sorber bed sorption test bed by testing the P-HMX and the F-HMX, discussed in chapter 5, is presented.

1.9.11. Matlab codes

In Appendix E, the following Matlab codes are presented:

- Matlab code used to process the G-LPJ data;
- Matlab codes used to process the two-sorber bed sorption data;
- Matlab code developed based on the 2-D analytical model for the P-HMX in Cartesian coordinate system;
- Matlab code developed based on the 2-D analytical model for the F-HMX in cylindrical coordinate system; and
- Matlab code to refine the intervals to increase the accuracy in 2-D analytical models.

1.9.12. Analysis of variance (ANOVA)

In Appendix F, a concise introduction to analysis of variance, ANOVA, used in chapter 4, is presented.

1.9.13. Drawings of sorber bed heat and mass exchangers

In Appendix G, the CAD drawings used to build the P-HMX and the F-HMX discussed in chapter 5.3, are presented.

1.9.14. Integration of sorption cooling systems in PEM fuel cell buses

In Appendix H, the integration of sorption cooling systems in PEM fuel cell buses is discussed.

2. Sorption performance enhancement using thermally conductive additives

2.1. Overview

In this chapter, for the first time in the literature, the trade-off between heat and mass transfer by adding thermally conductive additives to the sorbent is investigated. First, a critical literature review is conducted to identify the suitable additives for sorption systems and the appropriate methods to experimentally investigate their effect on the sorption performance. Furthermore, the procedure to prepare the composite sorbents is discussed. Moreover, measurements of thermal diffusivity and sorption isotherm are presented, which were performed by Dr. Maryam Khajehpour, a former Postdoctoral Fellow at LAEC. In addition, the gravimetric large pressure jump (G-LPJ) test bed is explained and the transient water uptake measurement is discussed. The G-LPJ test bed was custom-built in collaboration with Dr. Wendell Huttema, a former Postdoctoral Fellow, Dr. Claire McCague, a current postdoctoral fellow, and Dr. Khorshid Fayazmanesh, a PhD graduate at LAEC. Finally, the effect of graphite flake on the sorption performance is investigated. This chapter resulted in the following publications:

1) H. Bahrehmand, M. Khajehpour, M. Bahrami, Finding optimal conductive additive content to enhance the performance of coated sorption beds: An experimental study, *Applied Thermal Engineering*, 143 (2018) 308-315.
2) H. Bahrehmand, M. Khajehpour, W. Huttema, C. McCague, M. Bahrami, The impact of graphite flake on specific cooling power of sorption chillers, *Heat Power Cycles Conference*, Bayreuth, Germany, 2018.

2.2. Literature review

Sorber bed heat and mass exchangers (S-HMXs) need to be cooled and heated during the sorption and desorption processes, respectively. As such, the oscillatory thermal behavior of sorption cooling systems (SCS) makes the sorbent thermal diffusivity crucially important in their performance. Sorbent thermal diffusivity is one of the main limiting factors in the heat transfer between the sorbent and the heat transfer fluid (HTF) through the heat exchanger (HEX) [1], [2], [76], [93]–[95]. Hence, developing composite sorbents with higher thermal diffusivity can enhance the overall performance of the S-HMXs [96], [97]. The addition of highly conductive materials can form higher conductivity paths by providing “bridges” in the porous microstructure of the sorbent particles to increase the

overall thermal conductivity and diffusivity. However, at the same time, adding these additives will lead to a decrease in the active sorption material fraction and may increase the vapor transport resistance [98]. Moreover, many microporous adsorbents have open pore structures and high total pore volumes [99]. As a result, significant improvements in thermal diffusivity of microporous adsorbent materials have been limited to high additive fractions (>10 wt.%), compromising the total sorption capacity.

Demir et al. [100] used metallic particle additives to enhance the heat transfer rate through an unconsolidated adsorbent bed. Silica gel with metallic additives of copper, brass and aluminum (strips with 0.1 mm thickness, 2 mm width and 10 mm length) up to 15% in mass basis was investigated. They noticed that the addition of 15 wt.% of aluminum pieces to silica gel enhanced thermal conductivity of a pure silica gel bed by 242% (from 0.106 to 0.363 W/m K). They did not study the effects of the additives on the overall performance of adsorption cooling systems. Askalany et al. [101] studied the effect of using metallic additives on thermal conductivity of granular activated carbon (1-2 mm). Fillings of iron, copper and aluminum at different mass concentrations ranging from 10 to 30 wt.% have been studied. They reported that thermal conductivity increased with an increase in metallic additives concentrations. However, metallic additives may not be suitable for corrosive sorbents such as salt/porous matrix composites. Therefore, graphite particles/additives may be a better candidate when a corrosive sorbent is used. Compared to most metals, graphite has higher intrinsic thermal conductivity, lower molecular weight and excellent stability at high working temperatures [98], and therefore, can be a suitable additive to enhance the sorbent thermal diffusivity.

Graphite is by far the most studied additive for developing composite sorbents with the purpose of enhancing thermal conductivity [49]. When comparing different host matrices or/and additives, graphite presents the highest conductivity values [102]. For instance, Mauran et al. [103] reported thermal conductivities of about 10–40 $W\cdot(m\cdot K)^{-1}$ for a $CaCl_2$-expanded natural graphite (ENG) composite.

A summary of the existing studies on the effect of graphite additives on the heat and mass transfer of sorbent materials and the gap in the open literature are presented in **Table 5**. It can be seen that some of the studies did not report the water uptake, whereas the effect of graphite additive on water uptake is crucial in sorption performance and should be investigated. The majority of the studies that reported the water uptake, investigated the equilibrium uptake. However, in sorption cooling systems (SCS), the sorption rate is high at the beginning and decelerates as the sorbent approaches equilibrium. As a result, the

cycle time in SCS tend to be set short to keep the sorption rate high, resulting in higher sorption performance. Consequently, the sorbent material does not fully reach equilibrium in SCS [75]. Hence, in this study, a gravimetric large pressure jump (G-LPJ) test bed was custom-built to investigate the transient behavior of water uptake.

Furthermore, **Table 5** shows that the studies that investigate the transient water uptake, reported the sorption capacity per mass of active material. However, the additive mass, as part of the composite sorbent, should be included in the calculations of water uptake. By including the graphite mass in the denominator of water uptake, the transient water uptake reported would decrease because of high concentrations of graphite in the sorbent (as high as 50%). For example, it can be seen in **Table 5** that some of the studies reported very high thermal conductivities. Nonetheless, high concentrations of ENG were used, which considerably reduces the sorption capacity.

In this section, a number of $CaCl_2$-silica gel composite sorbents with 0-20 wt.% graphite flake content are prepared and tested in the custom-made G-LPJ test bed to study the counteracting effect of graphite additive on the transient heat and mass transfer performance of SCSs. Our water uptake calculations include the graphite mass.

Table 5. Summary of the existing studies on the effect of graphite additive on heat and mass transfer of the sorbent and the gap in the research

Ref.	**Sorbent**	**Thermally conductive additive**	**Increase in thermal conductivity $W\cdot(m\cdot K)^{-1}$**	**Uptake ($g\cdot g^{-1}$)**	**Gap in the research**
[104]	Packed bed zeolite	Expanded graphite	0.09 to 10	Not reported	Uptake not reported
[99]	4A-zeolite-based composite	Graphite (40%)	0.1 to 0.35	Equilibrium uptake decreased from 0.23 to 0.13	Equilibrium uptake reported
[105]	$CaCl_2$	Expanded graphite	Up to 9.2	Not reported	Uptake not reported
[106]	$CaCl_2$ and silica gel	Graphite flakes (20 %)	0.57 to 0.78	Equilibrium uptake decreased	Equilibrium uptake reported

				from 0.32 to 0.15	
[107]	silica gel	Expanded graphite (40%)	Up to 19	Transient uptake increased	Graphite weight was not included in calculations
[108]	silica gel	Expanded natural graphite treated with sulfuric acid (ENG-TSA)	Up to 20	Transient uptake increased	Graphite weight was not included in calculations

2.3. Sample preparation

A polyvinylpyrrolidone (PVP40) binder (40,000 MW, Amresco Inc.) was dissolved in water; subsequently, $CaCl_2$ and silica gel (SiliaFlash® B150, Silicycle, Inc., Quebec, Canada) and graphite flakes (consisting of both 150 μm fine particles and thin flakes up to 1.3 mm long, Sigma-Aldrich) were added to the aqueous solution. The composition, total mass and coating thickness of the sorbent composites prepared in this study are presented in **Table 6**. Mass percentages of 0–20 wt.% were selected for graphite flakes as the initial values. If the optimization study in Chapter 4 shows that the optimal design requires higher amounts, then higher amounts will be added and the measurements of thermal diffusivity and equilibrium uptake will be conducted. The slurry composites were coated on graphite sheets and dried at 70 °C and then cured at 180 °C in the oven, each for 1 hour. **Fig. 16** shows the composite sorbent with 0-20 wt.% graphite flake content coated on graphite sheets. Dry sorbent mass was measured using an analytical balance (OHAUS AX124) with an accuracy of 0.0001 g and the sorbent thickness was measured using a digital caliper (Mastercraft 58-6800-4) with an accuracy of 0.01 mm. The uncertainty in the calculation of graphite flake content in the sorbent was 5.07e-4–5.38e-4 wt.%.

Table 6. Compositions, dry mass, and coating thickness of the sorbent composite samples, shown in **Fig. 16**

No.	Silica gel (wt.%)	$CaCl_2$ (wt.%)	PVP40 (wt.%)	Graphite flake (wt.%)	Dry mass (g)	Coating Thickness (mm)
1	45.0	45.0	10.0	0.0	18.8068	5.15
2	42.5	42.5	10.0	5.0	18.7018	5.12
3	40.0	40.0	10.0	10.0	18.7841	5.08
4	37.5	37.5	10.0	15.0	18.6930	5.09
5	35.0	35.0	10.0	20.0	18.8815	5.06

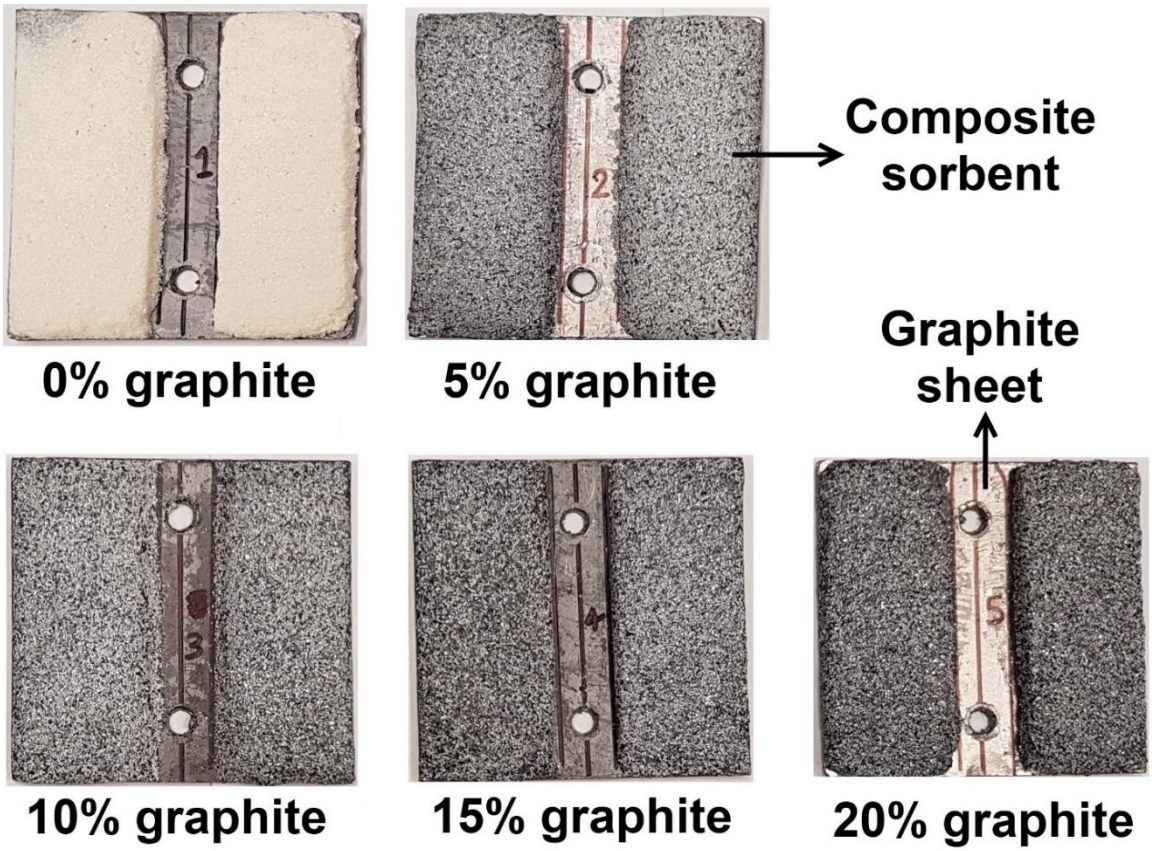

Fig. 16. The composite sorbents with 0-20 wt.% graphite flake content coated on graphite sheets, see **Table 6** for more details

2.4. Thermal diffusivity measurements

Thermal diffusivity of composite sorbents with different graphite flake contents was measured using a transient plane source, hot disk thermal constants analyzer, as per ISO 22007-2 [109] (TPS 2500S, ThermTest Inc., Frederiction, Canada), available in our lab.

Fig. 17 shows the picture and schematic of TPS adopted from Ref. [106]. Details of TPS testing can be found elsewhere [106].

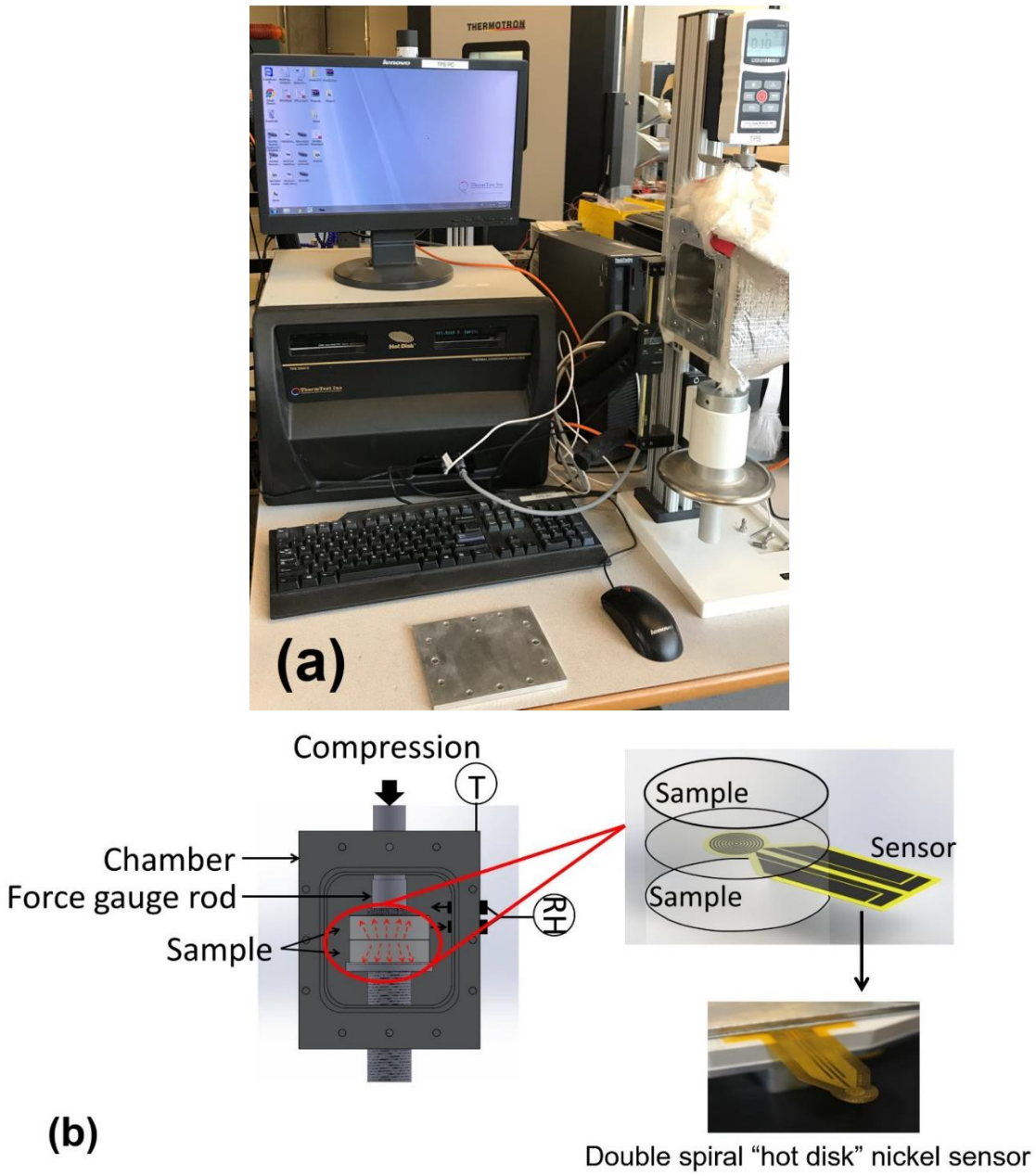

Fig. 17. (a) Picture; and (b) schematic of transient plane source (TPS) [106]

The tests were performed in a temperature and humidity-controlled chamber. Thermal diffusivity of the composite sorbents was tested five times to ensure repeatability and a standard deviation of 10% was observed. The samples were tested at 10% and 30% relative humidity at 40 °C to be consistent with G-LPJ measurements in Section 2.6. The averaged values of thermal diffusivity versus graphite flake content are plotted in **Fig. 18**.

It can be seen that the addition of 20 wt.% graphite flakes to the composite sorbent enhances thermal diffusivity by 500%. Such enhancement in thermal diffusivity is attributed to the dispersion of graphite flakes through the composite, and hence, the formation of conductive networks within the sorbent matrix. Moreover, we noticed a more pronounced increase in thermal diffusivity for samples with more than 10 wt.% graphite flakes. This “hockey stick” behavior can be explained by thermal percolation threshold [110]. The percolation threshold determines the probability that fillers/additives within a medium are sufficiently connected to form a conductive network [111]. Therefore, when a certain volume is available in the composite matrix, the graphite flakes should be added up to the amount that is enough for making a conductive network within the composite to increase thermal conductivity and diffusivity [110].

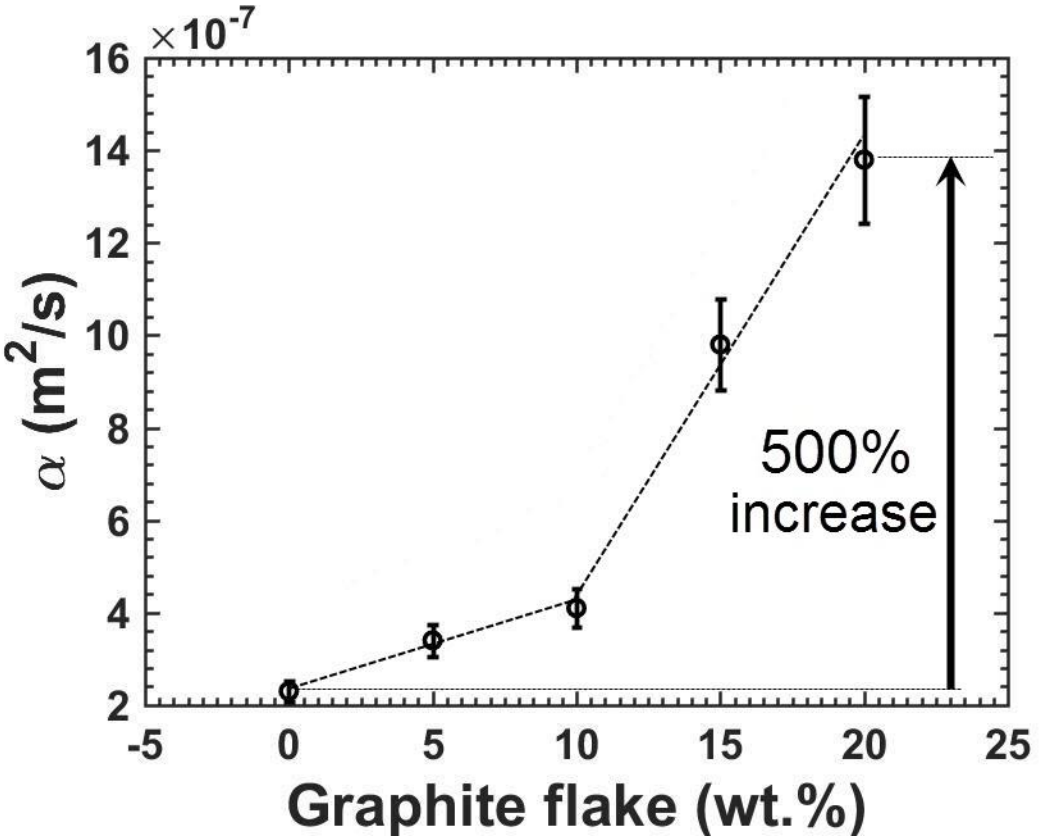

Fig. 18. Thermal diffusivity of the composite sorbents in **Table 6** versus graphite flake content, hockey-stick behavior between 0-10 wt.% and 10-20 wt.% graphite flakes

2.5. Material characterization

The composite microstructure was imaged using a scanning electron microscope (FEI/Aspex-Explorer) at room temperature. **Fig. 19** shows the SEM images of the graphite flakes used as thermally conductive additive. The SEM images reveal that the graphite

flakes have the average size of ~ 500 × 200 µm. **Fig. 20** shows the SEM images of the composite sorbent consisting of silica gel, $CaCl_2$ and PVP40, sample No. 1 in **Table 6**. **Fig. 21** and **Fig. 22** show the SEM images of the composite sorbents containing 5 wt.% and 20 wt.% graphite flakes, samples No. 2 and 5 in **Table 6**, respectively. The layers of graphite can be observed in **Fig. 21** (d) and (e), and **Fig. 22** (c)–(e). **Fig. 21** and **Fig. 22** Show the dispersion of the graphite flakes (demarcated in green in **Fig. 22** (a)) in between $CaCl_2$, silica gel particles, and a binder in the composite. The SEM images reveal that graphite flakes distributed in the composite are held by the polymer binder and form a thermally conductive network, which allows for better heat transfer through the composite. According to percolation theory [110]–[112] discussed in Section 2.4, it is important to consider the amount of the graphite flake relative to the available volume in the composite for their dispersion for percolation to occur, which increases thermal conductivity significantly.

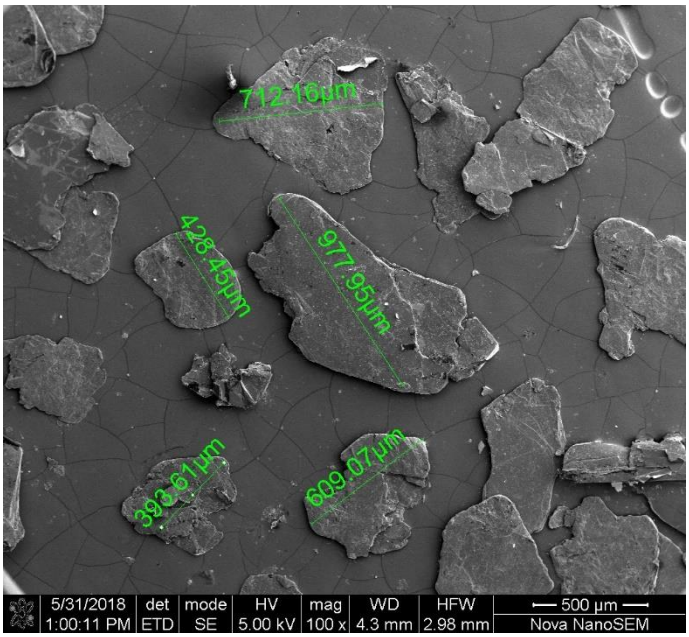

Fig. 19. SEM image of graphite flakes used as the thermally conductive additive

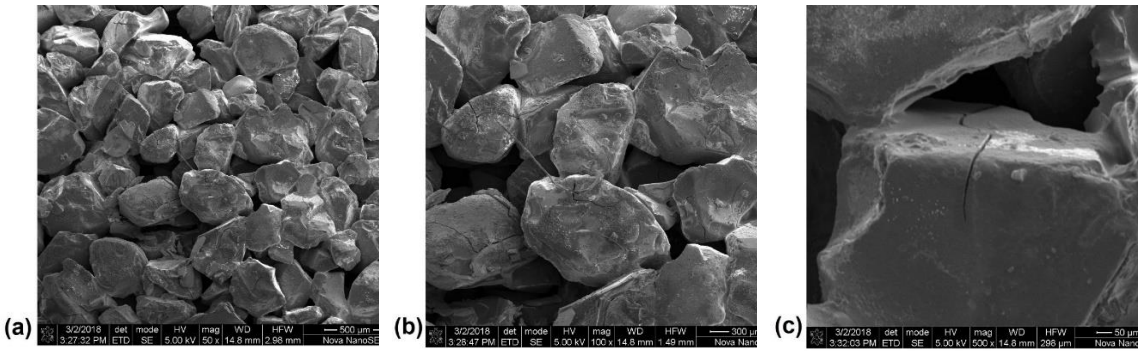

Fig. 20. SEM images of the composite sorbent consisting of 45 wt.% silica gel, 45 wt.% $CaCl_2$ and 10 wt.% PVP40, sample No. 1 in **Table 6**

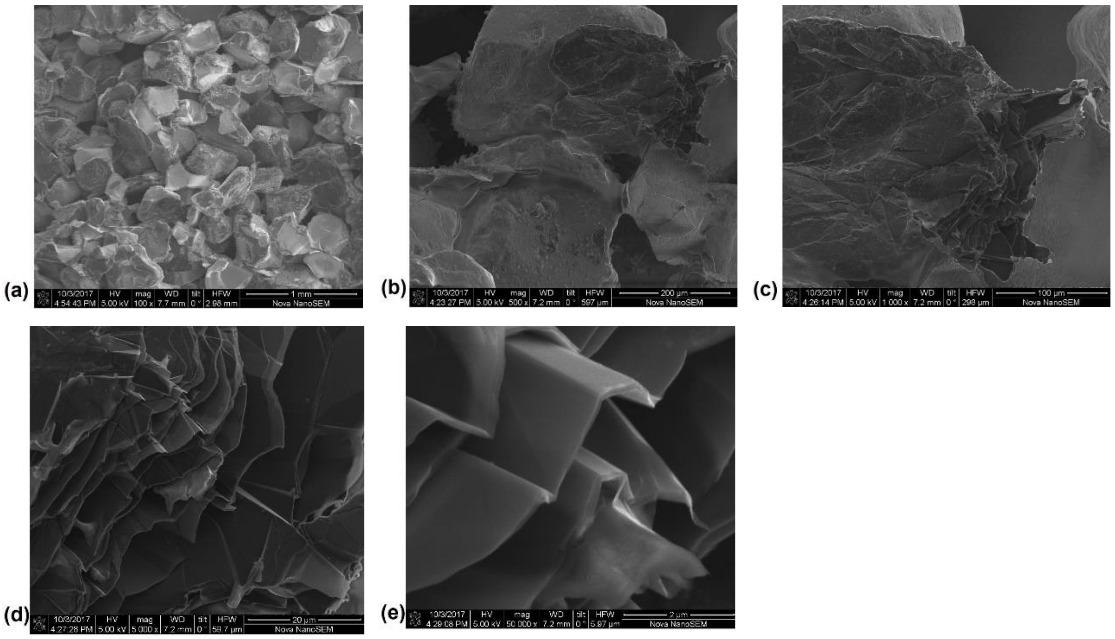

Fig. 21. SEM images of the composite sorbent consisting of 42.5 wt. % silica gel, 42.5 wt. % $CaCl_2$ and 10 wt. % PVP40, and 5 wt.% graphite flake, sample No. 2 in **Table 6**

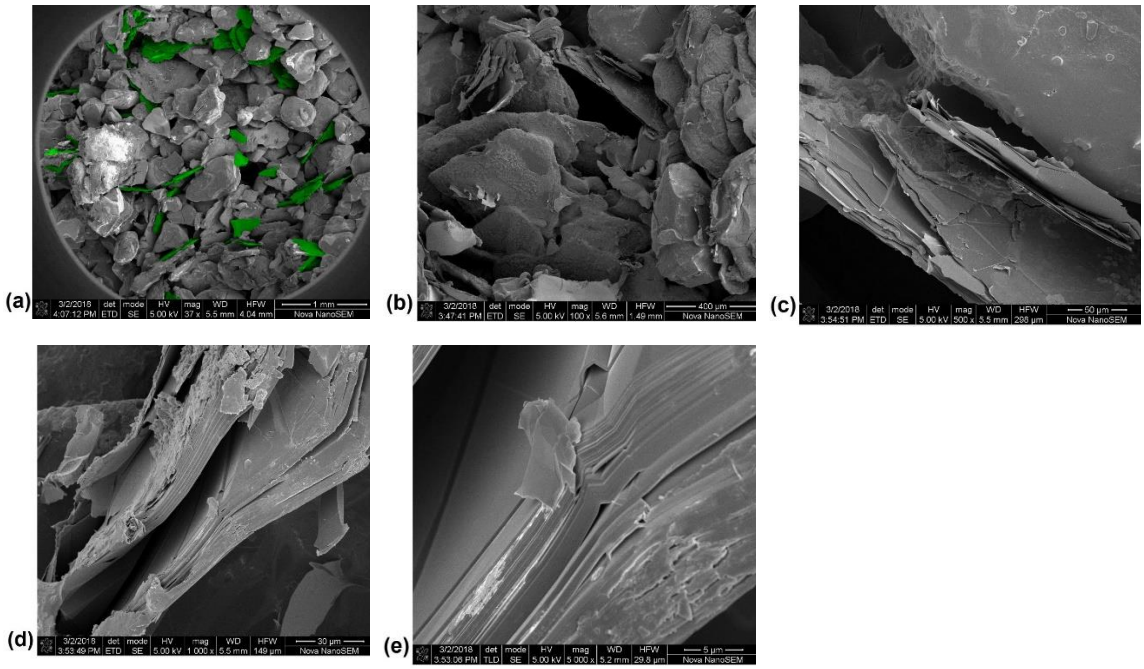

Fig. 22. SEM images of the composite sorbent consisting of 35 wt. % silica gel, 35 wt. % $CaCl_2$ and 10 wt. % PVP40, and 20 wt.% graphite flake, sample No. 5 in **Table 6**, graphite flakes are demarcated in green

Water sorption isotherms of the composite sorbents are obtained using an IGA-002 thermogravimetric sorption analyzer (TGA) (Hiden Isochema Ltd.). **Fig 23** shows the schematic and picture of the TGA [106]. Sorbent material was placed on the sample cell, which was held by a microbalance to measure the mass changes of the sorbent, while the temperature and pressure were controlled. The mass changes of the sorbent were collected in the range of 0.04–2.84 kPa with the pressure step of 0.2 kPa at 25°C. As expected, the composites with a higher content of conductive additives possessed less water uptake as they had less active sorbent material. More details regarding the TGA measurements can be found elsewhere [106].

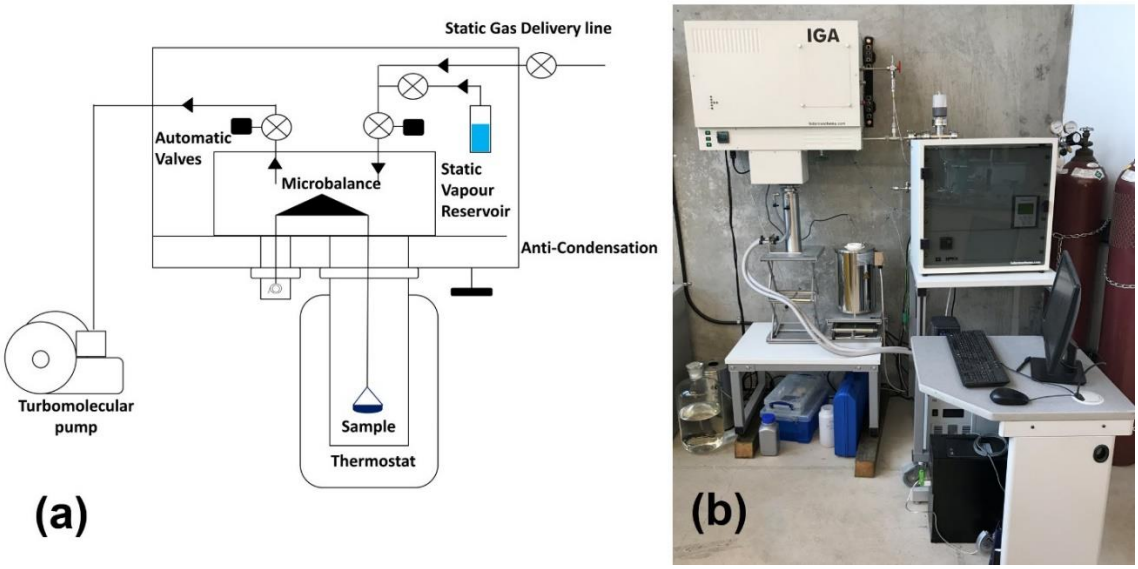

Fig 23. (a) Schematic; and (b) picture of IGA-002 thermogravimetric sorption analyzer (TGA) (Hiden Isochema Ltd.) [106]

Fig. 24 shows the water sorption isotherms of the composite sorbents obtained from the TGA. The pressure range, where the gravimetric large pressure jump (G-LPJ) measurements were performed, is demarcated on **Fig. 24**. More details on our G-LPJ tests can be found in section 2.6.

The Dubinin–Astakov (D–A) [94], [113] was fitted to the equilibrium uptake data using MATLAB and the following correlation was obtained with an R^2 of 0.9954.

$$\omega_{eq} = (1-\varphi)\left(9.01\exp\left(-0.5485\left(T\ln\left(\frac{p_0}{p}\right)\right)^{0.2850}\right)\right) \quad \text{[g water / g dry sorbent]} \tag{8}$$

where, φ is the ratio of graphite weight to the total composite weight (g graphite/g total dry sorbent), T is the sorbent temperature (K), p is the pressure of the sorber bed chamber (kPa), p_0 is the water saturation pressure at the sorbent temperature (kPa).

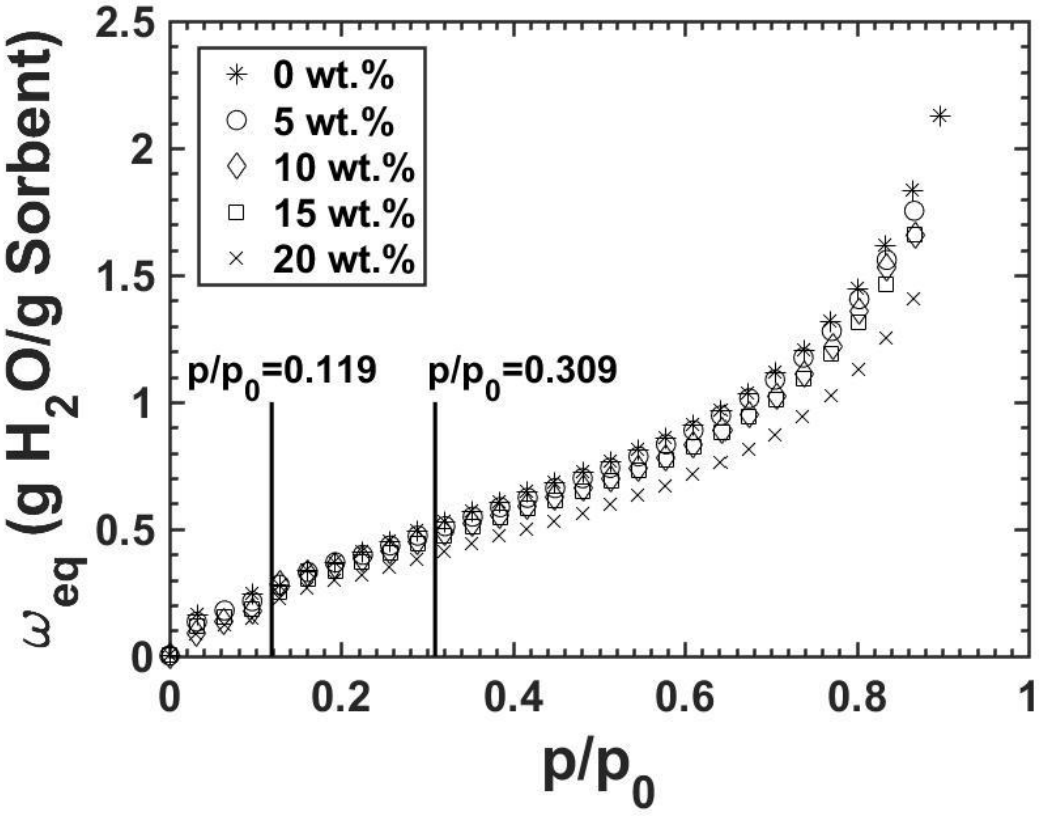

Fig. 24. Isotherms of the composite sorbents with 0-20 wt. % graphite flake contents in **Table 6**, isotherms were obtained at 25 °C, the p/p_0 range for G-LPJ tests is shown (0.119-0.309), the operating conditions for this range are T_{sorp}=39 °C, T_{evap}=20 °C and T_{cond}=1 °C

2.6. Gravimetric large pressure jump test bed

A gravimetric large pressure jump (G-LPJ) test bed was custom-built in our lab to investigate the transient heat and mass transfer performance of sorber bed heat and mass exchangers (S-HMXs). Sorbent materials consisting of $CaCl_2$, silica gel B150, PVP-40, and 0-20 wt.% graphite flakes were coated on 1.8 mm thick graphite sheets (with the density of 1,318 kg/m^3) and bolted to a copper heat exchanger as shown in **Fig. 25**. Heat transfer fluid (HTF) was pumped through the copper heat exchanger to maintain its temperature almost constant at 39 °C. The S-HMX and the copper heat exchanger were placed inside a vacuum chamber connected to a capillary-assisted evaporator acting as both condenser and evaporator, which had its temperature changed between 1°C and 20°C for desorption and sorption, respectively. The whole test bed was vacuumed for 6 hours using a vacuum pump to dry the sorbent material. The vacuum chamber was placed on a precision balance (ML4002E, Mettler Toledo) with an accuracy of 0.01 g to measure

the mass of the sorbate uptake. Five K-type thermocouples with an accuracy of 1.1 °C were passed via a feed-through in the vacuum chamber to measure the sorbent temperature. The pressure of the sorber bed and the evaporator was measured using a 722B Baratron pressure transducer (MKS instruments) with the accuracy of 0.5%. The instruments were interfaced with a PC through a data acquisition system and an in-house software built in the LabVIEW environment. Schematic diagram and a picture of our G-LPJ test bed are shown in **Fig. 26**.

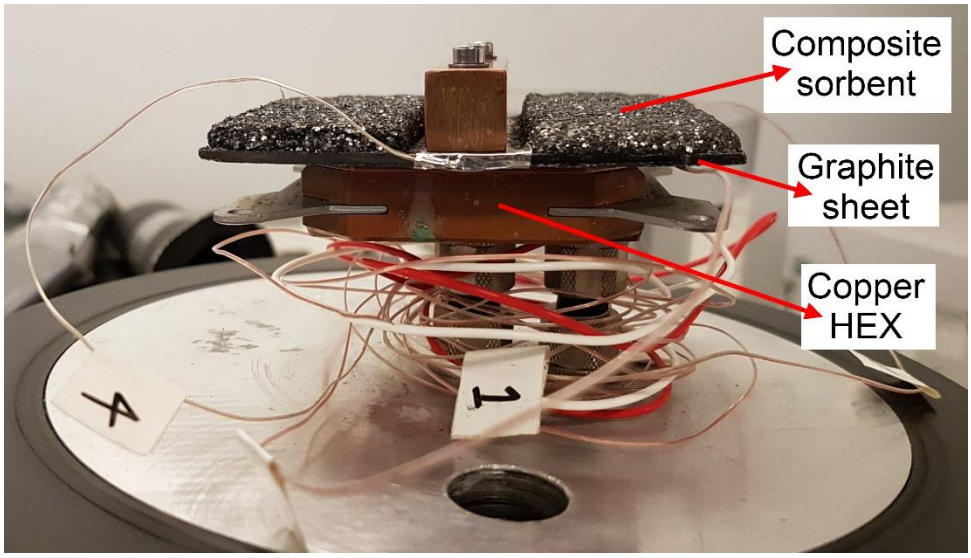

Fig. 25. A graphite-coated composite sorbent connected to the copper heat exchanger mounted inside the vacuum chamber, HEX: heat exchanger

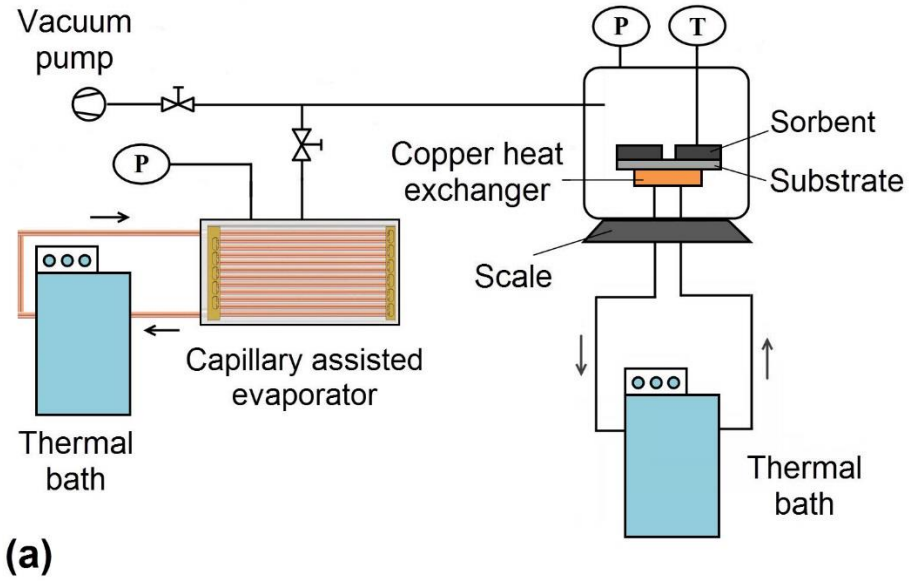

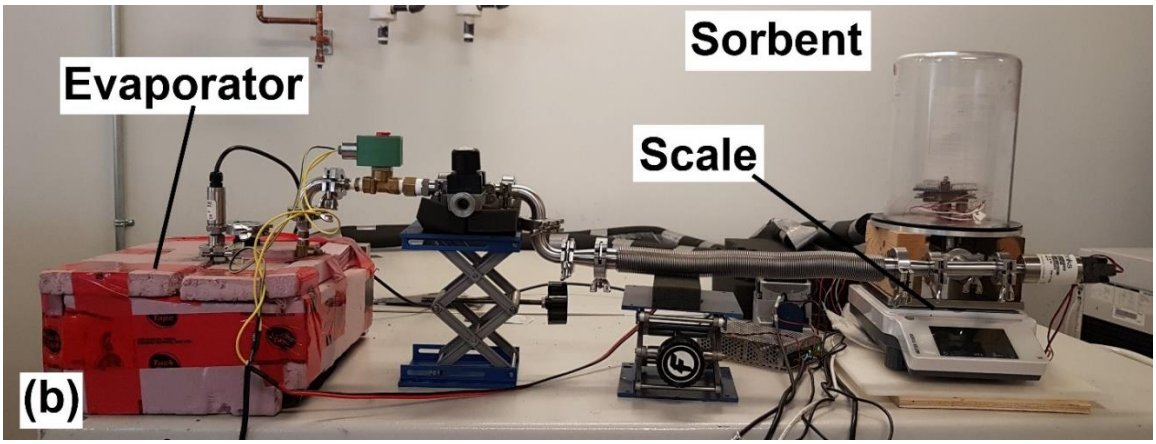

Fig. 26. (a) Schematic diagram; and (b) picture of the G-LPJ test bed, thermal baths are not shown in (b), the operating conditions for G-LPJ tests are T_{sorp}=39 °C, T_{evap}=20 °C and T_{cond}=1 °C

2.7. Results and discussion

Due to the small vibrations of the hose connected to the sorber bed chamber in our G-LPJ test bed, see **Fig. 26**, a very small shift occurs in the mass measurement within short time intervals. When all these small shifts are accumulated over time, they result in larger shifts. Nonetheless, considering the randomness of these shifts, the error decreases as more tests are done. Hence, each measurement was conducted five times and the maximum standard deviation of the equilibrium water uptake, i.e. water uptake when sorbent has reached saturation, was observed to be 7%. As an example, five water uptake measurements of the sorbent with 20 wt.% graphite flakes are plotted in **Fig. 27**.

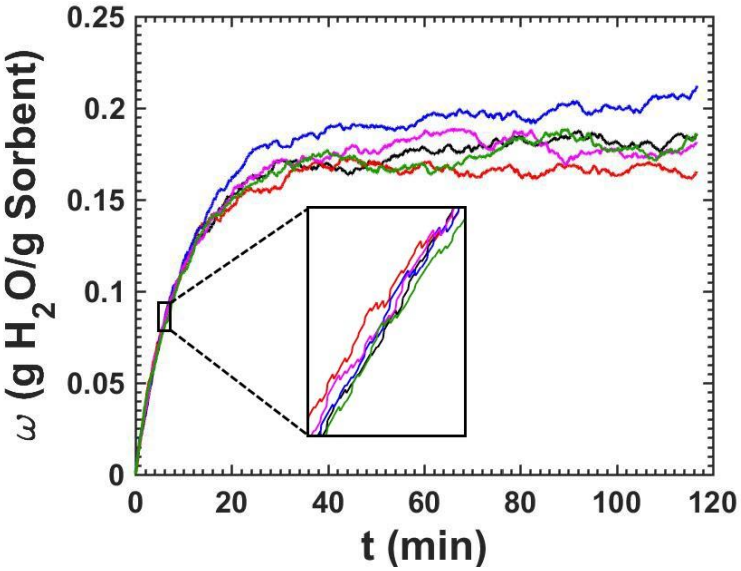

Fig. 27. Five water uptake measurements of the sorbent with 20 wt.% graphite flakes

Variation of chamber pressures of evaporator and sorber bed, sorbent temperature and water uptake versus time are shown in **Fig. 28**−**Fig. 30**. As shown in **Fig. 28**, during the sorption process, the evaporator and sorber bed pressure is 2.34 and 2.16 kPa, and during the desorption process, the condenser and sorber bed pressure is 0.65 and 0.83 kPa, respectively. These pressure values of the sorber bed and its temperature, i.e. 39 °C, correspond to p/p_0=0.309 and 0.119 for sorption and desorption processes, respectively (**Fig. 24**). Moreover, the large pressure jump at the beginning of each sorption and desorption process can be observed. As shown in **Fig. 29**, at the beginning of de/sorption process, the sorbent temperature de/increases rapidly due to the endo/exothermic nature of de/sorption processes, respectively, and high enthalpy of sorption. After this temperature drop/jump, the sorbent is heated/cooled to continue the de/sorption processes. The rate of these heat/cool processes after the temperature drop/jump determines the performance of sorption cooling systems. **Fig. 30** also depicts the water uptake variation during the desorption and sorption processes. It is noted that during the first sorption process, the temperature jump and the uptake are higher than the next sorption processes as the sorbent is vacuum dried before each test. Furthermore, **Fig. 30** shows that the de/sorption processes continued until the sorbent reached an equilibrium condition based on the sorption rate ($d\omega/dt$) for the last 10 min. The results presented in the following sections are the de/sorption processes after the first sorption process.

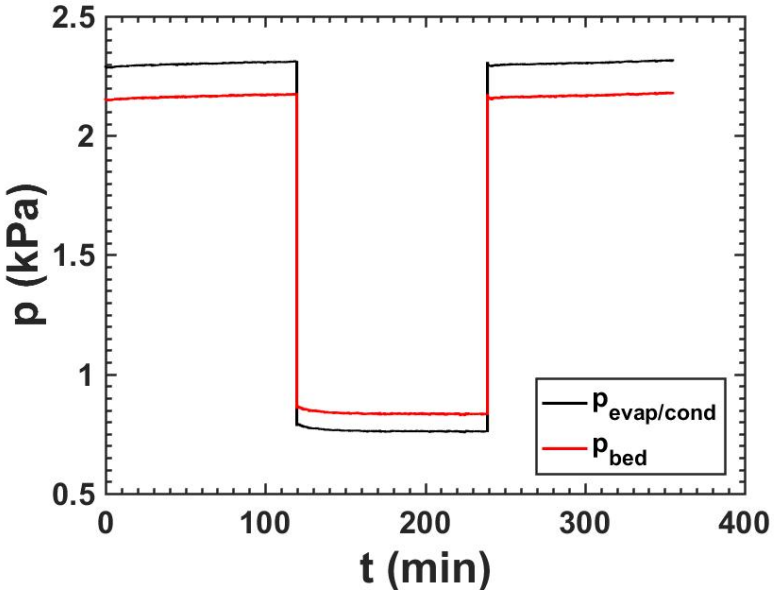

Fig. 28. Variation of pressures of the evaporator chamber and the sorber bed chamber over time for the composite sorbent with 20 wt.% graphite flakes. Data collected in our G-LPJ test bed. T_{sorp}=39 °C, T_{evap}=20 °C and T_{cond}=1 °C.

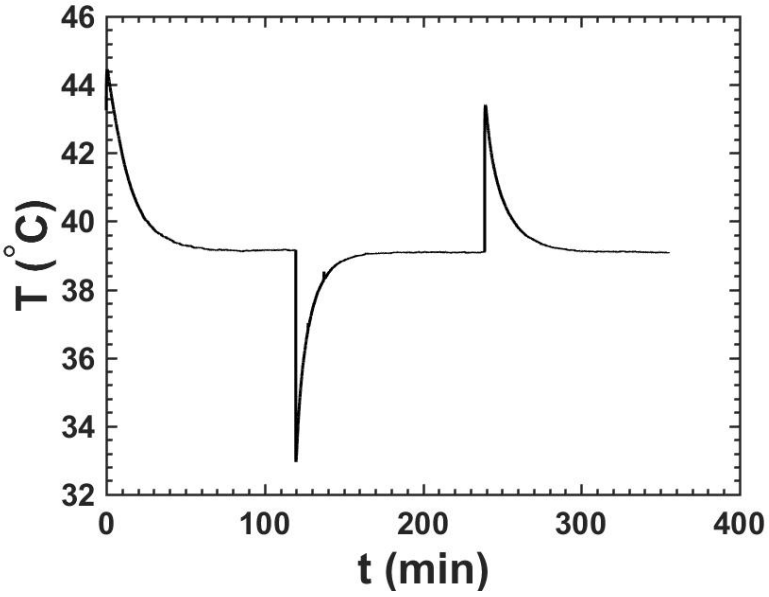

Fig. 29. Variation of the sorbent temperature over time for the composite sorbent with 20 wt.% graphite flakes. Data collected in our G-LPJ test bed. T_{sorp}=39 °C, T_{evap}=20 °C and T_{cond}=1 °C.

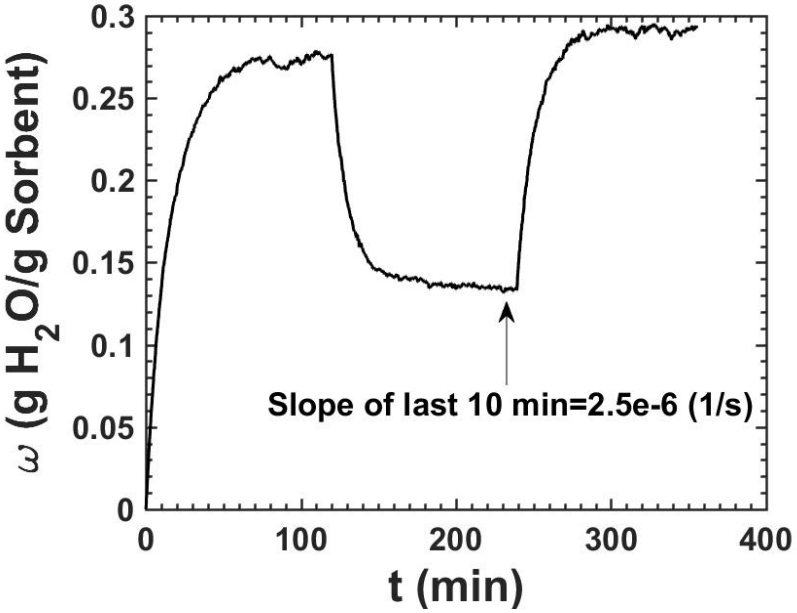

Fig. 30. Variation of water uptake over time for the composite sorbent with 20 wt.% graphite flakes. Data collected in our G-LPJ test bed. T_{sorp}=39 °C, T_{evap}=20 °C and T_{cond}=1 °C.

2.7.1. Effect of graphite flake on transient water uptake

Fig. 31 (a) shows the experimental variation of water uptake with time for various graphite flake content, and **Fig. 31** (b) shows both experimental and modeling results, presented in Chapter 0. As shown in **Fig. 31**, the equilibrium uptakes, measured with the G-LPJ test bed, are in good agreement with our TGA equilibrium data. Moreover, as can be seen, in the early stages of sorption, i.e. the first 20 minutes, the water uptake increases by increasing the graphite flakes content. The reason for this trend is that during this period, the heat generation rate in the sorbent is high. Hence, there is a higher need for enhanced sorbent thermal diffusivity; thus, increasing the amount of graphite flake enhances the sorption performance. However, as the sorbent approaches saturation, the trend starts to reverse, which means that the uptake increases with the decrease of graphite content. That is because: as the sorbent approaches equilibrium, the heat generation rate reduces. As a result, the need for enhanced heat transfer decreases. Consequently, the sorbent with a higher active material can uptake more, which leads to higher performance.

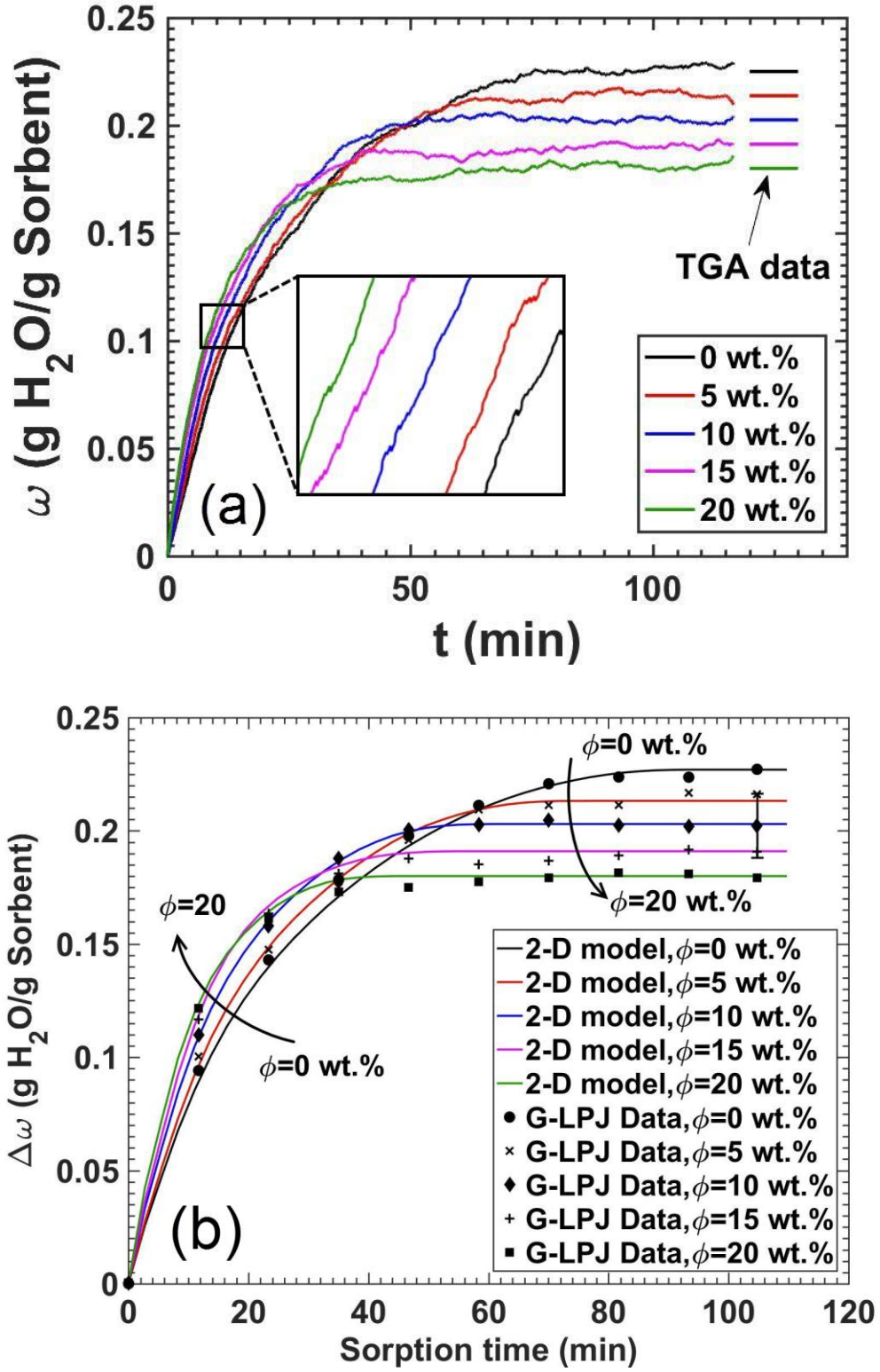

Fig. 31. Variation of water uptake versus time for composites with different graphite flake contents for T_{sorb}=39 °C, T_{evap}=20 °C, and T_{cond}=1 °C: (a) data collected in our G-LPJ test bed; and (b) 2-D model in Chapter 0 versus G-LPJ data

2.7.2. Effect of graphite flake on specific cooling power

Fig. 32 shows the experimental specific cooling power (SCP) data collected in our G-LPJ test bed and results obtained from the 2-D analytical model, introduced in Chapter 0, for various cycle times and different graphite flake content. The uncertainty analysis in the SCP calculation is presented in Appendix B. It can be seen that for relatively short cycle times, less than 20 minutes, adding graphite flake enhances the SCP because the sorbent thermal diffusivity increases. Furthermore, it can be observed that by reducing the cycle time, the SCP enhancement due to adding graphite flake, increases because the heat generation rate increases. However, for long cycle times, SCP decreases by increasing the graphite flake content because the amount of active material reduces. It is evident from **Fig. 32** that there is a need for the optimization of cycle time and the amount of graphite flake in the sorbent.

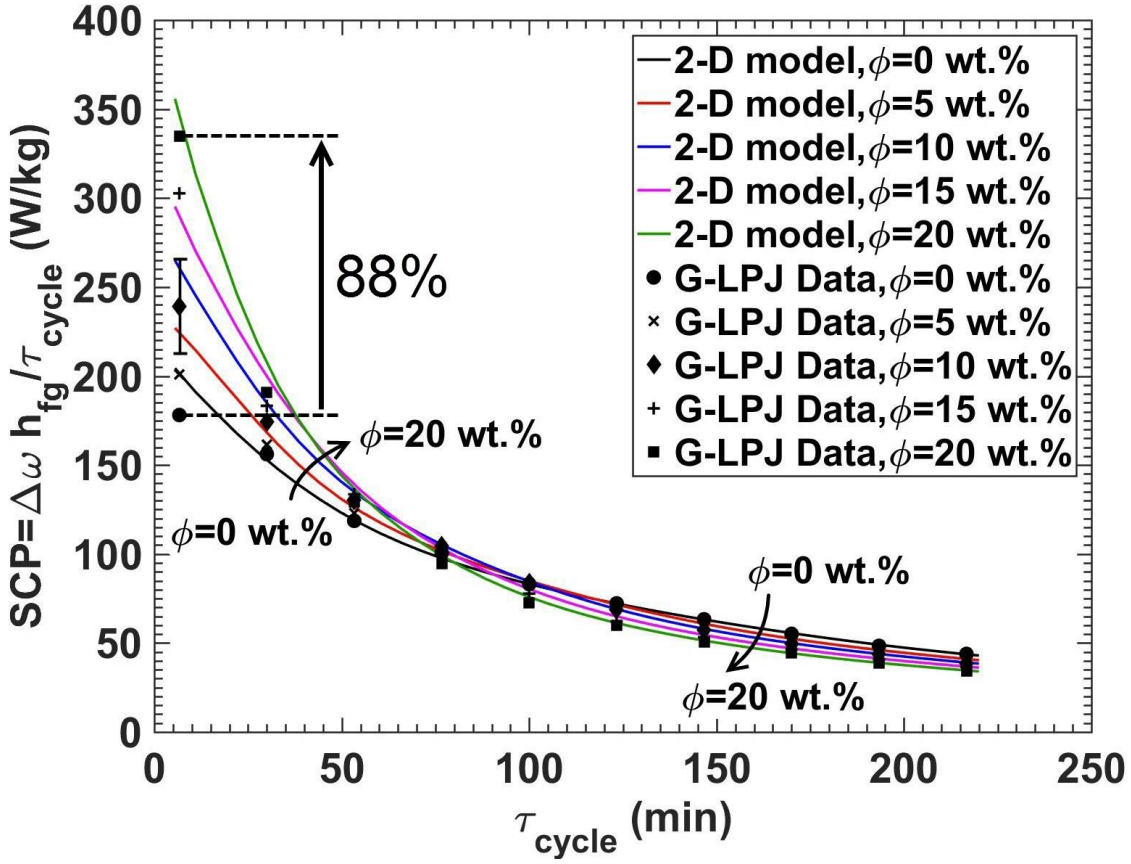

Fig. 32. Variation of specific cooling power (SCP) versus cycle time for various graphite flake contents

2.8. Conclusion

The effect of graphite flake additives on the performance of sorption cooling systems was studied using a custom-built G-LPJ test bed. It was found that in the early stages of sorption, the S-HMX performance was notably improved, e.g. from 178.1 to 334.9 W/kg for a 6-minute cycle time, by adding graphite flakes. This was due to the enhanced sorbent thermal diffusivity (from 0.23 to 1.38 mm^2/s). Also, it was shown that as the sorption rate reduces with time, the need for heat transfer enhancement, such as a graphite flake additive, decreases. Therefore, the graphite flake content and cycle time need to be optimized to achieve optimum SCP.

3. Analytical modeling of sorber bed heat and mass exchangers

3.1. Overview

In this chapter, for the first time in the literature, 2-D analytical models were developed that consider the spatial and temporal variation of water uptake and temperature in the sorber bed heat and mass exchangers (S-HMXs). The developed analytical models have low computation time, which is crucial for optimization and real-time control of the S-HMXs. The assumptions and solution methodology of the analytical models are presented for the plate-fin sorber bed heat and mass exchangers (P-HMX) in the Cartesian coordinate system and the finned-tube sorber bed heat and mass exchangers (F-HMX) in the cylindrical coordinate system. Moreover, an off-the-shelf engine oil cooler is used for validation of the model and as a benchmark for the optimized S-HMXs, which will be presented in Chapter 1. Furthermore, a parametric study is performed to investigate the effect of the S-HMX geometry, heat transfer characteristics and cycle time on the sorption performance. This chapter resulted in the following publications:

1) H. Bahrehmand, M. Bahrami, “An analytical design tool for sorber bed heat and mass exchangers of sorption cooling systems,” *International Journal of Refrigeration*, 100, 2019, 368-379.
2) H. Bahrehmand, M. Ahmadi, M. Bahrami, “Oscillatory heat transfer in coated sorber beds: An analytical solution,” *International Journal of Refrigeration* (2018), https://doi.org/10.1016/j.ijrefrig.2018.05.006.
3) H. Bahrehmand, M. Ahmadi, M. Bahrami, “Analytical modeling of oscillatory heat transfer in coated sorption beds,” *International Journal of Heat Mass and Transfer*, 121 (2018) 1–9.
4) H. Bahrehmand, M. Bahrami, “Analytical model for sorber bed heat and mass exchangers of sorption cooling systems,” *International Conference on Polygeneration*, Fukuoka, Japan, 2019.
5) S. Bahrehmand, K. Fayazmanesh, W. Huttema, M. Ahmadi, C. Mccague, M. Bahrami, “Analytical modeling of oscillatory heat transfer in coated sorption beds,” *International Sorption Heat Pump Conference*, Tokyo, Japan, August 2017.

3.2. Literature review

It was shown in Chapter 1 that there is a need for optimization of cycle time and the amount of graphite flake in the sorbent to acquire an optimum SCP. To optimize the S-

HMX, a model is required that considers the spatial and temporal variation of water uptake and temperature in the sorbent and the heat exchanger. In this chapter, we propose a new 2-D analytical model that can be used as a platform for the design and optimization of a plate-fin sorber bed heat and mass exchanger (P-HMX) and a finned-tube sorber bed heat and mass exchanger (F-HMX).

Many researchers have developed thermodynamic, lumped, numerical and analytical models of the S-HMX to enhance and optimize the performance of sorption cooling systems (SCS). A summary of available studies in the literature is presented in **Table 7**. However, one can conclude that the literature lacks an analytical model that includes the spatial and temporal variation of water uptake and temperature in the sorbent and the heat exchanger. Also, a model that yields a closed-form solution that can directly calculate the performance for a certain time as opposed to marching through time steps in the numerical models. This can decrease the computation time significantly, which is key for real-time control and optimization of the S-HMXs.

The present model is developed to address these challenges and is validated against experimental data collected from our custom-designed gravimetric large pressure jump (G-LPJ) test bed in Chapter 1, and the optimized S-HMXs built and tested in Chapter 1, as well as with off-the-shelf engine oil coolers presented in Section 3.6.

As explained in Chapter 1, graphite flakes can be added to the composite sorbent, consisting of $CaCl_2$, silica gel B150, and PVA binder to enhance its thermal diffusivity. Nonetheless, these thermally conductive graphite flakes reduce the active sorbent fraction in the composite, creating a need for establishing an optimum composition [11]. Using the validated closed-form solution, a parametric study is conducted to investigate the effect of the S-HMX geometry, heat transfer characteristics, and cycle time on SCS performance.

Table 7. Summary of modeling approaches of sorber bed heat and mass exchangers in sorption cooling systems

Modeling approach	Ref. No.	Characteristics of the parametric study	Merits	Limitations
Thermodynamic model	[114], [115]	• Driving temperature	• Very low computation time	• Predicts only the upper performance limits
Lumped model	[116]	• Cycle time	• Low computation time	• Uniform sorbent temperature • Uniform sorption of refrigerant • Neglects inter-particle heat and mass transfer resistances • Dependent on previous time steps
	[117]	• Fin spacing • Cycle time • Generation temperature lift		
	[118]			
	[119]	• Fin height • Fin spacing		
Steady state analytical lumped model	[120]	• Flat tube thickness • Fin pitch • Fin thickness • Water channel wall thickness	• Very low computation time	• Neglects transient behavior of system • Neglects inter-particle heat and mass transfer resistances
Numerical model	[121]	• Fin spacing • Number of fins	• Considers spatial and temporal variation of sorbent temperature and sorbate uptake	• High computation time • Dependent on previous time steps
	[122]	• Fin pitch • Fin thickness • Fin height • Diffusion coefficient • Particle size • Cycle time • Cycle ratio • Hot water temperature • Fluid velocity • Porosity		
	[123]	• Fin radius • Fin thickness • Number of fins		

	[124]	• Adsorbent bed thickness • Convective heat transfer coefficient • Sorbent Thermal conductivity		
	[125]	• Fin spacing • Fin height		
	[126]	• Particle diameter • Adsorbent bed thickness		
	[127] – [131]	• Fin height • Fin spacing • Particle diameter		
Present 2-D transient analytical model		• Graphite flake content in the sorbent • Fin height • Fin thickness • Sorbent thickness • Fluid channel height • Cycle time	• Low computation time • Considers 2-D spatial and temporal variation of sorbent temperature and sorbate uptake • Independent of previous time steps • Considers anisotropic thermal conductivity • Considers TCR at the interface between sorbent and fin	

Note: References [121], [122], [125], [128] consider thermal contact resistance at the interface between the sorbent and the HEX.

Plate fin heat and mass exchangers (P-HMX), i.e. rectangular fluid channels with rectangular fins, and finned-tube heat and mass exchanger (F-HMX), i.e. circular fluid tubes with annular fins are selected as the S-HMX due to their relatively high SCP and COP [75]. In the following sections, the development of the analytical model is explained in Cartesian and cylindrical coordinate systems for the P-HMX and the F-HMX, respectively.

3.3. Model development for plate fin sorber bed heat and mass exchangers

The solution domain of P-HMX, shown in **Fig. 33**, can be used to predict the performance of the entire S-HMX.

The following is the list of the assumptions used in the development of the present model:

1. Uniform sorbate pressure inside the sorbent;
2. Thermodynamic equilibrium of sorbent and sorbate;
3. Local thermal equilibrium between sorbent and sorbate;
4. The heat transfer fluid is assumed to have a constant temperature along the solution domain; justifiable due to the relatively higher heat capacity of the heat transfer fluid [132]; and
5. The boundaries of the sorbent and the fin, which are in contact with low-pressure refrigerant vapor, are assumed adiabatic. This is a fair hypothesis since the Biot number is low as shown below:

$$h\left(T_{vapor}-T_s\right)=k_s\frac{\partial T_s}{\partial y}\Rightarrow O\left(Bi_y\right)=O\left(\frac{ht_s}{k_s}\right)=\frac{0.5\times 0.001}{0.3}=0.0017$$
$$h\left(T_{vapor}-T_s\right)=k_s\frac{\partial T_s}{\partial x}\Rightarrow O\left(Bi_x\right)=O\left(\frac{hb}{k_s}\right)=\frac{0.5\times 0.01}{0.3}=0.017 \quad (9)$$
$$h\left(T_{vapor}-T_f\right)=k_f\frac{\partial T_f}{\partial x}\Rightarrow O\left(Bi_{x,f}\right)=O\left(\frac{hb}{k_f}\right)=\frac{0.5\times 0.01}{236.5}=2.11e-5$$

where, T is the temperature (K), k is thermal conductivity (W/(m K)), Bi is the Biot number (-), t_s is the sorbent thickness (m), and b is the fin height (m), respectively. Also, h is the convective heat transfer coefficient between the water vapor (the refrigerant) and the sorbent [133], [134]. It was shown by Wakao and Kaguei [134] that the interfacial convection and the external convection are of the same order of

magnitude. Also, the radiative heat transfer is negligible because of low temperature difference between the sorbent and its surrounding (10–20 K).

6. Thermophysical properties of the sorbent and HEX are assumed constant. Averaged values over the range of operating conditions are used, **Table 8**.
7. The convection term in the energy equation, which accounts for the sorbate convection inside the sorbent coating, is assumed negligible as the Peclet number, which represents the ratio of the convection to the diffusion term in the energy equation, is small as follows [132]:

$$O(\mathrm{Pe}) = O\left(\frac{\rho_g c_{p,g} u_g L}{k_s}\right) = \frac{10^{-2}\times 10^{3}\times 10^{-1}\times 10^{-3}}{10^{-1}} = 0.01 \qquad [-] \qquad (10)$$

where, L is the characteristic length, in the order of millimeters, u_g, vapor velocity, is in the order of 0.1 m/s [129], respectively. Also, ρ_g and $c_{p,g}$ are density and specific heat of water vapor, and are equal to 0.051 kg/m^3 and 1,904 J/kg K, respectively.

8. The sorbent coated on the tube in the gap between the sorbent coatings and the fins, i.e. t_{fs} shown in **Fig. 33**, is neglected as t_{fs} is much smaller than the fin height.

It should be noted that if the vapor passage of t_{fs} is included in the design, the boundary condition is zero temperature gradient due to negligible convection and radiation heat transfer as explained in Eq. (9) and (19). Furthermore, if the vapor passage is not included and the entire fin spacing is filled with the sorbent, i.e. zero t_{fs}, then the zero-temperature gradient boundary condition would still be valid because of symmetry. Thus, the model is applicable whether t_{fs} is included or not.

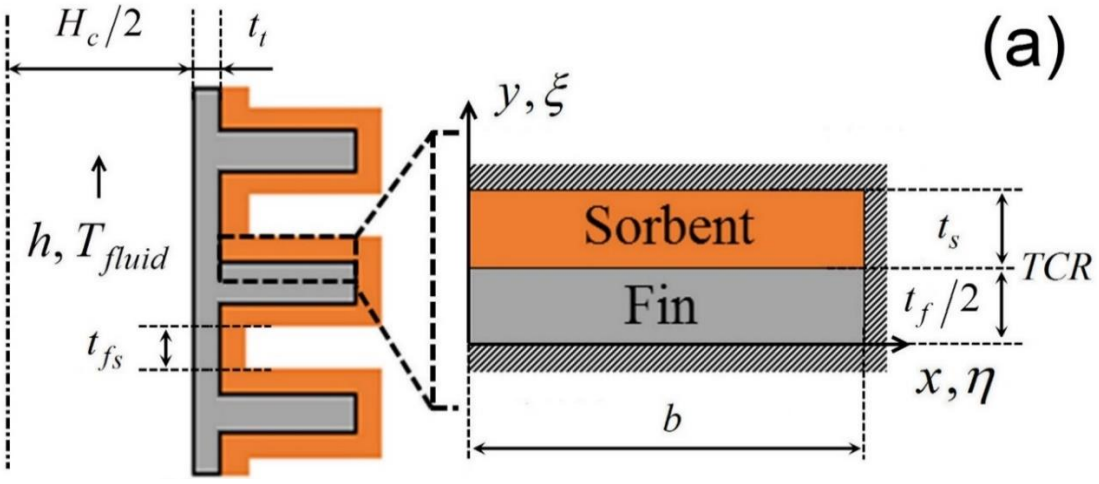

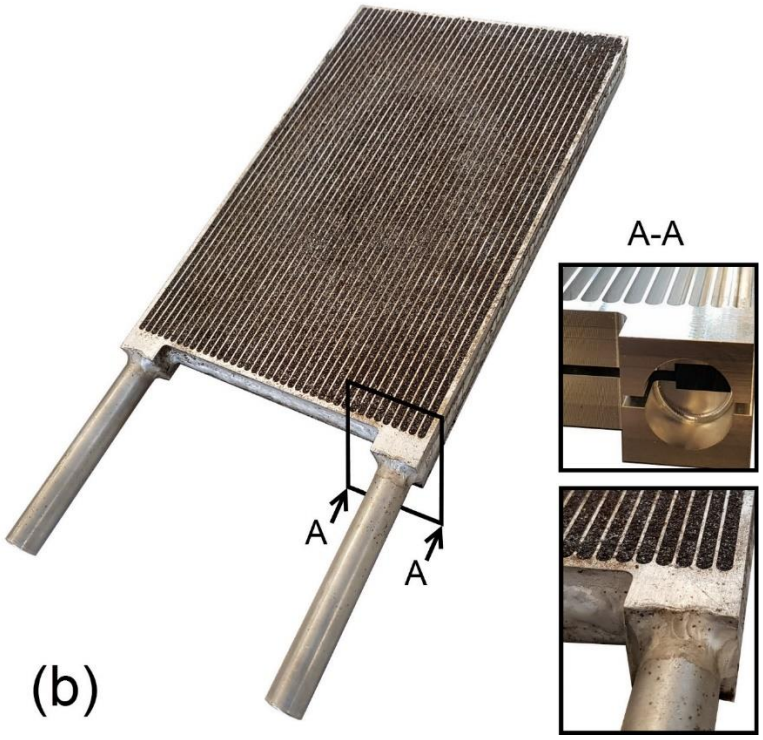

Fig. 33. (a) The solution domain of P-HMX; and (b) optimized P-HMX, which will be explained in Chapter 1, t_{fs} is zero in (b)

Using the aforementioned assumptions, the energy equation for the sorbent layer and the fin in the Cartesian coordinate system can be written as follows:

$$\frac{\partial T_i}{\partial t} = \alpha_{i,x} \frac{\partial^2 T_i}{\partial x^2} + \alpha_{i,y} \frac{\partial^2 T_i}{\partial y^2} + \frac{1}{\left(\rho c_p\right)_i} G_i(t)$$
$$T_i\left(x, y, t\right) \qquad (11)$$
$$i = s,\ f$$

$$G_i\left(t\right) = \begin{cases} \rho_s h_{ads} \dfrac{\partial \omega}{\partial t}, & i = s \\ 0, & i = f \end{cases} \qquad (12)$$

where, i=s, f represents the sorbent and fin domains, respectively. Also, ρ is the density (kg/m^3), ω is the water uptake (g water/g sorbent), h_{ads} is the sorption enthalpy (J/kg), and α is thermal diffusivity (m^2/s), respectively. The convective boundary conditions are:

$$\frac{1}{R_s}\left(T_s(0, y, t) - T_{fluid}\right) = k_s \frac{\partial T_s(0, y, t)}{\partial x} \qquad (13)$$

$$\frac{1}{R_f}\left(T_f(0,y,t)-T_{fluid}\right)=k_{f,x}\frac{\partial T_f(0,y,t)}{\partial x} \tag{14}$$

$$R_s=\frac{t_t}{k_{f,x}}+\frac{1}{h}+TCR\cdot A \quad \left(\frac{K\,m^2}{W}\right) \tag{15}$$

$$R_f=\frac{t_t}{k_{f,x}}+\frac{1}{h} \quad \left(\frac{K\,m^2}{W}\right) \tag{16}$$

where, t_t is the tube wall thickness (m), k is thermal conductivity (W/(m K)), h is the convective heat transfer coefficient of the heat transfer fluid (W/(m^2 K)), TCR is thermal contact resistance between the sorbent and the heat exchanger (K/W), and A is the surface area of the TCR interface (m^2), respectively. If fins and tubes of HEX are not in one piece and are attached together, TCR should be added to Eq. (16). Also, the convective heat transfer coefficient is calculated by the correlation proposed by Gnielinski [135], which is applicable for 3,000<Re<10^6. It should be noted that the Reynolds number in this study for the plate-fin sorber bed heat and mass exchanger (P-HMX) is between 7,800 and 9,700 for a fluid channel height of 4–8 mm, a fluid channel width of 1.3 cm, and a volumetric flow rate of 5 L/min, **Table 9**. The fluid regime is turbulent as the Reynolds number is more than 4,000.

$$h=0.012\frac{k_w}{2H_c}\left(\mathrm{Re}^{0.87}-280\right)\mathrm{Pr}^{0.4} \quad [\mathrm{W/m^2\,K}] \tag{17}$$

where, k_w is water thermal conductivity (W/(m K)), H_c is the tube channel height (m), Re is the Reynolds number (-), Pr is the Prandtl number (-), respectively. The adiabatic boundary conditions are:

$$\frac{\partial T(b,y,t)}{\partial x}=0 \tag{18}$$

$$\frac{\partial T_s(x,t_s+t_f,t)}{\partial y}=0 \tag{19}$$

where, b is fin height (m), t_s is sorbent thickness (m), and t_f is fin thickness (m), respectively. Due to symmetry, one can write the following for the lower side of the fin:

$$\frac{\partial T_f(x,0,t)}{\partial y}=0 \tag{20}$$

Thermal contact resistance (TCR) between the sorbent and the HEX surface is important and can be up to 28% of the total thermal resistance inside a sorber bed [1], [97], [136]. Hence, it is included in the present model as a parameter with a constant value. TCR at the silica gel/copper interface was measured by Sharafian et al. [136] using a guarded-hot plate apparatus under vacuum pressure, and the range of 1.3–3.8 K/W was reported. As can be seen in **Fig. 34**, the SCP values predicted by the present model are in good agreement with those measured with G-LPJ test bed for the reported range of TCR. Thus, TCR of 3 K/W was selected for this study. It is noted that the main uncertainty in SCP calculation is due to the mass measurement of the sorbate uptake and can result in the uncertainty of 0.5–3.5 W/kg. More information can be found in references [1], [2].

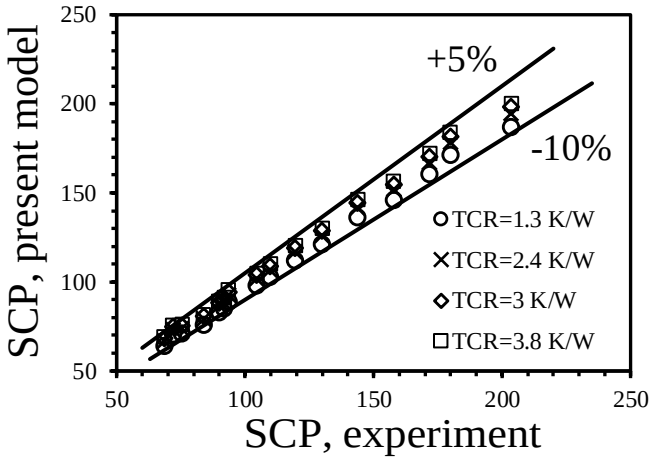

Fig. 34. Comparison of the model with G-LPJ data for the range of TCR measured in Ref. [136]

Continuity of heat flux as well as temperature jump/drop created by TCR are considered at the interface between the sorbent coating and fin as follows:

$$k_{f,y}\frac{\partial T_f(x,t_f,t)}{\partial y}=k_s\frac{\partial T_s(x,t_f,t)}{\partial y} \tag{21}$$

$$-k_{f,y}\frac{\partial T_f(x,t_f,t)}{\partial y}=\frac{1}{TCR\cdot A}\left(T_f(x,t_f,t)-T_s(x,t_f,t)\right) \tag{22}$$

where, $k_{f,y}$ is through-plane fin thermal conductivity (W/(m K)), k_s is sorbent thermal conductivity (W/(m K)), and t_f is fin thickness (m), respectively.

3.3.1. Solution methodology

The energy equation, Eqs. (11)–(22), is solved using the Eigenfunction Expansion Method. The Eigenfunction Expansion Method has been widely used in heat transfer problems, particularly for multi-layer domains, time-dependent boundary conditions and/or source terms [137]–[142].

The following non-dimensional variables can be defined.

$$\theta = \frac{T - T_{fluid}}{T_0 - T_{fluid}} \qquad \xi = \frac{y}{t_s + t_f} \qquad \eta = \frac{x}{b}$$

$$Bi_s = \frac{b}{R_s k_s} \qquad Bi_f = \frac{b}{R_f k_f} \qquad \kappa = \frac{k_s}{k_y}$$

$$\Lambda = \frac{t_s + t_f}{k_y TCR\, A} \qquad Fo = \frac{t\alpha_x}{b^2} \qquad \delta = \frac{b}{t_s + t_f}$$

$$\mu_y{}^2 = \frac{\alpha_y}{\alpha_x} \qquad \mu_s{}^2 = \frac{\alpha_s}{\alpha_x} \qquad \delta_f = \frac{t_f}{t_s + t_f}$$

where, θ is the dimensionless temperature, the Fourier number, Fo, is the dimensionless time, ξ and η are the dimensionless Cartesian coordinates, respectively. Using the aforementioned dimensionless variables, the dimensionless energy equation can be obtained as follows:

$$\begin{aligned} &\frac{\partial \theta_i}{\partial Fo} = \mu_{i,\eta}{}^2 \frac{\partial^2 \theta_i}{\partial \eta^2} + \left(\mu_{i,\xi}\delta\right)^2 \frac{\partial^2 \theta_i}{\partial \xi^2} + g_i(Fo) \\ &\theta_i\left(\eta, \xi, Fo\right) \\ &i = s,\, f \end{aligned} \tag{23}$$

where

$$g_i\left(Fo\right) = \begin{cases} \dfrac{h_{ads}}{c_{p,s}\left(T_0 - T_{fluid}\right)} \dfrac{\partial \omega}{\partial Fo}, & i = s \\ 0, & i = f \end{cases} \tag{24}$$

$$\mu_{i,\eta} = \begin{cases} 1, i = f \\ \mu_s, i = s \end{cases} \tag{25}$$

$$\mu_{i,\xi} = \begin{cases} \mu_y, i = f \\ \mu_s, i = s \end{cases} \tag{26}$$

where, h_{ads} is the sorption enthalpy (J/kg), c_p is the specific heat (J/ (kg K)), and ω is the water uptake (g water/g dry sorbent), respectively. Water uptake can be modelled in terms of the operating conditions, i.e. pressure and temperature of the S-HMX. A linear relationship is obtained between the water uptake and sorbent temperature for each pressure during the isobaric sorption and desorption processes. A detailed explanation is presented in section 3.5.

The dimensionless boundary conditions are:

$$\frac{\partial \theta_s(0,\xi,Fo)}{\partial \eta} - Bi_s \theta_s(0,\xi,Fo) = 0 \tag{27}$$

$$\frac{\partial \theta_f(0,\xi,Fo)}{\partial \eta} - Bi_f \theta_f(0,\xi,Fo) = 0 \tag{28}$$

$$\frac{\partial \theta_s(\eta,1,Fo)}{\partial \xi} = 0 \tag{29}$$

$$\frac{\partial \theta(1,\xi,Fo)}{\partial \eta} = 0 \tag{30}$$

$$\frac{\partial \theta_f(\eta,0,Fo)}{\partial \xi} = 0 \tag{31}$$

$$\frac{\partial \theta_f(\eta,\delta_f,Fo)}{\partial \xi} = \kappa \frac{\partial \theta_s(\eta,\delta_f,Fo)}{\partial \xi} \tag{32}$$

$$-\frac{\partial \theta_f(\eta,\delta_f,Fo)}{\partial \xi} = \Lambda\left(\theta_f(\eta,\delta_f,Fo) - \theta_s(\eta,\delta_f,Fo)\right) \tag{33}$$

The dimensionless energy equation, **Eqs.** (23)–(33), is solved using the Eigenfunction Expansion Method. The closed-form solution of the dimensionless temperature is as follows:

$$\theta(\eta,\xi,Fo) = \sum_{n=1}^{\infty}\sum_{m=1}^{\infty} X_n(\eta)\psi_{nm}(\xi)\Gamma_{nm}(Fo) \tag{34}$$

where, X and ψ are spatial Eigenfunctions in η and ξ directions, respectively. Also, Γ is the temporal Eigenfunction. Based on Eqs. (23)–(33), the following eigen-value problem can be established in η direction [143].

$$X'' + \gamma^2 X = 0 \tag{35}$$

$$X' - Bi\, X = 0 \text{ at } \eta = 0 \tag{36}$$

$$X' = 0 \text{ at } \eta = 1 \tag{37}$$

The following transcendental equation is obtained to evaluate the eigenvalues.

$$\gamma \tan(\gamma) = Bi \tag{38}$$

where, γ is the eigenvalue (-), and Bi is Biot number (-), respectively. The eigenfunction associated with each eigenvalue are given as follows:

$$X = \cos(\gamma\eta) + \tan(\gamma)\sin(\gamma\eta) \tag{39}$$

Moreover, the eigen-value problem in ξ direction can be established as follows:

$$\frac{d^2\psi}{d\xi^2} + \omega_k^2 \psi = 0 \tag{40}$$

$$\frac{d\psi}{d\xi}\Big|_{\xi=0,1} = 0 \tag{41}$$

where,

$$\omega_k{}^2 = \frac{\lambda r_k - q_k}{p_k},\ k = s, f \tag{42}$$

$$r_s = \frac{\left(\left(\rho c_p\right)_s - \left(\rho h_{ads} m'\right)_s\right) k_x}{\left(\rho c_p\right)_f \delta^2} \tag{43}$$

$$r_f = \frac{k_x}{\delta^2} \tag{44}$$

$$q_k = \left(\mu_{k,\eta}\gamma\right)^2 r_k \tag{45}$$

$$p_f = k_y \tag{46}$$

$$p_s = k_s \tag{47}$$

$$m' = \frac{d\omega}{dT_s} \tag{48}$$

where, ρ is density (kg/m^3), c_p is specific heat (J/(kg K)), h_{ads} is sorption enthalpy (J/kg), m' is the slope of the linear relationship between sorbent temperature and water uptake

(1/K), which is explained in Section 3.5, respectively. Eqs. (40)–(47) is a singular eigenvalue problem due to non-continuous p, r and q. Also, ω_k^2 can be positive, negative or zero depending on thermophysical properties and geometrical characteristics of the sorbent and the fin, as well as the eigenvalue in η direction (γ). Thus, the eigenvalue problem does not have a simple solution with eigenfunction and transcendental equation. The present thesis follows the solution proposed by Mikhailov and Vulchanov [144]. First, the eigenvalue problem is approximated by uniformly dividing the slabs (sorbent and fin) into n–1 intervals (n is an arbitrary number at first). The finer the division of the intervals, the more accurate the approximation. The new eigenvalue problem with boundary conditions are as follows:

$$\frac{d^2\psi}{d\xi^2} + \omega_k^2\psi = 0 \tag{49}$$

$$\frac{d\psi}{d\xi}\Big|_{\xi=0} = 0 \tag{50}$$

$$\psi_k = \psi_{k+1},\ k = 1, 2, ..., n-2 \tag{51}$$

$$p_k \frac{d\psi_k}{d\xi} = p_{k+1} \frac{d\psi_{k+1}}{d\xi},\ k = 1, 2, ..., n-2 \tag{52}$$

$$\frac{d\psi}{d\xi}\Big|_{\xi=1} = 0 \tag{53}$$

$$l_k = \xi_{k+1} - \xi_k \tag{54}$$

TCR at the interface between the sorbent and the fin is taken into account as an additional imaginary layer as follows:

$$\frac{d^2\psi}{d\xi^2} + \omega_k^2\psi = 0 \tag{55}$$

$$\omega_k = 0 \tag{56}$$

$$p_k \frac{d\psi_k}{d\xi} = \frac{t_s + t_f}{TCR \cdot A}\left(\psi_{k+1} - \psi_k\right) \tag{57}$$

Hence, thermal conductivity of this layer must satisfy the following equation for an arbitrary length of l_k.

$$p_k = \frac{\left(t_s + t_f\right) l_k}{TCR \cdot A} \tag{58}$$

where, t_s is sorbent thickness (m), t_f is fin thickness (m), *TCR* is thermal contact resistance between the sorbent and the heat exchanger (K/W), and *A* is the surface area of the TCR interface (m^2), respectively. The following eigenfunctions can be acquired for each interval ($\xi_k < \xi < \xi_{k+1}$).

$$\psi_k\left(\xi\right) = \psi_k\left(\xi_k\right)\frac{\sin\left(\omega_k\left(\xi_{k+1}-\xi\right)\right)}{\sin\left(\omega_k l_k\right)} + \psi_k\left(\xi_{k+1}\right)\frac{\sin\left(\omega_k\left(\xi-\xi_k\right)\right)}{\sin\left(\omega_k l_k\right)},\ {\omega_k}^2 > 0 \tag{59}$$

$$\psi_k\left(\xi\right) = \psi_k\left(\xi_k\right)\frac{\left(\xi_{k+1}-\xi\right)}{l_k} + \psi_k\left(\xi_{k+1}\right)\frac{\left(\xi-\xi_k\right)}{l_k},\ {\omega_k}^2 = 0 \tag{60}$$

$$\begin{aligned}\psi_k\left(\xi\right) &= \psi_k\left(\xi_k\right)\frac{\sinh\left(\omega_k^*\left(\xi_{k+1}-\xi\right)\right)}{\sinh\left(\omega_k^* l_k\right)} + \psi_k\left(\xi_{k+1}\right)\frac{\sinh\left(\omega_k^*\left(\xi-\xi_k\right)\right)}{\sinh\left(\omega_k^* l_k\right)},\ {\omega_k}^2 < 0 \\ \omega_k^* &= \sqrt{\mathrm{abs}\left({\omega_k}^2\right)}\end{aligned} \tag{61}$$

By substituting the afore mentioned eigenfunctions into the boundary conditions (Eqs. (50)–(53)), the following equations can be obtained to calculate the eigenfunctions for each interval.

$$\begin{aligned}&A_1\psi_0 - B_1\psi_1 = 0 \\ &-B_k\psi_{k-1} + \left(A_k + A_{k+1}\right)\psi_k - B_{k+1}\psi_{k+1} = 0, k = 1,2,...,n-1 \\ &-B_n\psi_{n-1} + A_n\psi_n = 0\end{aligned} \tag{62}$$

where,

$$\begin{aligned}B_k &= \frac{p_k\omega_k}{\sin\left(\omega_k l_k\right)},\ {\omega_k}^2 > 0 \\ B_k &= \frac{p_k}{l_k},\ {\omega_k}^2 = 0 \\ B_k &= \frac{p_k\omega_k^*}{\sinh\left(\omega_k^* l_k\right)},\ {\omega_k}^2 < 0\end{aligned} \tag{63}$$

$$A_k = B_k \cos\left(\omega_k l_k\right),\ \omega_k{}^2 > 0$$
$$A_k = B_k,\ \omega_k{}^2 = 0 \tag{64}$$
$$A_k = B_k \cosh\left(\omega_k^* l_k\right),\ \omega_k{}^2 < 0$$

Eq. (62) forms a linear system of (n+1) homogeneous equations for determination of the eigenfunctions as follows:

$$\left[K\right]\left\{\psi\right\} = 0 \tag{65}$$

By equating the determinant of coefficient matrix [K] to zero, the transcendental equation is acquired to evaluate the eigenvalues.

$$\det\left(\left[K\right]\right) = 0 \tag{66}$$

The eigenvalues are calculated using the algorithm proposed by Mikhailov and Vulchanov, which is based on a sign-count method [144], as follows:

The number of positive eigenvalues between zero and some prescribed positive value, $\tilde{\lambda}$, can be calculated as follows:

$$N\left(\tilde{\lambda}\right) = N_0\left(\tilde{\lambda}\right) + s\left(\left[K\left(\tilde{\lambda}\right)\right]\right) \tag{67}$$

$$N_0\left(\tilde{\lambda}\right) = \sum_{k=1}^{n} \mathrm{int}\left(\frac{\tilde{\omega}_k l_k}{\pi}\right) \tag{68}$$

$$\tilde{\omega}_k{}^2 = \frac{\tilde{\lambda} r_k - q_k}{p_k} \tag{69}$$

where, sign-count, i.e. $s\left(\left[K\left(\tilde{\lambda}\right)\right]\right)$, is the number of negative elements along the main diagonal of the triangulated form of $K\left(\tilde{\lambda}\right)$ and equal to the number of negative elements in the following sequence.

$$\frac{D_1}{D_0}, \frac{D_2}{D_1}, ..., \frac{D_n}{D_{n-1}} \tag{70}$$

where,

$$D_0 = 1, D_1 = A_1,$$
$$D_k = D_{k-1}\left(A_k + A_{k-1}\right) - D_{k-2} B_{k-1}{}^2, k = 2, ..., n-1 \tag{71}$$
$$D_n = D_{n-1}\left(A_n\right) - D_{n-2} B_{n-1}{}^2$$

Fig. 35 shows the algorithm used to acquire the eigenvalues. The order of eigenvalue, i, accuracy, ε_i, lower bound, λ_l, upper bound, λ_u, and the increment, $\tilde{\delta}$, are set and the iterations are performed until the accuracy is met. The accuracy in obtaining the eigenvalues is set to 0.001.

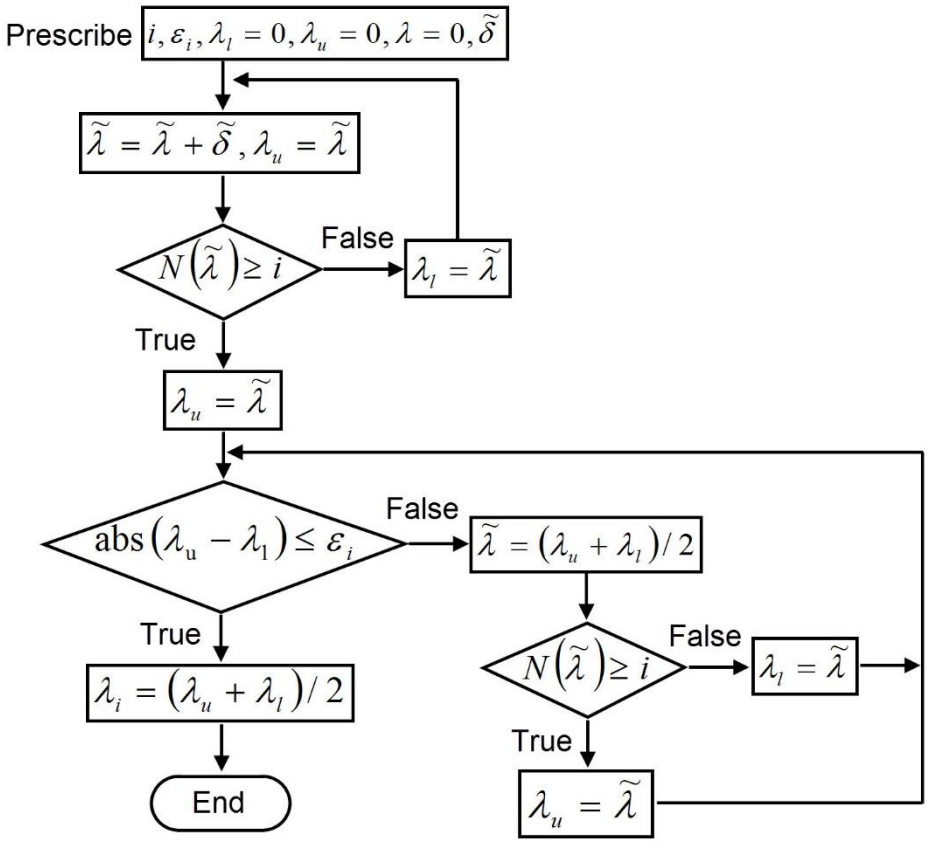

Fig. 35. Flow chart of the algorithm used to acquire the eigenvalues

Subsequently, the eigenfunctions are calculated as follows:

$$\psi_0 = -1 \tag{72}$$

$$\psi_1 = -A_1 / B_1 \tag{73}$$

$$\psi_{k+1} = \left(\left(A_k + A_{k+1} \right) \psi_k - B_k \psi_{k-1} \right) / B_{k+1}, k = 1, 2, ..., n-1 \tag{74}$$

Afterwards, the accuracy of the eigenfunctions is calculated for the last interval.

$$\text{abs}\left(-B_n \psi_{n-1} + A_n \psi_n \right) \leq \varepsilon_{global}, \varepsilon_{global} \cong \varepsilon_{\max} \cdot n \tag{75}$$

where, the accuracy is set to 1e-8 in the present study. If this accuracy requirement is not satisfied, then the intervals are refined based on the algorithm proposed by Mikhailov and Vulchanov [144] until it is satisfied as shown in **Fig. 36**.

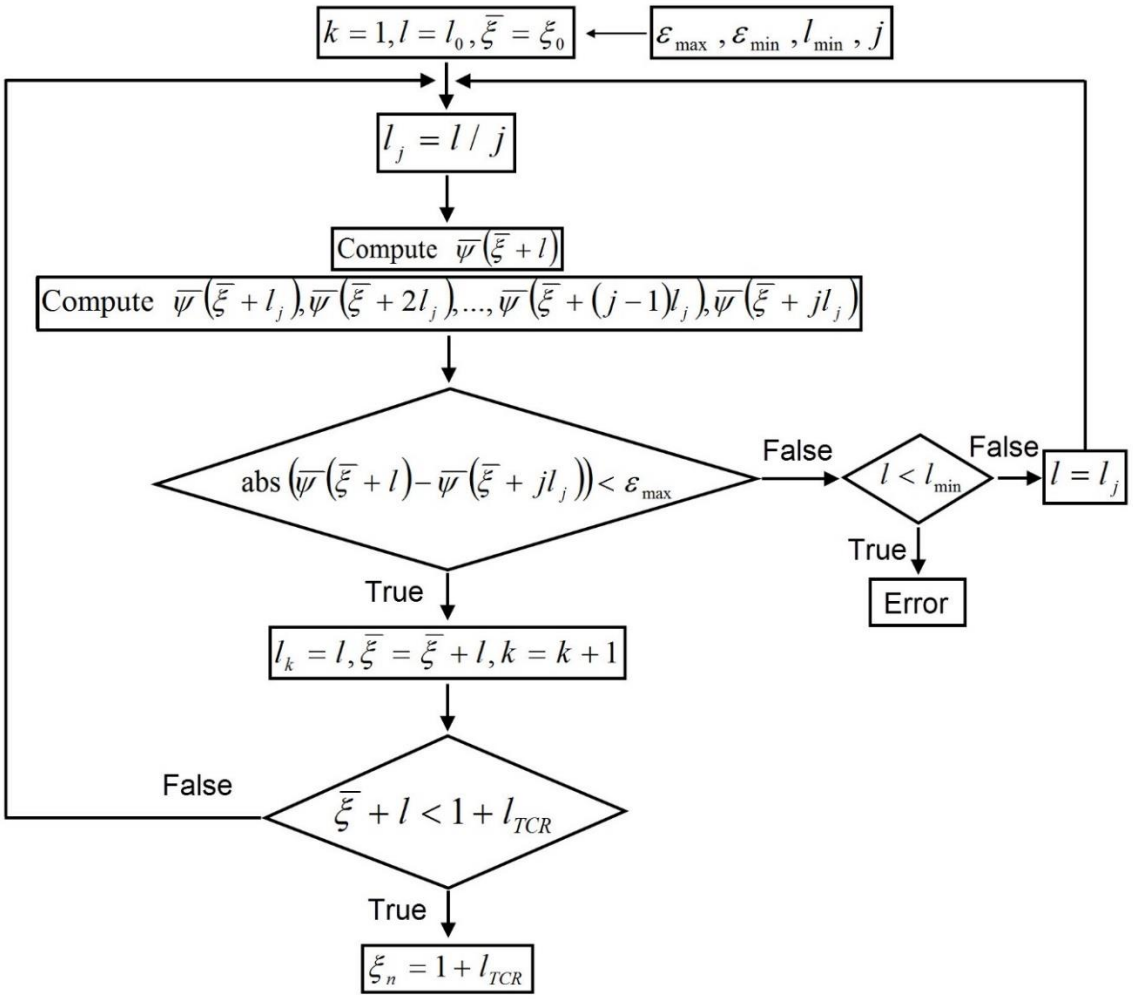

Fig. 36. Flow chart of the algorithm used to refine the intervals to increase the accuracy

Now that the eigenfunctions in η and ξ directions are calculated, the last step is to obtain the Gamma function (Γ) which represents the time variation of θ.

Every time-dependent function can be expanded in the form of an infinite series of products of the eigenfunctions in η and ξ directions.

$$g_i(Fo) = \sum_{n=1}^{\infty}\sum_{m=1}^{\infty} g^*_{nm}(Fo) X_n(\eta)\psi_{nm}(\xi) \tag{76}$$

where, using the orthogonal property of the Eigenfunctions

$$g_{nm}^{*}(Fo)=\frac{g_i(Fo)\int_0^1 Xd\eta\left(\sum_{k=1}^{n} r_k \int_{\xi_k}^{\xi_{k+1}} \psi_k d\xi\right)}{\int_0^1 X^2 d\eta\left(\sum_{k=1}^{n} r_k \int_{\xi_k}^{\xi_{k+1}} {\psi_k}^2 d\xi\right)} \tag{77}$$

By substituting Eq. (34) and (76) into Eq. (23), an ordinary differential equation for Gamma function can be acquired as follows:

$$\frac{d\Gamma}{dFo}=g_{nm}^{*}(Fo)-\lambda\Gamma \tag{78}$$

Finally, the Gamma function is calculated by Eq. (79).

$$\Gamma=e^{-\lambda Fo}\left(C_{nm}+\int_{Fo'=0}^{Fo} g_{nm}^{*}(Fo')e^{\lambda Fo'}dFo'\right) \tag{79}$$

where,

$$C_{nm}=\frac{\int_0^1 Xd\eta\left(\sum_{k=1}^{n} r_k \int_{\xi_k}^{\xi_{k+1}} \psi_k d\xi\right)}{\int_0^1 X^2 d\eta\left(\sum_{k=1}^{n} r_k \int_{\xi_k}^{\xi_{k+1}} {\psi_k}^2 d\xi\right)} \tag{80}$$

A code is developed in MATLAB that calculates the eigenvalues and eigenfunctions in η and ξ (non-dimensional) coordinates, as well as Gamma function as a function of Fourier number (dimensionless time), which is presented in Appendix E. The closed-form of the dimensionless transient 2-D temperature domain is found in a series form as follows:

$$\theta(\eta,\xi,Fo)=\sum_{n=1}^{\infty}\sum_{m=1}^{\infty} X_n(\eta)\psi_{nm}(\xi)\Gamma_{nm}(Fo) \tag{81}$$

Our study indicates that the first 2 terms in eigenfunction X (n =1 and 2) and one term in eigenfunction ψ (m =1) yield the accuracy of 99% in the temperature distribution calculation. Each run takes about 1.5 min on a 3.4 GHz PC, which is substantially lower than computation time that would take a similar numerical heat and mass transfer model.

3.4. Model development for finned-tube sorber bed heat and mass exchanger

The model methodology is similar to that of the P-HMX in Section 3.3, with the only difference of cylindrical coordinate system and the corresponding eigenvalue problems. The solution domain of the F-HMX, shown in **Fig. 37**, can be used to predict the performance of the entire S-HMX.

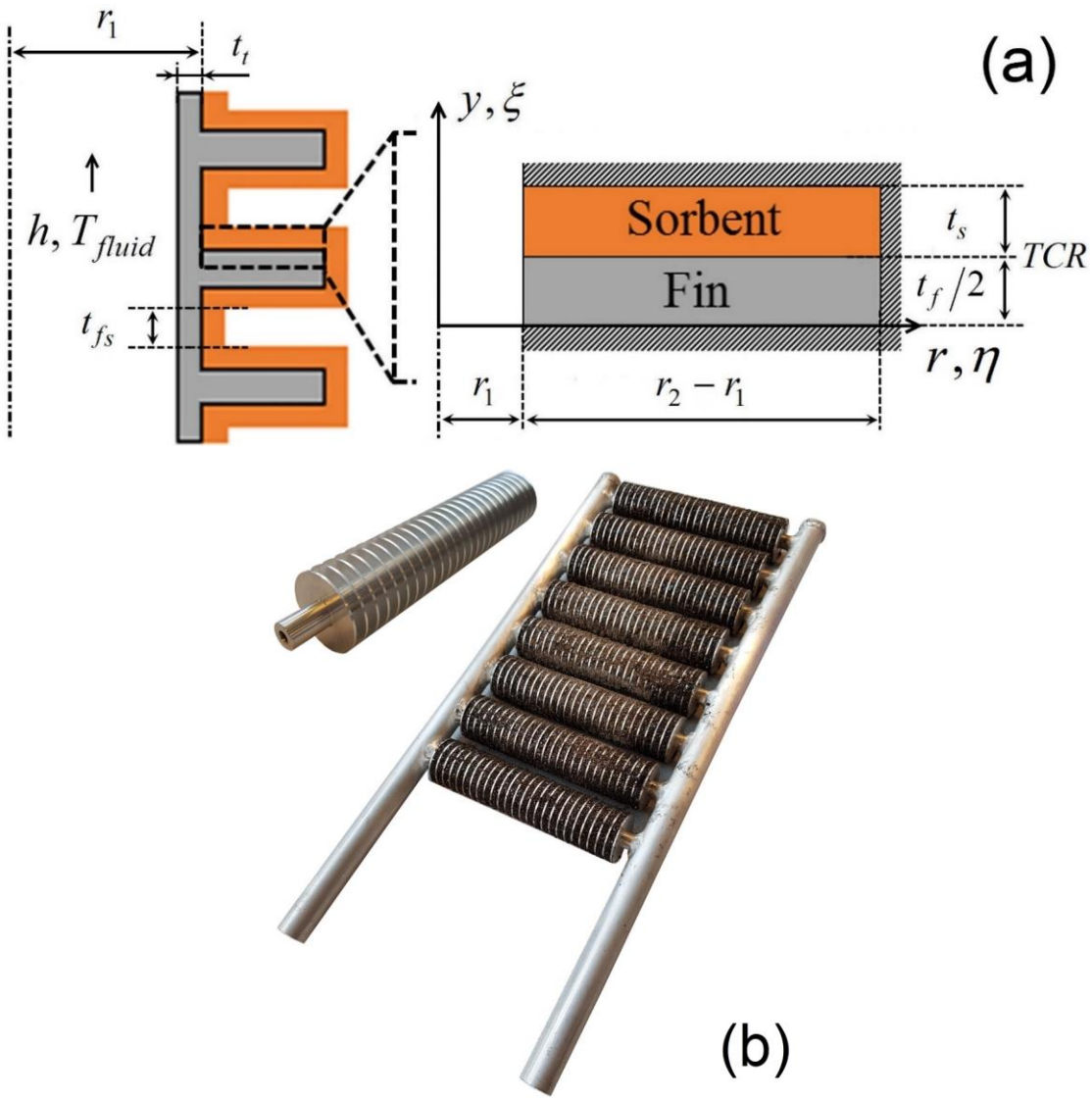

Fig. 37. (a) The solution domain; and (b) the optimized F-HMX, which will be explained in Chapter 1

The assumptions in the model development are the same as those of the previous section. The governing energy equation is similar to that of the Cartesian coordinate

system with the conduction term in r-direction in cylindrical coordinate system rather than x-direction, as follows:

$$\frac{\partial T_i}{\partial t} = \alpha_{i,r}\left(\frac{\partial^2 T_i}{\partial r^2} + \frac{1}{r}\frac{\partial T_i}{\partial r}\right) + \alpha_{i,y}\frac{\partial^2 T_i}{\partial y^2} + \frac{1}{\left(\rho c_p\right)_i} G_i(t)$$
$$T_i\left(r, y, t\right)$$
$$i = s,\ f \tag{82}$$

$$G_i\left(t\right) = \begin{cases} \rho_s h_{ads}\dfrac{\partial \omega}{\partial t}, & i = s \\ 0, & i = f \end{cases} \tag{83}$$

where, i=s, f represents the sorbent and fin domains, respectively. Also, ρ is the density (kg/m^3), ω is the water uptake (g water/g sorbent), h_{ads} is the sorption enthalpy (J/kg), and α is thermal diffusivity (m^2/s), respectively. The convective boundary conditions are:

$$\frac{1}{R_s}\left(T_s(r_1, y, t) - T_{fluid}\right) = k_s \frac{\partial T_s(r_1, y, t)}{\partial r} \tag{84}$$

$$\frac{1}{R_f}\left(T_f(r_1, y, t) - T_{fluid}\right) = k_{f,r} \frac{\partial T_f(r_1, y, t)}{\partial r} \tag{85}$$

$$R_s = 2\pi r_1 t_s\left(\frac{\ln\left(r_1/\left(r_1 - t_t\right)\right)}{2\pi k_{f,r} t_s} + \frac{1}{2\pi\left(r_1 - t_t\right)t_s h} + TCR\right) \quad \left(\frac{K\,m^2}{W}\right) \tag{86}$$

$$R_f = 2\pi r_1 t_f\left(\frac{\ln\left(r_1/\left(r_1 - t_t\right)\right)}{2\pi k_{f,r} t_f} + \frac{1}{2\pi\left(r_1 - t_t\right)t_f h}\right) \quad \left(\frac{Km^2}{W}\right) \tag{87}$$

where, t_t is the tube wall thickness (m), r_1 is tube radius (m), k is thermal conductivity (W/(m K)), h is the convective heat transfer coefficient of the heat transfer fluid (W/(m^2 K)), TCR is thermal contact resistance between the sorbent and the heat exchanger (K/W), and A is the surface area of the TCR interface (m^2), respectively. Also, the convective heat transfer coefficient is calculated by the correlation proposed by Gnielinski [135], which is applicable for 3,000<Re<10^6. It should be noted that the Reynolds number in this study for the finned-tube sorber bed heat and mass exchanger (F-HMX) is between 13,100 and 26,200 for a tube diameter of 4–8 mm and a volumetric flow rate of 5 L/min, **Table 9**. The Reynolds number for model validation is 6,300 for tube diameter of 1.65 cm, **Table 8**. The fluid regime is turbulent as the Reynolds number is more than 4,000.

$$h = 0.012\frac{k_w}{2r_1}\left(\mathrm{Re}^{0.87} - 280\right)\mathrm{Pr}^{0.4} \tag{88}$$

where, k_w is water thermal conductivity (W/(m K)), H_c is the tube channel height (m), Re is Reynolds number (-), Pr is Prandtl number (-), respectively. The adiabatic boundary conditions are:

$$\frac{\partial T(r_2, y, t)}{\partial r} = 0 \tag{89}$$

$$\frac{\partial T_s(r, t_s + t_f, t)}{\partial y} = 0 \tag{90}$$

where, r_2 is the summation of tube radius and fin height (m), t_s is sorbent thickness (m), and t_f is fin height (m), respectively. Due to symmetry, one can write the following for the lower side of the fin:

$$\frac{\partial T_s(r, t_s + t_f, t)}{\partial y} = 0 \tag{91}$$

Continuity of heat flux, as well as temperature jump/drop created by TCR are considered at the interface between the sorbent coating and fin as follows:

$$k_{f,y}\frac{\partial T_f(r, t_f, t)}{\partial y} = k_s\frac{\partial T_s(r, t_f, t)}{\partial y} \tag{92}$$

$$-k_{f,y}\frac{\partial T_f(r, t_f, t)}{\partial y} = \frac{1}{TCR \cdot A}\left(T_f(r, t_f, t) - T_s(r, t_f, t)\right) \tag{93}$$

where, $k_{f,y}$ is through-plane fin thermal conductivity (W/(m K)), k_s is sorbent thermal conductivity (W/(m K)), and t_f is fin thickness (m), respectively.

3.4.1. Solution methodology

Similar to section 3.3.1, the energy equation, **Eqs.** (82)–(93), is solved using the Eigenfunction Expansion Method as follows:

The following non-dimensional variables can be defined.

$$\theta = \frac{T - T_{fluid}}{T_0 - T_{fluid}} \qquad \xi = \frac{y}{t_s + t_f} \qquad \eta = \frac{r}{r_2}$$

$$Bi_s = \frac{r_2}{R_s k_s} \qquad Bi_f = \frac{r_2}{R_f k_f} \qquad \kappa = \frac{k_s}{k_y}$$

$$\Lambda = \frac{t_s + t_f}{k_y TCR\, A} \qquad Fo = \frac{t\alpha_r}{{r_2}^2} \qquad \delta = \frac{r_2}{t_s + t_f}$$

$${\mu_y}^2 = \frac{\alpha_y}{\alpha_r} \qquad {\mu_s}^2 = \frac{\alpha_s}{\alpha_r} \qquad \delta_f = \frac{t_f}{t_s + t_f}$$

$$\delta_r = \frac{r_1}{r_2}$$

where, θ is the dimensionless temperature, the Fourier number, Fo, is the dimensionless time, ξ and η are the dimensionless cylindrical coordinates. Using the aforementioned dimensionless variables, the dimensionless energy equation can be obtained as follows:

$$\begin{aligned} &\frac{\partial \theta_i}{\partial Fo} = {\mu_{i,\eta}}^2 \left(\frac{\partial^2 \theta_i}{\partial \eta^2} + \frac{1}{\eta} \frac{\partial \theta_i}{\partial \eta} \right) + \left(\mu_{i,\xi} \delta \right)^2 \frac{\partial^2 \theta_i}{\partial \xi^2} + g_i(Fo) \\ &\theta_i \left(\eta, \xi, Fo \right) \\ &i = s,\, f \end{aligned} \tag{94}$$

where

$$g_i\left(Fo\right) = \begin{cases} \dfrac{h_{ads}}{c_{p,s}\left(T_0 - T_{fluid}\right)} \dfrac{\partial \omega}{\partial Fo}, & i = s \\ 0, & i = f \end{cases} \tag{95}$$

$$\mu_{i,\eta} = \begin{cases} 1, i = f \\ \mu_s, i = s \end{cases} \tag{96}$$

$$\mu_{i,\xi} = \begin{cases} \mu_y, i = f \\ \mu_s, i = s \end{cases} \tag{97}$$

where, h_{ads} is the sorption enthalpy (J/kg), c_p is the specific heat (J/ (kg K)), and ω is the water uptake (g water/g dry sorbent), respectively. The dimensionless boundary conditions are:

$$\frac{\partial \theta_s(\delta_r, \xi, Fo)}{\partial \eta} - Bi_s \theta_s(\delta_r, \xi, Fo) = 0 \tag{98}$$

$$\frac{\partial \theta_f(\delta_r,\xi,Fo)}{\partial \eta} - Bi_f \theta_f(\delta_r,\xi,Fo) = 0 \tag{99}$$

$$\frac{\partial \theta_s(\eta,1,Fo)}{\partial \xi} = 0 \tag{100}$$

$$\frac{\partial \theta(1,\xi,Fo)}{\partial \eta} = 0 \tag{101}$$

$$\frac{\partial \theta_f(\eta,0,Fo)}{\partial \xi} = 0 \tag{102}$$

$$\frac{\partial \theta_f(\eta,\delta_f,Fo)}{\partial \xi} = \kappa \frac{\partial \theta_s(\eta,\delta_f,Fo)}{\partial \xi} \tag{103}$$

$$-\frac{\partial \theta_f(\eta,\delta_f,Fo)}{\partial \xi} = \Lambda\left(\theta_f(\eta,\delta_f,Fo) - \theta_s(\eta,\delta_f,Fo)\right) \tag{104}$$

The difference between the F-HMX model and the P-HMX in Section 3.3, is the eigen-value problem in η direction. In Cartesian coordinates, the eigenfunctions in η direction are sinusoidal, whereas in cylindrical coordinate, they are in the from of Bessel functions.

Based on Eqs. (94)–(104), the following eigen-value problem can be established in η direction.

$$\Phi'' + \frac{1}{\eta}\Phi' + \gamma^2 \Phi = 0 \tag{105}$$

$$\Phi' - Bi\,\Phi = 0 @ \eta = \delta_r \tag{106}$$

$$\Phi' = 0 @ \eta = 1 \tag{107}$$

The following transcendental equation is obtained to evaluate the eigenvalues.

$$-\gamma J_1(\gamma\delta_r) + \frac{\gamma J_1(\gamma)}{Y_1(\gamma)} Y_1(\gamma\delta_r) - BiJ_0(\gamma\delta_r) + Bi\frac{J_1(\gamma)}{Y_1(\gamma)} Y_0(\gamma\delta_r) = 0 \tag{108}$$

where, γ is the eigenvalue (-), and Bi is Biot number (-), respectively. The eigenfunction associated with each eigenvalue are given as follows:

$$\Phi = J_0(\gamma\eta) - \frac{J_1(\gamma)}{Y_1(\gamma)} Y_0(\gamma\eta) \tag{109}$$

where, the Bessel functions of the first and second kind are

$$J_m(\eta)=\sum_{k=0}^{\infty}\frac{(-1)^k}{k!(k+m)!}\left(\frac{\eta}{2}\right)^{2k+m} \tag{110}$$

$$Y_m(\eta)=\lim_{\alpha\to m}\left(\frac{J_\alpha(\eta)\cos(\alpha\pi)-J_{-\alpha}(\eta)}{\sin(\alpha\pi)}\right) \tag{111}$$

where, m is an integer. Furthermore, the coefficient of Gamma function needs to be updated

$$\Gamma=e^{-\lambda Fo}\left(C_{nm}+\int_{Fo'=0}^{Fo}g_{nm}^{*}(Fo')e^{\lambda Fo'}dFo'\right) \tag{112}$$

$$C_{nm}=\frac{\int_{\delta_r}^{1}\Phi d\eta\left(\sum_{k=1}^{n}r_k\int_{\xi_k}^{\xi_{k+1}}\psi_k d\xi\right)}{\int_{\delta_r}^{1}\Phi^2 d\eta\left(\sum_{k=1}^{n}r_k\int_{\xi_k}^{\xi_{k+1}}{\psi_k}^2 d\xi\right)} \tag{113}$$

The rest of the solution is similar to that of the Cartesian coordinate presented in Section 3.3. A code is developed in MATLAB that calculates the eigenvalues and eigenfunctions in η and ξ (non-dimensional) coordinates as well as Gamma function as a function of Fourier number (dimensionless time), which is presented in Appendix E. The closed-form of the dimensionless transient 2-D temperature domain is found in a series form as follows:

$$\theta(\eta,\xi,Fo)=\sum_{n=1}^{\infty}\sum_{m=1}^{\infty}\Phi_n(\eta)\psi_{nm}(\xi)\Gamma_{nm}(Fo) \tag{114}$$

where, X and ψ are spatial Eigenfunctions in η and ξ directions, respectively. Also, Γ is the temporal Eigenfunction. Our study indicates that the first term in eigenfunction Φ (n =1) and one term in eigenfunction ψ (m =1) yield the accuracy of 99% in the temperature distribution calculation. Each run takes about 1.5 min on a 3.4 GHz PC.

3.5. Water uptake modeling

S-HMXs go through two isosteric processes, i.e. cooling and heating, during which the water uptake remains almost constant because the valves to the evaporator and condenser are closed. Each isosteric process is followed by an isobaric process when the S-HMX is connected to the evaporator or condenser, and sorption or desorption occurs.

During isobaric processes, the pressure of the S-HMX chamber is almost equal to that of the evaporator or condenser and assumed constant. **Fig. 38** shows the variation of water uptake versus sorbent temperature for each isobaric process obtained from a gravimetric large pressure jump (G-LPJ) test bed with T_{evap}=20 °C and T_{cond}=1 °C, see Chapter 1. It can be seen that the equilibrium water uptake collected from a Thermogravimetric analyzer (TGA) is close to the transient data measured using our custom-built G-LPJ test bed. The TGA measurement procedure was explained in Section 2.5. **Fig. 38** shows that the first two assumptions in the model development are valid; i.e.

1. Uniform sorbate pressure inside the sorbent; and
2. Thermodynamic equilibrium of sorbent and sorbate.

Therefore, for each isobaric process with the pressure equal to the saturation pressure at condenser or evaporator temperature, a relationship can be acquired between the water uptake and sorbent temperature. For simplicity in the 2-D analytical model, this relationship is approximated linearly.

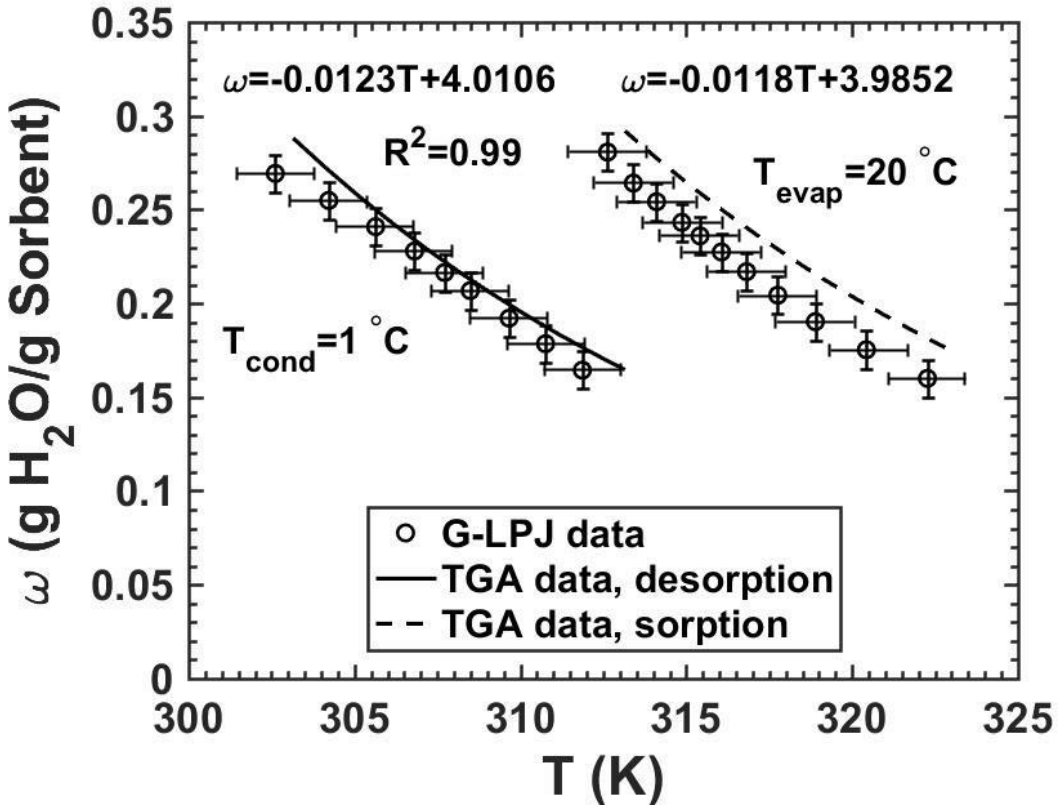

Fig. 38. Variation of water uptake versus sorbent temperature for large pressure jump tests, T_{sorp}=39 °C , T_{evap}=20 °C and T_{cond}=1 °C

Fig. 39 shows the isobaric processes acquired from the TGA for pressure values corresponding to T_{evap}=15 °C and T_{cond}=30 °C for large temperature jump (LTJ) tests.

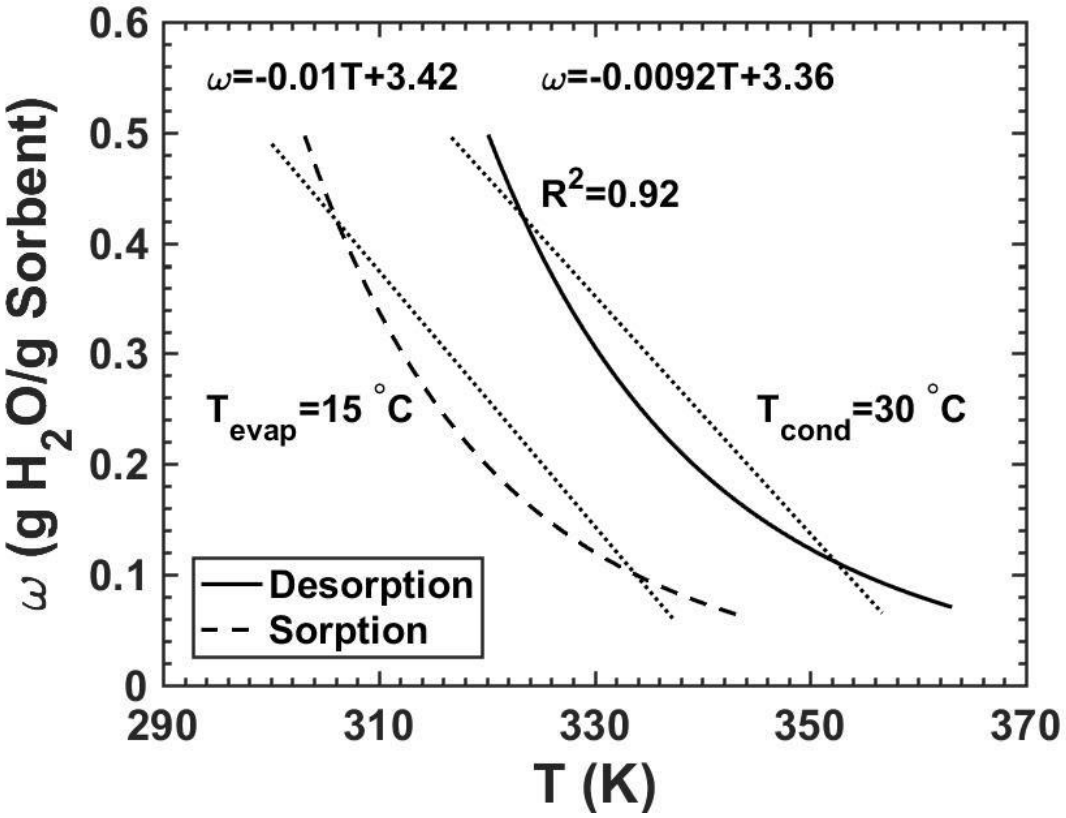

Fig. 39. Variation of water uptake versus sorbent temperature for large temperature jump tests, T_{evap}=15 °C, T_{sorp}=T_{cond}=30 °C and T_{des}=90 °C

3.6. Model validation

The 2-D analytical model for the P-HMX was validated with the G-LPJ data in Chapter 1, **Fig. 31** and **Fig. 32**. Also, in Section 3.6.1, the F-HMX model is validated with off-the-shelf finned-tube heat and mass exchangers tested in the two-sorber bed sorption test bed. In Chapter 5, optimized S-HMXs of the P-HMX and the F-HMX are designed, built and tested, which will be used to further validate the analytical models in Section 5.5.3, **Fig. 72**.

3.6.1. F-HMX model validation

Fig. 40 shows the off-the-shelf S-HMX used in this study, which is an engine oil cooler manufactured by Hayden Automotive (model #1268). The S-HMX was coated with a composite sorbent consisting of $CaCl_2$, silica gel B150, PVA, and graphite flakes. Details

of the S-HMX geometry and heat transfer characteristics are listed in **Table 8**. This S-HMX was the closest off-the-shelf heat exchanger to the solution domain of the F-HMX model, shown in **Fig. 37** (a). Thus, it was used to validate the model and as a benchmark to compare the optimized S-HMXs developed in Chapter 5. A two-sorber bed sorption test bed was custom-built to test the S-HMXs. The test bed will be elaborated in Section 5.4. **Fig. 41** shows a schematic and a picture of the two-sorber bed sorption test bed.

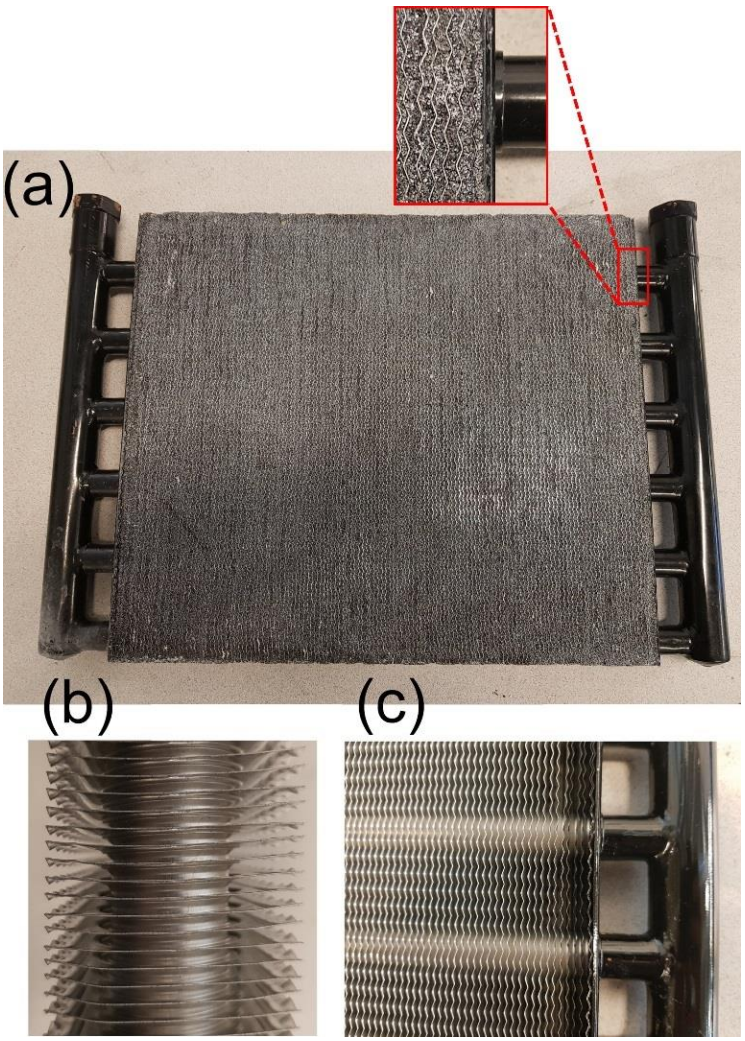

Fig. 40. (a) Sorber bed coated with the composite sorbent, $CaCl_2$, silica gel B150, PVA and graphite flakes, and the finned-tube HEX without sorbent coating; (b) top view; and (c) front view

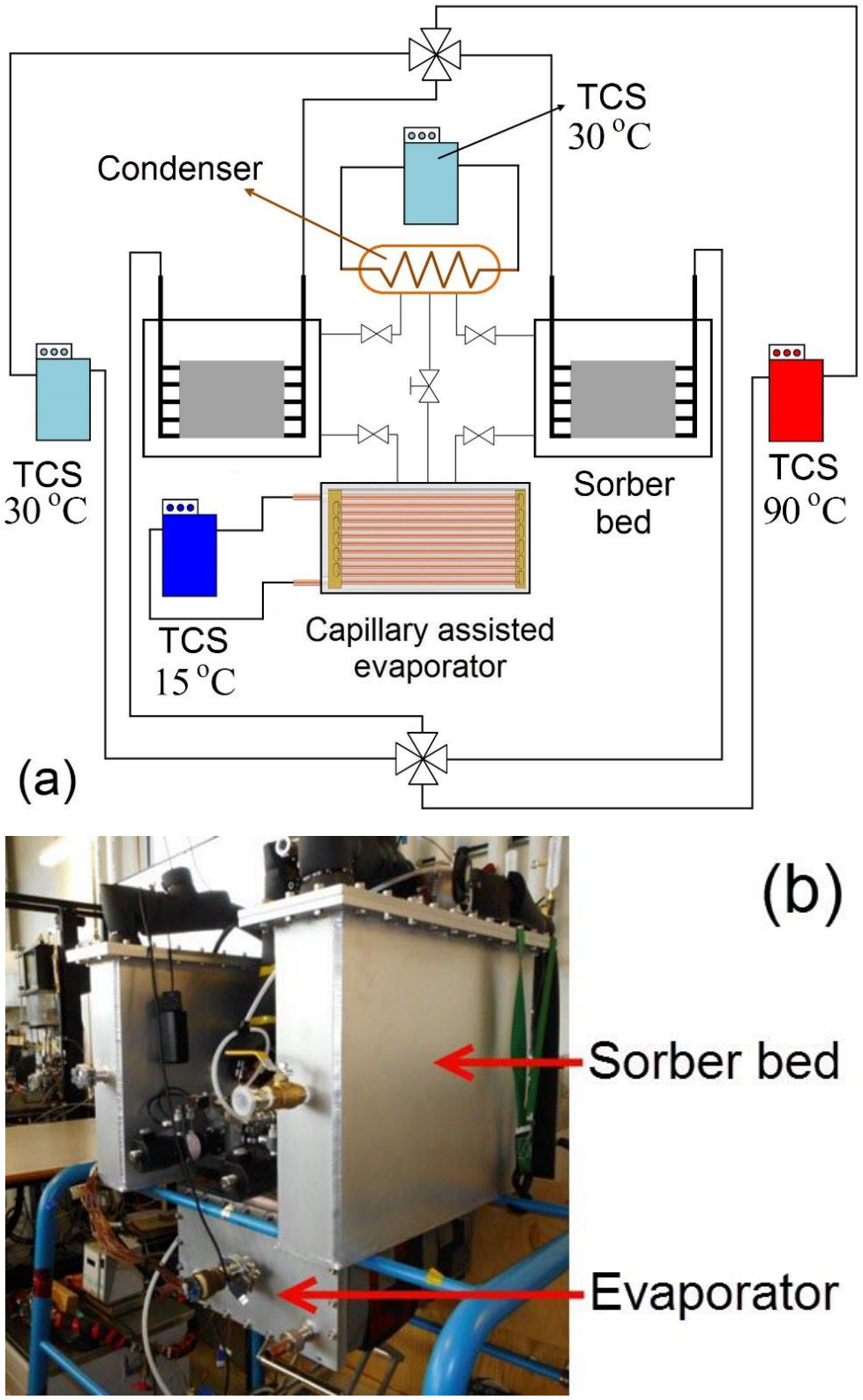

Fig. 41. (a) Schematic and (b) a picture of the two-sorber bed sorption test bed, TCS: temperature control system

Table 8. Graphite flake content in the sorbent, thermophysical properties, geometrical specifications, and SCS cycle parameters used for the model validation.

	Sorbent		**Al fin**	**Copper tube**
ϕ (wt. %)	0	20	–	–
ρ (kg/m^3)	654	675	2700	8932
c (J/kgK)	1004	1120	896	386
α (m^2/s)	2.3e-7	1.3e-6	6.9e-5	1.1e-4
h_{ads} (J/kg)	2.77e6		–	–
t (mm)	1.12		0.15	1.55
b and D (cm)	b=1.24		b=1.24	D=1.65
τ (min)	In **Fig. 6**			
$\dot{V}$ (L/min)	5			
$TCR{\cdot}A$ (K·m^2/W)	0.0019 [1]			
T_{evap} (°C)	15			
T_{cond} (°C)	30			
T_{ads} (°C)	30			
T_{des} (°C)	90			

The relationships used to model the water uptake in terms of sorbent temperature for isobaric desorption and sorption processes were shown in **Fig. 39**.

Fin height ranges from 1.08 to 1.40 cm around the tubes in the heat exchanger shown in **Fig. 40**. Over this range of fin height, the maximum change in SCP and COP is 0.7% and 3%, respectively, compared to the SCP and COP obtained using the average fin height used in this study, i.e., 1.24 cm, listed in **Table 8**. Therefore, the average fin height is used for the model validation. **Fig. 42** shows the comparison between the SCP and COP calculated using the proposed analytical model against the data measured using the two-sorber bed sorption test bed. It can be seen in **Fig. 42**, that the present model is in a good agreement with the experimental data. Furthermore, **Fig. 42** shows that the S-HMX with 0 wt.% graphite flake generates higher SCP and COP than the one with 20 wt.%. The reason is that the main heat transfer resistance in the S-HMX is that of the fins and HTF due to the low fin thickness and high tube radius, respectively. Consequently, by increasing the graphite flake content in the sorbent, the active material decreases, which reduces the performance. While the enhanced thermal diffusivity does not result in higher

performance as the heat transfer is limited by HEX and HTF. More information is presented in section 3.7.1, **Fig. 51** and **Fig. 52**.

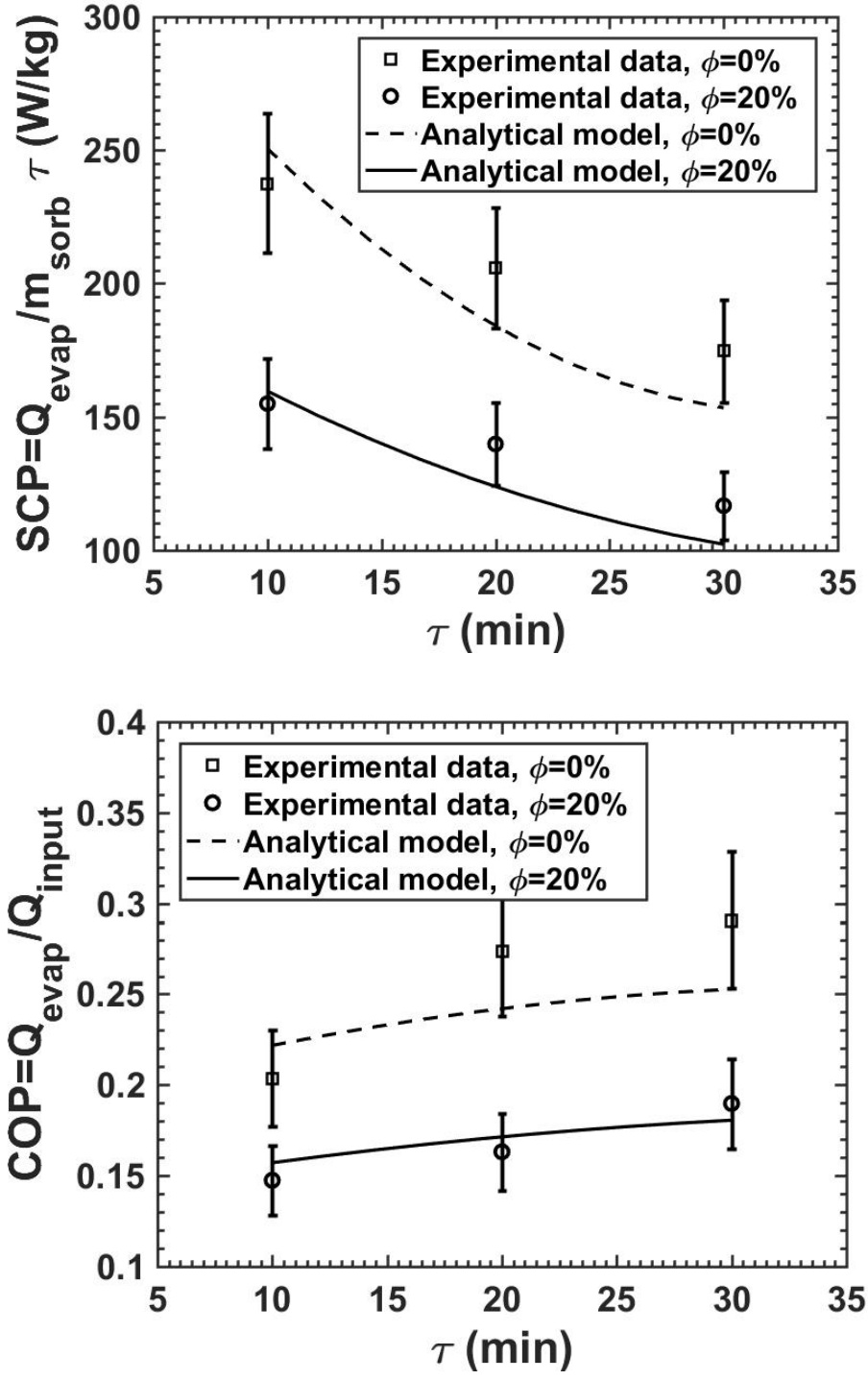

Fig. 42. Comparison between the present analytical model and the experimental data collected from our two-sorber bed sorption test bed for 0 and 20 wt.% graphite flake content in the sorbent composite; see **Table 8** for more details, T_{evap}=15 °C, T_{sorp}=T_{cond}=30 °C and T_{des}=90 °C

3.7. Results and discussion

The conduction heat transfer rate in the S-HMX is defined by **Eqs.** (115) and (116) [145].

$$\dot{q}_x = -k_x A_x \frac{\partial T}{\partial x} \quad \text{[W]} \qquad (115)$$

$$\dot{q}_y = -k_y A_y \frac{\partial T}{\partial y} \quad \text{[W]} \qquad (116)$$

where, k is thermal conductivity (W/(m K)) and A is the heat transfer surface area (m^2). The heat transfer rate can be non-dimensionalized as follows:

$$\dot{q}_x^* = \frac{b}{k_x \left(t_s + t_f\right)\left(T_0 - T_{fluid}\right)} \dot{q}_x = -\frac{\partial \theta}{\partial \eta} \quad \text{[-]} \qquad (117)$$

$$\dot{q}_y^* = \frac{b}{k_x \left(t_s + t_f\right)\left(T_0 - T_{fluid}\right)} \dot{q}_y = -\frac{k_y b^2}{k_x \left(t_s + t_f\right)^2} \frac{\partial \theta}{\partial \xi} \quad \text{[-]} \qquad (118)$$

where, b is fin height (m), t_s is sorbent thickness (m), t_f is fin thickness (m), k is thermal conductivity (W/(m K)), T_0 is the initial temperature (K), T_{fluid} is the temperature of the heat transfer fluid (HTF) (K), respectively. **Fig. 43** shows a vector plot of dimensionless heat transfer rate, Eq. (117) and (118), predicted by the proposed analytical solution, in the sorbent and the fin during sorption at Fo=32 (t=5 min) for b=3 cm, t_f=1 mm and t_s=3mm, τ=10 min, ϕ=10 wt.% and H_c=4mm. It can be seen that the majority of the heat generated inside the sorbent, is transferred from the sorbent to the fin in ξ direction; and subsequently from the fin to HTF in η direction. For example, the heat flux at the base of the sorbent and the fin is 0.02 W/m and 3.87 W/m, respectively. The reason for this is the higher thermal diffusivity of the fin compared to that of sorbent coating. Therefore, the regions of the sorbent that are closer to the fin and HTF, i.e. bottom left corner of the sorbent coating, have the highest heat transfer rate and thus sorption rate. The heat transfer rate reduces from the bottom left corner of the sorbent to the top right corner as thermal resistance increases. Hence, the fin thickness should be higher at the fin base to have a high heat transfer surface area and it can decrease along the fin to reduce the HEX thermal inertia. Alternatively, the sorbent thickness should be higher at the base where the heat transfer resistance is the lowest, and decrease along the fin. These two variable thicknesses of the fin and the sorbent could be combined to increase the performance. This is added to the recommendations for future work in section 6.4.

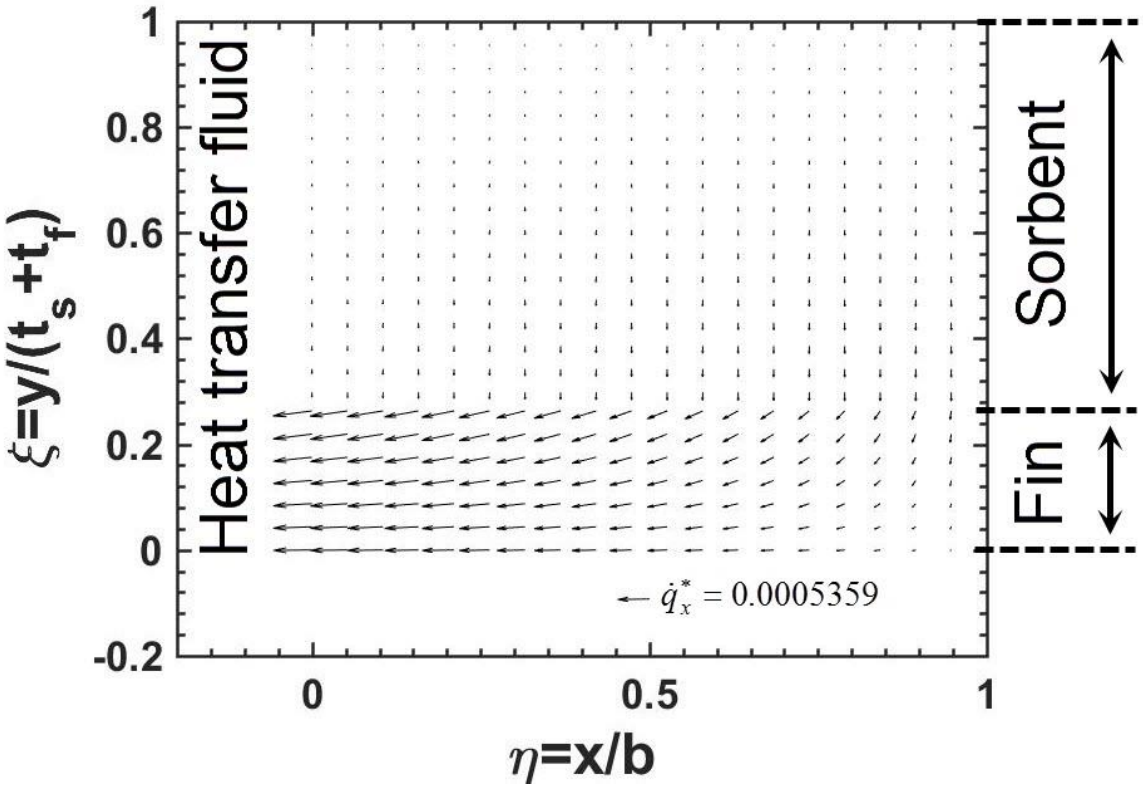

Fig. 43. Vector plot of dimensionless heat transfer rate in the sorbent and the fin during sorption at Fo=32 (t=5 min), b=3 cm, t_f=1 mm and t_s=3mm, τ=10 min, ϕ=10 wt.% and H_c=4mm

Fig. 44 (a), (b) and (c) shows the contours of dimensionless temperature, temperature and differential water uptake predicted by the present analytical solution, respectively, at Fo=32 (t=5 min) for b=3 cm, t_f=1 mm and t_s=3mm, τ=10 min, ϕ=10 wt.% and H_c=4mm. It can be seen in **Fig. 44** (a) that the fin temperature in ξ direction is almost uniform due to low heat transfer resistance of the fin in ξ direction, mainly due to small fin thickness, high fin thermal diffusivity, and high heat transfer surface area of the fins. Also, a temperature drop at the interface between sorbent and fin (ξ =0.25) can be observed, which is due to thermal contact resistance (TCR) considered in the model. Moreover, it is seen in **Fig. 44** that the highest temperature exists at the top right corner of the sorbent as the heat travels the farthest to be removed by the heat transfer fluid (HTF). Consequently, this area has the lowest water uptake. Thus, from the top right corner of the sorbent to the bottom left corner, the water uptake increases as the temperature decreases because of the higher heat transfer rate from the sorbent to the fin.

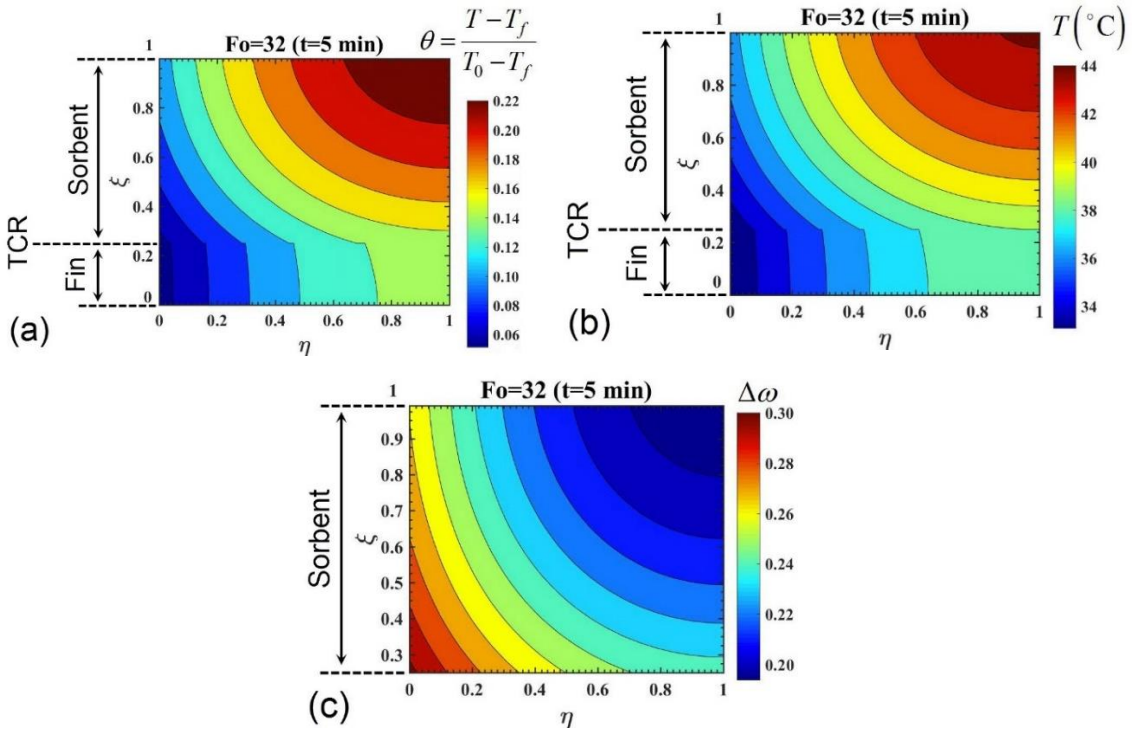

Fig. 44. Contours of (a) dimensionless temperature; (b) temperature; and (b) differential water uptake at Fo=32 (t=5 min) for b=3 cm, t_f=1 mm and t_s=3mm, τ=10 min, ϕ=10 wt.% and H_c=4mm

3.7.1. Parametric study and performance evaluation

A comprehensive parametric study is performed in which the S-HMX is considered as a baseline case (**Table 9**) and each parameter is varied systematically, while all others are kept constant. To have a fair comparison between the F-HMX and P-HMX, the sorbent volume is set equal as follows:

$$\pi\left(r_2^{\,2} - r_1^{\,2}\right)t_s = 2bt_sL \tag{119}$$

$$L = \frac{\pi}{2}\left(r_2 + r_1\right) \tag{120}$$

where, L is the fluid channel width for P-HMX, r_1 is HTF tube radius (m), b is the fin height (m), r_2 is the summation of r_1 and b (m), and t_s is the sorbent thickness (m), respectively.

Fig. 45–**Fig. 51** show the variation of SCP and COP with fin height, fin thickness, sorbent thickness, fluid tube radius or channel height, graphite flake content in the sorbent, and the cycle time. SCP, COP and the parameters are normalized with respect to the baseline case of the F-HMX in **Table 9**. The following can be observed.

Table 9. Graphite flake content in the sorbent, thermophysical properties, geometrical specifications, and SCS cycle parameters used for the baseline case and model validation.

	Sorbent	**Aluminum 6061 fin**
ϕ (wt. %)	10	–
ρ (kg/m^3)	665	2700
c (J/kgK)	1082	896
α (m^2/s)	4.1e-7	6.9e-5
h_{ads} (J/kg)	2.77e6	–
t (mm)	2	2
r_1, $H_o/2$ (mm)	3	
r_2 (mm)	23, (b=20 mm)	
τ (min)	15	
$\dot{V}$ (L/min)	5	
$TCR{\cdot}A$ (K·m^2/W)	0.0019[1]	
T_{evap} (°C)	15	
T_{cond} (°C)	30	
T_{ads} (°C)	30	
T_{des} (°C)	90	
$SCP_{F\text{-}HMX}$ (W/kg)	540	
$SCP_{P\text{-}HMX}$ (W/kg)	715	
$COP_{F\text{-}HMX}$	0.50	
$COP_{P\text{-}HMX}$	0.56	

Fig. 45 shows that by increasing the fin height, SCP decreases as the heat transfer resistance along the fin increases. Nonetheless, by increasing the fin height, COP increases and then decreases. By increasing the fin height, evaporative and desorption heat, as well as the sensible heat of sorbent, sorbate (water) and HEX increase. The sensible heat of sorbent and sorbate increase more than others as it increases linearly with the fin height. Also, the evaporative and desorption heat increase because the amount of sorbent increases, but not linearly as the heat transfer resistance along the fin in the S-HMX increases, which reduces the evaporative and desorption heat. Increasing the fin height increases HEX sensible energy less than others because of the constant part of the HEX tube. Overall, since both numerator and denominator in Eq. (7) increase

with fin height, there is an optimum point for the fin height corresponding to maximum COP.

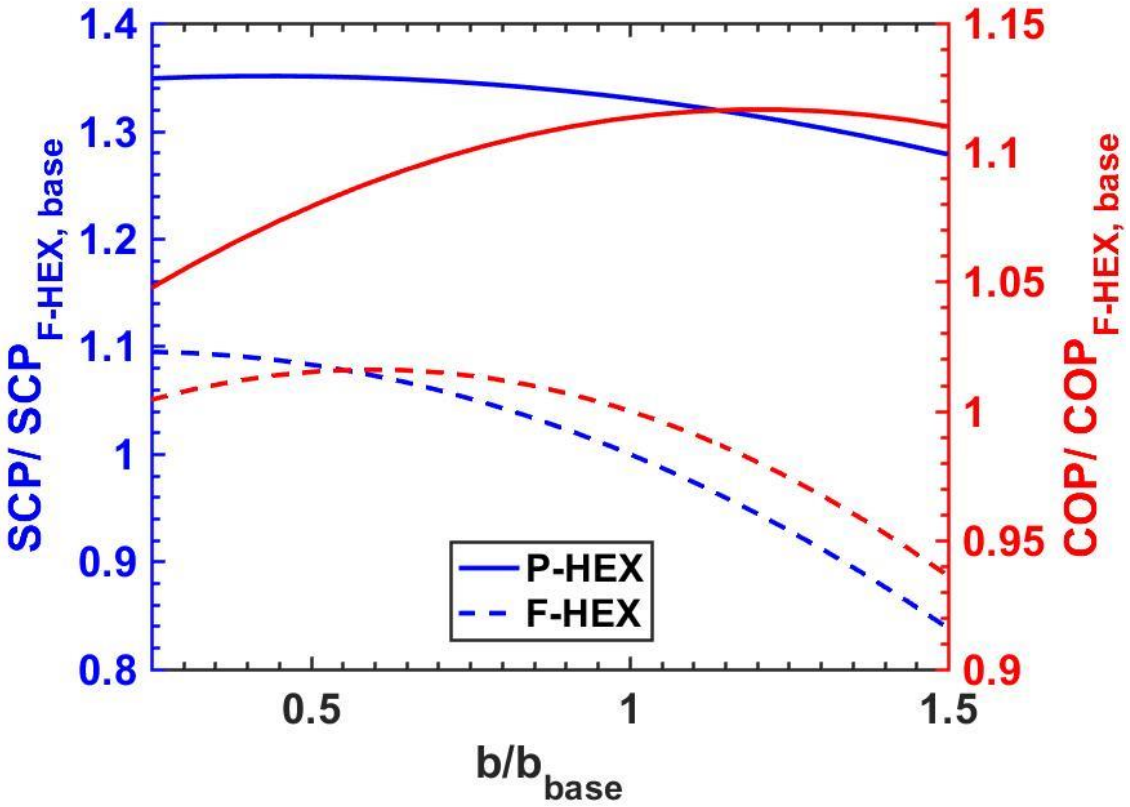

Fig. 45. Variation of SCP and COP with fin height, parameters are normalized with respect to the baseline case of the F-HMX in **Table 9**

Also, **Fig. 45** shows that the P-HMX can provide higher SCP and COP, due to two main reasons. One reason is that in the F-HMX, the amount of sorbent increases as it gets farther away from the heat transfer fluid (HTF), which increases the heat transfer resistance, see **Fig. 46**. The other reason is that the P-HMX offers two design parameters, namely, fluid channel height and width, so that an optimum convective heat transfer coefficient can be achieved for a small fluid channel height, while keeping the heat transfer surface area large enough with the fluid channel width. However, there is only one design parameter in the F-HMX, i.e. fluid tube radius. To have an optimum convective heat transfer coefficient with a small fluid tube radius, the heat transfer surface area would decrease significantly, which is highly undesirable.

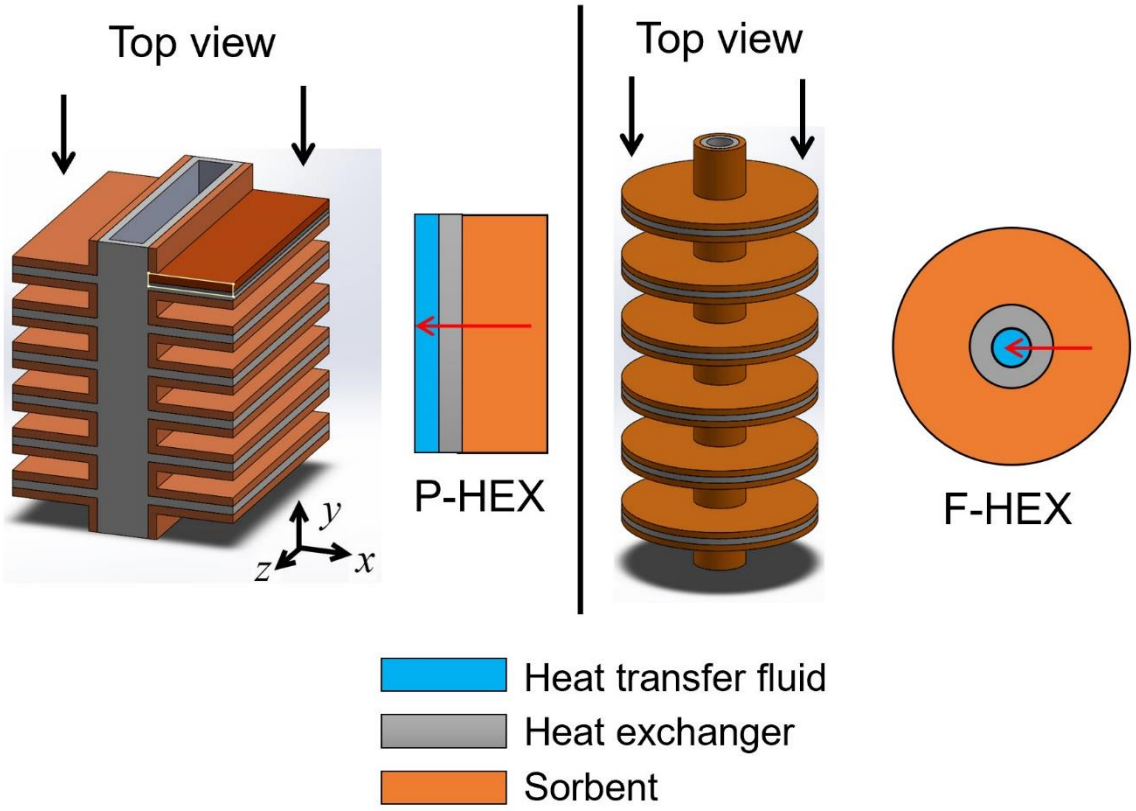

Fig. 46. Schematic of the sorber bed heat and mass exchangers for a plate-fin (P-HMX) and a finned-tube (F-HMX)

Fig. 47 shows that by increasing the fin thickness, SCP increases as the heat transfer along the fin enhances due to more cross-sectional area. However, by increasing the fin thickness, COP reduces because the HEX thermal inertia increases.

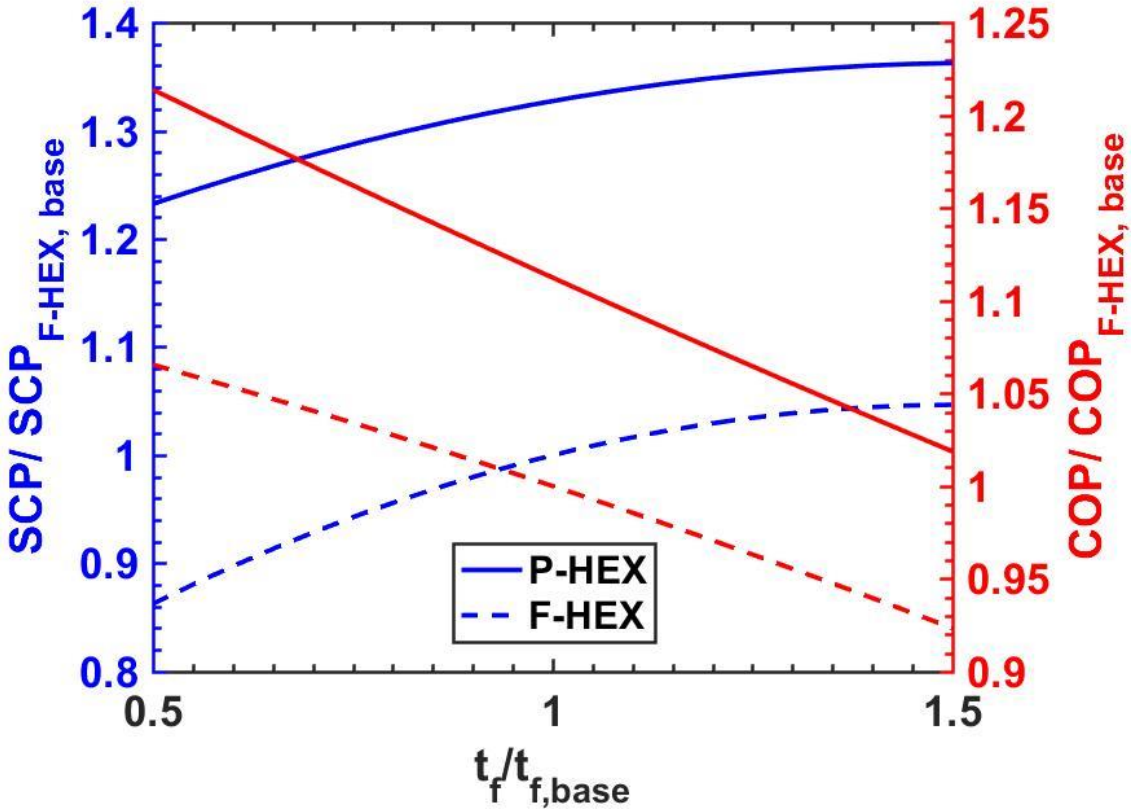

Fig. 47. Variation of SCP and COP with fin thickness. Parameters are normalized with respect to the baseline case of the F-HMX in **Table 9**

Fig. 48 shows that by increasing the sorbent thickness, SCP decreases as the sorbent heat transfer resistance increases. Nevertheless, by increasing the sorbent thickness, COP increases at first and then starts to decrease. The reason for this is that the sensible energy of sorbent and water increase linearly. Both evaporative and desorption energy increase, but less than that of sorbent sensible energy, due to the increased heat transfer resistance in the sorbent. HEX sensible energy remains constant. Since both numerator and denominator in Eq. (7) increase, there exists an optimum sorbent thickness, which maximizes the COP.

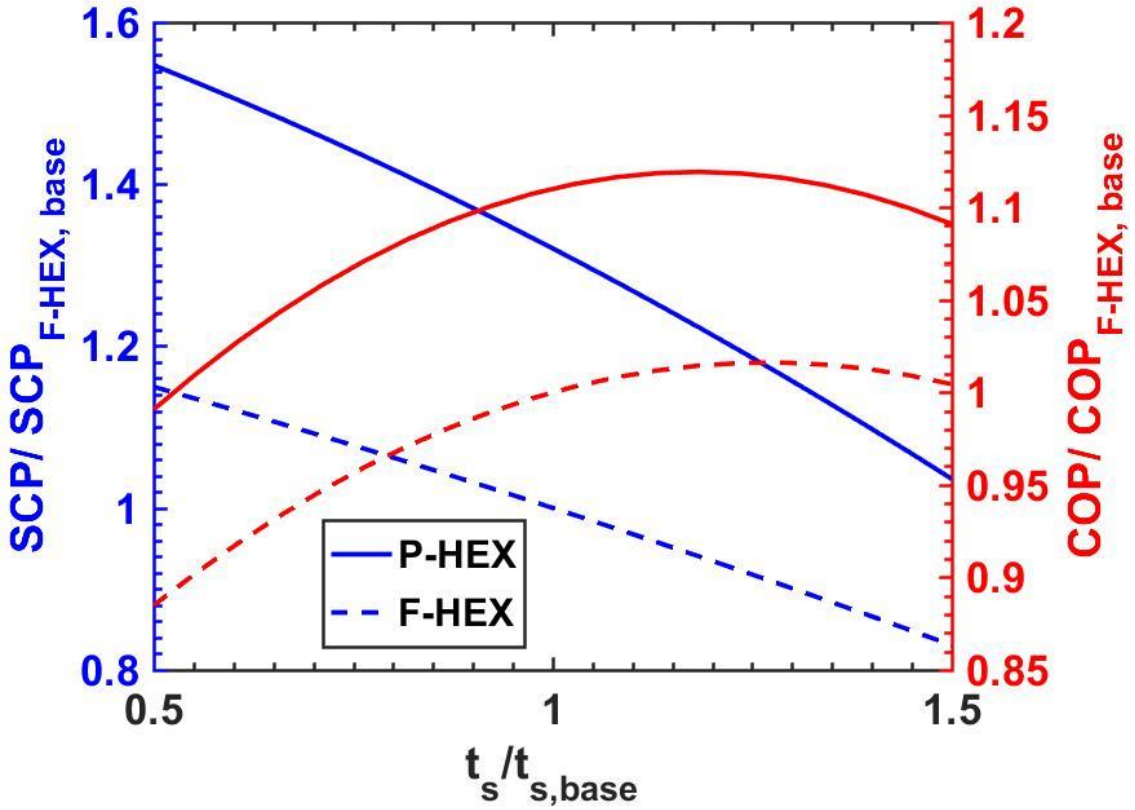

Fig. 48. Variation of SCP and COP with sorbent thickness, parameters are normalized with respect to the baseline case of the F-HMX in **Table 9**

Fig. 49 shows that by reducing the fluid channel height and tube radius, both SCP and COP increase as the convective heat transfer coefficient of the heat transfer fluid increases, but they increase slightly because the heat transfer resistance of the heat transfer fluid is not the main resistance.

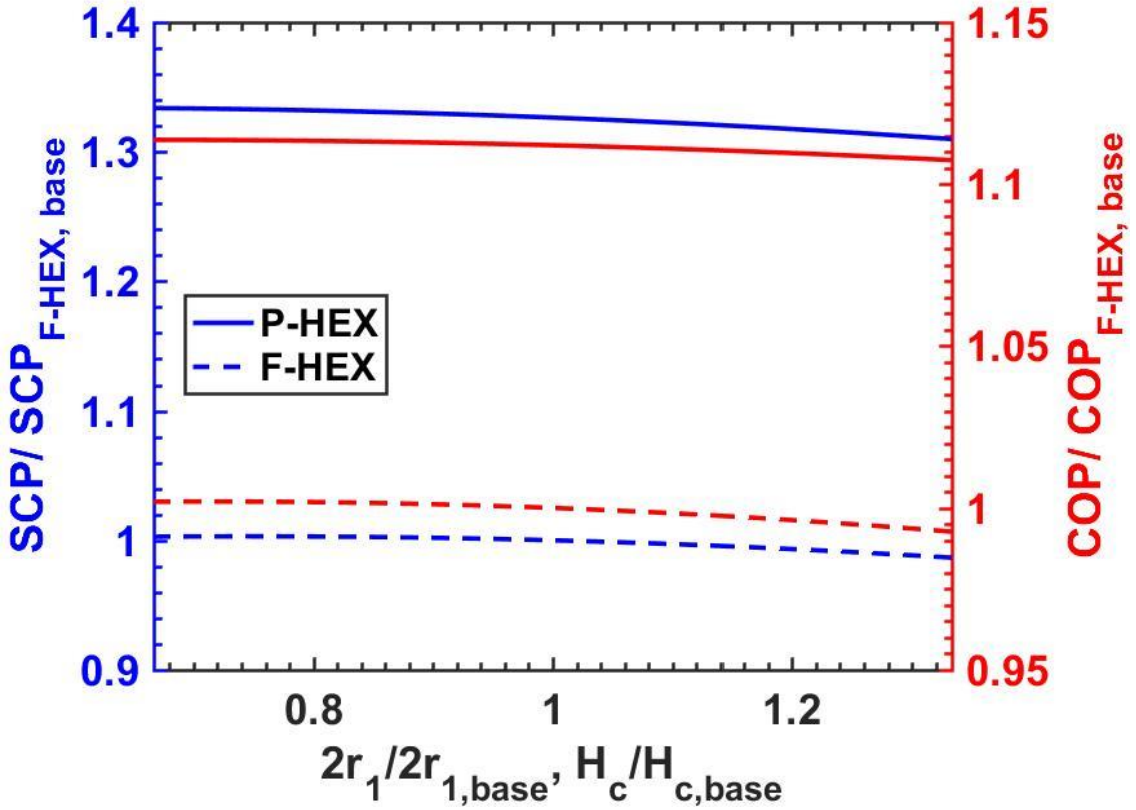

Fig. 49. Variation of SCP and COP with fluid channel height or fluid tube diameter. Parameters are normalized with respect to the baseline case of the F-HMX in **Table 9**

Sorption rate is high at the early stages of sorption and decreases as the sorbent approaches saturation. Consequently, by decreasing the cycle time, SCP increases as the sorption rate, and thus, the evaporative cooling power increases. However, by reducing the cycle time, COP decreases because more energy is needed to overcome the S-HMX thermal inertia compared to the desorption heat. These trends can be observed in **Fig. 50**.

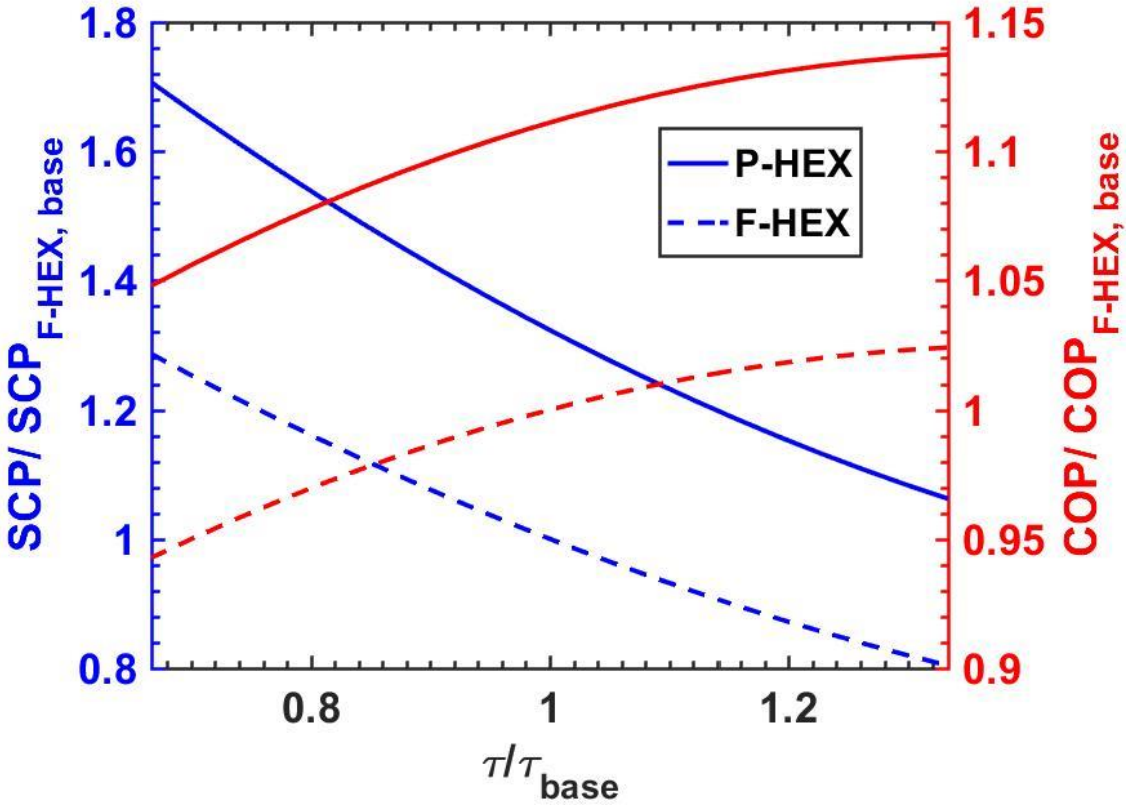

Fig. 50. Variation of SCP and COP with cycle time. Parameters are normalized with respect to the baseline case of the F-HMX in **Table 9**

Adding graphite flakes to the sorbent enhances its thermal diffusivity notably (up to 500%, Section 2.4) and reduces the active sorbent material. It is key to select an optimum amount of graphite flake additive, which depends on the S-HMX geometry, cycle time, and heat transfer characteristics. If the main thermal resistance in the S-HMX is the sorbent, by increasing the graphite flake content, SCP increases to the point where the heat transfer becomes limited by the heat exchanger (HEX) or the heat transfer fluid (HTF). After this point, SCP starts to decrease by any further increase in the graphite flake content because the active sorbent material is reduced. This trend can be seen in **Fig. 51**. The same trend can be observed for COP. On the other hand, if the sorbent thermal resistance is not the main thermal resistance in the S-HMX, adding graphite flakes does not increase the performance as the heat transfer is limited by other thermal resistances in the S-HMX, e.g. the HEX and/or the HTF. Therefore, adding graphite flakes reduces the performance since it decreases the active sorbent material, see **Fig. 52**. In this case, the enhanced sorbent thermal diffusivity does not increase the total heat transfer noticeably as the heat transfer is limited by the thin fin, i.e. 0.1 mm thickness.

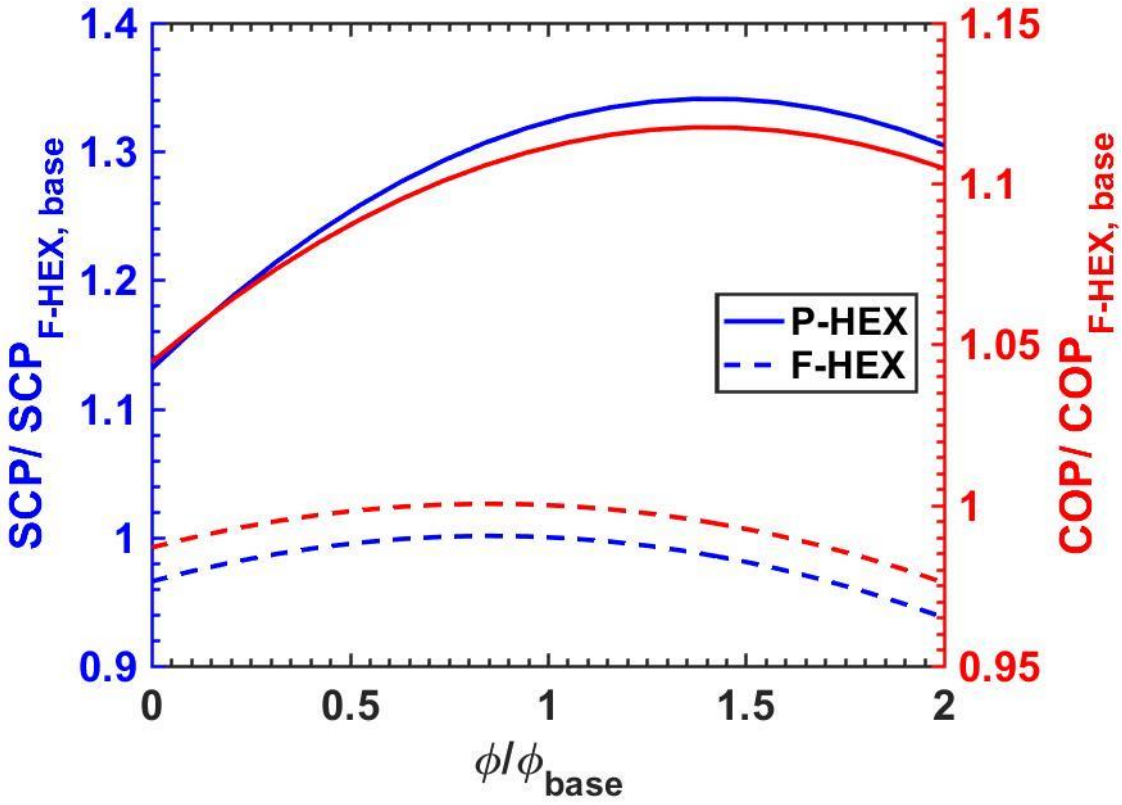

Fig. 51. Variation of SCP and COP with graphite flake content in the sorbent. Parameters are normalized with respect to the baseline case of the F-HMX in **Table 9**

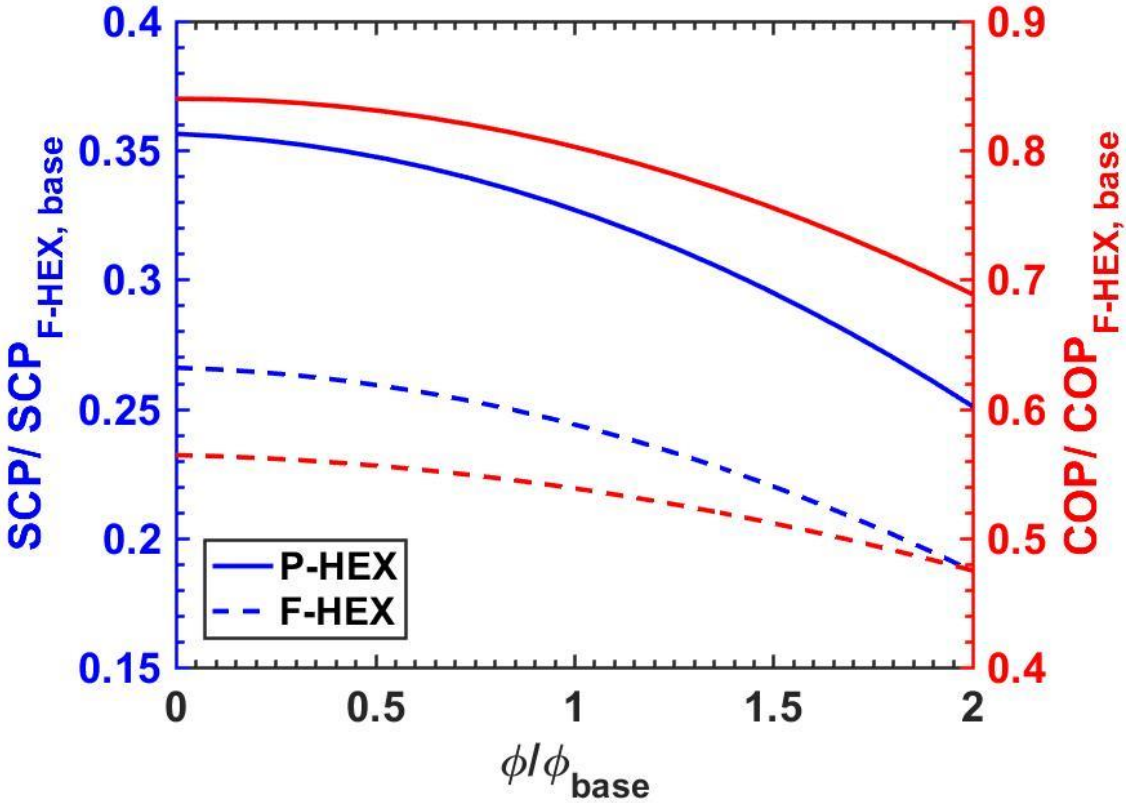

Fig. 52. Variation of SCP and COP with graphite flake content in the sorbent for b=2 cm, t_s=1 mm, t_f=0.1 mm, $r_1=H_d/2$=3 mm and τ=15 min, SCP, COP. Parameters are normalized with respect to the baseline case of the F-HMX in **Table 9**

It is evident that the geometrical and heat transfer characteristics of the sorbent, heat exchanger and heat transfer fluid should be optimized simultaneously because even one large resistance in the heat transfer between the sorbent and heat transfer fluid through the heat exchanger can limit the performance. Moreover, **Fig. 45**–**Fig. 51** indicate that the S-HMX geometry, heat transfer characteristics, and cycle time have conflicting effects on SCP and COP, and thus, SCP and COP should be optimized simultaneously to establish an optimal design.

3.8. Conclusion

Novel 2-D analytical models were developed for the P-HMX and the F-HMX that consider the spatial and temporal variation of water uptake and temperature in the sorbent and the heat exchanger. The analytical models were successfully validated with the experimental data collected from the custom-built G-LPJ and two-sorber bed sorption test bed. The present analytical model provides a reliable and easy-to-use design and

optimization tool for the S-HMXs of SCS. Also, the solution methodology can be applied to other sorber bed geometries by changing the eigenvalue problems. It was shown that the S-HMX geometry and heat transfer characteristics should be optimized simultaneously because if even one thermal resistance remains large inside the S-HMX, sorbent, HEX and/or HTF, it can limit the heat transfer and overall performance of SCS. Moreover, it was indicated that the geometrical and heat transfer characteristics of the S-HMXs, i.e. fin height, fin thickness, sorbent thickness, graphite flake content in the sorbent, and cycle time, have counteracting effects on SCP and COP. Hence, multi-objective optimization of the S-HMXs should be conducted considering all these parameters to find an optimal design for SCP and COP, and therefore, increase the SCS performance.

4. Analysis of variance (ANOVA) and optimization of sorber bed heat and mass exchangers

4.1. Overview

In this chapter, first, a critical literature review is carried out to show the gap in the literature to perform a simultaneous multi-objective optimization of the sorber bed heat and mass exchanger (S-HMX) design and operating parameters. To address this gap, the 2-D analytical models developed in the previous chapter, are used to conduct analysis of variance (ANOVA) to pinpoint the key parameters affecting the sorption performance. Furthermore, for the first time in the literature, a simultaneous multi-objective optimization is conducted on the S-HMX's key parameters achieving the optimum sorption performance. This chapter resulted in the following publications:

1) H. Bahrehmand, M. Bahrami, Optimized sorber bed heat exchangers for sorption cooling systems, submitted to *Applied Thermal Engineering*, 2020.
2) H. Bahrehmand, M. Bahrami, Development of novel sorber bed heat exchangers for sorption cooling systems, *International Sorption Heat Pump Conference*, Berlin, Germany, August 2021.
3) H. Bahrehmand, M. Bahrami, Improved coefficient of performance in sorption systems, *International Sorption Heat Pump Conference*, Berlin, Germany, August 2021.
4) H. Bahrehmand, M. Bahrami, Optimal design of sorber beds for sorption systems, 5th the *IEA Experts Meetings*, University of Ottawa, Canada, May 2019.

4.2. Literature review

It was discussed in the previous chapters that to tackle the low performance of sorption cooling systems (SCS), sorber bed heat and mass exchangers (S-HMXs), consisting of the sorbent, heat exchanger and the heat transfer fluid, should be specifically designed and optimized for SCS. In the previous chapter, 2-D analytical models were developed for the P-HMX and the F-HMX of the SCS as a platform for design and optimization of the S-HMXs. **Table 10** presents a summary of available studies in which optimization was conducted on the operating conditions and/or the S-HMX design. Most studies optimize the variables and/or objective functions in an asynchronous manner, while the optimization should be performed simultaneously. In addition, the available studies with simultaneous optimization have not optimized all the S-HMX components, i.e., the sorbent, the heat

exchanger and the heat transfer fluid. In this chapter, the geometrical and heat transfer characteristics of the entire S-HMX are optimized simultaneously to acquire the optimal SCP and COP. To do that, first, an analysis of variance (ANOVA) is conducted to find the key parameters to the performance of SCS. Subsequently, a simultaneous optimization study is carried out to obtain a set of optimum solutions for SCP and COP.

Table 10. Summary of the existing studies on optimization of sorption cooling systems

Ref. No.	**Optimization variables**	**Objective functions**	**Optimization type**
[125]	• Fin pitch • Fin length	• Differential sorbate uptake	Asynchronous
[146]	• Cycle time • Sorption to desorption time	• SCP • COP	Simultaneous
[147]	• Sorber diameter	• Differential sorbate uptake • COP	Asynchronous
[148]	• Cycle time • Mass recovery time	• SCP • COP	Asynchronous
[149]	• Desorption temperature • Cooling temperature • Heat transfer fluid flow rate • Sorption to desorption time • Mass recovery time • Heat recovery time	• SCP • COP	Asynchronous
[122]	• Fin pitch • Fin thickness • Fin height • Diffusion coefficient • Particle size • Cycle time • Cycle ratio • Temperature of hot water • Fluid velocity • Porosity	• SCP • COP	Asynchronous

[150]	• Desorption temperature • Cycle time • Heat and mass recovery time	• SCP • COP	Simultaneous
[151]	• Fin spacing	• Sorbent temperature difference • Adsorber bed/adsorbent mass	Simultaneous
[152]	• Cycle time	• VSCP • COP	Asynchronous
[153]	• Cooling time • Mass recovery time • Heat recovery time	• SCP • COP	Asynchronous
[154]	• Cycle time	• SCP • COP	Asynchronous
[155]	• Mass recovery time • Switch time • Cycle time	• COP • SCP	Asynchronous
[119]	• Fin height • Fin spacing	• COP • SCP	Asynchronous
[156]	• Cycle time • Sorption/desorption time	• COP • SCP	Asynchronous
[157]	• Sorption time • Desorption time • Particle diameter • Number of fins	• COP • SCP	Simultaneous
[158]	• Cycle time • Mass recovery time • Preheating and precooling time	• SCP • COP	Asynchronous
[131]	• Fin spacing	• SCP • COP	Asynchronous

		• TCP	
[159]	• Sorption time • Desorption time	• COP • TCP	Simultaneous
[160]	• Desorption/adsorption time • Fin height • Fin number	• SCP • COP	Asynchronous

4.3. Analysis of variance (ANOVA)

Analysis of variance (ANOVA) is a systematic method that can be used to evaluate the impact of design parameters on the performance by calculating the sums of square, level of contribution, F-statistic ratio and p-value, see Ref. [161]–[163] and Appendix F for more details. In this study, the effect of the S-HMX design parameters on the SCP and COP is investigated using ANOVA in MATLAB and the 2-D analytical models. The Box–Behnken design [164] with three levels of design parameters shown in **Table 11** is used to generate the sample points. The design parameters used in **Table 11** are shown in **Fig. 33** and **Fig. 37** in Chapter 0.

Table 11. Three levels of the S-HMX design parameters

	Level 1	**Level 2 (baseline case)**	**Level 3**
Fin height (b (cm))	1	2	3
Fin thickness (t_f (mm))	1	2	3
Sorbent thickness (t_s (mm))	1	2	3
Graphite flake content in sorbent (ϕ (wt. %))	0	10	20
Cycle time (τ (min))	10	15	20
Fluid tube radius (r_1, $H_c/2$ (mm))	2	3	4

Using the Box–Behnken design, an ANOVA is carried out to find out which parameters have a significant contribution to SCP and COP of the S-HMX. Interactions between variables are included in the error term. **Fig. 53** shows the level of contribution of each design parameter to the SCP and the COP for the two targeted sorber bed heat and mass exchangers, the P-HMX and the F-HMX. The following can be concluded:

- The sorbent thickness and cycle time have the highest level of contribution to SCP.

- The fin thickness, fin height and the amount of graphite flake (thermally conductive additive) in the sorbent have the second largest level of contribution to SCP.
- The heat transfer fluid (HTF) channel height and tube radius have the lowest level of contribution to SCP. The reason is that the selected range of channel height and tube radius was low enough such that their heat transfer resistance was less than that of HEX and the sorbent. The level of contribution would be higher if larger channel heights or tube radii was selected.
- Fin thickness and sorbent thickness have the largest impact on COP.
- Cycle time, fin height and the amount of graphite flake in the sorbent have a relatively lower effect on COP.
- The heat transfer fluid (HTF) channel height and tube radius have the lowest impact on COP.

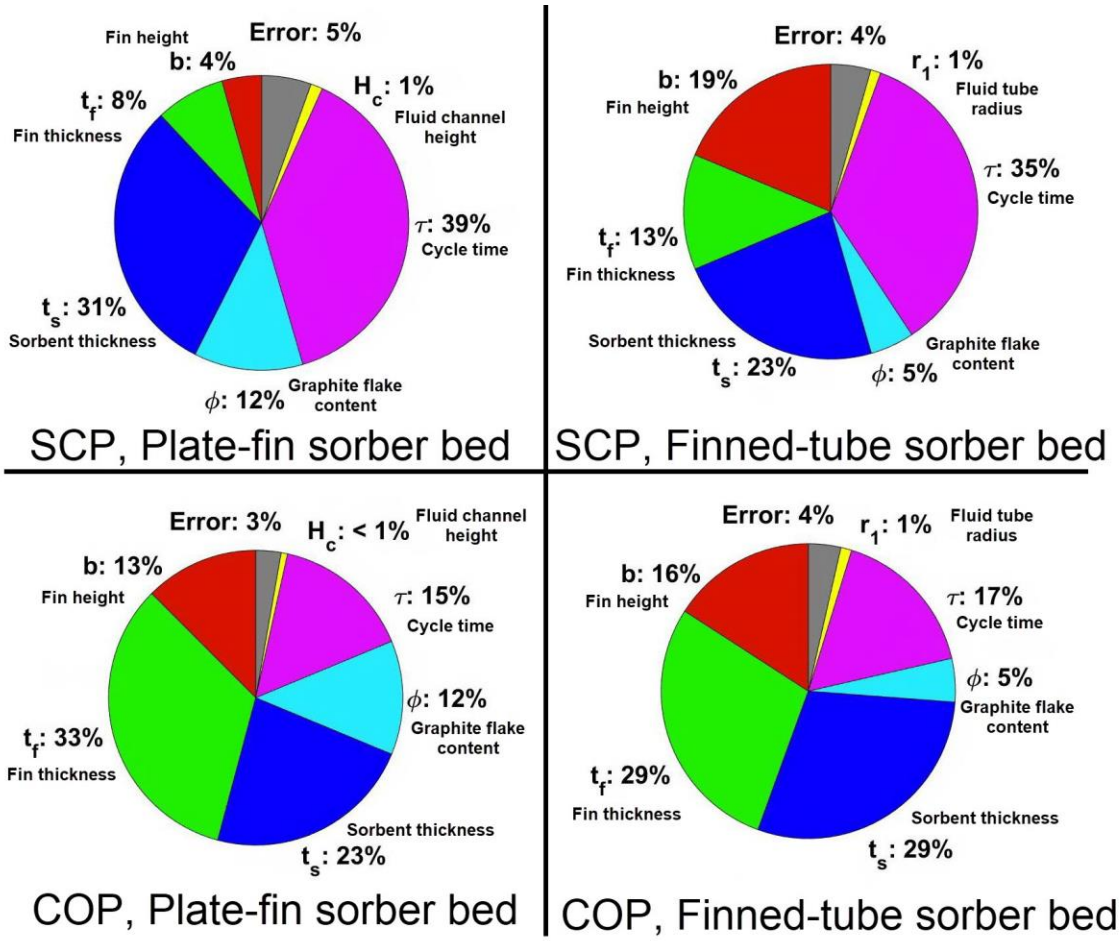

Fig. 53. Level of contribution of design parameters to the SCP and the COP of the P-HMX and the F-HMX; the design parameters are shown in **Fig. 33** and **Fig. 37** in Chapter 3.

Table 12 presents the p-value of each design parameter for the SCP and the COP of the P-HMX and the F-HMX. It can be seen that all of the design parameters have significant contribution to SCP and COP because all the p-values are lower than 0.05 level of significance. Hence, the entire S-HMX, consisting of the sorbent, heat exchanger and heat transfer fluid, should be optimized simultaneously to achieve an optimal set of SCP and COP.

Table 12. p-value of design parameters to the SCP and the COP of the P-HMX and the F-HMX

	P-HMX		**F-HMX**	
	SCP	COP	SCP	COP
b	5.85e-6	6.66e-16	1.78E-15	7.77e-16
t_f	1.61e-8	8.14e-36	8.72E-13	3.19e-27
t_s	7.05e-28	2.76e-28	4.16E-26	1.39e-28
ϕ	4.41e-11	6.66e-16	2.48E-7	2.86e-8
τ	5.64e-34	2.58e-21	9.04E-36	3.33e-16
r_1, $H_c/2$	1.22e-2	1.03e-2	1.03E-2	2.75e-3

4.4. Optimization study

It was shown in Chapter 3 and in Section 4.3 that the S-HMX geometry, heat transfer characteristics and cycle time should be optimized simultaneously. Moreover, it was indicated that the geometrical and heat transfer characteristics of the S-HMXs, and cycle time, have conflicting effects on SCP and COP. Hence, multi-objective optimization of the S-HMXs should be conducted considering all these parameters to find an optimal design for SCP and COP.

Using the 2-D analytical models and multi-objective genetic algorithm, the geometry and heat transfer characteristics of the F-HMX and the P-HMX are determined to optimize SCP and COP. The constraints are defined based on the parametric study in Section 3.7.1 and Ref. [6], and ANOVA in Section 4.3. The variables are: i) a fin height of 1–3 cm; ii) a fin thickness of 0.5–3 mm; iii) a sorbent thickness of 1–3 mm; iv) a graphite flake content of 0–20 wt.%, v) a cycle time of 10–20 min; and vi) a fluid channel height of 4–8 mm or tube radius 2–4 mm. The multi-objective optimization problem can be represented as follows [165].

$$\begin{aligned} &\min_{\text{wrt } \vec{x}} \left[-\text{SCP}, -\text{COP}\right] \\ &\vec{x} = \left[b, t_f, t_s, \phi, \tau, r_1\right] \end{aligned} \tag{121}$$

where, wrt is an acronym for “with respect to”, b is fin height (m), t_f is fin thickness (m), t_s is sorbent thickness (m), ϕ is graphite flake content in sorbent (wt.%), τ is cycle time

(min), H_c is fluid channel height in the P-HMX (m), and r_1 is fluid tube radius in the F-HMX (m). Using the multi-objective genetic algorithm in MATLAB, 15,401 times the Cartesian analytical model and 16,451 times, the cylindrical analytical model code, written in MATLAB, was used to evaluate the SCP and the COP of the P-HMX and the F-HMX, respectively. Function tolerance and cross over fraction were set to 1e-6 and 0.8, respectively. The sets of optimum solutions for the F-HMX and the P-HMX, i.e. the trade-off between SCP and COP, are presented in **Fig. 54** and **Fig. 55**, respectively. The design that can achieve SCP of 757 W/kg and COP of 0.55 is selected for the F-HMX, and the design with the SCP of 976 W/kg and COP of 0.60 is selected for the P-HMX, due to an optimal compromise between SCP and COP, as well as satisfying the performance target, i.e. SCP > 700 W/kg and COP > 0.55. The P-HMX and the F-HMX optimum design was built and tested, which is discussed in the following chapter.

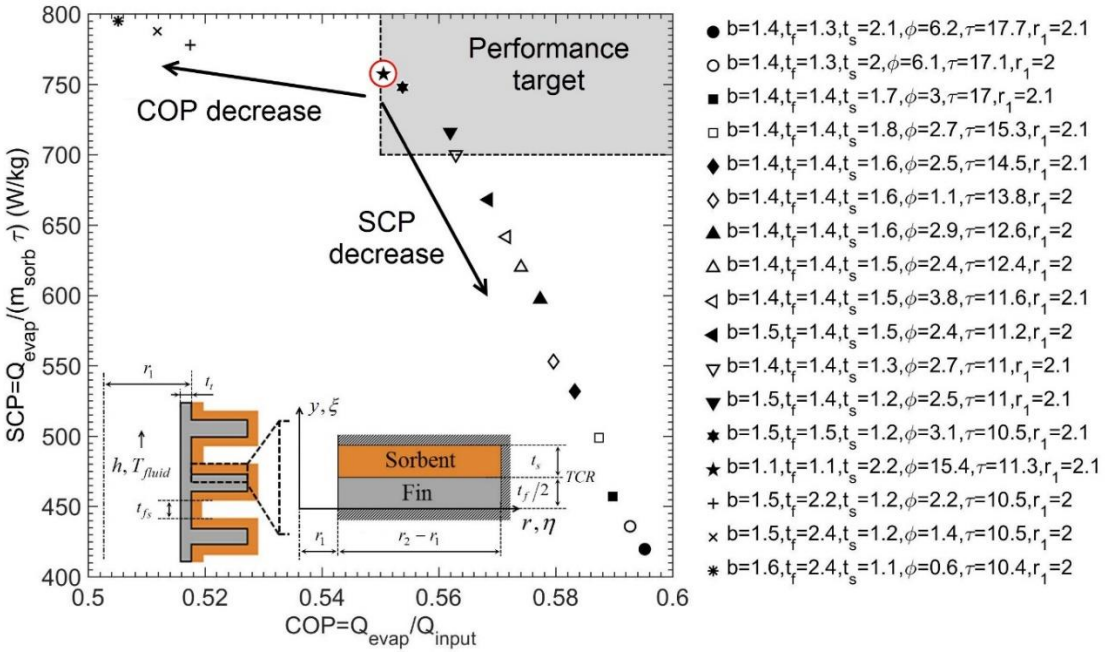

Fig. 54. Set of optimum solutions for the F-HMX (trade-off between SCP and COP), *b*: fin height (r_2-r_1) (cm), t_f: fin thickness (mm), t_s: sorbent thickness (mm), ϕ: graphite flake content in sorbent (wt.%), τ: cycle time (min), r_1: fluid tube radius (mm).

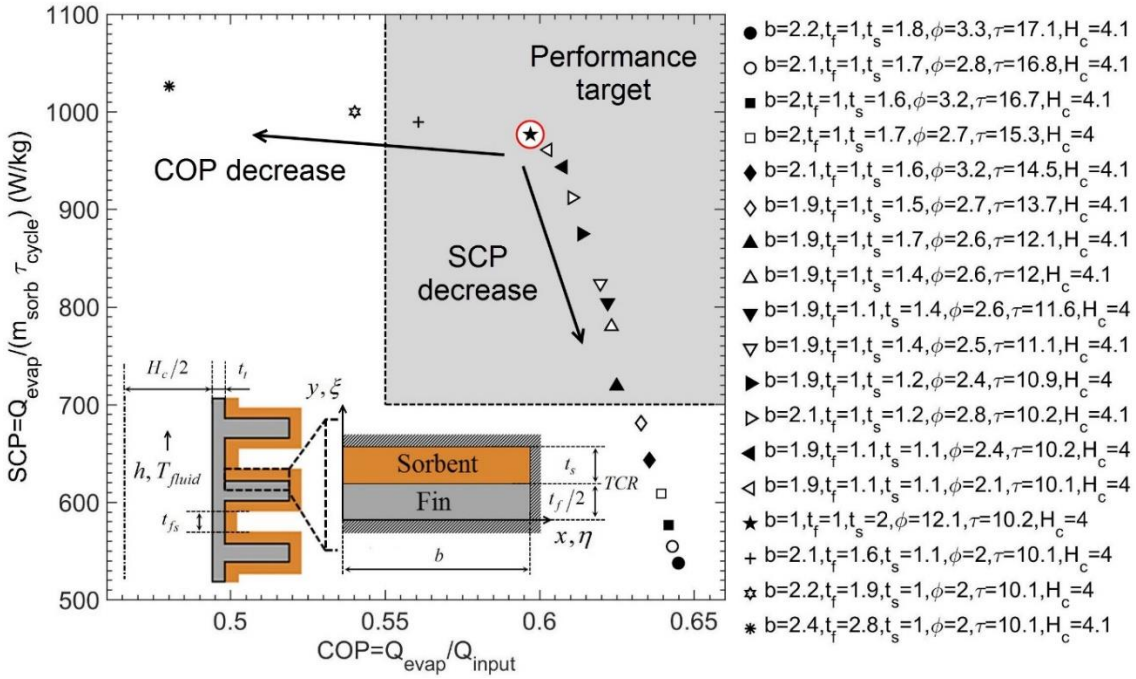

Fig. 55. Set of optimum solutions for the P-HMX (trade-off between SCP and COP), b: fin height (cm), t_f: fin thickness (mm), t_s: sorbent thickness (mm), ϕ: graphite flake content in sorbent (wt.%), τ: cycle time (min), H_C: fluid channel height (mm).

4.5. Conclusion

In this section, an analysis of variance (ANOVA) was conducted on the geometrical specifications, heat transfer characteristics and cycle time of the S-HMX to find the level of significance of the S-HMX design parameters to the SCP and the COP. The results showed that the entire S-HMX, consisting of the sorbent, heat exchanger and the heat transfer fluid, should be optimized simultaneously to achieve optimal SCP and COP. Moreover, a multi-objective optimization study was performed on the geometry and heat transfer characteristics of the P-HMX and the F-HMX to find the optimal SCP and COP. A design with an SCP of 976 W/kg and a COP of 0.60 was selected for the P-HMX and a design with an SCP of 757 W/kg and a COP of 0.55 was selected for the F-HMX due to an optimal compromise between the SCP and the COP, which will be discussed in the next chapter.

5. Development of optimized sorber bed heat and mass exchangers

5.1. Overview

In this chapter, for the first time in the literature, sorber bed heat and mass exchangers (S-HMXs) of a plate fin sorber bed heat and mass exchanger (P-HMX) and a finned-tube sorber bed heat and mass exchanger (F-HMX) were specifically designed for sorption cooling systems based on the optimization study. The manufacturing procedure and characteristics of the optimized P-HMX and F-HMX are presented. The two-sorber bed sorption test bed was initially custom-built by Dr. Amir Sharafian, a PhD graduate and Dr. Wendell Huttema, a former Postdoctoral Fellow at LAEC. The two-sorber bed sorption test bed was improved and modified to test the optimized S-HMXs in the present study. The modifications included (i) four-way valves for the S-HMX heat transfer fluids, (ii) lids of the vacuum chambers, and (iii) sensors with higher accuracy. Finally, the experimental results are presented and the optimized S-HMXs performance is evaluated. This chapter resulted in the following publications:

1) H. Bahrehmand, M. Bahrami, Optimized sorber bed heat exchangers for sorption cooling systems, submitted to *Applied Thermal Engineering*, 2020.
2) H. Bahrehmand, M. Bahrami, Development of novel sorber bed heat exchangers for sorption cooling systems, *International Sorption Heat Pump Conference*, Berlin, Germany, August 2021.
3) H. Bahrehmand, M. Bahrami, Improved coefficient of performance in sorption systems, *International Sorption Heat Pump Conference*, Berlin, Germany, August 2021.
4) H. Bahrehmand, M. Bahrami, Optimal design of sorber beds for sorption systems, 5th *IEA Experts Meetings*, University of Ottawa, Canada, May 2019.

5.2. Literature review

In the previous chapter, the entire P-HMX and F-HMX, consisting of the sorbent, heat exchanger and heat transfer fluid, were optimized. In this chapter, the optimized S-HMXs are designed, built and tested as a proof-of-concept for the S-HMXs of sorption cooling systems (SCS).

Many researchers have developed S-HMXs to tackle the issue of low performance of an SCS. A summary of the available studies with a compromise between specific cooling

power (SCP) and the coefficient of performance (COP) is presented in **Table 13**. The performance has been enhanced considerably over the past decade. However, most of the performance enhancement can be attributed to the utilization of zeolite-based sorbents, such as SAPO-34 and AQSOA FAM Z02, which are rather expensive, due to their synthesis process [76]. Furthermore, the majority of uptake in zeolite-based sorbents occurs in a narrow range of relative pressure, p/p_0, which may limit their application to relatively high desorption temperature, i.e. heat source of 80-90 °C, and a low condenser temperature, i.e. about 30 °C. This narrow range of the zeolite-based sorbents isotherms is shown in **Fig. 9**. The objective of this study is to develop an S-HMX that provides high SCP and COP over a large range of operating conditions.

In the present study, novel S-HMXs are developed and tested based on the optimized designs. The sorbent material used is comprised of silica gel and $CaCl_2$, graphite flakes as a thermally conductive additive and PVA as binder. It should be noted that these composite sorbents have lower cost and higher market availability compared to the zeolite-based sorbents [166]. Moreover, the sorption performance of these composites takes place over the entire range of relative pressure, $0.06<p/p_0<0.4$, which is more appropriate for air-conditioning applications [11] , **Fig. 9**.

Table 13. A summary of the available studies with a reasonable compromise between SCP and COP

Ref.	Sorption pair	S-HMX	τ (min)	Q_{evap} (kW)	SCP (W/kg)	COP
[167]	Coating silica gel+$CaCl_2$(SWS-1L)/water	Aluminum finned tube	10	0.48	137	0.15
[168]	Coating AQSOA-FAM-Z02/water	Extruded aluminum finned-tube heat exchanger	–	0.442	294.67	0.21
[169]	Silica gel/water	Aluminum finned tube	6	1.9	158	0.29
[170]	Loose grain $LiNO_3$–Silica KSK/water (SWS-9L)	Aluminum finned flat tube	6.4	–	318	0.176
[146]	Loose grain AQSOA-FAM Z02/water	Aluminum finned flat tube	7	0.155	394	0.6
[92]	Coating zeolite, SAPO-34/water	Aluminum finned flat tube	5	–	675	0.24

[171]	Coating SAPO-34/water	Aluminum sintered metal fiber structures soldered on flat fluid channels	10	5	852	0.4
[172]	Coating AQSOA-FAM-Z02/water	Finned tube (copper)	1.5	1.5	872	0.27
[12], Section 3.6.1	Coating silica gel+$CaCl_2$/water	Aluminum finned-copper tube engine oil cooler	10	0.306	235	0.2

5.3. Characteristics of the P-HMX and the F-HMX

The P-HMX and the F-HMX were built based on the optimization study in Section 4.4. The specifications of the P-HMX and the F-HMX are presented in **Table 14**. Aluminum was selected as the S-HMX material as explained in Appendix A.1. **Fig. 56** (a) shows two halves of the P-HMX with a fin side and a fluid channel side. The spacing between the fins, the serpentine fluid channels and the half-circle regions for the aluminum tubes were machined out of two aluminum 6061 plates using our CNC milling machine. Moreover, male and female connections were machined on the plates for alignment. After that, two halves of the P-HMX and two aluminum tubes were welded together. Building the P-HMX by extrusion can reduce the manufacturing cost significantly, but it increases the capital cost due to the die required; hence, it is more suitable for mass production. Furthermore, **Fig. 57** (a) shows the aluminum finned-tubes used to manufacture the F-HMX. The aluminum finned-tubes were built using our CNC lathe machine and welded to aluminum tubes as headers. Two plugs were machined and welded to the ends of the aluminum tube header. The diameter of the finned-tubes is 4 mm, and the tube header diameter is 13 mm. Thus, the pressure drop in the finned-tubes is two orders of magnitude larger than that of the tube header. Consequently, the fluid flow in the eight finned-tubes can be assumed to be uniformly distributed.

Subsequently, the fin spacings of the P-HMX and the F-HMX were filled with the slurry solution of the optimum composite sorbent shown in **Table 14**. The composite sorbent was dried at 80 °C and then cured at 180 °C in the oven. **Fig. 56** (b) and **Fig. 57** (b) show the assembled P-HMX and F-HMX coated with the optimum composite sorbent, respectively.

Table 14. Specifications of the P-HMX and the F-HMX

Characteristics	**P-HMX**	**F-HMX**
Fin height (cm)	1	1.1
Fin thickness (mm)	1	1.1
Fin spacing (mm)	4	4.4
Fluid channel height/fluid tube diameter (mm)	4	4
Fluid channel width (cm)	1.27	–
Total length without the tubes (cm)	31	32
Total width (cm)	20	20
Tube outer diameter (cm)	1.9	1.9
Tube length (cm)	12	12
Volume without the tubes outside the vacuum chamber (L)	1.7	2.05
Mass of heat exchanger without sorbent coating and tubes outside the vacuum chamber (kg)	1.72	1.04
Mass of sorbent coating (kg)	0.587	0.379
Mass of heat transfer fluid (water) (kg)	0.498	0.123
Mass ratio of sorbent coating to heat exchanger	0.34	0.36
Mass percentage of silica gel B150	39	37.5
Mass percentage of $CaCl_2$	39	37.5
Mass percentage of PVA	10	10
Mass percentage of graphite flakes	12	15

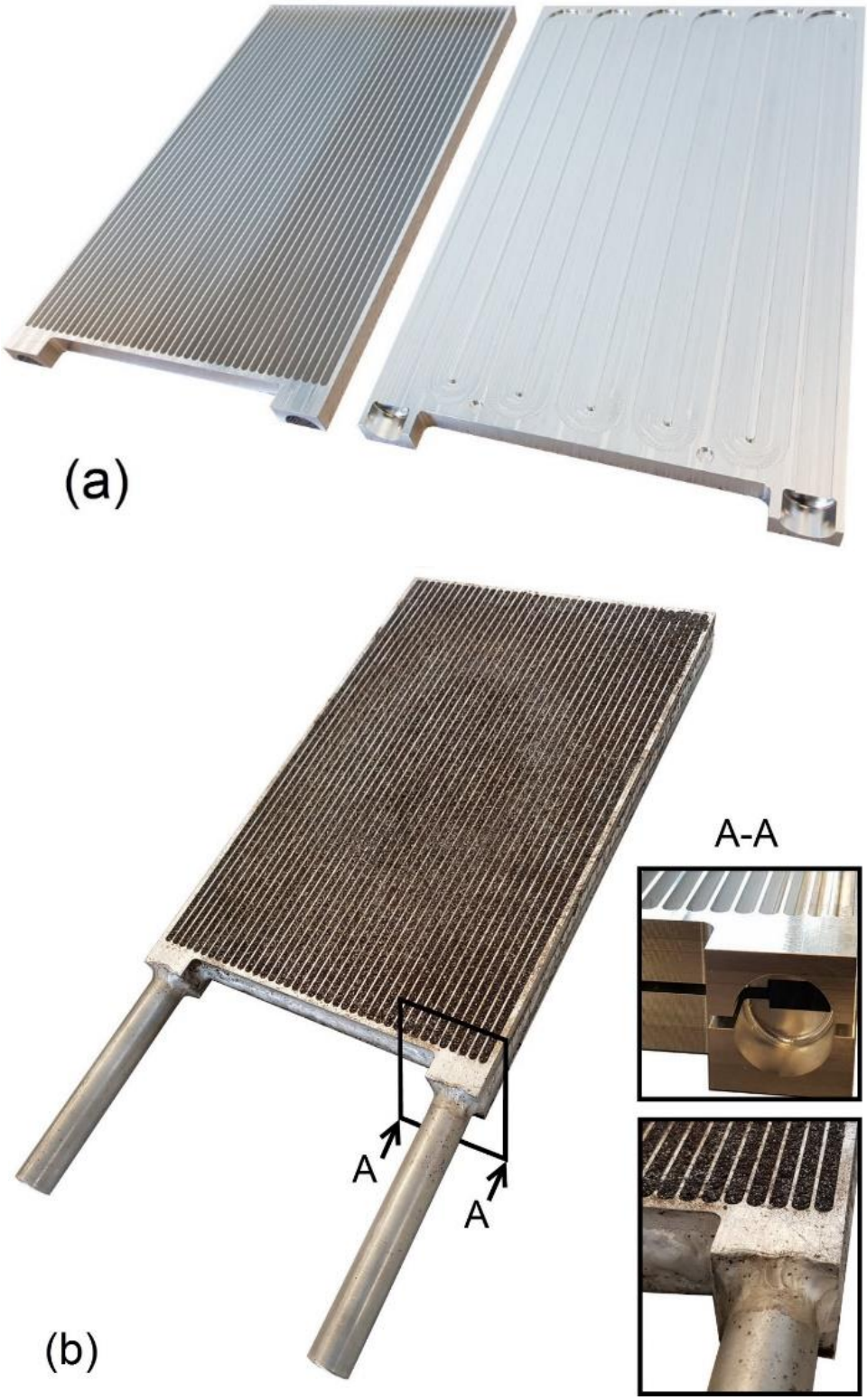

Fig. 56. (a) Two halves of the P-HMX showing the fin side and the fluid channel side; and (b) assembled P-HMX coated with the composite sorbent, silica gel, $CaCl_2$, PVA and graphite flakes

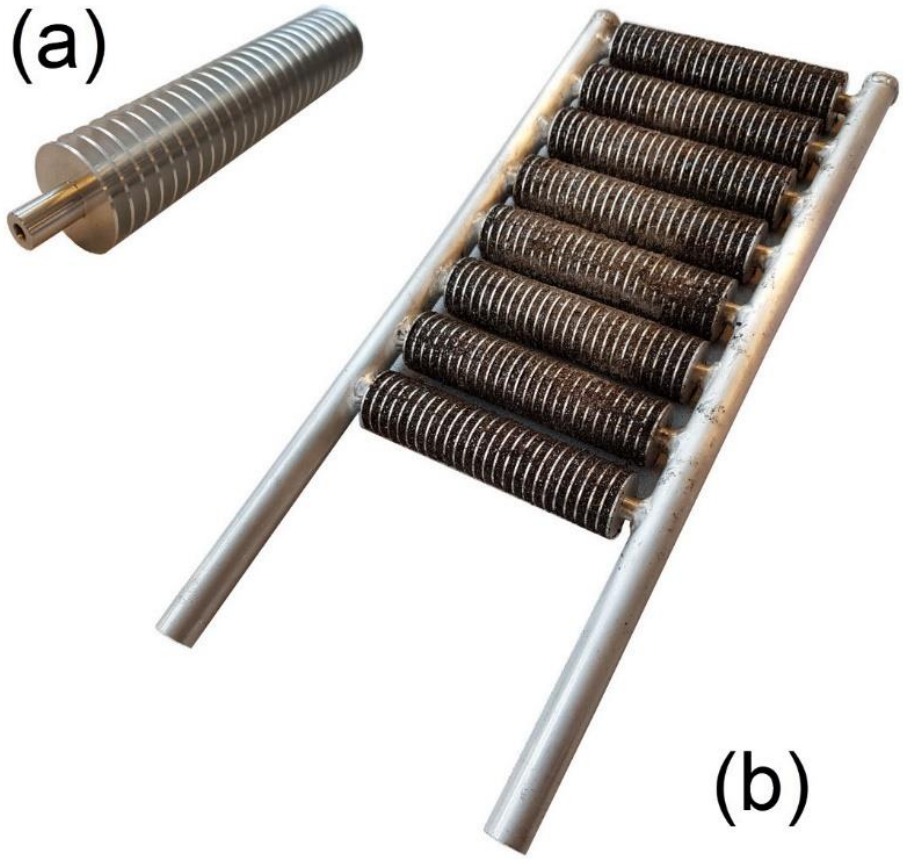

Fig. 57. (a) One aluminum finned-tube; and (b) assembled F-HMX coated with the composite sorbent, silica gel, $CaCl_2$, PVA and graphite flakes

5.4. Experimental test bed and measurements

Fig. 58 shows the schematic and the picture of a two-sorber bed sorption test bed custom-built to test the P-HMX and the F-HMX. The P-HMX and the F-HMX were placed inside the aluminum vacuum chambers on the sides, a custom-designed capillary-assisted evaporator was positioned in the bottom aluminum vacuum chamber, and two helical coil and shell heat exchangers were used as a condenser at the top. Check valves were installed between the S-HMXs and the condenser and gate valves were installed between the evaporator and the S-HMXs. A needle valve with high precision flow adjustment (Speedivalve SP16K, Edwards) and a U-tube were installed between the condenser and the evaporator. The whole system was vacuumed for 6 hours before the tests. Two temperature control systems were used to keep the evaporator at 15 ˚C and the condenser at 30 ˚C. Furthermore, two temperature control systems were set to 90 ˚C and 30 ˚C for desorption and sorption processes, respectively. Two four-way valves were employed to

switch the heat transfer fluid (HTF) between the two S-HMXs for desorption and sorption processes. One of the four-way valves was set to have a delay at the beginning of each process to push the high- and low-temperature HTF in the S-HMXs and hoses back to high- and low-temperature reservoirs of temperature control systems to perform a heat recovery process. The time delay was calculated as 10 s based on the flow rate of the heat transfer fluid and the fluid volume in the S-HMXs and the hoses. The heat recovery method is discussed in more details in Appendix A.2. RTD (PT100) temperature sensors (Omega, model #PR-13-2-100-1/8-6-E) with an accuracy of 0.15 °C and pressure transducers with a 0-34.5 kPa operating range (Omega, model #PX309-005AI) and a 0.4 kPa accuracy were installed to monitor and record the temperature and pressure variations in each component of the sorption test bed over time. Positive displacement flow meters (FLOMEC, Model # OM015S001-222) with an accuracy of 0.5% of reading were installed to measure the flow rate of the HTF of the condenser, evaporator and the cooling circuit of the S-HMX. Since the positive displacement flow meters may impede the flow at higher temperatures, and ultrasonic flowmeter (Kobold model DUK-1xx6) with an accuracy of 0.7% of reading was used to measure the flow rate of the high-temperature HTF to the S-HMXs. The instruments were interfaced with a PC through a data acquisition system and in-house software built in the LabVIEW environment. Experiments were performed continuously until the system reached an oscillatory steady state. The maximum uncertainties in the calculations of SCP and COP were calculated 10.6 % and 12.5 %, respectively. More information on the custom-designed capillary-assisted evaporator can be found in Ref. [173]. More information on uncertainty analysis is presented in Appendix B.

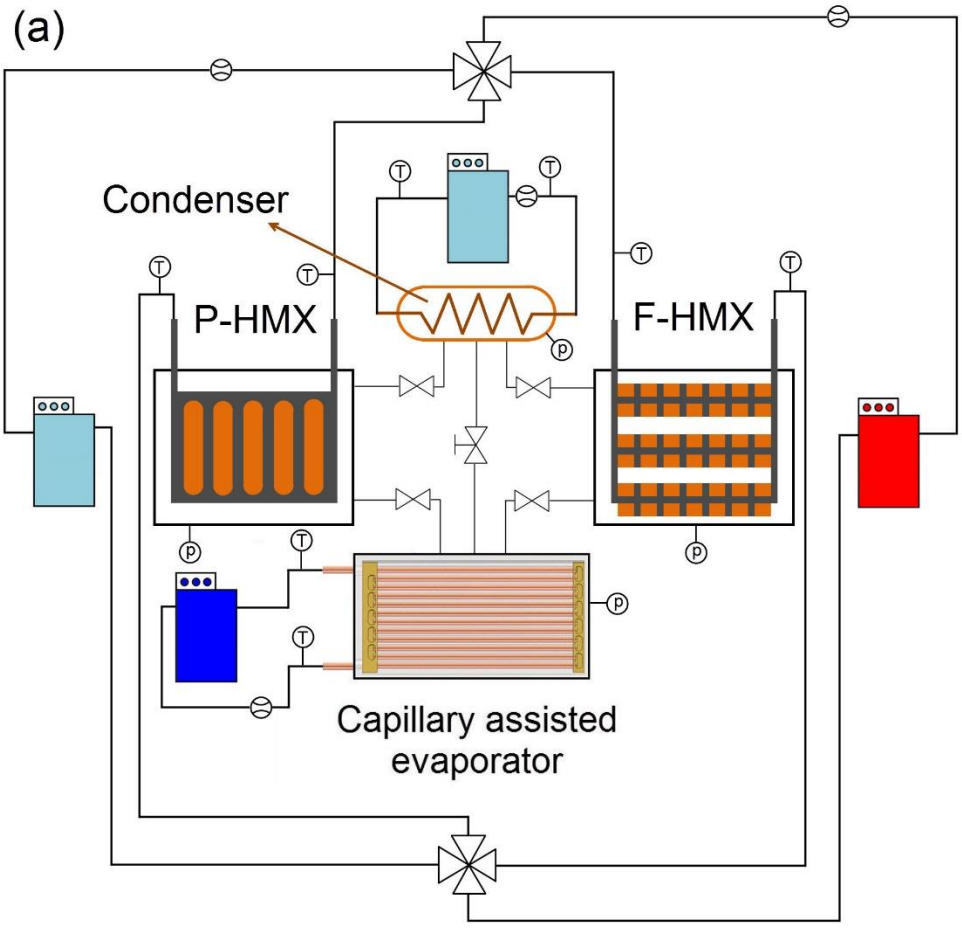
(a)
Condenser
P-HMX
F-HMX
Capillary assisted
evaporator

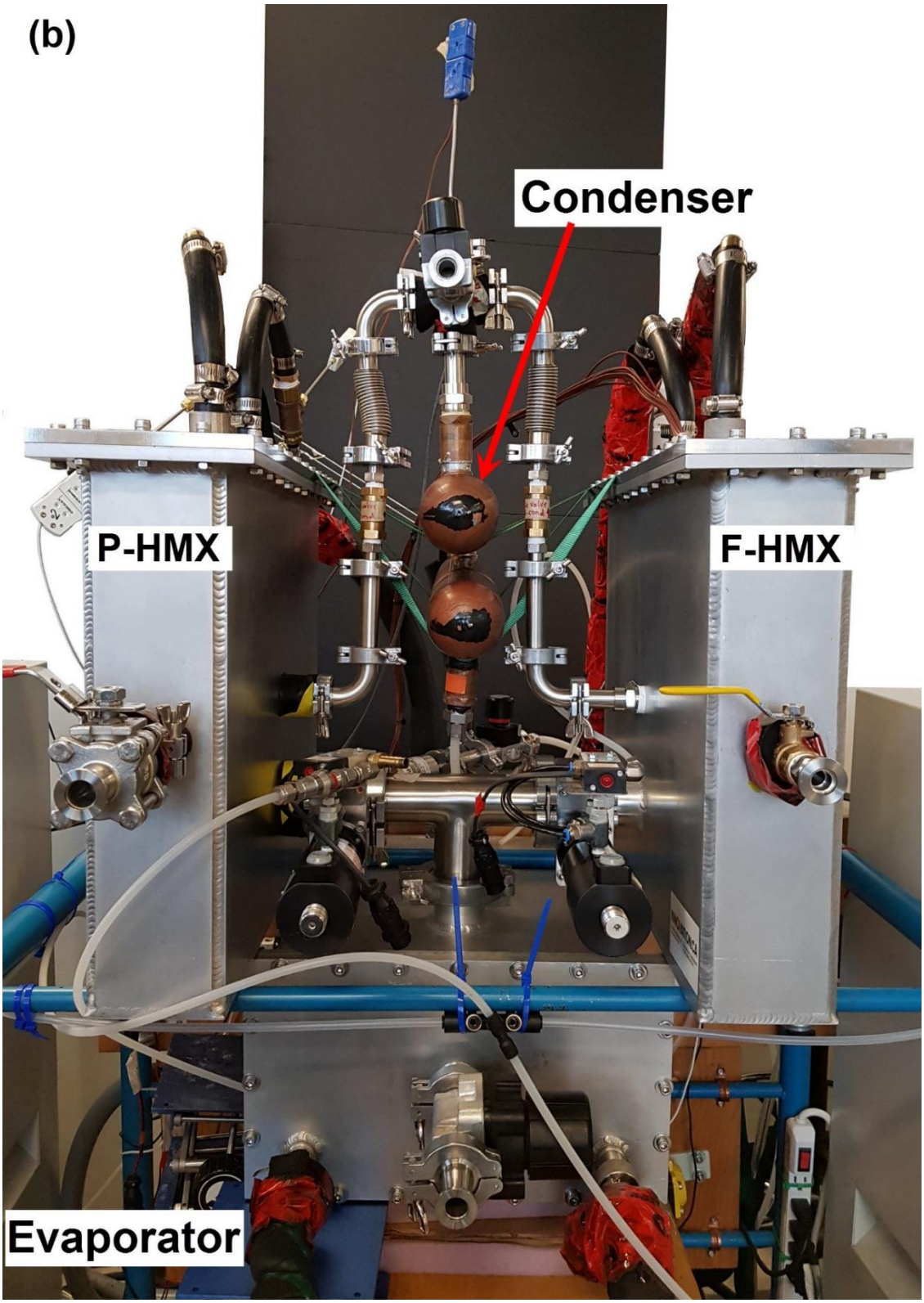

Fig. 58. (a) Schematic; and (b) a picture of the two-sorber bed sorption test bed, capillary-assisted evaporator in the chamber at the bottom, the P-HMX and the F-HMX in the chambers on the sides, two helical coil and shell heat exchangers as the condenser at the top

5.5. Results and discussions

Fig. 59 shows the temporal variation of pressure of the P-HMX, the F-HMX, condenser and evaporator. It can be seen in **Fig. 59** that the S-HMXs have higher pressures than the condenser during desorption and lower pressure than the evaporator during sorption, which are the driving force for sorption cycles. It can be observed that the P-HMX causes higher pressure during desorption and lower pressure during sorption compared to those of the F-HMX as the P-HMX desorbs and ad/absorbs more water as seen in **Fig. 60**.

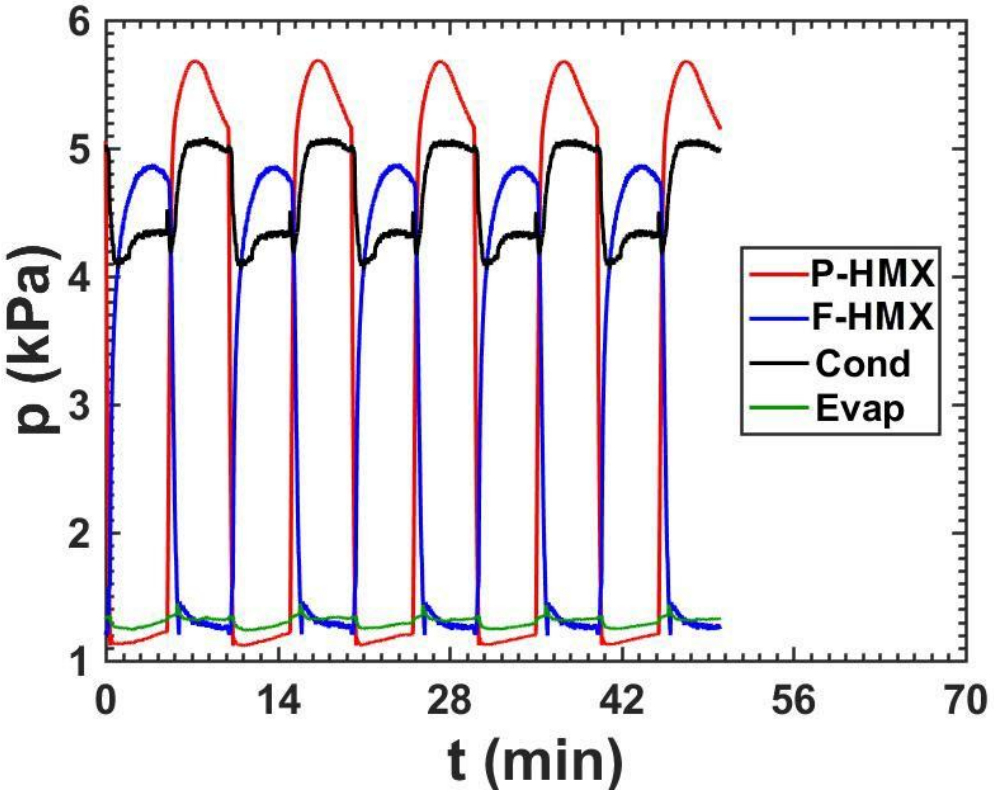

Fig. 59. Temporal variation of pressure of the P-HMX, the F-HMX, the condenser and evaporator, for T_{des}=90ºC, T_{sorp}= T_{cond} =30ºC, T_{evap}=15ºC and τ_{cycle}=10min

Fig. 60 shows the temporal variation of inlet and outlet temperatures of HTF to the evaporator. The temperature difference between the inlet and outlet HTF of the evaporator indicates the cooling power generated by the P-HMX and the F-HMX. The half-cycles with minimum temperature at about 13.5 ºC correspond to the P-HMX. The reasons for the higher cooling power provided by the P-HMX are: (i) the higher performance of the P-HMX, explained in Section 3.7.1; and (ii) more sorbent material of the P-HMX compared to the F-HMX (0.587 kg vs 0.379 kg).

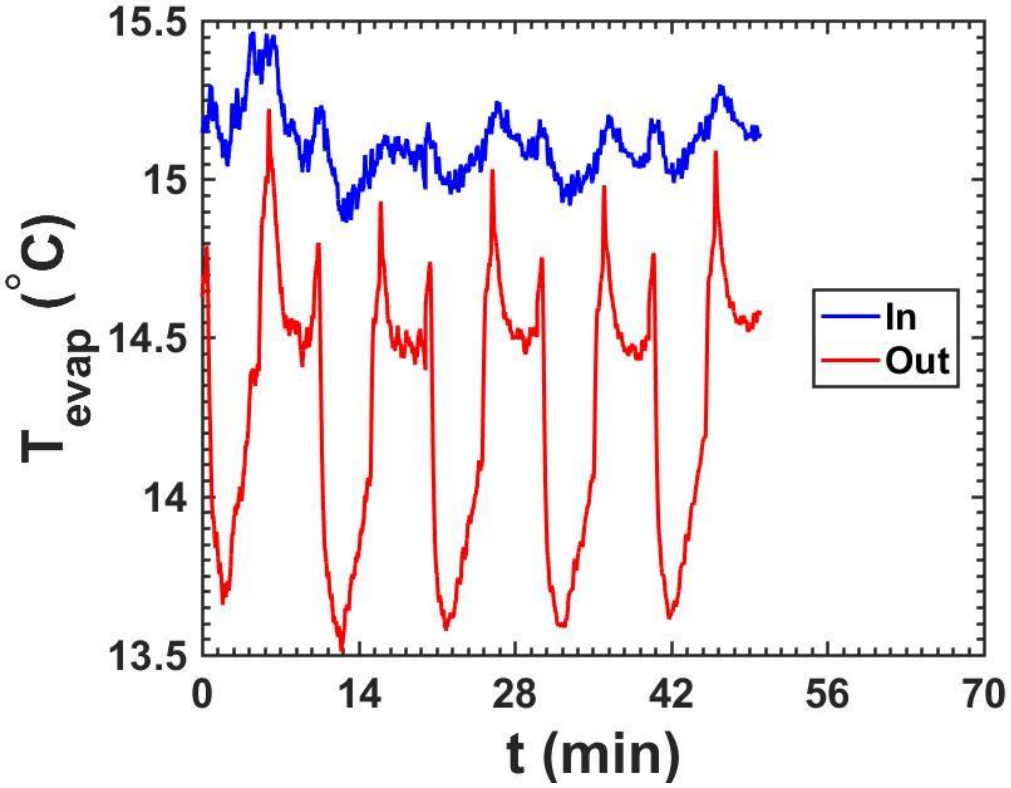

Fig. 60. Temporal variation of inlet and outlet temperatures of HTF to evaporator, for T_{des}=90ºC, T_{sorp}= T_{cond} =30ºC, T_{evap}=15ºC and τ_{cycle}=10min

Fig. 61 shows the temporal variation of inlet and outlet temperatures of HTF to the P-HMX and the F-HMX. As can be observed in **Fig. 61**, the temperature differences between the inlet and outlet HTF to the P-HMX is smaller than the F-HMX because the flow rate is higher when the temperature control systems (TCS) are connected to the P-HMX compared to the F-HMX due to higher pressure drop of the F-HMX. For example, the flowrates of the P-HMX and the F-HMX are 11.45 l/min and 4.23 l/min during desorption, and 14.02 l/min and 4.16 l/min during sorption, respectively. Based on the experiments and the analytical model, the performance of the P-HMX and the F-HMX does not change significantly for flow rates higher than 2 l/min because the HTF thermal resistance is not the main one. This is shown in **Fig. 62**. Flow rate of 2 l/min corresponds to the Reynolds number of 3,883 for P-HMX and 10,501 for F-HMX.

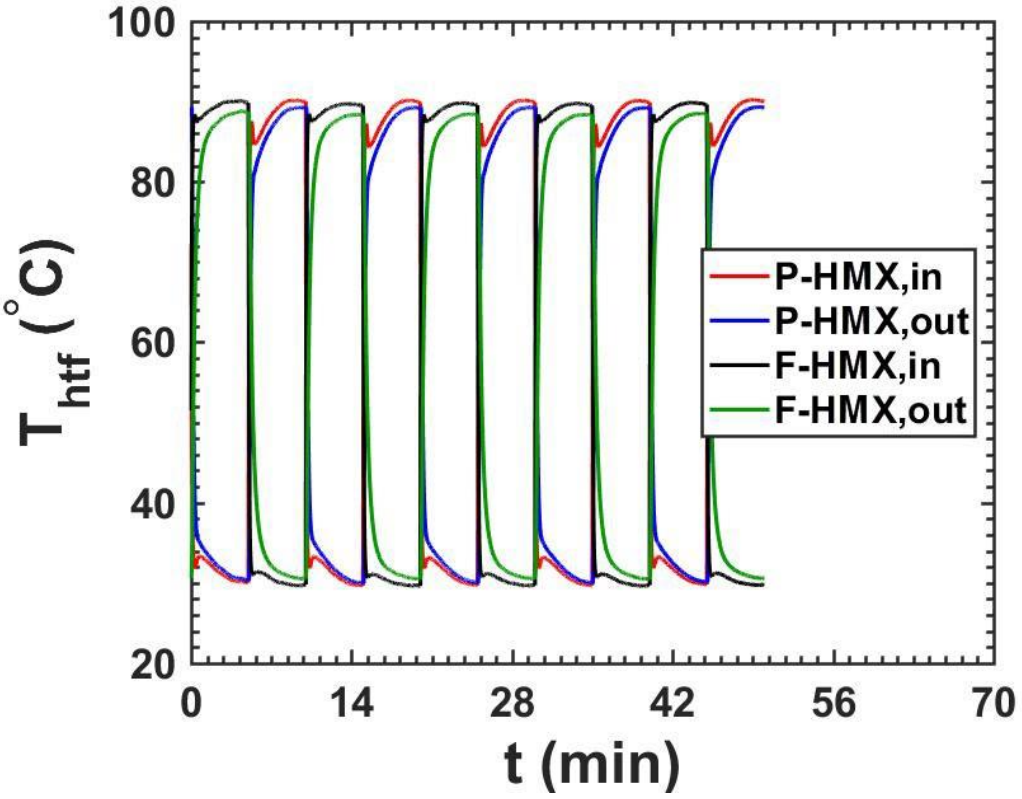

Fig. 61. Temporal variation of inlet and outlet temperatures of the HTF to the P-HMX and the F-HMX, for T_{des}=90ºC, T_{sorp}= T_{cond} =30ºC, T_{evap}=15ºC and τ_{cycle}=10min; HTF: heat transfer fluid

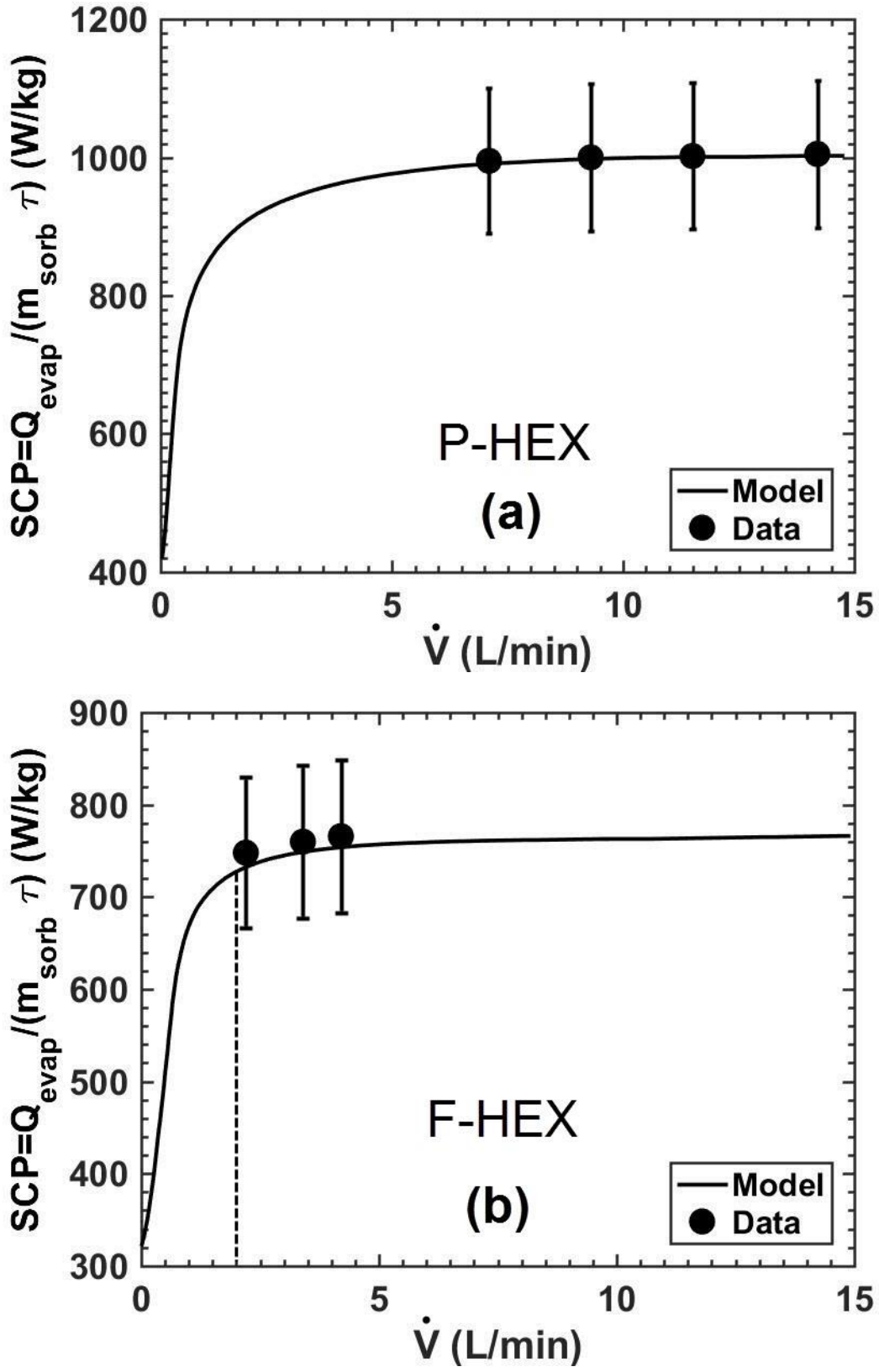

Fig. 62. Variation of SCP with volumetric flow rate of heat transfer fluid for (a) the P-HMX; and (b) the F-HMX

Fig. 63 shows the temporal variation of temperatures of inlet and outlet HTF, fin and sorbent in the F-HMX. It can be seen in **Fig. 63** that the average fin temperature of the F-HMX is close to the HTF outlet temperature. Moreover, it can be observed that the average sorbent temperature has a bump with a delay after the beginning of each sorption and desorption process. After this point, there is a higher temperature difference between the sorbent and the fin. The reason is that due to thermal inertia of the S-HMX, there is a delay in the time when the sorbent temperature is high enough for desorption and low enough for sorption. This delay can be observed in **Fig. 59**, when the S-HMX pressure is almost equal to that of evaporator and condenser, and the sorption and desorption processes begin. It takes the sorber beds a specific time (in this case, about 25 s) to reach the evaporator and condenser pressure to start the sorption and desorption due to thermal inertia. We open the valves when that happens, otherwise the beds would desorb to the evaporator instead of adsorbing.

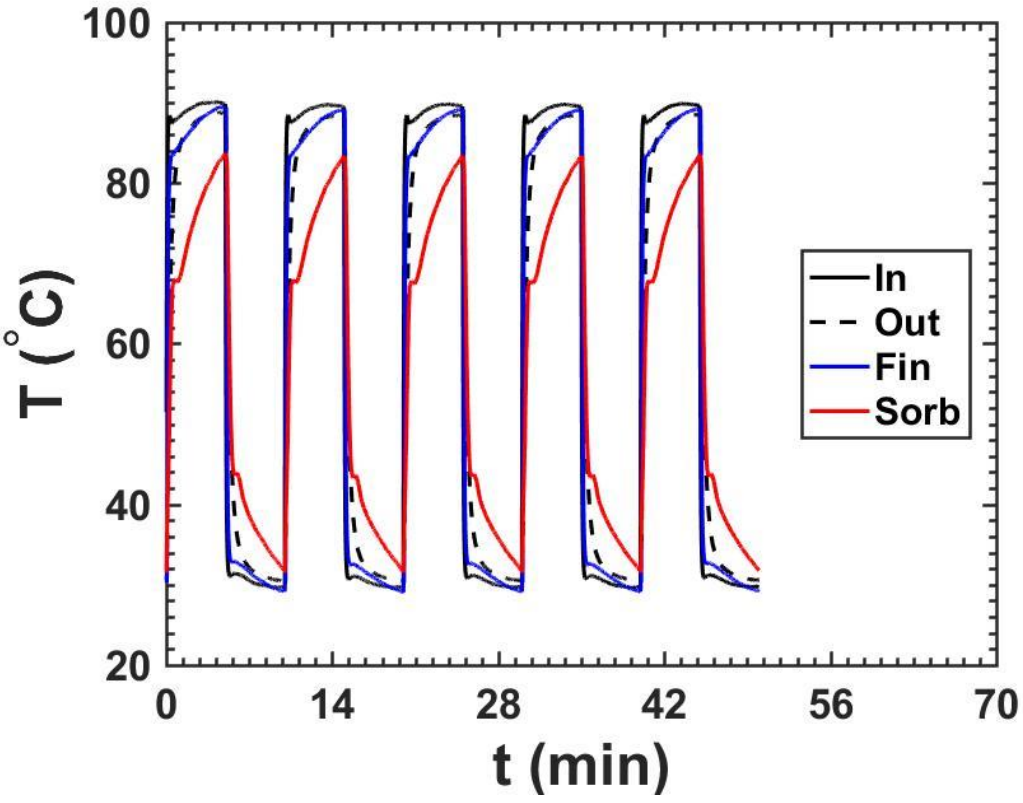

Fig. 63. Temporal variation of temperatures of inlet and outlet HTF, fin and sorbent in the F-HMX, for T_{des}=90ºC, T_{sorp}= T_{cond} =30ºC, T_{evap}=15ºC and τ_{cycle}=10min

5.5.1. Performance evaluation of the P-HMX and the F-HMX

The baseline case for the operating condition of sorption air-conditioning is considered T_{des}=90 °C, T_{sorp}=T_{cond}=30 °C, T_{evap}=15 °C, and τ_{cycle}=10 min. For the baseline case, the P-HMX achieves an SCP of 1,005 W/kg sorbent and a COP of 0.60, whereas the F-HMX yields an SCP of 766 W/kg and a COP of 0.55. **Fig. 64** shows the performance of the P-HMX and the F-HMX versus the previously published studies in **Table 13**, in terms of COP and SCP per: (a) sorbent mass; (b) mass of sorbent and HEX; (c) the S-HMX mass consisting of sorbent, HEX and HTF; and (d) the S-HMX volume. It can be seen that the P-HMX provides the highest SCP and COP using the silica gel/$CaCl_2$ composite sorbent with their sorption occurring over the entire range of $0.06<p/p_0<0.4$, which is the range of air-conditioning applications [11]. On the other hand, zeolite-based sorbents, such as SAPO-34 and AQSOA FAM Z02, were employed in Ref. [13], [168], [38]–[40], with their sorption taking place in a narrow range of p/p_0, which limits the application to a relatively high desorption temperature, i.e. a heat source of 80-90 °C, and low condenser temperature, i.e. ambient temperature at about 30 °C. It can be seen that the P-HMX provides 4.3 times higher SCP, and 3 times higher COP compared to an off-the-shelf heat exchanger, an engine oil cooler coated with a composite sorbent consisting of $CaCl_2$, silica gel B150 and PVA, presented in Section 3.6.1 and Ref. [12]. It clearly demonstrates the potential of specific design and optimization of the S-HMX for SCS.

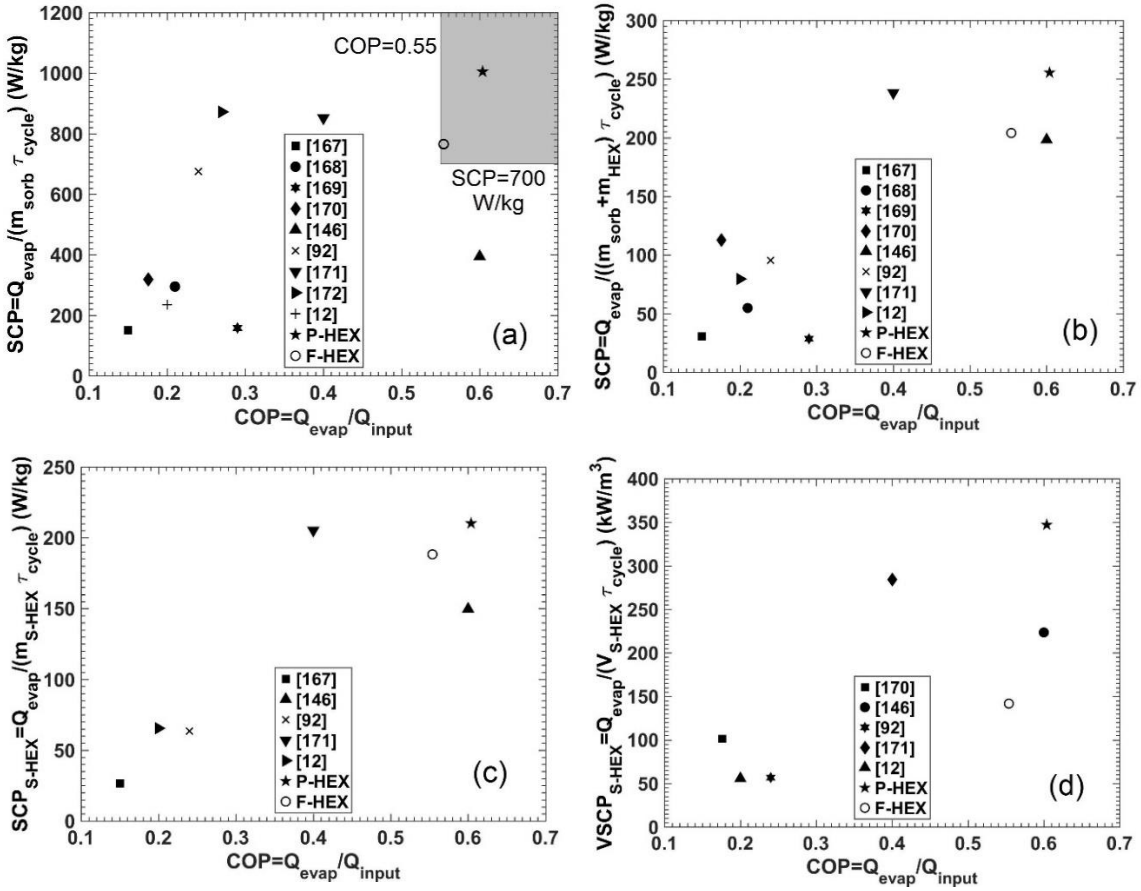

Fig. 64. Comparison of the P-HMX and the F-HMX versus the available studies in **Table 13** in terms of the COP and: (a) the SCP per sorbent mass; (b) the SCP per mass of sorbent and HEX; (c) the $SCP_{S\text{-}HMX}$; and (d) the $VSCP_{S\text{-}HMX}$

5.5.2. Effect of operating conditions

Fig. 65 shows the variation of the SCP and COP of the P-HMX and the F-HMX with cycle time. It can be observed in **Fig. 65** (a) that by decreasing the cycle time, the SCP increases as the sorption rate is higher at the beginning of sorption and reduces as the sorbent approaches saturation. In addition, it is seen in **Fig. 65** (b) that by decreasing the cycle time, the COP reduces because the heat required to overcome the S-HMX thermal inertia increases compared to the heat consumed for desorption.

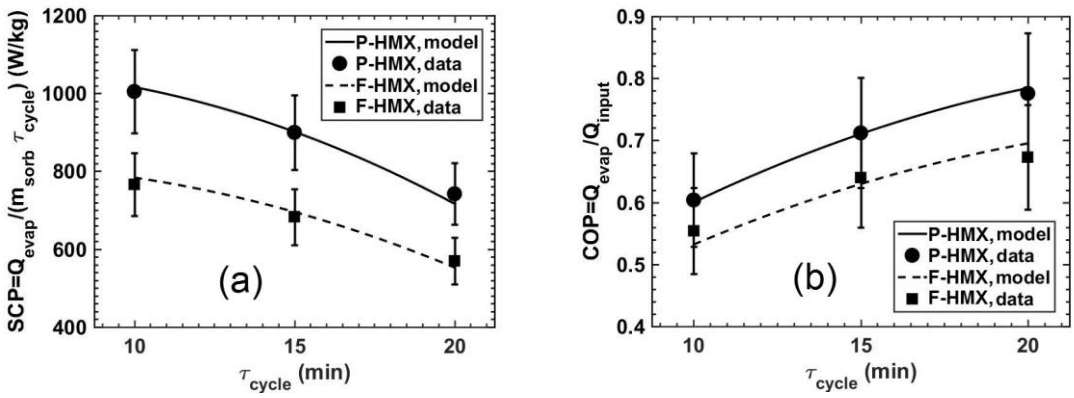

Fig. 65. Variation of the SCP and the COP of the P-HMX and the F-HMX with cycle time, T_{des}=90 °C, T_{sorp}=T_{cond}=30 °C and T_{evap}=15 °C

Fig. 66 shows the variation of the SCP and COP of the P-HMX and the F-HMX with desorption temperature. **Fig. 66** (a) shows that by increasing the desorption temperature, the SCP increases because the differential water uptake between sorption and desorption increases as indicated in **Fig. 67**. **Fig. 66** (b) shows that by increasing the desorption temperature, the COP increases and then decreases; thus, there is an optimum desorption temperature corresponding to the maximum COP. The reason for this is the conflicting effects of increasing the SCP and increasing the sensible energy required to overcome the S-HMX thermal inertia due to the higher temperature difference between desorption and sorption, by increasing the desorption temperature.

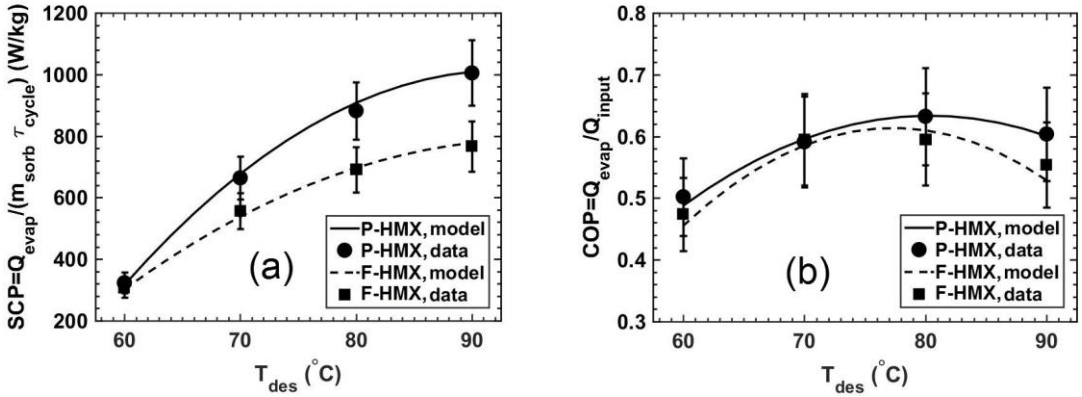

Fig. 66. Variation of the SCP and the COP of the P-HMX and the F-HMX with desorption temperature, τ_{cycle}=10 min, T_{sorp}=T_{cond}=30 °C and T_{evap}=15 °C

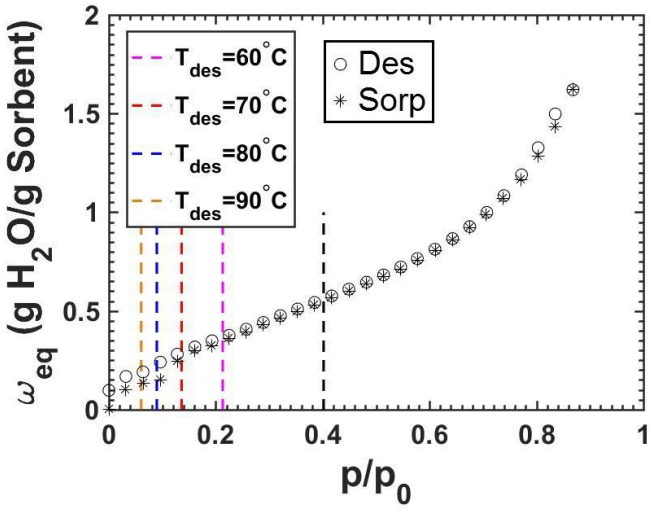

Fig. 67. Range of differential water uptake and p/p_0 for different desorption temperatures. The isotherm plots are for composite sorbents with 39wt.% silica gel B150, 39wt.% $CaCl_2$, 10wt.% PVA binder and 12wt.% graphite flakes, isotherms from Section 2.5, isotherms were obtained at 25 °C

Fig. 68 shows the variation of the SCP and the COP of the P-HMX and the F-HMX with sorption and condenser temperature. It can be observed in **Fig. 68** (a) that by increasing the sorption and condenser temperature, SCP reduces as the differential water uptake between sorption and desorption decreases as shown in **Fig. 69**. Furthermore, **Fig. 68** (b) shows that by increasing the sorption and condenser temperature, COP remains almost constant. The reason for this is the conflicting effects of decreasing SCP and decreasing the sensible energy required to overcome the S-HMX thermal inertia due to a lower temperature difference between desorption and sorption, by increasing the sorption and condenser temperature.

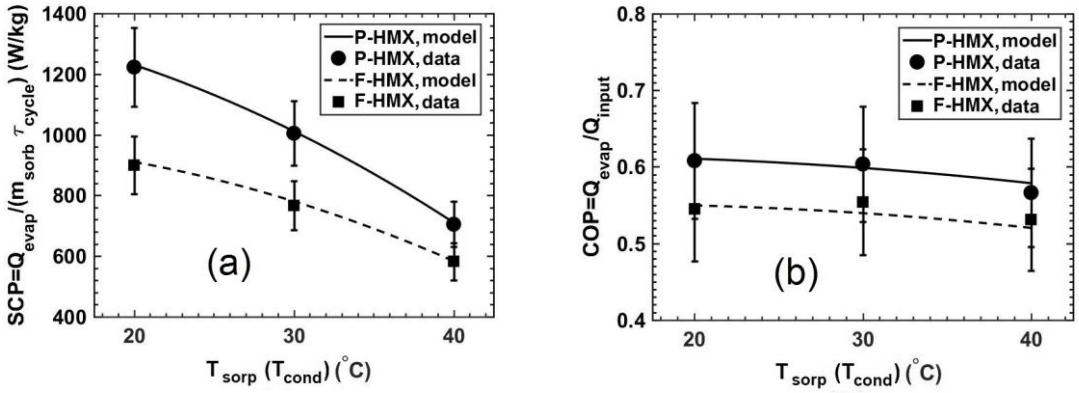

Fig. 68. Variation of the SCP and the COP of the P-HMX and the F-HMX with ambient temperature (sorption and condenser temperatures), τ_{cycle}=10 min, T_{des}=90 °C and T_{evap}=15 °C

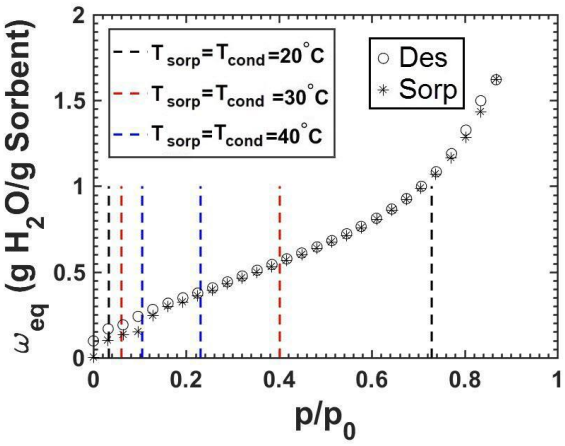

Fig. 69. Range of differential water uptake and p/p_0 for different ambient temperatures (sorption and condenser temperatures). The isotherm plots are for composite sorbents with 39wt.% silica gel B150, 39wt.% $CaCl_2$, 10wt.% PVA binder and 12wt.% graphite flakes, isotherms from Section 2.5, isotherms were obtained at 25 °C

Fig. 70 shows the variation of the SCP and the COP of the P-HMX and the F-HMX with evaporator temperature. It can be observed in **Fig. 70** (a) and (b) that by increasing the evaporator temperature, both the SCP and the COP increase because of higher differential water uptake between sorption and desorption as shown in **Fig. 71**.

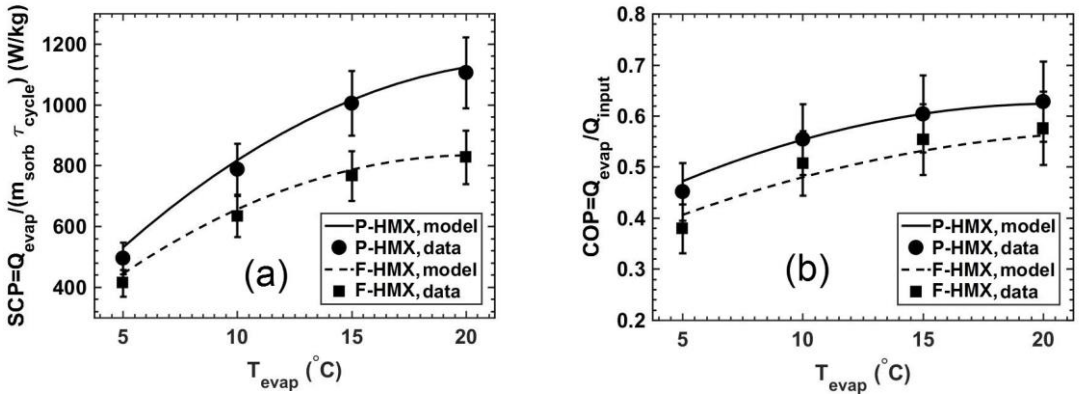

Fig. 70. Variation of the SCP and the COP of the P-HMX and the F-HMX with evaporator temperature, τ_{cycle}=10 min, $T_{sorp}=T_{cond}$=30 °C and T_{des}=90 °C

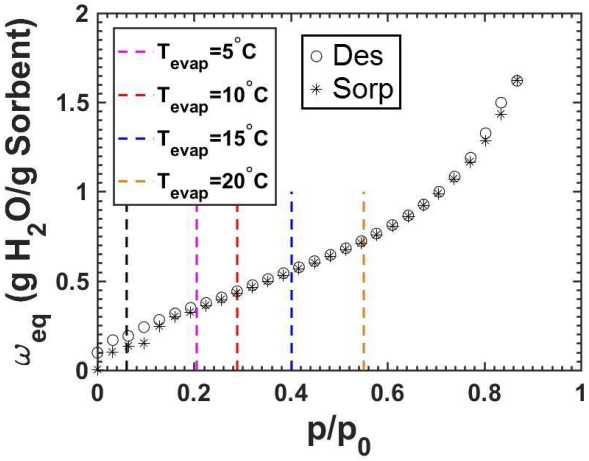

Fig. 71. Range of differential water uptake and p/p_0 for different evaporator temperatures. The isotherm plots are for composite sorbents with 39wt.% silica gel B150, 39wt.% $CaCl_2$, 10wt.% PVA binder and 12wt.% graphite flakes, isotherms from Section 2.5, isotherms were obtained at 25 °C

5.5.3. Validation of the 2-D analytical models

Fig. 72 shows the SCP and the COP of the P-HMX and the F-HMX obtained from the 2-D analytical models presented in Chapter 0 versus the data acquired by the experiments for a variety of operating conditions, i.e. different desorption temperatures, sorption and condenser temperatures, evaporator temperatures and cycle times. As can be observed, the maximum relative difference between the modeling results and experimental data is 6% and 7% for the SCP and the COP, respectively.

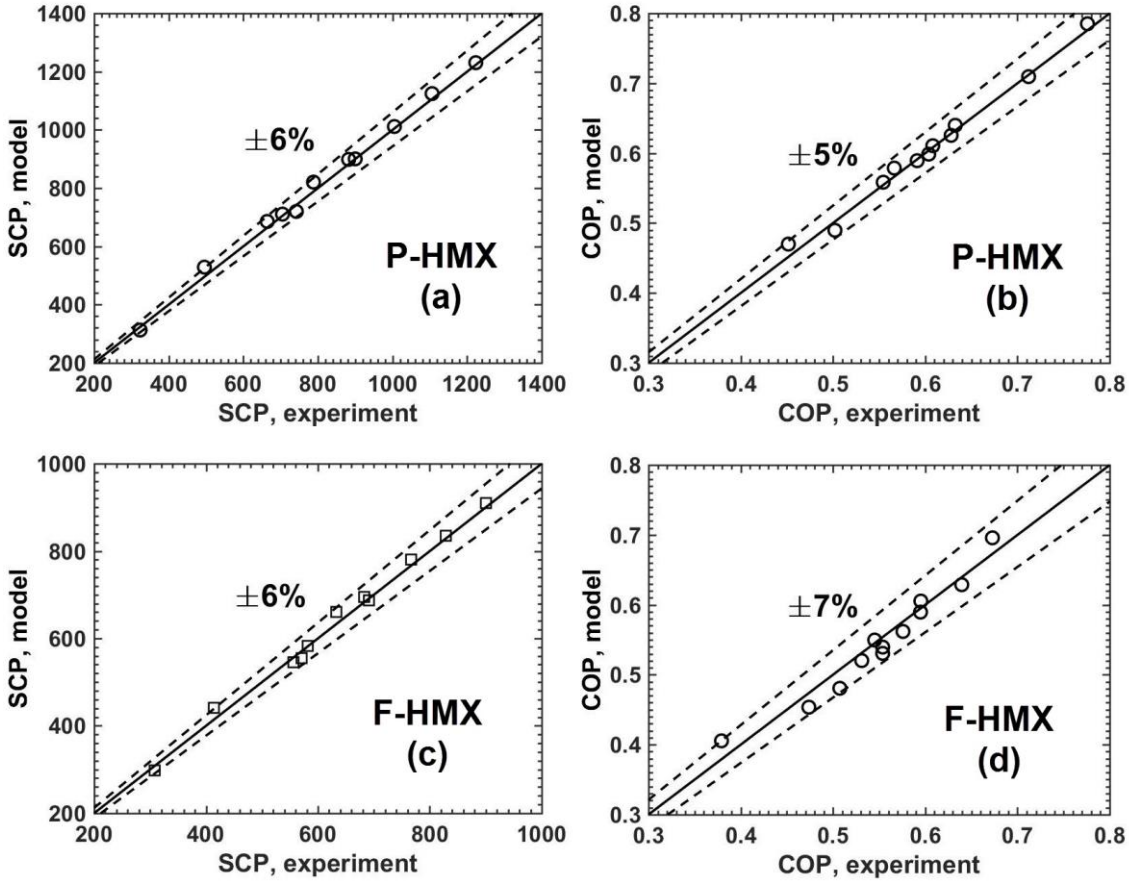

Fig. 72. Validation of the 2-D analytical model with the experimental data for the P-HMX in terms of (a) the SCP; and (b) the COP, and the F-HMX in terms of (c) the SCP and (d) the COP

5.6. Conclusion

The optimum designs selected in Chapter 0 were designed and built considering the optimized characteristics of i) fin thickness; ii) fin height, iii) sorbent thickness; iv) fluid channel height; v) the amount of thermally conductive additive in the sorbent; and vi) cycle time. It was shown that compared to the state-of-the-art, the P-HMX provides the highest SCP of 1,005 W/kg sorbent, and the highest COP of 0.60. Furthermore, the F-HMX yielded the SCP of 766 W/kg and COP of 0.55. The results showed that the optimized P-HMX can produce 4.3 times higher SCP, and 3 times higher COP in comparison with the off-the-shelf S-HMX presented in Section 3.6.1. The present P-HMX has been tested under various operating conditions: i) desorption temperatures, 60 to 90 °C; ii) sorption and condenser temperature, 20–40 °C; iii) evaporator temperature, 5–20 °C; and iv) cycle time, 10–20 min. The SCP in the range of 320–1,230 W/kg and the COP of 0.40–0.80 were measured in our testbed over the range of targeted operating conditions.

6. Conclusions, contributions, limitations, potential for further development and broader implementation, and future research

6.1. Conclusion and summary of thesis

This PhD project was set out to specifically design and optimize sorber bed heat and mass exchangers (S-HMXs) for sorption systems. The focus of this study was the application of sorption cooling systems for air conditioning and refrigeration. However, the methodology of modeling, ANOVA, design, optimization, manufacturing and testing can be applied to other applications of sorption systems, such as heat pumps, heat transformers, heat storage, dehumidification, desalination and gas separation.

In Chapter 1, the future trends of cooling energy demand and peak power load was presented. Also, an introduction to cooling technologies for air conditioning (AC) and refrigeration was provided. It was shown that vapor compression refrigeration (VCR) is the dominant technology currently used because of high performance, compactness, and low cost. Nonetheless, VCR systems have significant GHG emissions. Also, with the increasing trend of AC usage, the grid and power plants would require significant investment to cope with the peak load by VCR. The substantial potential of sorption cooling systems (SCS) as an alternative to VCR was discussed due to environmentally friendly sorption pairs and utilization of low-grade thermal energy, which is non-payable and abundant in different sectors. Suitable sorption pairs were selected to achieve the target for the present PhD study. The need for research was shown by comparing SCS with VCR in terms of the performance parameters. The rationale behind the selection of the target performance parameters was elaborated.

In Chapter 2, a critical literature review was conducted to find the most suitable thermally conductive additives to enhance sorbent thermal diffusivity. Graphite flakes were selected due to their high thermal conductivity, low molecular weight, corrosion resistance, and excellent stability at high working temperatures. Sample preparation and measurements of thermal diffusivity and sorption isotherm were explained. For the first time in the literature, the conflicting effects of graphite flake additives in the sorbent were studied using a custom-built gravimetric large pressure jump (G-LPJ) test bed. It was found that in the early stages of sorption, the S-HMX performance was notably improved, e.g. from 178.1 to 334.9 W/kg for a 6 min cycle time, by adding graphite flakes, which enhanced sorbent thermal diffusivity (from 0.23 to 1.38 mm^2/s). Also, it was shown that as

the sorption rate reduces with time, the need for heat transfer enhancement, i.e. using a graphite flake additive, decreases. Therefore, the graphite flake content and the cycle time need to be optimized to achieve optimum SCP.

In Chapter 3, for the first time, 2-D analytical models were developed that consider the spatial and temporal variation of water uptake and temperature in the sorber bed heat and mass exchangers (S-HMX), and have a low computation time, which is crucial for the optimization and real-time control of the S-HMXs. The detailed analytical solution methodology was presented in this chapter for the plate fin sorber bed heat and mass exchangers (P-HMX) in Cartesian coordinate system and finned-tube sorber bed heat and mass exchangers (F-HMX) in cylindrical coordinate system. The analytical model was validated using the data collected from the G-LPJ test bed and two-sorber bed sorption test bed. A parametric study was performed to investigate the effect of the S-HMX geometry, heat transfer characteristics and cycle time on sorption performance, i.e. the SCP and COP. It was shown that the S-HMX parameters have conflicting effects on the SCP and COP; thus, both the SCP and COP should be optimized in a multi-objective optimization study. Moreover, it was shown that the S-HMX geometry and heat transfer characteristics should be optimized simultaneously because if even one thermal resistance remains large inside the S-HMX, sorbent, heat exchanger (HEX) and/or heat transfer fluid (HTF), it can limit the heat transfer and overall performance of SCS. The developed analytical model can be applied to other sorption applications, such as heat pumps, heat transformers, and thermal energy storage systems, by changing the operating conditions and objective functions. Furthermore, the analytical model can be implemented to other S-HMX geometries by developing the pertinent eigen-value problems.

In Chapter 4, the analysis of variance (ANOVA) was carried out to find the key parameters of the S-HMXs affecting their sorption performance. The results showed that the entire S-HMX, consisting of the sorbent, heat exchanger and the heat transfer fluid, should be optimized simultaneously to achieve optimal SCP and COP. Moreover, for the first time in the literature, a simultaneous multi-objective optimization study was performed on the geometry, heat transfer characteristics and cycle time of the P-HMX and the F-HMX to find the optimal SCP and COP. A design with an SCP of 976 W/kg and a COP of 0.60 was selected for the P-HMX and a design with an SCP of 757 W/kg and a COP of 0.55 was selected for the F-HMX due to an optimal compromise between the SCP and COP.

In Chapter 5, For the first time in the literature, the S-HMXs of the P-HMX and the F-HMX were specifically designed for sorption cooling systems based on the optimum design parameters. It was shown that compared to the state-of-the-art, the P-HMX provides the highest SCP, i.e. 1,005 W/kg sorbent, and the highest COP, i.e. 0.60. Furthermore, the F-HMX yielded an SCP of 766 W/kg and a COP of 0.55. The results showed that by optimization of the S-HMX, performance can be increased significantly, i.e. 4.3 times higher SCP, and 3 times higher COP, compared to the off-the-shelf S-HMX. The present P-HMX was tested under various operating conditions: i) desorption temperatures, 60–90 °C; ii) sorption and condenser temperatures, 20–40 °C; iii) an evaporator temperature, 5–20 °C; and iv) cycle time, 10–20 min. An SCP in the range of 320–1,230 W/kg and a COP of 0.40–0.80 were measured in our test bed over the range of targeted operating conditions.

6.2. Contributions

The main novelties and contributions of the present PhD project can be summarized as follows:

- Construction of a gravimetric large pressure jump (G-LPJ) test bed to study the counteracting trends of thermally conductive additives on heat and mass transfer;
- Development of novel 2-D analytical closed-form models of the S-HMXs that can accurately predict spatial and temporal variation of uptake and temperature with low computation time;
- Implementation of analysis of variance (ANOVA) to identify the S-HMX key parameters governing their performance;
- Performing a simultaneous multi-objective optimization of key parameters of the S-HMXs to achieve optimum SCP and COP;
- Design and construction of optimized S-HMXs of P-HMXs and F-HMXs;
- Construction of two-sorber bed sorption test bed to test the S-HMXs;
- Achievement of an SCP of 1,005 W/kg and a COP of 0.60 for P-HMXs, which are higher than the state-of-the-art, and higher than the performance target: an SCP > 700 W/kg and a COP > 0.55. Also, a cooling power of 0.59 kW higher than the performance target of 0.5 kW;
- Enhancement of the sorption performance using the specific design and optimization of S-HMX, i.e. 4.3 times higher SCP, and 3 times higher COP, compared to the off-the-shelf S-HMX;

- Attainment of SCP in the range of 320–1,230 W/kg and COP in the range of 0.40–0.80 for different operating conditions: i) desorption temperatures, 60–90 °C; ii) sorption and condenser temperatures, 20–40 °C, iii) evaporator temperature, 5–20 °C; and iv) cycle time, 10–20 min.

6.3. Limitations, potential for further development and implementation to other sorption applications

The limitations, potential for further development and implementation of the present thesis to other sorption applications are listed in the following.

1. The analytical model can be used if the assumptions in section 3.3 are satisfied. The assumptions of
   - uniform sorbate pressure inside the sorbent,
   - thermodynamic equilibrium of sorbent and sorbate,
   - local thermal equilibrium between sorbent and sorbate, and
   - negligible convection term in the energy equation

   are essential for the model development. If they are not met, the model would require major modifications, such as addition of mass transfer equations and convection terms. However, the assumptions of
   - constant temperature of heat transfer fluid along the solution domain,
   - adiabatic boundary conditions,
   - constant thermo-physical properties, and
   - negligible gap between the sorbent coatings

   are not vital and broader assumptions can be added to the model by
   - semi-analytical modeling, including numerical methods in the analytical model,
   - changing the boundary conditions in the eigenvalue problems,
   - variable thermo-physical properties and semi-analytical modeling by dividing the solution domain into the intervals where the properties are constant, and
   - the model is valid for both negligible and significant gap between the sorbent coatings,

   , respectively.

   Moreover, the analytical model was developed for sorption cooling systems. Nonetheless, it can be used for other closed sorption systems, such as heat transformers, heat pumps, thermal energy storage systems, and desalination. The model would require significant modifications for the open sorption systems, namely

sorption dehumidification, and gas separation applications. Additional layers of the flow stream and convection terms should be added to the solution domain and the governing equations.

2. Thermally conductive additives other than graphite flakes can be used to increase the sorbent thermal diffusivity. Moreover, sorbents other than silica gel/$CaCl_2$ can be employed as the sorbent. The measurements of equilibrium uptake and thermo-physical properties should be conducted for the new sorbents and implemented to the model as the inputs. The assumptions related to the sorbent should be checked as mentioned above.
3. ANOVA and optimization study should be performed using the modified analytical models for different sorption applications. The operating conditions and objective functions should be modified accordingly. For example, for heat transformers, the ambient temperature is used to cool the condenser, the low-grade thermal energy is used to heat the evaporator and sorber beds during desorption, while the sorber beds generate higher-grade thermal energy. Furthermore, the objective functions of specific heating power and coefficient of performance could be used to assess the heat transformer performance. Optimal design should be selected based on the limitations and constraints, such as available mass, volume, heat source, and cost.
4. New sorber beds should be built based on the new optimization study. The custom-built two-sorber bed sorption test bed can be used to test the new sorber beds for closed sorption systems by changing the operating conditions at the setpoints of the temperature control systems and modifying the vacuum chambers to fit to the new sorber beds. Nevertheless, a new test bed should be custom-built for open sorption systems.
5. It should be noted that this study was carried out focusing on the sorber beds of the sorption systems assuming ideal evaporators and condensers, meaning the evaporators and condensers do not limit the performance. The entire methodology of the modeling, ANOVA, optimization, manufacturing and testing should be performed on the evaporator and condenser of the sorption systems to achieve an optimal performance. A model is needed to optimize and control the operation of the sorption systems, including the sorber beds, evaporator and condenser, for different operating conditions and various demand loads.

6.4. Future research

The recommendations for future research are as follows:

- Investigation of other S-HMX designs, such as a pin fin HMX and a radial fin HMX, or modifications of the same P-HMX and F-HMX used in this study, e.g. variable thicknesses of the fin and the sorbent along the fins. The methodology of the analytical model developed in this study, can be applied to other geometries by developing the pertinent eigenvalue problems. Investigation of nature-inspired S-HMX.
- Approximation of the water uptake relationship with the sorbent temperature with a quadratic function and solve the governing equations semi-analytically.
- Design and development of S-HMX out of graphite or plastic instead of aluminum due to the low heat capacity, low weight and resistance against corrosion. Investigation of corrosion-resistant coatings on aluminum. Corrosion testing of the heat exchanger and outgassing rate with respect to the number of sorption cycles.
- Optimization of S-HMX considering the power consumption of the heat transfer fluid pumps and their pressure drop.
- Design and development of compact and light vacuum chambers with proper sealing to reduce the weight and volume of SCS.
- Implementation of the proposed approach in this PhD project to other sorption applications, namely heat pumps, heat transformers, heat storage, dehumidification, desalination and gas separation. All the steps taken in the present PhD project to specifically design and optimize the S-HMXs for sorption cooling systems, can be applied to other sorption applications by changing the operating conditions and the target performance indices.
- Large-scale modeling and optimization of the S-HMXs. In this study, the objective was to design and optimize the S-HMXs for 0.5 kW cooling power. The S-HMXs and the system can be scaled up to increase the cooling power to fulfill the requirements of vehicles and houses. A large-scale model is required to design and optimize the system operation, such as the configuration of the heat transfer fluid.
- System-level modeling and optimization of the sorption systems. Different components of the sorption systems, such as the S-HMXs, evaporators, condensers, and expansion valves, should be modelled together. This model can

be used to optimize the design and operating parameters of the sorption systems to further increase the performance.

- A real-time control system is required to control the operation of sorption systems for different operating conditions, namely heat source temperature, heat source heating power, sorption and condenser temperatures, and evaporator temperature. Based on different operating conditions, this control system can optimize the system operation such as cycle time to yield the maximum power.

References

[1] H. Bahrehmand, M. Ahmadi, and M. Bahrami, “Analytical modeling of oscillatory heat transfer in coated sorption beds,” *Int. J. Heat Mass Transf.*, vol. 121, pp. 1–9, 2018.

[2] H. Bahrehmand, M. Ahmadi, and M. Bahrami, “Oscillatory heat transfer in coated sorber beds: An analytical solution,” *Int. J. Refrig.*, 2018.

[3] *Building Energy Data Book*. U.S. Department of Energy, 2012.

[4] A. A. Askalany, M. Salem, I. M. Ismael, A. H. H. Ali, M. G. Morsy, and B. B. Saha, “An overview on adsorption pairs for cooling,” *Renew. Sustain. Energy Rev.*, vol. 19, pp. 565–572, 2013.

[5] W. Pridasawas, *Solar-driven refrigeration systems with focus on the ejector cycle*, no. 06/55. Department of Energy Technology, Royal Institute of Technology, 2006, 2006.

[6] J. M. Pinheiro, S. Salustio, J. Rocha, A. A. Valente, and C. M. Silva, “Adsorption heat pumps for heating applications,” *Renew. Sustain. Energy Rev.*, vol. 119, no. April, p. 109528, 2019.

[7] W. Goetzler, R. Zogg, J. Young, and C. Johnson, “Alternatives to Vapor-Compression HVAC Technology,” *ASHRAE J.*, vol. 56, p. 12, 2014.

[8] C. Formann, I. Muritala, R. Pardemann, and B. Meyer, “Estimating the global waste heat potential,” *Renew. Sustain. Energy Rev.*, vol. 57, pp. 1568–1579, 2016.

[9] “https://www.nrcan.gc.ca,” 2018. .

[10] R. Farrington and J. Rugh, “Impact of vehicle air-conditioning on fuel economy, tailpipe emissions, and electric vehicle range.,” in *Proceeding of the Earth Technologies Forum*, 2000.

[11] H. Bahrehmand, M. Khajehpour, and M. Bahrami, “Finding optimal conductive additive content to enhance the performance of coated sorption beds: An experimental study,” *Appl. Therm. Eng.*, vol. 143, no. July, pp. 308–315, 2018.

[12] H. Bahrehmand and M. Bahrami, “An analytical design tool for sorber bed heat exchangers of sorption cooling systems,” *Int. J. Refrig.*, vol. 100, pp. 368–379, 2019.

[13] H. Bahrehmand and M. Bahrami, “Development of novel sorber bed heat exchangers for sorption cooling systems,” *Submitt. to Appl. Therm. Eng.*, 2020.

[14] International Energy Agency, “The Future of Cooling,” 2018.

[15] International Energy Agency, “Air conditioning use emerges as one of the key drivers of global electricity-demand growth,” 2018.

[16] Zion Market Research, “Global Air Conditioning Market Will Reach USD 292.7 Billion By 2025,” 2019.

[17] G. Restuccia, A. Freni, and G. Maggio, “A zeolite-coated bed for air conditioning adsorption systems: Parametric study of heat and mass transfer by dynamic simulation,” *Appl. Therm. Eng.*, vol. 22, no. 6, pp. 619–630, 2002.

[18] S. Jiangzhou, R. Wang, Y. Lu, Y. Xu, and J. Wu, “Experimental investigations on adsorption air-conditioner used in internal-combustion locomotive driver-cabin,” *Appl Therm Eng*, vol. 22, pp. 1153–62., 2002.

[19] Z. Tamainot-Telto, S. J. Metcalf, and R. E. Critoph, “Novel compact sorption generators for car air conditioning ´ ne ´ rateur compact a ` sorption pour le Nouveau ge conditionnement d ’ air automobile,” *Int. J. Refrig.*, vol. 32, no. 4, pp. 727–733, 2009.

[20] İ. Uçkan, T. Yılmaz, E. Hürdoğan, and O. Büyükalaca, “Experimental investigation of a novel configuration of desiccant based evaporative air conditioning system,” *Energy Convers Manag*, vol. 65, pp. 606–15., 2013.

[21] R. Oliveira, V. Silveira, and R. Wang, “Experimental study of mass recovery adsorption cycles for ice making at low generation temperature,” *Appl Therm Eng*, vol. 26, pp. 303–11, 2006.
[22] M. Aneke, B. Agnew, C. Underwood, and M. Menkiti, “Thermodynamic analysis of alternative refrigeration cycles driven from waste heat in a food processing application Analyse thermodynamique des cycles frigorifiques innovants ´ s par la chaleur re ´ cupe ´ re ´ e dans une application de ˆne entraı transfor,” *Int. J. Refrig.*, vol. 35, no. 5, pp. 1349–1358, 2012.
[23] B. Dawoud, “A hybrid solar-assisted adsorption cooling unit for vaccine storage,” *Renew Energy*, vol. 32, pp. 947–64, 2007.
[24] J. Steven Brown and P. A. Domanski, “Review of alternative cooling technologies,” *Appl. Therm. Eng.*, vol. 64, no. 1–2, pp. 252–262, 2014.
[25] R. E. Sonntag, C. Borgnakke, and G. J. Van Wylen, *Fundamentals of Thermodynamics*, Sixth. Wiley, 2003.
[26] J. R. Barbosa, G. B. Ribeiro, and P. A. De Oliveira, “A state-of-the-art review of compact vapor compression refrigeration systems and their applications,” *Heat Transf. Eng.*, vol. 33, no. 4–5, pp. 356–374, 2012.
[27] EnergyStar, “ENERGY STAR Most Efficient 2020 — Central Air Conditioners and Air Source Heat Pumps,” 2020.
[28] X. She *et al.*, “Energy-efficient and -economic technologies for air conditioning with vapor compression refrigeration: A comprehensive review,” *Appl. Energy*, vol. 232, no. October, pp. 157–186, 2018.
[29] J. Lee, J. Kim, J. Park, and C. Bae, “Effect of the air-conditioning system on the fuel economy in a gasoline engine vehicle,” *J. Automob. Eng.*, vol. 227, no. 1, pp. 66–77, 2012.
[30] V. Johnson, “Fuel used for vehicle air conditioning: a state-by-state thermal comfort-based approach,” *SAE Pap.*, 2002.
[31] Hexa Research, “Automotive HVAC Market Size By Application (Heavy Commercial Vehicles (HCVs), Light Commercial Vehicles (LCVs), Passenger Cars), By Technology (Manual, Automatic), Industry Analysis Report, Regional Outlook (U.S., Canada, Germany, UK, India, China, Japan,” 2016.
[32] H. Sadighi Dizaji, E. J. Hu, and L. Chen, “A comprehensive review of the Maisotsenko-cycle based air conditioning systems,” *Energy*, vol. 156, pp. 725–749, 2018.
[33] H. Caliskan, I. Dincer, and A. Hepbasli, “Exergetic and sustainability performance comparison of novel and conventional air cooling systems for building applications.,” *Energy Build*, vol. 43, pp. 1461–72, 2011.
[34] C. Zhan and X. Zhao, “Comparative study of the performance of the M-Cycle counter-flow and cross-flow heat exchangers for indirect evaporative coolinge paving the path toward sustainable cooling of buildings.,” *Energy*, vol. 36, pp. 6790–805, 2011.
[35] C. Zhan, X. Zhao, S. Smith, and S. . Riffat, “Numerical study of a M-Cycle cross-flow heat exchanger for indirect evaporative cooling.,” *Build Env.*, vol. 46, pp. 657–68., 2011.
[36] Y. Heredia-Aricapaa, J. M. Belman-Floresa, A. Mota-Babiloni, J. Serrano-Arellano, and J. J. García-Pabón, “Overview of low GWP mixtures for the replacement of HFC refrigerants: R134a, R404A and R410A,” *Int. J. Refrig.*, vol. 111, pp. 113–123, 2020.
[37] M. O. McLinden, A. F. Kazakov, J. Steven Brown, and P. A. Domanski, “A thermodynamic analysis of refrigerants: Possibilities and tradeoffs for Low-GWP refrigerants,” *Int. J. Refrig.*, vol. 38, no. 1, pp. 80–92, 2014.

[38] T. Okamura, R. Rachi, N. Hirano, and S. Nagaya, “Improvement of 100 W class room temperature magnetic refrigerator,” in *Proc. 2nd Int. Conf. Magn. refrigeration room temp*, 2007.
[39] A. Tura and A. Rowe, “Progress in the characterization and optimization of a permanent magnet magnetic refrigerator,” in *Proc. 3rd Int. Conf. Magn. refrigeration room temp*, 2009.
[40] S. K. Fischer, J. J. Tomlinson, and P. J. Hughes, “Energy and global warming impacts of not-in-kind and next generation CFC and HCFC alternatives,” *ORNL*, 1994.
[41] B. L. Minner, J. E. Braun, and L. Mongeau, “Theoretical evaluation of the optimal performance of a thermoacoustic refrigerator,” *ASHRAE Trans.*, vol. 103, no. 1, pp. 873–887, 1997.
[42] D. Kim and C. A. Infante Ferreira, “Solar refrigeration options – a state-of-the-art review.,” *Int J Refrig*, vol. 31, pp. 3–15, 2008.
[43] J. Meng, X. Wang, and X. Zhang, “Transient modeling and dynamic characteristics of thermoelectric cooler.,” *Appl Energy*, vol. 108, pp. 340–8, 2013.
[44] M. Ewert, M. Agrella, D. DeMonbrun, J. Frahm, D. Bergeron, and D. Berchowitz, “Experimental evaluation of a solar PV refrigerator with thermoelectric, Stirling, and vapour compression heat pumps.,” in *Proc. ASES Sol. 98 Conf., Albuquerque, USA*, 1998.
[45] Global Cooling Inc., “Stirling Ultracold,” 2020. [Online]. Available: https://www.stirlingultracold.com/.
[46] A. Sharafian, “Waste heat-driven adsorption cooling systems for vehicle air conditioning applications,” Simon Fraser University, 2015.
[47] R. Nikbakhti, X. Wang, A. K. Hussein, and A. Iranmanesh, “Absorption cooling systems – Review of various techniques for energy performance enhancement,” *Alexandria Eng. J.*, vol. 59, no. 2, pp. 707–738, 2020.
[48] R. Gomri, “Investigation of the potential of application of single effect and multiple effect absorption cooling systems,” *Energy Convers. Manag.*, vol. 51, pp. 1629–1636., 2010.
[49] L. F. Cabeza, A. Sole, and C. Barreneche, “Review on sorption materials and technologies for heat pumps and thermal energy storage,” *Renew. Energy*, vol. 110, pp. 3–39, 2017.
[50] K. Korhammer *et al.*, “Sorption and thermal characterization of composite materials based on chlorides for thermal energy storage q,” *Appl. Energy*, vol. 162, pp. 1462–1472, 2016.
[51] M. O. M. . Abdullah, I. A. . I. A. W. Tan, and L. . L. S. Lim, “Automobile adsorption air-conditioning system using oil palm biomass-based activated carbon: A review,” *Renew. Sustain. Energy Rev.*, vol. 15, no. 4, pp. 2061–2072, 2011.
[52] H. Demir, M. Mobedi, and S. Ulku, “A review on adsorption heat pump : Problems and solutions,” *Renew. Sustain. Energy Rev.*, vol. 12, pp. 2381–2403, 2008.
[53] J. Ling-Chin, H. Bao, Z. Ma, W. Taylor, and A. P. Roskilly, “State-of-the-Art Technologies on Low-Grade Heat Recovery and Utilization in Industry,” *Energy Convers—Current Technol. Futur. TrendsAl-Bahadly I.H.; IntechOpen London*, 2018.
[54] Canadian Energy Systems Analysis Research (CESAR), “Canadian Energy Flows,” 2013. [Online]. Available: https://www.cesarnet.ca/visualization/sankey-diagrams-canadas-energy-systems.
[55] M. Verde, K. Harby, R. de Boer, and J. M. Corberán, “Performance evaluation of a waste-heat driven adsorption system for automotive air-conditioning: Part I – Modeling and experimental validation,” *Energy*, vol. 116, pp. 526–538, 2016.

[56] L. Jianbo, L. Kai, H. Xiaolong, Z. Chen, C. Fulin, and K. Xiangqiang, “A novel absorption–compression combined refrigeration cycle activated by engine waste heat,” *Energy Convers. Manag.*, vol. 205, no. October 2019, p. 112420, 2020.
[57] X. Liu, M. Q. Nguyen, J. Chu, T. Lan, and M. He, “A novel waste heat recovery system combing steam Rankine cycle and organic Rankine cycle for marine engine,” *J. Clean. Prod.*, p. 121502, 2020.
[58] Z. Liu, N. Xie, and S. Yang, “Thermodynamic and parametric analysis of a coupled LiBr/H2O absorption chiller/Kalina cycle for cascade utilization of low-grade waste heat,” *Energy Convers. Manag.*, vol. 205, no. August 2019, p. 112370, 2020.
[59] NFI Group Inc, “f-cell HFC,” in *f-cell + HFC*, 2019.
[60] M. V. Oro, R. G. de Oliveira, and E. Bazzo, “An integrated solution for waste heat recovery from fuel cells applied to adsorption systems,” *Appl. Therm. Eng.*, vol. 136, no. December 2017, pp. 747–754, 2018.
[61] G. Khoury and D. Clodic, “Method of test and measurements of fuel consumption due to air conditioning operation on the New Prius II hybrid vehicle.,” *SAE Tech Pap no2005-01-2049*, 2005.
[62] J. Lee, S. Kwon, Y. Lim, M. Chon, and D. Kim, “Effect of air-conditioning on driving range of electric vehicle for various driving modes.,” *SAE Tech. Pap.*, 2013.
[63] S. M. Aceves, “An analytical comparison of adsorption and vapor compression air conditioners for electric vehicle applications,” *Trans. ASME*, vol. 118, pp. 16–21, 1996.
[64] S. J. Gregg and K. S. . Sing, *Adsorption, Surface Area, and Porosity*, 2nd ed. Academic Press, 1982.
[65] L. W. Wang, R. Z. Wang, and R. G. Oliveira, “A review on adsorption working pairs for refrigeration,” *Renew. Sustain. Energy Rev.*, vol. 13, no. 3, pp. 518–534, 2009.
[66] R. T. Yang, “Gas separation by Adsorption Methods,” in *Publishing House of Chemical Industry, Beijing, China,* 1991.
[67] L. F. Cabeza, A. Solï¿½, and C. Barreneche, “Review on sorption materials and technologies for heat pumps and thermal energy storage,” *Renew. Energy*, vol. 110, pp. 3–39, 2017.
[68] K. N. Aboua, Y. A. Yobouet, K. B. Yao, D. L. Goné, and A. Trokourey, “Investigation of dye adsorption onto activated carbon from the shells of Macoré fruit,” *J. Environ. Manage.*, vol. 156, pp. 10–14, 2015.
[69] C. K. Zacharis, “Accelerating the quality control of pharmaceuticals using monolithic stationary phases: A review of recent HPLC applications,” *J. Chromatogr. Sci.*, vol. 47, no. 6, pp. 443–451, 2009.
[70] K. Y. Hor *et al.*, “Evaluation of physicochemical methods in enhancing the adsorption performance of natural zeolite as low-cost adsorbent of methylene blue dye from wastewater,” *J. Clean. Prod.*, vol. 118, no. February, pp. 197–209, 2016.
[71] ASHRAE, *Energy Standard for Buildings Except Low-Rise Residential Buildings*. 2019.
[72] R. Z. Wang, L. Wang, and J. Wu, *Adsorption refrigeration technology, theory and application*. Wiley, 2014.
[73] R. K. AL-Dadah, S. Mahmoud, E. Hussein, P. Youssef, and F. Al-Mousawi, “Metal Organic Framework Materials for Adsorption Heat Pumps,” in *HEAT POWERED CYCLES*, 2018, pp. 31–43.
[74] Y. Luo, H. H. Funke, J. L. Falconer, and R. D. Noble, “Adsorption of CO2, CH4, C3H8, and H2O in SSZ-13, SAPO-34, and T-Type Zeolites,” *Ind. Eng. Chem. Res.*, vol. 55, p. 9749−9757, 2016.
[75] A. Sharafian and M. Bahrami, “Assessment of adsorber bed designs in waste-heat driven adsorption cooling systems for vehicle air conditioning and refrigeration,”

Renew. Sustain. Energy Rev., vol. 30, pp. 440–451, 2014.
[76] A. Freni *et al.*, *Characterization of Zeolite-Based Coatings for Adsorption Heat Pumps*. SPRINGER BRIEFS IN APPLIED SCIENCES AND TECHNOLOGY, 2015.
[77] C. McCague, K. Fayazmanesh, C. Berlanga, and M. Bahrami, "Evaluation of CaCl2-silica gel sorbent for water sorption cooling systems," in *IX Minsk International Seminar "Heat Pipes, Heat Pumps, Refrigerators, Power Sources,"* 2015.
[78] Y. Tanashev, A. Krainov, and Y. I. Aristov, "Thermal conductivity of composite sorbents 'salt in porous matrix' for heat storage and transformation," *Appl. Therm. Eng.*, vol. 61, pp. 401–407, 2013.
[79] L. Gordeeva and Y. I. Aristov, "Composites 'salt inside porous matrix' for adsorption heat transformation: a current state-of-the-art and new trends," *Int. J. Low-Carbon Tech.*, vol. 7, pp. 288–302., 2012.
[80] "Rooftop HVAC System for Coach and Transit, Athenia AM II Series," *Corporate white paper from Ingersoll Rand, Thermo king*, 2016. .
[81] "Rooftop air conditioning units for buses and coaches," *Corporate white paper from Espar Heating Systems*, 2013. [Online]. Available: https://www.eberspaecher-na.com/fileadmin/data/countrysites/EB_Kanada/images/AC310350_SpecSheet_WEB_READY_052913.pdf.
[82] Invensor, "Adsorption Chiller, InvenSor LTC 10 e plus," 2020.
[83] Invensor, "Adsorption Chiller InvenSor LTC 30 e plus," 2020.
[84] Invensor, "Adsorption Chiller InvenSor LTC 90 e plus," 2020.
[85] Fahrenheit cooling innovations, "Technical data sheets," 2019.
[86] SolabCool, "SolabChiller," 2018.
[87] NISHIYODO KUCHOUKI CO. LTD (HIJC Inc.), "ADCM models," 2007.
[88] Mitsubishi Plastics, "Mitsubishi Plastics M-TYPE," 2015.
[89] Mayekawa (MYCOM), "AdRef-Noa, adsorption chillers with zeolite," 2020.
[90] R. E. Critoph, "Performance estimation of convective thermal wave adsorption cycles," *Appl. Therm. Eng.*, vol. 16, no. 5 SPEC. ISS., pp. 429–437, 1996.
[91] A. Freni, G. Maggio, A. Sapienza, A. Frazzica, G. Restuccia, and S. Vasta, "Comparative analysis of promising adsorbent/adsorbate pairs for adsorptive heat pumping, air conditioning and refrigeration," *Appl. Therm. Eng.*, vol. 104, pp. 85–95, 2016.
[92] A. Freni, L. Bonaccorsi, L. Calabrese, A. Caprì, A. Frazzica, and A. Sapienza, "SAPO-34 coated adsorbent heat exchanger for adsorption chillers," *Appl. Therm. Eng.*, vol. 82, pp. 1–7, 2015.
[93] W. D. Wu, H. Zhang, and D. W. Sun, "Mathematical simulation and experimental study of a modified zeolite 13X-water adsorption refrigeration module," *Appl. Therm. Eng.*, vol. 29, pp. 645–651.
[94] Y. Zhao, E. Hu, and A. Blazewicz, "Dynamic modelling of an activated carbon–methanol adsorption refrigeration tube with considerations of interfacial convection and transient pressure process," *Appl. Energy*, vol. 95, pp. 276–284, 2012.
[95] A. Sharafian, C. McCague, and M. Bahrami, "Impact of fin spacing on temperature distribution in adsorption cooling system for vehicle A/C applications," *Int. J. Refrig.*, vol. 51, pp. 135–143, 2015.
[96] K. C. Chan and C. Y. H. Chao, "A theoretical model on the effective stagnant thermal conductivity of an adsorbent embedded with a highly thermal conductive material," *Int. J. Heat Mass Transf.*, vol. 65, pp. 863–872, 2013.
[97] A. Rezk, R. K. Al-Dadah, S. Mahmoud, and A. Elsayed, "Effects of contact resistance and metal additives in finned-tube adsorbent beds on the performance of silica gel/water adsorption chiller," *Appl. Therm. Eng.*, vol. 53, no. 2, pp. 278–284, 2013.

[98] S. Yang, H. Kim, S. Narayanan, and I. S. McKay, “Dimensionality effects of carbon-based thermal additives for microporous adsorbents,” *Mater. Des.*, vol. 85, pp. 520–526, 2015.
[99] L. Pino, Y. Aristov, G. Cacciola, and G. Restuccia, “Composite materials based on zeolite 4A for adsorption heat pumps,” *Adsorption*, vol. 3, pp. 33–40, 1997.
[100] H. Demir, M. Mobedi, and S. Ulku, “The use of metal piece additives to enhance heat transfer rate through an unconsolidated adsorbent bed,” *Int. J. Refrig*, vol. 33, pp. 714–720, 2010.
[101] A. A. Askalany, S. K. Henninger, M. Ghazy, and B. B. Saha, “Effect of improving thermal conductivity of the adsorbent on performance of adsorption cooling system,” *Appl. Therm. Eng.*, vol. 110, pp. 695–702, 2017.
[102] D. Aydin, S. P. Casey, and S. Riffat, “The latest advancements on thermochemical heat storage systems,” *Renew. Sustain. Energy Rev*, vol. 41, pp. 356–367, 2015.
[103] S. Mauran, P. Parades, and F. L’haridon, “Heat and mass transfer in consolidated reacting beds for thermochemical systems,” *Heat. Recover. Syst.*, vol. 13, pp. 315–319, 1993.
[104] J. J. Guilleminot, J. B. Chalfen, and A. Choisier, “Heat and mass transfer characteristics of composites for adsorption heat pumps,” in *International Absorption Heat Pump Conference, AES 31, ASME, New York*, 1993.
[105] K. Wang, J. Y. Wu, R. Z. Wang, and L. W. Wang, “Effective thermal conductivity of expanded graphite-CaCl2composite adsorbent for chemical adsorption chillers,” *Energy Convers. Manag.*, vol. 47, no. 13–14, pp. 1902–1912, 2006.
[106] K. Fayazmanesh, C. McCague, and M. Bahrami, “Consolidated adsorbent containing graphite flakes for heat-driven water sorption cooling systems,” *Appl. Therm. Eng.*, vol. 123, pp. 753–760, 2017.
[107] T. Eun, H. Song, J. Hun Han, K. Lee, and J. Kim, “Enhancement of heat and mass transfer in silica-expanded graphite composite blocks for adsorption heat pumps:: Part I. Characterization of the composite blocks: Amélioration du transfert de chaleur de blocs en matériaux composite graphite-silice expansé/d,” *Int. J. Refrig.*, vol. 23, no. 1, pp. 64–73, 2000.
[108] X. Zheng, L. W. Wang, R. Z. Wang, T. S. Ge, and T. F. Ishugah, “Thermal conductivity, pore structure and adsorption performance of compact composite silica gel,” *Int. J. Heat Mass Transf.*, vol. 68, pp. 435–443, 2014.
[109] ISO22007-2, “Plastics-determination of thermal conductivity and thermal diffusivity-part 2: transient plane heat source (hot disc) method.” 2008.
[110] M. Khajehpour, C. McCague, S. Shokoya, and M. Bahrami, “Effect of Conductive Additives on Performance of CaCl2-Silica Gel Sorbent Materials,” in *Heat Power Cycles conference*, 2018.
[111] S. Kirkpatrick, “Percolation and Conduction,” *Rev. Mod. Phys.*, vol. 45, no. 4, 1973.
[112] B. Ghanbarian and H. Daigle, “Thermal conductivity in porous media: Percolation-based effective-medium approximation,” *Water Resour. Res.*, vol. 52, pp. 295–314, 2016.
[113] R. E. Critoph, “Simulation of a continuous multiple-bed regenerative adsorption cycle,” *Int. J. Refrig.*, vol. 24, no. 5, pp. 428–437, 2001.
[114] Z. Tamainot-Telto, S. J. Metcalf, R. E. Critoph, Y. Zhong, and R. Thorpe, “Carbon – ammonia pairs for adsorption refrigeration applications : ice making , air conditioning and heat pumping Les couples charbon actif-ammoniac pour les applications ` adsorption : fabrication de glace , frigorifiques a ` chaleur conditionnement d ’,” *Int. J. Refrig.*, vol. 32, no. 6, pp. 1212–1229, 2009.
[115] S. Henninger, M. Schicktanz, P. Hugenell, S. H, and H. Henning, “Evaluation of methanol adsorption on activated carbons for thermally driven chillers, part I:

thermophysical characterisation.," *Int J Refrig*, vol. 35, pp. 543–553, 2012.
[116] Q. W. Pan and R. Z. Wang, "Study on operation strategy of a silica gel-water adsorption chiller in solar cooling application," *Sol. Energy*, vol. 172, no. February, pp. 24–31, 2018.
[117] R. Ahmed and R. Al-Dadah, "Physical and operating conditions effects on silica gel/water adsorption chiller performance.," *Appl Energy*, vol. 89, pp. 142–149., 2012.
[118] B. Saha, I. El-Sharkawy, A. Chakraborty, and S. Koyama, "Study on an activated carbon fiber-ethanol adsorption chiller: part I – system description and modelling.," *Int J Refrig*, vol. 30, pp. 86–95, 2007.
[119] Z. Rogala, "Adsorption chiller using flat-tube adsorbers – Performance assessment and optimization," *Appl. Therm. Eng.*, vol. 121, pp. 431–442, 2017.
[120] M. Verde, K. Harby, and J. M. Corberán, "Optimization of thermal design and geometrical parameters of a flat tube-fin adsorbent bed for automobile air-conditioning," *Appl. Therm. Eng.*, vol. 111, pp. 489–502, 2017.
[121] A. El Fadar, "Thermal behavior and performance assessment of a solar adsorption cooling system with finned adsorber," *Energy*, vol. 83, pp. 674–684, 2015.
[122] S. W. Hong, S. H. Ahn, O. K. Kwon, and J. D. Chung, "Optimization of a fin-tube type adsorption chiller by design of experiment," *Int. J. Refrig.*, vol. 49, pp. 49–56, 2015.
[123] A. Çağlar, "The effect of fin design parameters on the heat transfer enhancement in the adsorbent bed of a thermal wave cycle," *Appl. Therm. Eng.*, vol. 104, pp. 386–393, 2016.
[124] I. Solmus, D. Andrew, S. Rees, C. Yamalı, and D. Baker, "A two-energy equation model for dynamic heat and mass transfer in an adsorbent bed using silica gel/water pair," *Int. J. Heat Mass Transf.*, vol. 55, pp. 5275–5288, 2012.
[125] J. Li, M. Kubota, F. Watanabe, N. Kobayashi, and M. Hasatani, "Optimal Design of a Fin-type Silica Gel Tube Module in the Silica Gel / Water Adsorption Heat Pump," *J. Chem. Eng. Japan*, vol. 37, no. 4, pp. 551–557, 2004.
[126] R. H. Mohammed, O. Mesalhy, M. L. Elsayed, and L. C. Chow, "Novel compact bed design for adsorption cooling systems: Parametric numerical study," *Int. J. Refrig.*, vol. 80, pp. 238–251, 2017.
[127] H. Niazmand and I. Dabzadeh, "Numerical simulation of heat and mass transfer in adsorbent beds with annular fins," *Int. J. Refrig.*, vol. 35, pp. 581–593, 2012.
[128] H. Niazmand, H. Talebian, and M. Mahdavikhah, "Bed geometrical specifications effects on the performance of silica/water adsorption chillers Effets des spécifications géométriques du lit sur la performance des refroidisseurs à adsorption au gel de silice/eau," *Int. J. Refrig.*, vol. 35, no. 8, pp. 2261–2274, 2012.
[129] M. Mahdavikhah and H. Niazmand, "Effects of plate finned heat exchanger parameters on the adsorption chiller performance," *Appl. Therm. Eng.*, vol. 50, pp. 939–949, 2013.
[130] M. Mohammadzadeh Kowsari, H. Niazmand, and M. M. Tokarev, "Bed configuration effects on the finned flat-tube adsorption heat exchanger performance: Numerical modeling and experimental validation," *Appl. Energy*, vol. 213, no. October 2017, pp. 540–554, 2018.
[131] B. Golparvar, H. Niazmand, A. Sharafian, and A. Ahmadian Hosseini, "Optimum fin spacing of finned tube adsorber bed heat exchangers in an exhaust gas-driven adsorption cooling system," *Appl. Energy*, vol. 232, no. September, pp. 504–516, 2018.
[132] W. Wu, H. Zhang, and D. Sun, "Mathematical simulation and experimental study of a modified zeolite 13X–water adsorption refrigeration module," *Appl. Therm. Eng.*,

vol. 29, pp. 645–651, 2009.
[133] Y. Zhao, E. Hu, and A. Blazewicz, “Dynamic modelling of an activated carbon–methanol adsorption refrigeration tube with considerations of interfacial convection and transient pressure process,” *Appl. Energy*, vol. 95, pp. 276–284, 2012.
[134] N. Wakao and S. Kaguei, *Heat and Mass Transfer in Packed Beds*, vol. 23. 1982.
[135] V. Gnielinski, “New equations for heat and mass transfer in turbulent pipe and channel flow,” *Int. Chem. Eng.*, vol. 16, no. 2, pp. 359–368, 1976.
[136] A. Sharafian, K. Fayazmanesh, C. Mccague, and M. Bahrami, “Thermal conductivity and contact resistance of mesoporous silica gel adsorbents bound with polyvinylpyrrolidone in contact with a metallic substrate for adsorption cooling system applications,” *Int. J. Heat Mass Transf.*, vol. 79, pp. 64–71, 2014.
[137] S. Singh, P. K. Jain, and Rizwan-uddin, “Analytical Solution for Three-Dimensional, Unsteady Heat Conduction in a Multilayer Sphere,” *J. Heat Transfer*, vol. 138, no. 10, p. 101301, 2016.
[138] A. J. Moghadam, “Exact Solution of Electroviscous Flow and Heat Transfer in a Semi-annular Microcapillary,” *J. Heat Transfer*, vol. 138, no. 1, p. 011702, 2015.
[139] S. Julius, B. Leizeronok, and B. Cukurel, “Nonhomogeneous Dual-Phase-Lag Heat Conduction Problem: Analytical Solution and Select Case Studies,” *J. Heat Transfer*, vol. 140, no. 3, p. 031301, 2017.
[140] P. Biswas and S. Singh, “Orthogonal Eigenfunction Expansion Method for One-Dimensional Dual-Phase Lag Heat Conduction Problem With Time-Dependent Boundary Conditions,” *J. Heat Transfer*, vol. 140, no. 3, p. 034501, 2017.
[141] C. Weng, C. Chen, and C. S. Fin, “Transient Response of a Composite Straight Fin,” *J. Heat Transfer*, vol. 105, no. May 1983, pp. 307–311, 2014.
[142] M. Fakoor-Pakdaman, M. Ahmadi, F. Bagheri, and M. Bahrami, “Optimal Time-Varying Heat Transfer in Multilayered Packages With Arbitrary Heat Generations and Contact Resistance,” *J. Heat Transfer*, vol. 137, no. 8, p. 081401, 2015.
[143] M. D. Mikhailov and M. N. Ozisik, “Transient conduction in a three-dimensional composite slab,” *Int. J. Heat Mass Transf.*, vol. 29, pp. 340-342., 1986.
[144] M. D. Mikhailov and N. L. Vulchanov, “Computational Procedure for Sturm-Liouville Problems,” *J. Comput. Phys.*, vol. 50, pp. 323–336, 1983.
[145] J. P. P. Holman, *Heat Transfer*. McGraw-Hill, 2010.
[146] A. Sapienza, S. Santamaria, A. Frazzica, and A. Freni, “Influence of the management strategy and operating conditions on the performance of an adsorption chiller,” *Energy*, vol. 36, pp. 5532–5538, 2011.
[147] M. Louajari, A. Mimet, and A. Ouammi, “Study of the effect of finned tube adsorber on the performance of solar driven adsorption cooling machine using activated carbon – ammonia pair,” *Appl. Energy*, vol. 88, no. 3, pp. 690–698, 2011.
[148] Q. W. Pan, R. Z. Wang, Z. S. Lu, and L. W. Wang, “Experimental investigation of an adsorption refrigeration prototype with the working pair of composite adsorbent-ammonia,” vol. 72, 2014.
[149] C. Y. Tso, K. C. Chan, C. Y. H. Chao, and C. L. Wu, “Experimental performance analysis on an adsorption cooling system using zeolite 13X / CaCl 2 adsorbent with various operation sequences,” vol. 85, pp. 343–355, 2015.
[150] L. Q. Zhu, Z. W. Gong, B. X. Ou, and C. L. Wu, “Performance Analysis of Four Types of Adsorbent Beds in a Double-Adsorber Adsorption Refrigerator,” *Procedia Eng.*, vol. 121, pp. 129–137, 2015.
[151] A. Sharafian, C. McCague, and M. Bahrami, “Impact of fin spacing on temperature distribution in adsorption cooling system for vehicle A/C applications,” *Int. J. Refrig.*, vol. 51, pp. 135–143, 2015.
[152] A. Sapienza *et al.*, “An innovative adsorptive chiller prototype based on 3 hybrid

coated / granular adsorbers," *Appl. Energy*, vol. 179, pp. 929–938, 2016.
[153] Q. W. Pan, R. Z. Wang, L. W. Wang, and D. Liu, "Design and experimental study of a silica gel-water adsorption chiller with modular adsorbers," *Int. J. Refrig.*, vol. 67, pp. 336–344, 2016.
[154] A. Frazzica *et al.*, "Design , realization and testing of an adsorption refrigerator based on activated carbon / ethanol working pair," *Appl. Energy*, vol. 174, pp. 15–24, 2016.
[155] B. Zajaczkowski, "Optimizing performance of a three-bed adsorption chiller using new cycle time allocation and mass recovery," *Appl. Therm. Eng.*, vol. 100, pp. 744–752, 2016.
[156] V. Palomba, B. Dawoud, A. Sapienza, S. Vasta, and A. Frazzica, "On the impact of different management strategies on the performance of a two-bed activated carbon / ethanol refrigerator : An experimental study," *Energy Convers. Manag.*, vol. 142, pp. 322–333, 2017.
[157] U. Bau *et al.*, "Dynamic optimisation of adsorber-bed designs ensuring optimal control Constraints," *Appl. Therm. Eng.*, vol. 125, pp. 1565–1576, 2017.
[158] K. Chan, C. Tso, C. Wu, and C. Y. H. Chao, "Enhancing the performance of a zeolite 13X / CaCl 2 – water adsorption cooling system by improving adsorber design and operation sequence," *Energy Build.*, vol. 158, pp. 1368–1378, 2018.
[159] U. Bau and A. Bardow, "Pareto-optimal performance of one-bed adsorption chillers by easy-to- implement heat-flow-based control," *Appl. Therm. Eng.*, vol. 159, no. February, p. 113590, 2019.
[160] M. B. Elsheniti, M. A. Hassab, and A. Attia, "Examination of effects of operating and geometric parameters on the performance of a two-bed adsorption chiller," *Appl. Therm. Eng.*, vol. 146, no. September 2018, pp. 674–687, 2019.
[161] O. J. Dunn and V. A. Clark, *Applied Statistics: Analysis of Variance and Regression*. New York: Wiley, 1974.
[162] J. H. Goodnight and F. M. Speed, *Computing Expected Mean Squares*. Cary, NC: SAS Institute, 1978.
[163] R. V. Hogg and J. Ledolter, *Engineering Statistics*. New York: MacMillan, 1987.
[164] G. Box and D. Behnken, "Some new three level designs for the study of quantitative variables," *Technometrics*, vol. 2, pp. 455–475, 1960.
[165] J. S. Arora, *Introduction to Optimum Design*. 2004.
[166] A. Freni, L. Calabrese, A. Malara, P. Frontera, and L. Bonaccorsi, "Silica gel micro fibres by electrospinning for adsorption chillers," *Energy*, vol. 187, p. 115971, 2019.
[167] A. Freni, F. Russo, S. Vasta, M. Tokarev, Y. Aristov, and G. Restucci, "An advanced solid sorption chiller using SWS-1L," *Appl Therm Eng*, vol. 27, pp. 2200–2204, 2007.
[168] B. Dawoud, P. Höfle, and S. Chmielewski, "Experimental investigation of the effect of zeolite coating thickness on the performance of a novel zolite-water adsorption heat pump module," in *Tenth international conference enhanced building operations*, 2010, pp. 1–8.
[169] M. Verde, J. M. Corberan, R. de Boer, and S. Smeding, "Modelling of a waste heat driven silica gel/water adsorption cooling system comparison with experimental results," in *ISHPC conference, Padua, Italy*, 2011, pp. 7–8.
[170] Y. Aristov, A. Sapienza, D. Ovoshchnikov, A. Freni, and G. Restuccia, "Reallocation of adsorption and desorption times for optimisation of cooling cycles," *Int J Refrig*, vol. 35, pp. 525–31, 2012.
[171] U. Wittstadt *et al.*, "A novel adsorption module with fiber heat exchangers: Performance analysis based on driving temperature differences," *Renew. Energy*, vol. 110, pp. 154–161, 2017.

[172] Z. He *et al.*, “Study on the performance of compact adsorption chiller with vapor valves,” *Appl. Therm. Eng.*, vol. 126, pp. 37–42, 2017.
[173] A. Sharafian, S. M. Nemati Mehr, P. C. Thimmaiah, W. Huttema, and M. Bahrami, “Effects of adsorbent mass and number of adsorber beds on the performance of a waste heat-driven adsorption cooling system for vehicle air conditioning applications,” *Energy*, vol. 112, pp. 481–493, 2016.
[174] A. Alahmera, S. Ajiba, and X. Wang, “Comprehensive strategies for performance improvement of adsorption air conditioning systems: A review,” *Renew. Sustain. Energy Rev.*, vol. 99, pp. 138–158, 2019.
[175] Q. W. Pan, R. Z. Wang, and L. W. Wang, “Comparison of different kinds of heat recoveries applied in adsorption refrigeration system,” *Int. J. Refrig.*, vol. 55, pp. 37–48, 2015.
[176] R. J. Moffat, “Describing the uncertainties in experimental results,” *Exp. Therm. Fluid Sci.*, vol. 1, pp. 3–17, 1988.

Appendix A: Enhancement of coefficient of performance (COP)

Advanced cycles such as thermal regeneration cycles (thermal and forced convective/wave cycle), cascade cycles and multi-stages schemes have been proposed to enhance COP of SCS [174]. However, these cycles increase the complexity and more importantly the mass, volume and the cost of the system, which results in lower cooling power per overall mass. Therefore, alternative solutions need to be found to increase COP without increasing the mass and volume of the system.

It was explained in section 1.6, that coefficient of performance (COP) can be increased by: i) enhancing the heat and mass transfer processes inside the S-HMX, which increases both the evaporative cooling energy and the desorption heat, which overall increases COP, and ii) decreasing the sensible energy required to overcome thermal inertia of the heat exchanger (HEX), sorbent material, refrigerant inside the sorbent and the heat transfer fluid.

Fig. A 1 shows the share of desorption heat and sensible energy of each component of the S-HMX, i.e. heat exchanger (HEX), sorbent material, refrigerant inside the sorbent and the heat transfer fluid, for the optimized P-HMX. The results are obtained from 2-D analytical model validated by the experiments. It can be seen in **Fig. A 1** that 55% of the input energy is consumed to desorb water from the sorbent, whereas 45% of the input energy is wasted to overcome the S-HMX thermal inertia. For the same conditions, by increasing the amount of sorbent and refrigerant inside the sorbent, COP increases; thus, 5% and 9% of the input energy, consumed to overcome thermal inertia of the sorbent and the water inside the sorbent, cannot be decreased. Therefore, the only portions of the input energy that can be decreased are the energy spent on thermal inertia of the heat transfer fluid and heat exchanger, 18% and 13%, respectively.

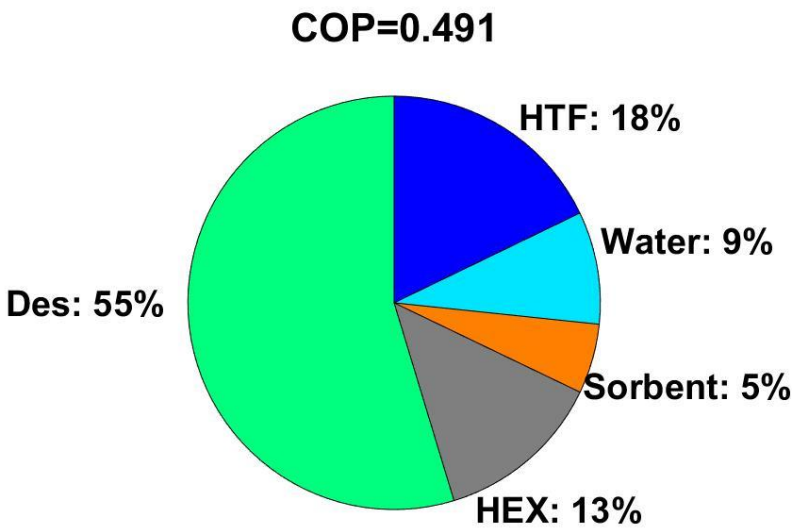

Fig. A 1. Share of desorption heat and the sensible energy of the heat exchanger (HEX), sorbent material, water inside the sorbent and the heat transfer fluid in the input energy

In this study, thermal inertia of the heat exchanger was minimized by (i) optimizing the P-HMX geometry for optimum SCP and COP and (ii) building the P-HMX out of aluminum, which has lower heat capacity compared to the common metals used for heat exchanger production, such as copper and stainless steel. The justification for selection of aluminum as the S-HMX material is explained in Appendix A.1. Furthermore, COP can be significantly increased by removing the heat transfer fluid (HTF) thermal inertia using heat recovery methods, discussed in Appendix A.2.

A.1: Thermal inertia of the heat exchanger (HEX)

Fig. A 2 shows the impact of HEX thermal conductivity and heat capacity on the COP of SCS. It can be seen that by increasing thermal conductivity, the COP increases to a certain point and then plateaus. The reason behind this is that by increasing thermal conductivity, the heat transfer in the S-HMX enhances, which increases both evaporator and desorption heat in Eq. (7), ultimately increasing the COP. This trend continues to the point where the heat exchanger heat transfer resistance becomes comparable to that of the sorbent and/or the HTF. Beyond this point, increasing HEX thermal conductivity does not increase COP noticeably because the heat transfer is limited elsewhere, namely the sorbent and/or the HTF. This point depends on the design and the materials of the S-

HMX, namely sorbent, HEX and HTF, and should be included in the material selection and the design process.

In addition, **Fig. A 2** shows that by reducing the HEX heat capacity while thermal conductivity is kept constant, the COP increases as HEX sensible heat in Eq. (7) decreases. Also, it can be observed that the upper limit of COP for the baseline case in **Table 9**, is 0.72 if the HEX heat capacity was set to zero.

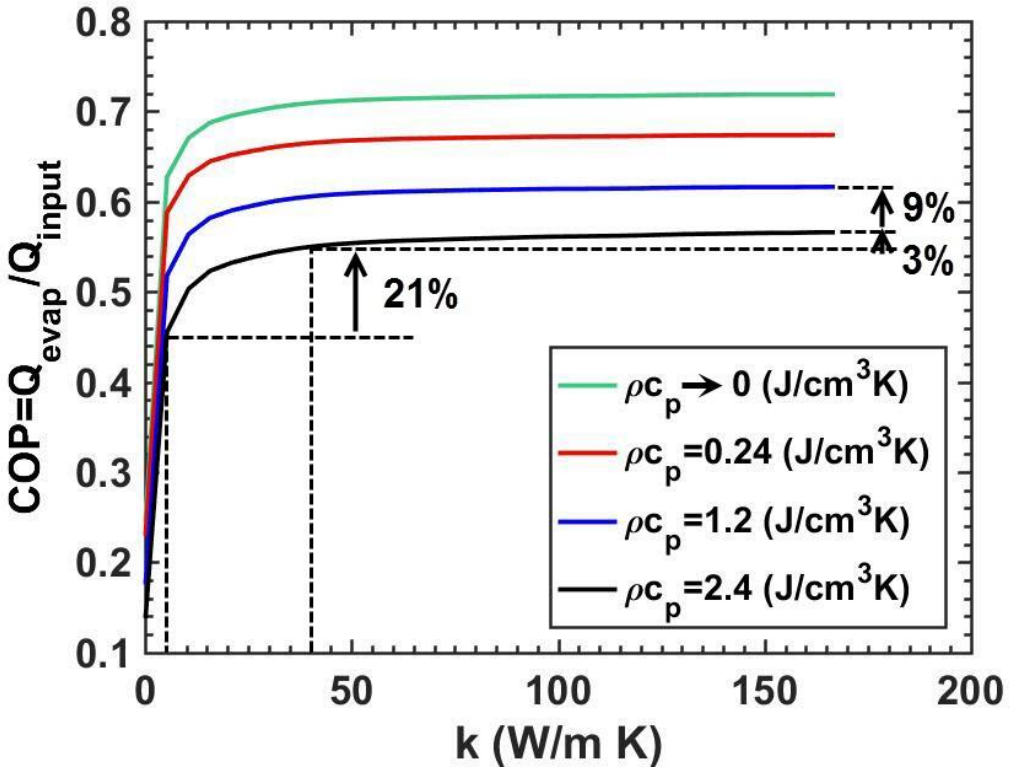

Fig. A 2. COP vs thermal conductivity and heat capacity of heat exchanger (HEX) for the baseline case of the S-HEX in **Table 9**

Fig. A 3 shows the SCP and COP of the S-HMX for a number of materials for the heat exchanger with a range of thermophysical properties listed in **Table A 1**. It can be observed in **Fig. A 3** (a) that by increasing thermal conductivity, SCP increases as the evaporative cooling power increases. It can be seen in **Fig. A 3** (b) that by increasing thermal diffusivity of the HEX material, the COP increases. It can be seen in **Fig. A 3** that the only exception is copper. Even though copper has a high thermal diffusivity, it yields a COP lower than materials such as aluminum 6061 with lower thermal diffusivity; this is due to copper's relatively high thermal inertia. It was shown in **Fig. A 2** that HEX thermal conductivity increases the COP to a point and then plateaus as the heat transfer of the S-HMX will be limited by the sorbent and/or HTF. In copper's case, its high thermal

conductivity is not needed; however, its high heat capacity results in a relatively lower COP. This is an important finding since it clearly shows that in material selection of HEX, both thermal conductivity and heat capacity should be taken into account, and thermal diffusivity alone should not be used.

Furthermore, it can be observed in **Table A 1** that conductive polymer and natural graphite sheets have anisotropic thermal conductivity. It was shown in section 3.7 that the heat transfer resistance of fins in the S-HMX in its in-plane direction is two orders of magnitude larger than that of its through-plane. Consequently, the effect of in-plane is more pronounced than its through-plane thermal conductivity. This can be seen in **Fig. A 3** that using natural graphite sheet, the highest COP can be achieved despite its low through-plane thermal conductivity thanks to its high in-plane thermal diffusivity. Overall, it can be seen that aluminum provides the highest SCP and relatively high COP. Graphite can generate slightly higher COP, 6%, but aluminum was selected as the S-HMX material in this study due to the manufacturability and durability of the sorbent coating on aluminum. Other than these thermo-physical properties, graphite is corrosion resistant, which is highly desirable when corrosive sorbents of $CaCl_2$ are used. Therefore, graphite is recommended as the S-HMX material for future work.

Table A 1. Thermophysical properties of various materials used for HEX

Material	k **(W/ m K)**	ρ **(kg/m^3)**	c_p **(J/kg K)**	α **(mm^2/s)**
Glass	1	8000	840	0.149
Paper	0.18	930	1340	0.144
Stainless steel	14.74	7902	471.9	3.953
Ceramic, alumina	18	3690	880	5.543
Conductive polymer*	k_x=15, k_y=3.5**	1760	1260	α_x=6.764, α_y=1.578
Copper	401.8	8936	383	117.400
Titanium	22.08	4501	518.1	9.468
Platinum	73.12	21454	132.5	25.722
Zink	121.3	7144	387.5	43.817
Al 6061	167	2700	896	69.031
Gold	317.7	19306	128.7	127.863
Silver	429.1	10504	234.3	174.354

Resin-impregnated graphite	k_x=300, k_y=5	1838	895	α_x=182.370, α_y=3.039
Natural graphite sheet	k_x=300, k_y=5	1550	748	α_x=258.754, α_y=4.312

* LNP KONDUIT COMPOUND OX11315, SABIC Innovative Plastics
** subscripts of x and y denote ‘in-plane’ and ‘through-plane’ directions, respectively.

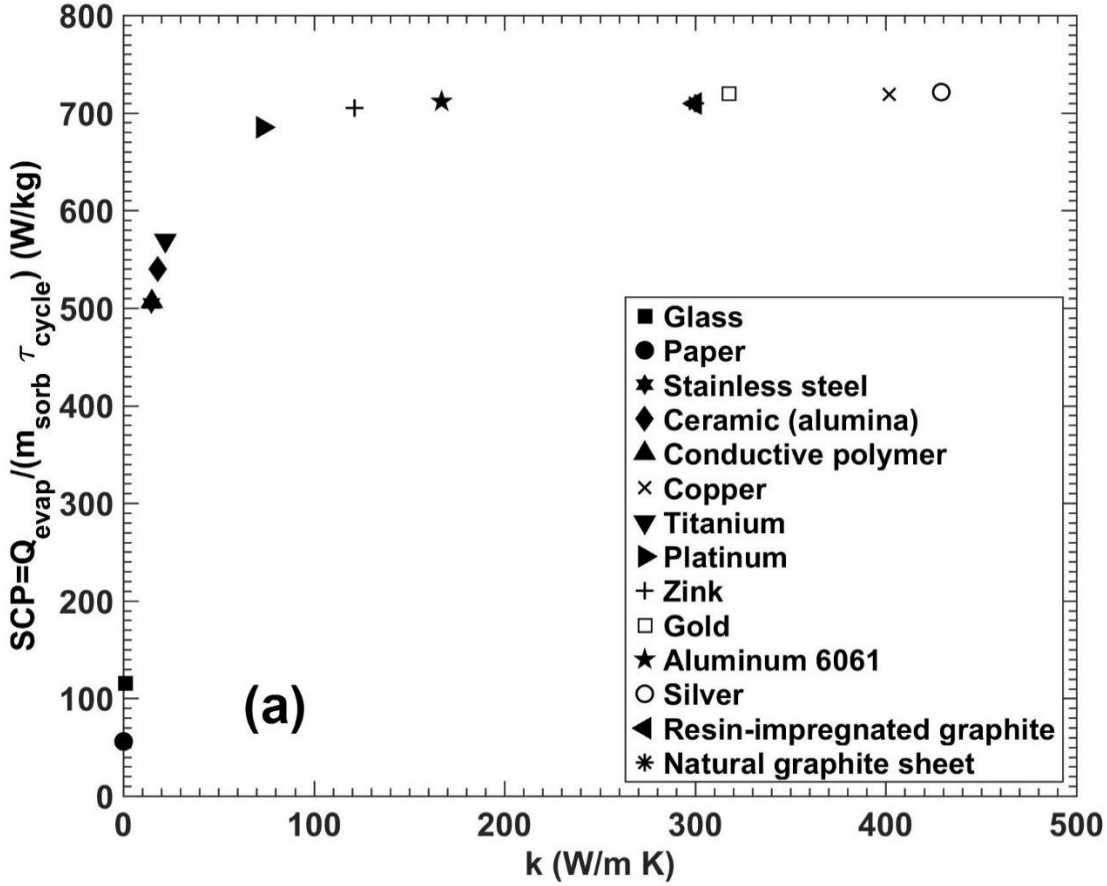

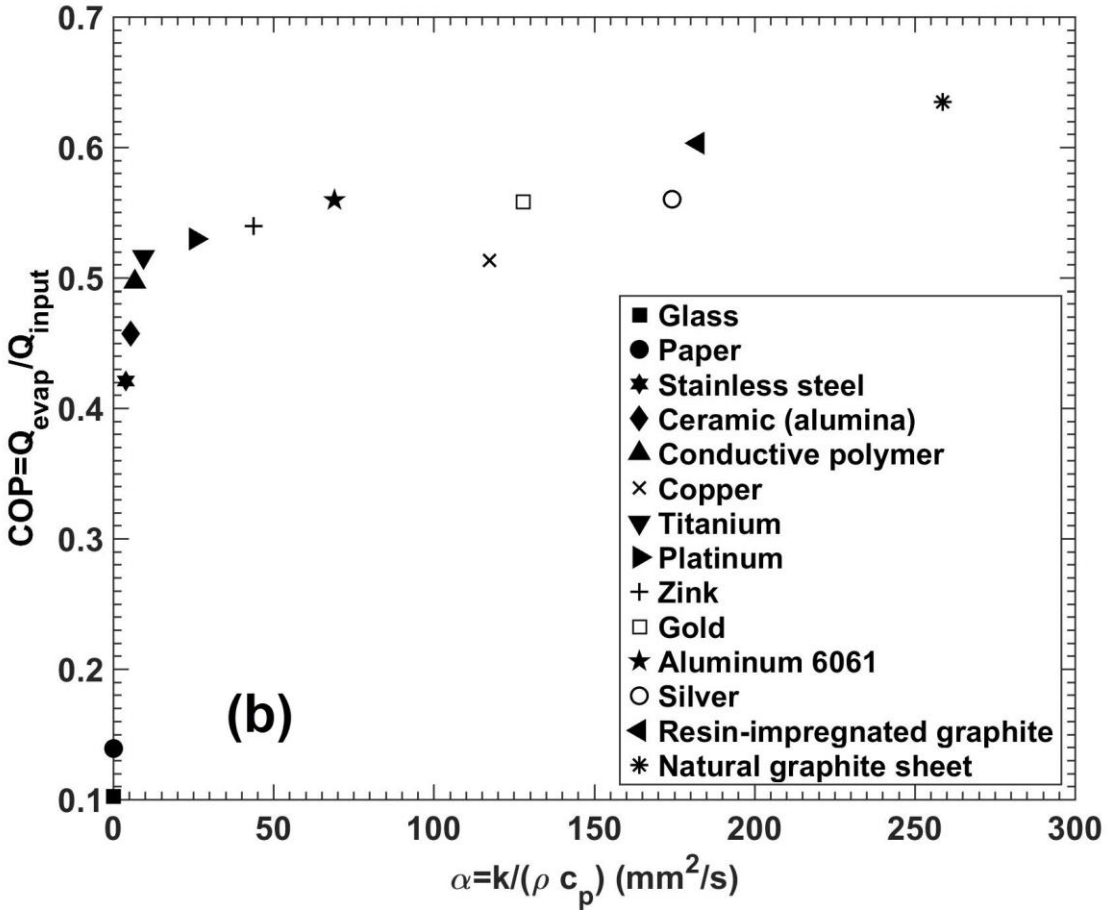

Fig. A 3. (a) SCP and (b) COP of the S-HMX; HEX made from various materials with different thermal diffusivities listed in Table A 1

A.2: Thermal inertia of the heat transfer fluid (HTF); heat recovery methods

Thermal inertia of the heat transfer fluid (HTF) can be eliminated fully using a heat recovery method. **Fig. A 4** presents a schematic of how heat recovery is performed. The low-grade heat source supplies heat to the S-HMX during the desorption process and the ambient cools the S-HMX during the sorption process. When switched between desorption and sorption process, the high-temperature HTF in the S-HMX that was desorbing, can be used to pre-heat the other S-HMX that is entering the desorption process. This way, the preheating is done without using the external heat source and leads to a higher COP.

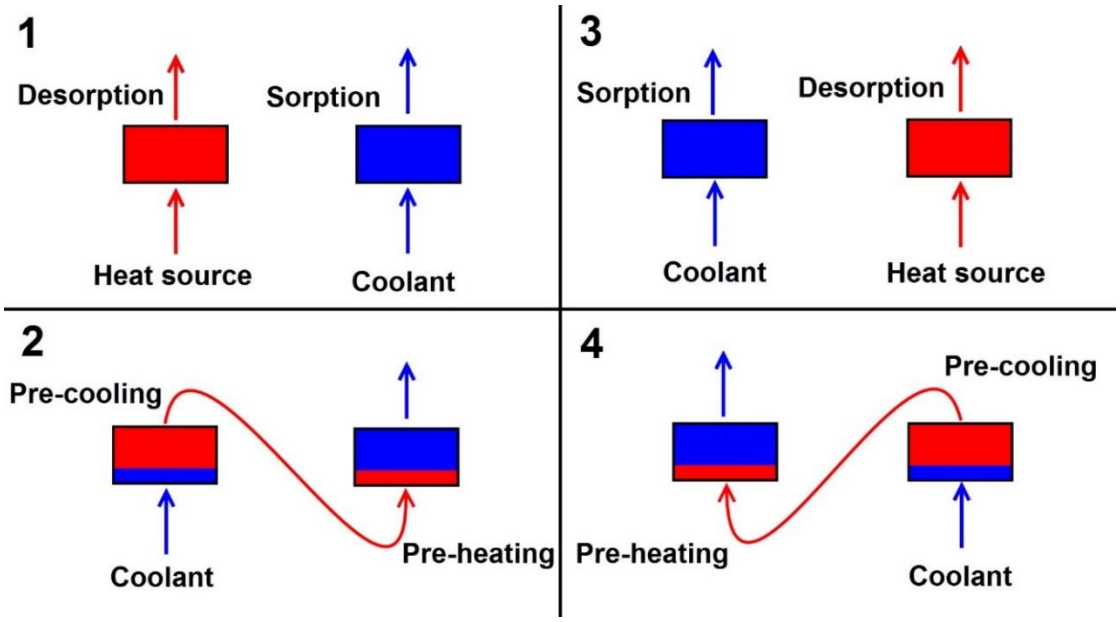

Fig. A 4. Schematic of heat recovery in the heat transfer fluid (HTF) circulation in sorption systems

There are three heat recovery methods in the literature: i) circular, ii) serial, and iii) passive [174]. **Fig. A 5** shows a schematic of these methods, respectively. Pan et al. [175] compared the methods and reported that the serial and passive methods provide higher performance than circular. Furthermore, it can be seen in **Fig. A 5** that passive heat recovery does not require additional pumping, valves or piping as opposed to circular and serial heat recovery methods, which reduces the total weight of the system and complexity. Hence, passive heat recovery method is preferred in our study to increase the COP.

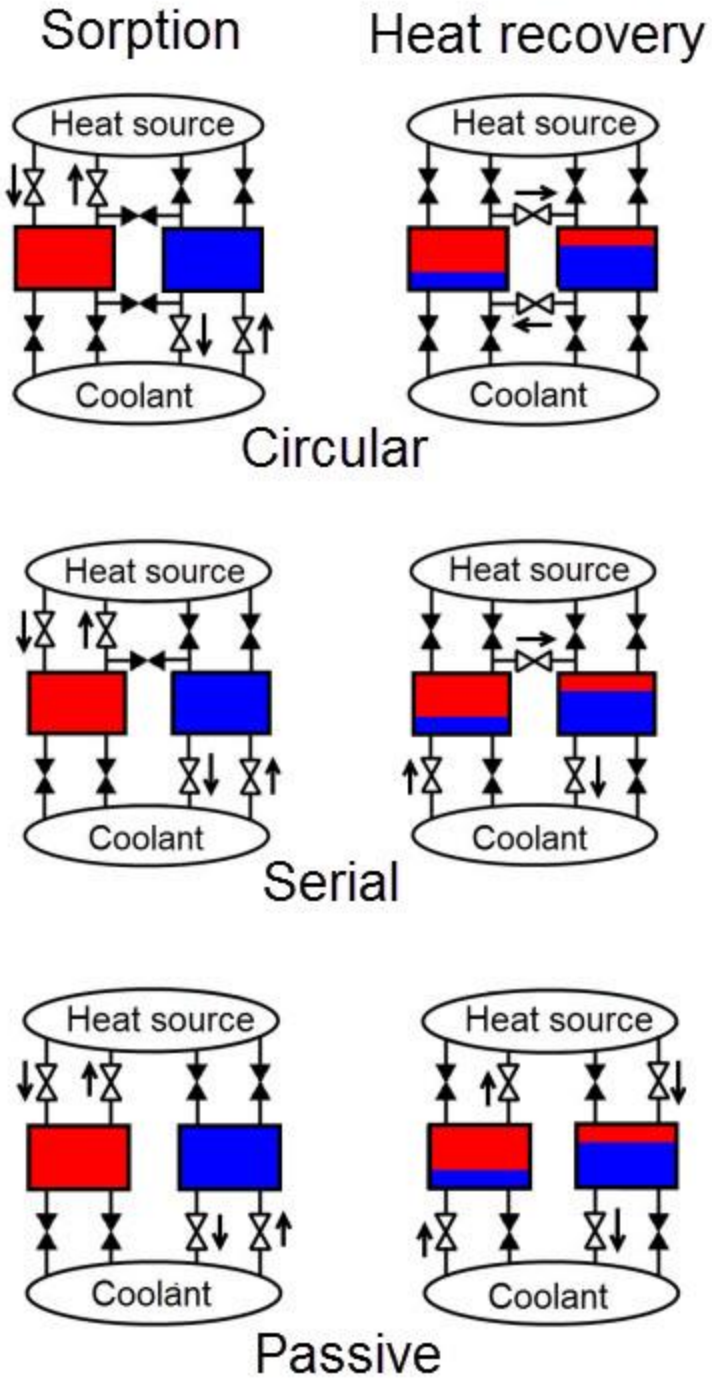

Fig. A 5. Schematic of different heat recovery methods, circular, serial and passive [20]

Passive heat recovery can be implemented using two four-way valves instead of eight two-way valves, which decreases complexity and facilitates the system control. One of the four-way valves is set to have a delay at the beginning of each process to push the high- and low-temperature HTF in the S-HMX and hoses back to high- and low-temperature

reservoirs of temperature control systems, TCS. **Fig. A 6** shows that in processes 1 and 3, one of the S-HMXs is desorbing while the other is ad/absorbing, whereas in processes 2 and 4, which occur during the time delay of the valves, pre-cooling and pre-heating, i.e. heat recovery, is performed. The time delay can be calculated based on the flow rate of the heat transfer fluid and the fluid volume in the S-HMXs and the hoses.

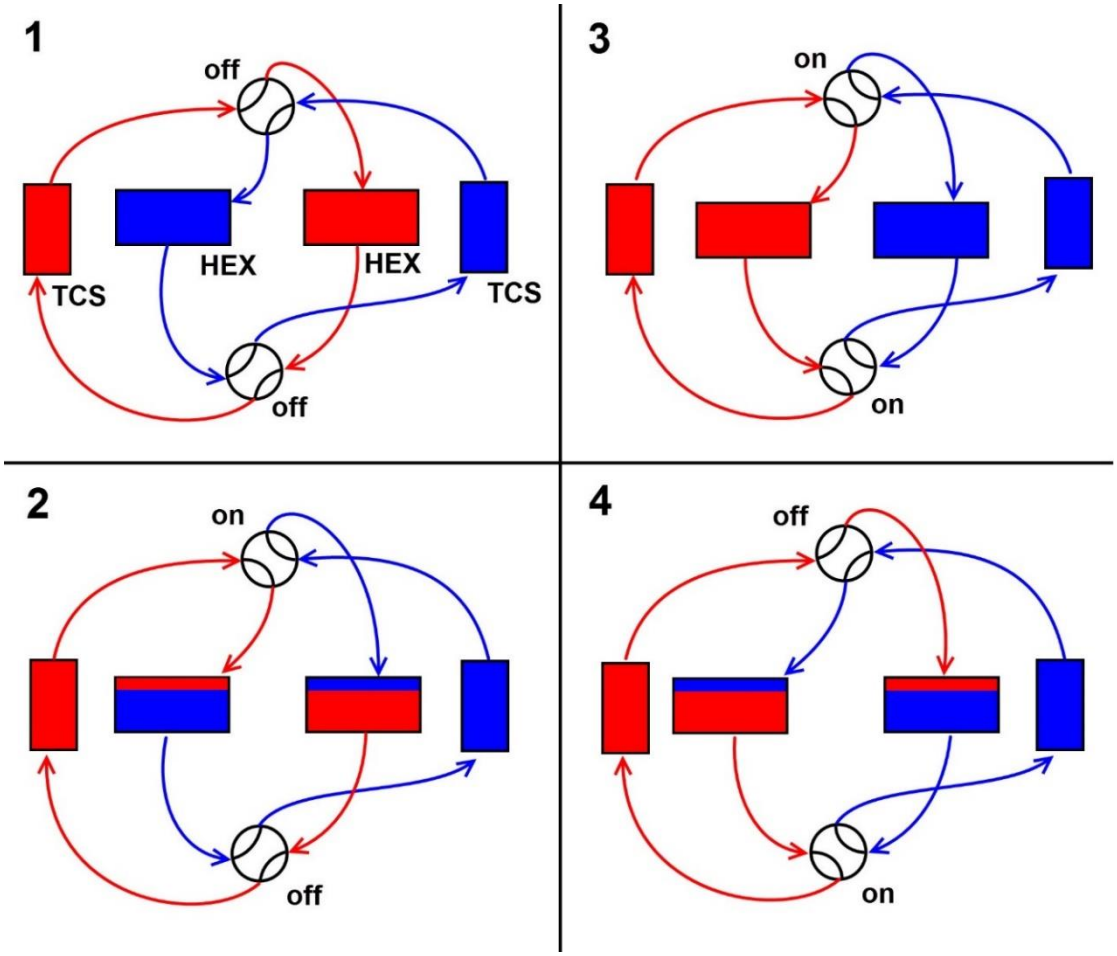

Fig. A 6. Schematic of passive heat recovery method performed with two four-way valves and a time delay

Fig. A 7 shows the share of desorption heat and sensible energy of each component of the P-HMX, i.e. heat exchanger (HEX), sorbent material, refrigerant inside the sorbent by eliminating the heat transfer fluid thermal inertia using the passive heat recovery method. The results are obtained from our 2-D analytical model validated by the experiments. It can be observed that COP increases from 0.491 to 0.598 by removing the heat transfer fluid thermal inertia.

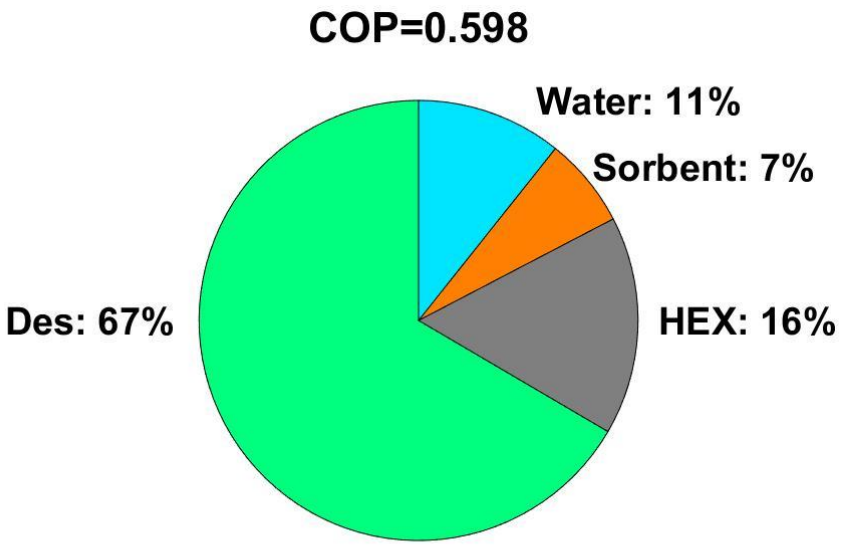

Fig. A 7. Share of desorption heat and the sensible energy of the heat exchanger (HEX), sorbent material, water inside the sorbent by eliminating the heat transfer fluid thermal inertia using the passive heat recovery method

Appendix B: Uncertainty analysis

B.1: Uncertainty analysis of the measurements in chapter 2

The uncertainty in SCP calculation is obtained based on the method proposed by Moffat [176] as follows.

$$\frac{\delta SCP}{SCP} = \frac{\delta \Delta\omega}{\Delta\omega} = \frac{\sqrt{2}\delta\omega}{\Delta\omega} \tag{B.1}$$

$$\omega = \frac{m_{sorbate}}{m_{sorbent}} \tag{B.2}$$

$$\frac{\delta\omega}{\omega} = \sqrt{\left(\frac{\delta m_{sorbate}}{m_{sorbate}}\right)^2 + \left(\frac{\delta m_{sorbent}}{m_{sorbent}}\right)^2} \cong \left(\frac{\delta m_{sorbate}}{m_{sorbate}}\right) = \frac{0.01g}{m_{sorbate}} \tag{B.3}$$

Sorbent mass was measured using an analytical balance (OHAUS AX124) with the accuracy of 0.0001 g, whereas the sorbate mass change was measured by precision balance (ML4002E, Mettler Toledo) with the accuracy of 0.01 g. Therefore, the sorbent mass uncertainty was negligible compared to that of sorbate.

Finally, the uncertainty in SCP calculation is obtained using Eq. (B.5). Substituting the sorbent mass and differential sorbate uptake in Eq. (B.5), the SCP uncertainty is estimated to be between 0.24–3.83% for different samples and cycle times.

$$\delta\omega = \frac{0.01g}{m_{sorbent}} \tag{B.4}$$

$$\frac{\delta SCP}{SCP} = \frac{0.01\sqrt{2}}{m_{sorbent}\,\Delta\omega} \tag{B.5}$$

B.2: Uncertainty analysis of the measurements in chapter 1

The uncertainty in the calculation of evaporative cooling energy and desorption energy is obtained based on the method proposed by Moffat [176] as follows.

$$\left(\frac{\delta Q_{evap}}{Q_{evap}}\right)^2 = \left(\frac{\delta \dot{m}}{\dot{m}}\right)^2 + \left(\frac{\delta\Delta T}{\Delta T}\right)^2 + \left(\frac{\delta\Delta t}{\Delta t}\right)^2 = 0.005^2 + \left(\frac{0.15\sqrt{2}}{2}\right)^2 + \left(\frac{\sqrt{2}}{1200}\right)^2 = 0.01125 \tag{B.6}$$

$$\left(\frac{\delta Q_{des}}{Q_{des}}\right)^2 = \left(\frac{\delta \dot{m}}{\dot{m}}\right)^2 + \left(\frac{\delta\Delta T}{\Delta T}\right)^2 + \left(\frac{\delta\Delta t}{\Delta t}\right)^2 = 0.005^2 + \left(\frac{0.15\sqrt{2}}{3.2}\right)^2 + \left(\frac{\sqrt{2}}{1200}\right)^2 = 0.00439 \tag{B.7}$$

Specific cooling power (SCP) is defined as the ratio of evaporative cooling energy to the product of cycle time and dry sorbent mass, Eq. (B.8). Coefficient of performance (COP) is defined as the ratio of evaporative cooling energy to the desorption energy, Eq. (B.9).

$$SCP = \frac{Q_{evap}}{m_{sorb}\tau_{cycle}} \tag{B.8}$$

$$COP = \frac{Q_{evap}}{Q_{des}} \tag{B.9}$$

The uncertainty in SCP and COP calculation is as follows.

$$\frac{\delta SCP}{SCP} = \sqrt{\left(\frac{\delta Q}{Q}\right)^2 + \left(\frac{\delta m}{m}\right)^2 + \left(\frac{\delta \tau}{\tau}\right)^2} = \sqrt{0.01125 + \left(\frac{1}{600}\right)^2 + \left(\frac{1}{1200}\right)^2} = 0.106 \tag{B.10}$$

$$\frac{\delta COP}{COP} = \sqrt{\left(\frac{\delta Q_{evap}}{Q_{evap}}\right)^2 + \left(\frac{\delta Q_{des}}{Q_{des}}\right)^2} = \sqrt{0.01125 + 0.00439} = 0.125 \tag{B.11}$$

Appendix C: Gravimetric large pressure jump (G-LPJ) data

Table C1 shows the water uptake measured by G-LPJ test bed for composite sorbents containing 0–20 wt.% graphite flake, see **Table 6** for more information. The data was measured every second in G-LPJ, but shown every 2 minutes in Table C1 to reduce the number of data points. The full data points are shown in **Fig. 31** (a) in section 1.

Table C1. Uptake measurements from G-LPJ test bed for composite sorbents containing ϕ=0–20 wt.% graphite flake, see **Table 6**

***t* (s)**	***t* (min)**	***ω* (g H_2O / g sorbent)**				
		***ϕ*=0wt.%**	***ϕ*=5wt.%**	***ϕ*=10wt.%**	***ϕ*=15wt.%**	***ϕ*=20wt.%**
1	0.01667	-0.00006	0.00004	0.00017	0.00087	0.00003
120	2	0.01708	0.01936	0.02235	0.03199	0.03489
240	4	0.03398	0.03973	0.04673	0.05634	0.06189
360	6	0.05144	0.05973	0.06762	0.07735	0.08211
480	8	0.06888	0.07624	0.08561	0.09567	0.09981
600	10	0.08367	0.09079	0.09976	0.10674	0.11316
720	12	0.09618	0.10172	0.11115	0.11847	0.12364
840	14	0.10763	0.11148	0.12135	0.12802	0.13271
960	16	0.11681	0.12074	0.12953	0.13689	0.14149
1080	18	0.12540	0.12849	0.13910	0.14532	0.14600
1200	20	0.13322	0.13550	0.14806	0.15357	0.15264
1320	22	0.13975	0.14426	0.15480	0.16027	0.15708
1440	24	0.14589	0.15012	0.16019	0.16516	0.16288
1560	26	0.15031	0.15606	0.16490	0.16968	0.16405
1680	28	0.15584	0.16077	0.17090	0.17236	0.16652
1800	30	0.16318	0.16712	0.17531	0.17340	0.16806
1920	32	0.16908	0.17050	0.17929	0.17743	0.17054
2040	34	0.17539	0.17326	0.18464	0.17971	0.17185
2160	36	0.17965	0.17833	0.19013	0.18133	0.17301
2280	38	0.18391	0.18241	0.19211	0.18384	0.17356
2400	40	0.18909	0.18559	0.19421	0.18804	0.17524
2520	42	0.19199	0.18867	0.19464	0.18789	0.17499
2640	44	0.19491	0.19312	0.19775	0.18727	0.17504
2760	46	0.19756	0.19532	0.20015	0.18712	0.17615
2880	48	0.19899	0.19909	0.19986	0.18750	0.17478
3000	50	0.19950	0.20080	0.20117	0.18760	0.17421
3120	52	0.20107	0.20369	0.20163	0.18712	0.17483
3240	54	0.20483	0.20568	0.20320	0.18504	0.17554
3360	56	0.20670	0.20682	0.20212	0.18539	0.17638

3480	58	0.20960	0.20922	0.20198	0.18513	0.17713
3600	60	0.21291	0.20979	0.20420	0.18380	0.17980
3720	62	0.21520	0.21169	0.20348	0.18516	0.17824
3840	64	0.21597	0.21236	0.20464	0.18780	0.17884
3960	66	0.21802	0.21218	0.20467	0.18678	0.17910
4080	68	0.22020	0.21180	0.20584	0.18694	0.17920
4200	70	0.22075	0.21133	0.20466	0.18678	0.17917
4320	72	0.22104	0.21095	0.20220	0.18897	0.17882
4440	74	0.22352	0.21006	0.20198	0.18819	0.17935
4560	76	0.22576	0.21037	0.20373	0.18814	0.18053
4680	78	0.22440	0.21184	0.20295	0.18884	0.18238
4800	80	0.22499	0.21126	0.20294	0.18915	0.18231
4920	82	0.22421	0.21222	0.20196	0.18953	0.18121
5040	84	0.22502	0.21535	0.20321	0.18879	0.18005
5160	86	0.22537	0.21485	0.20150	0.18925	0.18108
5280	88	0.22455	0.21391	0.20097	0.19044	0.18286
5400	90	0.22411	0.21571	0.20168	0.19179	0.18253
5520	92	0.22432	0.21689	0.20113	0.19234	0.18297
5640	94	0.22410	0.21577	0.20251	0.19124	0.18124
5760	96	0.22489	0.21548	0.20274	0.18980	0.18097
5880	98	0.22499	0.21447	0.20387	0.18993	0.18017
6000	100	0.22669	0.21589	0.20362	0.19000	0.17959
6120	102	0.22756	0.21585	0.20260	0.18972	0.17894
6240	104	0.22660	0.21585	0.20308	0.19141	0.18041
6360	106	0.22757	0.21564	0.20174	0.19132	0.18055
6480	108	0.22802	0.21375	0.20150	0.19086	0.18015
6600	110	0.22895	0.21386	0.20115	0.18916	0.18056
6720	112	0.22832	0.21299	0.20037	0.19112	0.18210
6840	114	0.22648	0.21352	0.20105	0.19269	0.18232
6960	116	0.22809	0.21181	0.20240	0.19112	0.18337

Appendix D: Optimized sorber bed heat and mass exchangers data

Table D1–Table D11 show the time variation of HTF temperature inlet and outlet, pressure and HTF flow rate of P-HMX, the F-HMX, evaporator, and condenser, and the average temperatures of the fin and the sorbent in the F-HMX for different operating conditions. These experimental results were obtained from the two-sorber bed sorption test bed for plate-fin (P-HMX) and finned-tube (F-HMX) sorber bed heat and mass exchangers. It should be noted that data was collected every second from the test bed, but is shown every minute in Table D1–Table D11 to reduce the number of data points.

Table D1. Time variation of HTF temperature inlet and outlet, pressure and HTF flow rate of P-HMX, the F-HMX, evaporator, and condenser, and the average temperatures of the fin and the sorbent in the F-HMX for T_{des}=90ºC, T_{sorp}= T_{cond}=30ºC, T_{evap}=15ºC, τ_{cycle}=10min

t (s)	$T_{in,\ the\ P\text{-}HMX}$ (ºC)	$T_{out,\ the\ P\text{-}HMX}$ (ºC)	$p_{P\text{-}HMX}$ (kPa)	p_{cond} (kPa)	$p_{F\text{-}HMX}$ (kPa)	p_{evap} (kPa)	$\dot{V}_{evap}$ (lpm)	$\dot{V}_{cold}$ (lpm)	$\dot{V}_{hot}$ (lpm)	$T_{in,\ the\ F\text{-}HMX}$ (ºC)	$T_{out,\ the\ F\text{-}HMX}$ (ºC)	$T_{in,\ evap}$ (ºC)	$T_{out,\ evap}$ (ºC)	T_{fin} (ºC)	T_{sorb} (ºC)
1	72.2	89.3	5.1	5.0	1.2	1.3	14.9	15.3	3.7	51.5	30.6	15.1	14.6	30.2	31.5
60	33.1	34.3	1.1	4.1	4.1	1.3	14.9	14.0	4.2	88.0	83.5	15.1	13.8	84.3	67.7
120	31.7	32.5	1.1	4.2	4.7	1.2	14.9	14.0	4.2	89.2	86.9	15.0	13.6	86.3	73.5
180	30.6	31.2	1.2	4.3	4.8	1.3	14.9	14.0	4.2	89.8	88.0	15.0	13.8	87.9	77.9
240	30.0	30.4	1.2	4.3	4.8	1.3	14.9	14.0	4.2	89.8	88.5	15.1	14.0	88.9	81.1
300	33.4	30.1	1.2	4.3	4.7	1.3	14.9	14.0	4.2	83.6	88.5	15.1	14.2	89.2	83.5
360	85.6	83.4	5.4	4.8	1.4	1.4	14.9	4.2	11.4	31.2	35.8	15.2	15.1	32.6	43.7
420	88.3	86.7	5.7	5.0	1.3	1.3	14.9	4.2	11.5	30.5	32.1	15.3	14.7	31.6	38.6
480	89.8	88.6	5.6	5.0	1.3	1.3	14.9	4.2	11.5	30.0	31.2	15.2	14.6	30.5	35.8
540	90.2	89.3	5.4	5.0	1.3	1.3	14.9	4.2	11.4	29.8	30.7	15.2	14.5	29.7	33.6
600	90.0	89.3	5.1	5.0	1.3	1.3	14.9	4.2	11.4	29.8	30.6	15.2	14.6	29.2	31.8

Table D2. Time variation of HTF temperature inlet and outlet, pressure and HTF flow rate of P-HMX, the F-HMX, evaporator, and condenser, and the average temperatures of the fin and the sorbent in the F-HMX for T_{des}=90ºC, T_{sorp}= T_{cond}=30ºC, T_{evap}=15ºC, τ_{cycle}=15min

t (s)	$T_{in,\ the\ P\text{-}HMX}$ (ºC)	$T_{out,\ the\ P\text{-}HMX}$ (ºC)	$p_{P\text{-}HMX}$ (kPa)	p_{cond} (kPa)	$p_{F\text{-}HMX}$ (kPa)	p_{evap} (kPa)	$\dot{V}_{evap}$ (lpm)	$\dot{V}_{cold}$ (lpm)	$\dot{V}_{hot}$ (lpm)	$T_{in,\ the\ F\text{-}HMX}$ (ºC)	$T_{out,\ the\ F\text{-}HMX}$ (ºC)	$T_{in,\ evap}$ (ºC)	$T_{out,\ evap}$ (ºC)	T_{fin} (ºC)	T_{sorb} (ºC)
1	89.2	88.7	4.8	4.7	1.4	1.4	14.9	15.3	3.7	30.0	30.7	15.4	14.9	31.8	31.5
60	33.4	34.7	1.1	4.7	4.7	1.3	14.8	14.1	4.2	87.3	81.9	15.4	14.3	83.1	67.7
120	32.1	32.9	1.1	5.0	5.2	1.3	14.8	14.0	4.2	88.8	86.3	15.3	14.0	85.6	73.5
180	30.9	31.5	1.2	5.3	5.5	1.3	14.9	14.0	4.2	89.7	87.8	15.3	14.1	87.6	77.9
240	30.1	30.6	1.2	5.6	5.8	1.3	14.9	14.0	4.2	89.9	88.4	15.4	14.2	88.8	81.1
300	29.9	30.2	1.2	5.8	5.9	1.3	14.9	14.0	4.2	89.8	88.6	15.4	14.4	89.3	83.5
360	29.8	30.0	1.3	5.9	6.1	1.3	14.9	14.0	4.2	89.5	88.5	15.5	14.6	89.3	85.3
420	29.8	30.0	1.3	5.9	6.0	1.3	14.9	14.0	4.2	89.3	88.4	15.5	14.7	89.2	86.7
480	85.1	80.0	5.0	4.2	3.9	1.4	14.8	4.2	11.4	31.0	49.6	15.5	15.1	35.8	51.9
540	86.6	84.6	5.7	4.7	1.4	1.4	14.8	4.2	11.5	31.2	33.8	15.5	15.2	35.1	44.3
600	88.9	87.4	5.8	4.8	1.4	1.4	14.9	4.2	11.5	30.5	31.9	15.5	15.0	33.9	40.9
660	90.1	88.9	5.6	4.8	1.4	1.4	14.8	4.2	11.5	30.0	31.2	15.4	14.9	32.7	38.4
720	90.3	89.3	5.3	4.8	1.4	1.4	14.9	4.2	11.5	29.9	30.8	15.4	14.9	32.0	36.5
780	89.9	89.2	5.0	4.8	1.4	1.4	14.8	4.2	11.5	29.9	30.7	15.4	14.9	31.5	34.7
840	89.5	88.9	4.9	4.7	1.4	1.4	14.9	4.2	11.5	30.0	30.6	15.4	14.9	31.3	33.3
900	89.2	88.7	4.8	4.7	1.4	1.4	14.9	4.2	11.5	30.0	30.7	15.4	14.9	31.0	32.2

Table D3. Time variation of HTF temperature inlet and outlet, pressure and HTF flow rate of P-HMX, the F-HMX, evaporator, and condenser, and the average temperatures of the fin and the sorbent in the F-HMX for T_{des}=90ºC, T_{sorp}= T_{cond}=30ºC, T_{evap}=15ºC, τ_{cycle}=20min

t (s)	$T_{in,\ the\ P\text{-}HMX}$ (ºC)	$T_{out,\ the\ P\text{-}HMX}$ (ºC)	$p_{P\text{-}HMX}$ (kPa)	p_{cond} (kPa)	$p_{F\text{-}HMX}$ (kPa)	p_{evap} (kPa)	$\dot{V}_{evap}$ (lpm)	$\dot{V}_{cold}$ (lpm)	$\dot{V}_{hot}$ (lpm)	$T_{in,\ the\ F\text{-}HMX}$ (ºC)	$T_{out,\ the\ F\text{-}HMX}$ (ºC)	$T_{in,\ evap}$ (ºC)	$T_{out,\ evap}$ (ºC)	T_{fin} (ºC)	T_{sorb} (ºC)
1	89.2	88.8	5.2	5.3	1.2	1.2	14.9	15.3	3.7	30.0	30.6	15.4	15.0	31.7	31.5
60	33.4	34.8	0.8	5.3	4.8	1.1	14.8	14.1	4.2	87.0	80.2	15.5	14.7	82.8	67.7
120	32.8	33.5	0.8	5.4	5.4	1.1	14.9	14.0	4.2	88.0	85.6	15.3	14.3	84.7	73.5
180	31.8	32.3	0.9	5.7	5.7	1.1	14.9	14.0	4.2	89.1	87.3	15.3	14.2	86.4	77.9
240	30.9	31.4	0.9	6.0	6.0	1.1	14.9	14.0	4.2	89.7	88.2	15.3	14.3	87.8	81.1
300	30.3	30.6	1.0	6.2	6.2	1.1	14.9	14.0	4.2	89.9	88.7	15.4	14.4	88.7	83.5
360	30.0	30.3	1.0	6.3	6.4	1.1	14.9	14.0	4.2	89.9	88.9	15.4	14.5	89.2	85.3
420	29.9	30.1	1.0	6.4	6.6	1.1	14.9	14.0	4.2	89.7	88.9	15.4	14.7	89.3	86.7
480	29.8	30.0	1.0	6.5	6.6	1.1	14.9	14.0	4.2	89.5	88.7	15.5	14.8	89.3	87.7
540	29.8	30.0	1.0	6.5	6.6	1.1	14.8	14.0	4.2	89.4	88.6	15.5	14.8	89.2	88.3
600	29.9	30.0	1.0	6.5	6.6	1.1	14.9	12.7	5.1	89.2	88.5	15.5	14.9	89.0	88.4
660	84.5	82.2	6.0	4.9	2.5	1.2	14.8	4.2	11.5	31.4	38.8	15.5	15.2	35.6	48.6
720	86.6	85.1	6.3	5.3	1.2	1.2	14.8	4.2	11.5	31.2	33.3	15.5	15.3	34.8	43.4
780	88.5	87.3	6.4	5.4	1.2	1.2	14.8	4.2	11.5	30.6	31.9	15.5	15.1	33.9	40.7
840	89.7	88.7	6.3	5.4	1.1	1.2	14.9	4.2	11.5	30.2	31.2	15.4	15.0	33.0	38.5
900	90.2	89.4	6.1	5.4	1.1	1.2	14.8	4.2	11.5	30.0	30.8	15.4	15.0	32.3	36.6
960	90.3	89.6	5.8	5.4	1.2	1.2	14.9	4.2	11.5	29.9	30.6	15.4	15.0	31.8	35.1
1020	90.0	89.5	5.6	5.4	1.2	1.2	14.9	4.2	11.5	29.9	30.5	15.4	15.0	31.5	33.8
1080	89.7	89.3	5.4	5.4	1.2	1.2	14.9	4.2	11.5	29.9	30.5	15.5	15.0	31.3	32.8
1140	89.4	89.0	5.3	5.3	1.2	1.2	14.9	4.2	11.5	30.0	30.5	15.5	15.0	31.1	32.0
1200	89.2	88.8	5.3	5.3	1.2	1.2	14.9	4.2	11.5	30.0	30.6	15.4	15.0	31.0	31.5

Table D4. Time variation of HTF temperature inlet and outlet, pressure and HTF flow rate of P-HMX, the F-HMX, evaporator, and condenser, and the average temperatures of the fin and the sorbent in the F-HMX for T_{des}=80ºC, T_{sorp}= T_{cond}=30ºC, T_{evap}=15ºC, τ_{cycle}=10min

t (s)	$T_{in,}$ the P-HMX (ºC)	$T_{out,}$ the P-HMX (ºC)	p_{P-HMX} (kPa)	p_{cond} (kPa)	p_{F-HMX} (kPa)	p_{evap} (kPa)	$\dot{V}_{evap}$ (lpm)	$\dot{V}_{cold}$ (lpm)	$\dot{V}_{hot}$ (lpm)	$T_{in,}$ the F-HMX (ºC)	$T_{out,}$ the F-HMX (ºC)	$T_{in,}$ evap (ºC)	$T_{out,}$ evap (ºC)	T_{fin} (ºC)	T_{sorb} (ºC)
1	65.2	79.5	4.7	4.8	1.4	1.5	14.9	15.3	3.7	47.9	30.5	15.1	14.7	30.2	31.5
60	32.5	33.6	1.3	4.1	3.9	1.4	14.9	14.0	4.2	78.4	74.6	15.1	14.0	75.2	60.7
120	31.4	32.1	1.3	4.2	4.5	1.4	14.9	14.0	4.2	79.4	77.5	15.0	13.8	76.9	65.5
180	30.5	31.0	1.3	4.3	4.6	1.4	14.9	14.0	4.2	79.8	78.4	15.0	13.9	78.2	69.0
240	30.0	30.3	1.3	4.3	4.6	1.4	14.9	14.0	4.2	79.9	78.8	15.1	14.1	79.0	71.6
300	32.8	30.1	1.3	4.3	4.5	1.4	14.9	14.0	4.2	74.7	78.8	15.1	14.3	79.3	73.5
360	76.4	74.6	5.0	4.6	1.6	1.5	14.9	4.2	11.4	31.0	34.8	15.2	15.1	32.1	41.4
420	78.7	77.3	5.2	4.8	1.4	1.5	14.9	4.2	11.5	30.4	31.7	15.3	14.7	31.3	37.2
480	79.9	78.8	5.1	4.8	1.4	1.4	14.9	4.2	11.5	30.0	31.0	15.2	14.6	30.4	35.0
540	80.2	79.4	4.9	4.8	1.4	1.4	14.9	4.2	11.4	29.8	30.6	15.2	14.6	29.7	33.2
600	80.0	79.4	4.7	4.7	1.4	1.5	14.9	4.2	11.4	29.8	30.5	15.2	14.7	29.3	31.7

Table D5. Time variation of HTF temperature inlet and outlet, pressure and HTF flow rate of P-HMX, the F-HMX, evaporator, and condenser, and the average temperatures of the fin and the sorbent in the F-HMX for T_{des}=70ºC, T_{sorp}= T_{cond}=30ºC, T_{evap}=15ºC, τ_{cycle}=10min

t (s)	$T_{in,}$ the P-HMX (ºC)	$T_{out,}$ the P-HMX (ºC)	p_{P-HMX} (kPa)	p_{cond} (kPa)	p_{F-HMX} (kPa)	p_{evap} (kPa)	$\dot{V}_{evap}$ (lpm)	$\dot{V}_{cold}$ (lpm)	$\dot{V}_{hot}$ (lpm)	$T_{in,}$ the F-HMX (ºC)	$T_{out,}$ the F-HMX (ºC)	$T_{in,}$ evap (ºC)	$T_{out,}$ evap (ºC)	T_{fin} (ºC)	T_{sorb} (ºC)
1	58.2	69.6	4.4	4.6	1.5	1.6	14.9	15.3	3.7	44.3	30.4	15.1	14.8	30.1	31.5
60	32.0	32.8	1.4	4.1	3.8	1.5	14.9	14.0	4.2	68.8	65.7	15.1	14.3	66.1	53.8
120	31.1	31.6	1.4	4.1	4.3	1.5	14.9	14.0	4.2	69.5	68.0	15.0	14.1	67.4	57.4
180	30.4	30.7	1.4	4.2	4.5	1.5	14.9	14.0	4.2	69.9	68.8	15.0	14.2	68.5	60.1
240	30.0	30.2	1.4	4.2	4.5	1.5	14.9	14.0	4.2	70.0	69.0	15.1	14.4	69.1	62.1
300	32.2	30.0	1.4	4.2	4.4	1.5	14.9	14.0	4.2	65.8	69.1	15.1	14.5	69.4	63.5
360	67.1	65.7	4.6	4.4	1.7	1.6	14.9	4.2	11.4	30.7	33.8	15.2	15.1	31.7	39.0
420	69.0	67.8	4.8	4.6	1.5	1.5	14.9	4.2	11.5	30.3	31.4	15.3	14.8	31.0	35.8
480	70.0	69.1	4.8	4.6	1.5	1.5	14.9	4.2	11.5	29.9	30.7	15.2	14.7	30.3	34.2
540	70.2	69.6	4.6	4.6	1.5	1.5	14.9	4.2	11.4	29.8	30.4	15.2	14.7	29.7	32.8
600	70.1	69.6	4.5	4.5	1.5	1.5	14.9	4.2	11.4	29.8	30.3	15.2	14.8	29.4	31.7

Table D6. Time variation of HTF temperature inlet and outlet, pressure and HTF flow rate of P-HMX, the F-HMX, evaporator, and condenser, and the average temperatures of the fin and the sorbent in the F-HMX for T_{des}=60ºC, T_{sorp}= T_{cond}=30ºC, T_{evap}=15ºC, τ_{cycle}=10min

t (s)	$T_{in,}$ the P-HMX (ºC)	$T_{out,}$ the P-HMX (ºC)	p_{P-HMX} (kPa)	p_{cond} (kPa)	p_{F-HMX} (kPa)	p_{evap} (kPa)	$\dot{V}_{evap}$ (lpm)	$\dot{V}_{cold}$ (lpm)	$\dot{V}_{hot}$ (lpm)	$T_{in,}$ the F-HMX (ºC)	$T_{out,}$ the F-HMX (ºC)	$T_{in,}$ evap (ºC)	$T_{out,}$ evap (ºC)	T_{fin} (ºC)	T_{sorb} (ºC)
1	51.2	58.0	4.2	4.4	1.6	1.6	14.9	15.3	3.7	40.7	30.9	15.1	14.9	30.4	31.5
60	31.5	32.0	1.5	4.1	3.8	1.5	14.9	14.0	4.2	59.1	57.0	15.1	14.7	57.0	46.8
120	30.8	31.1	1.5	4.1	4.2	1.5	14.9	14.0	4.2	59.7	58.6	15.0	14.6	58.0	49.3
180	30.2	30.5	1.5	4.2	4.4	1.5	14.9	14.0	4.2	60.0	59.2	15.0	14.7	58.8	51.2
240	29.9	30.1	1.5	4.2	4.4	1.6	14.9	14.0	4.2	60.0	59.4	15.1	14.7	59.3	52.5
300	31.6	30.3	1.5	4.2	4.3	1.6	14.9	14.0	4.2	56.9	59.2	15.1	14.8	59.4	53.5
360	57.9	57.0	4.4	4.3	1.7	1.7	14.9	4.2	11.4	30.5	32.7	15.2	15.1	31.2	36.7
420	59.3	58.6	4.6	4.4	1.6	1.6	14.9	4.2	11.5	30.2	30.9	15.3	15.0	30.7	34.5
480	60.0	59.5	4.6	4.4	1.6	1.6	14.9	4.2	11.5	29.9	30.5	15.2	15.0	30.1	33.3
540	60.2	59.8	4.4	4.4	1.6	1.6	14.9	4.2	11.4	29.8	30.3	15.2	14.9	29.8	32.4
600	60.1	59.8	4.4	4.4	1.6	1.6	14.9	4.2	11.4	29.8	30.2	15.2	14.9	29.5	31.6

Table D7. Time variation of HTF temperature inlet and outlet, pressure and HTF flow rate of P-HMX, the F-HMX, evaporator, and condenser, and the average temperatures of the fin and the sorbent in the F-HMX for T_{des}=90ºC, T_{sorp}= T_{cond}=20ºC, T_{evap}=15ºC, τ_{cycle}=10min

t (s)	$T_{in,}$ the P-HMX (ºC)	$T_{out,}$ the P-HMX (ºC)	p_{P-HMX} (kPa)	p_{cond} (kPa)	p_{F-HMX} (kPa)	p_{evap} (kPa)	$\dot{V}_{evap}$ (lpm)	$\dot{V}_{cold}$ (lpm)	$\dot{V}_{hot}$ (lpm)	$T_{in,}$ the F-HMX (ºC)	$T_{out,}$ the F-HMX (ºC)	$T_{in,}$ evap (ºC)	$T_{out,}$ evap (ºC)	T_{fin} (ºC)	T_{sorb} (ºC)
1	69.2	89.2	3.4	3.2	0.5	0.6	14.9	15.3	3.7	45.1	20.7	15.1	14.5	20.3	23.2
60	23.6	25.1	0.5	2.2	2.5	0.6	14.9	14.0	4.2	87.7	82.2	15.1	13.6	83.4	64.5
120	22.1	23.0	0.5	2.4	2.9	0.6	14.9	14.0	4.2	89.0	86.3	15.0	13.3	85.7	71.2
180	20.8	21.4	0.5	2.5	3.0	0.6	14.9	14.0	4.2	89.7	87.6	15.0	13.5	87.6	76.2
240	20.0	20.5	0.5	2.5	3.0	0.6	14.9	14.0	4.2	89.8	88.1	15.1	13.7	88.7	79.8
300	23.9	20.0	0.5	2.5	2.9	0.6	14.9	14.0	4.2	82.5	88.3	15.1	14.0	89.2	82.6
360	84.8	82.2	3.6	2.9	0.7	0.6	14.9	4.2	11.4	21.4	26.8	15.2	15.1	23.1	37.1
420	88.0	86.0	3.8	3.2	0.6	0.6	14.9	4.2	11.5	20.6	22.5	15.3	14.6	21.9	31.2
480	89.7	88.2	3.8	3.2	0.6	0.6	14.9	4.2	11.5	20.0	21.4	15.2	14.4	20.6	28.1
540	90.2	89.1	3.6	3.2	0.6	0.6	14.9	4.2	11.4	19.8	20.9	15.2	14.4	19.7	25.6
600	90.0	89.1	3.4	3.1	0.5	0.6	14.9	4.2	11.4	19.8	20.7	15.2	14.5	19.1	23.5

Table D8. Time variation of HTF temperature inlet and outlet, pressure and HTF flow rate of P-HMX, the F-HMX, evaporator, and condenser, and the average temperatures of the fin and the sorbent in the F-HMX for T_{des}=90ºC, T_{sorp}= T_{cond}=40ºC, T_{evap}=15ºC, τ_{cycle}=10min

t (s)	$T_{in,}$ the P-HMX (ºC)	$T_{out,}$ the P-HMX (ºC)	p_{P-HMX} (kPa)	p_{cond} (kPa)	p_{F-HMX} (kPa)	p_{evap} (kPa)	$\dot{V}_{evap}$ (lpm)	$\dot{V}_{cold}$ (lpm)	$\dot{V}_{hot}$ (lpm)	$T_{in,}$ the F-HMX (ºC)	$T_{out,}$ the F-HMX (ºC)	$T_{in,}$ evap (ºC)	$T_{out,}$ evap (ºC)	T_{fin} (ºC)	T_{sorb} (ºC)
1	75.2	85.3	7.8	8.2	1.3	1.5	14.9	15.3	3.7	57.9	44.1	15.1	14.8	40.7	43.2
60	42.5	43.6	1.2	7.3	6.6	1.4	14.9	14.0	4.2	88.4	84.5	15.1	14.2	85.0	72.1
120	41.4	42.1	1.3	7.4	7.7	1.4	14.9	14.0	4.2	89.4	87.4	15.0	14.1	86.7	76.9
180	40.5	41.0	1.3	7.5	8.0	1.5	14.9	14.0	4.2	89.8	88.4	15.0	14.2	88.1	80.4
240	40.0	40.3	1.3	7.5	8.0	1.5	14.9	14.0	4.2	89.9	88.7	15.1	14.3	88.9	82.9
300	42.8	40.1	1.3	7.5	7.8	1.5	14.9	14.0	4.2	84.7	88.9	15.1	14.5	89.6	84.9
360	86.4	84.6	8.4	8.0	1.7	1.6	14.9	4.2	11.4	41.0	44.9	15.2	15.1	42.2	53.0
420	88.7	87.3	8.8	8.2	1.5	1.5	14.9	4.2	11.5	40.4	41.8	15.3	14.8	41.3	48.8
480	89.9	88.8	8.7	8.2	1.4	1.5	14.9	4.2	11.5	40.0	41.0	15.2	14.7	40.4	46.6
540	90.2	89.4	8.3	8.2	1.5	1.5	14.9	4.2	11.4	39.8	40.6	15.2	14.7	39.7	44.9
600	90.0	89.4	8.2	8.2	1.4	1.5	14.9	4.2	11.4	39.8	40.5	15.2	14.7	39.3	43.4

Table D9. Time variation of HTF temperature inlet and outlet, pressure and HTF flow rate of P-HMX, the F-HMX, evaporator, and condenser, and the average temperatures of the fin and the sorbent in the F-HMX for T_{des}=90ºC, T_{sorp}= T_{cond}=30ºC, T_{evap}=5ºC, τ_{cycle}=10min

t (s)	$T_{in,}$ the P-HMX (ºC)	$T_{out,}$ the P-HMX (ºC)	$p_{P\text{-}HMX}$ (kPa)	p_{cond} (kPa)	$p_{F\text{-}HMX}$ (kPa)	p_{evap} (kPa)	$\dot{V}_{evap}$ (lpm)	$\dot{V}_{cold}$ (lpm)	$\dot{V}_{hot}$ (lpm)	$T_{in,}$ the F-HMX (ºC)	$T_{out,}$ the F-HMX (ºC)	$T_{in,}$ evap (ºC)	$T_{out,}$ evap (ºC)	T_{fin} (ºC)	T_{sorb} (ºC)
1	72.2	84.5	4.9	5.0	0.5	0.7	14.9	15.3	3.7	51.5	33.7	5.0	4.7	32.6	31.5
60	33.1	34.0	0.5	4.0	3.9	0.6	14.9	14.0	4.2	88.0	84.1	5.0	4.3	84.7	67.7
120	31.7	32.3	0.5	4.2	4.6	0.6	14.9	14.0	4.2	89.2	87.3	4.9	4.2	86.6	73.5
180	30.6	31.0	0.5	4.3	4.8	0.6	14.9	14.0	4.2	89.8	88.3	4.9	4.3	88.1	77.9
240	30.0	30.3	0.6	4.3	4.8	0.7	14.9	14.0	4.2	89.8	88.7	5.0	4.4	89.0	81.1
300	33.4	31.0	0.6	4.3	4.7	0.7	14.9	14.0	4.2	83.6	87.8	5.0	4.5	88.6	83.5
360	85.6	84.0	5.3	4.7	0.8	0.7	14.9	4.2	11.4	31.2	35.1	5.1	5.0	32.4	43.7
420	88.3	87.1	5.6	5.0	0.6	0.7	14.9	4.2	11.5	30.5	31.9	5.1	4.8	31.4	38.6
480	89.8	88.9	5.5	5.0	0.6	0.7	14.9	4.2	11.5	30.0	31.0	5.0	4.7	30.4	35.8
540	90.2	89.5	5.3	5.0	0.6	0.7	14.9	4.2	11.4	29.8	30.6	5.0	4.7	29.7	33.6
600	90.0	89.5	5.0	4.9	0.6	0.7	14.9	4.2	11.4	29.8	30.5	5.0	4.7	29.3	31.8

Table D10. Time variation of HTF temperature inlet and outlet, pressure and HTF flow rate of P-HMX, the F-HMX, evaporator, and condenser, and the average temperatures of the fin and the sorbent in the F-HMX for T_{des}=90ºC, T_{sorp}= T_{cond}=30ºC, T_{evap}=10ºC, τ_{cycle}=10min

t (s)	$T_{in,}$ the P-HMX (ºC)	$T_{out,}$ the P-HMX (ºC)	p_{P-HMX} (kPa)	p_{cond} (kPa)	p_{F-HMX} (kPa)	p_{evap} (kPa)	$\dot{V}_{evap}$ (lpm)	$\dot{V}_{cold}$ (lpm)	$\dot{V}_{hot}$ (lpm)	$T_{in,}$ the F-HMX (ºC)	$T_{out,}$ the F-HMX (ºC)	$T_{in,}$ evap (ºC)	$T_{out,}$ evap (ºC)	T_{fin} (ºC)	T_{sorb} (ºC)
1	72.2	87.3	5.0	5.0	0.9	1.0	14.9	15.3	3.7	51.5	32.1	10.0	9.6	31.1	31.5
60	33.1	34.2	0.8	4.1	4.0	1.0	14.9	14.0	4.2	88.0	83.8	10.0	9.0	84.5	67.7
120	31.7	32.4	0.8	4.2	4.6	1.0	14.9	14.0	4.2	89.2	87.1	9.9	8.8	86.5	73.5
180	30.6	31.1	0.9	4.3	4.8	1.0	14.9	14.0	4.2	89.8	88.1	9.9	8.9	88.0	77.9
240	30.0	30.4	0.9	4.3	4.8	1.0	14.9	14.0	4.2	89.8	88.6	10.0	9.1	88.9	81.1
300	33.4	30.5	0.9	4.3	4.7	1.0	14.9	14.0	4.2	83.6	88.2	10.0	9.2	89.0	83.5
360	85.6	83.7	5.4	4.8	1.1	1.0	14.9	4.2	11.4	31.2	35.4	10.1	10.0	32.5	43.7
420	88.3	86.9	5.6	5.0	1.0	1.0	14.9	4.2	11.5	30.5	32.0	10.1	9.6	31.5	38.6
480	89.8	88.7	5.6	5.0	1.0	1.0	14.9	4.2	11.5	30.0	31.1	10.0	9.5	30.5	35.8
540	90.2	89.4	5.3	5.0	1.0	1.0	14.9	4.2	11.4	29.8	30.7	10.0	9.5	29.7	33.6
600	90.0	89.4	5.1	5.0	0.9	1.0	14.9	4.2	11.4	29.8	30.5	10.0	9.5	29.2	31.8

Table D11. Time variation of HTF temperature inlet and outlet, pressure and HTF flow rate of P-HMX, the F-HMX, evaporator, and condenser, and the average temperatures of the fin and the sorbent in the F-HMX for T_{des}=90ºC, T_{sorp}= T_{cond}=30ºC, T_{evap}=20ºC, τ_{cycle}=10min

t (s)	$T_{in,}$ the P-HMX (ºC)	$T_{out,}$ the P-HMX (ºC)	p_{P-HMX} (kPa)	p_{cond} (kPa)	p_{F-HMX} (kPa)	p_{evap} (kPa)	$\dot{V}_{evap}$ (lpm)	$\dot{V}_{cold}$ (lpm)	$\dot{V}_{hot}$ (lpm)	$T_{in,}$ the F-HMX (ºC)	$T_{out,}$ the F-HMX (ºC)	$T_{in,}$ evap (ºC)	$T_{out,}$ evap (ºC)	T_{fin} (ºC)	T_{sorb} (ºC)
1	72.2	90.1	5.7	5.6	1.8	1.9	14.9	15.3	3.7	51.5	30.0	20.0	19.4	29.6	31.5
60	33.1	34.4	1.7	4.7	4.7	1.8	14.9	14.0	4.2	88.0	83.3	20.0	18.6	83.2	67.7
120	31.7	32.6	1.7	4.8	5.3	1.8	14.9	14.0	4.2	89.2	86.9	19.9	18.3	85.2	73.5
180	30.6	31.2	1.8	4.9	5.4	1.8	14.9	14.0	4.2	89.8	88.0	19.9	18.5	86.8	77.9
240	30.0	30.4	1.8	4.9	5.4	1.9	14.9	14.0	4.2	89.8	88.4	20.0	18.7	87.7	81.1
300	33.4	29.9	1.8	4.9	5.3	1.9	14.9	14.0	4.2	83.6	88.7	20.0	19.0	88.3	83.5
360	85.6	83.3	6.0	5.4	2.0	2.0	14.9	4.2	11.4	31.2	35.9	20.1	20.0	32.6	43.7
420	88.3	86.6	6.3	5.6	1.9	1.9	14.9	4.2	11.5	30.5	32.2	20.1	19.5	31.5	38.6
480	89.8	88.5	6.2	5.6	1.9	1.9	14.9	4.2	11.5	30.0	31.2	20.0	19.4	30.5	35.8
540	90.2	89.2	6.0	5.6	1.9	1.9	14.9	4.2	11.4	29.8	30.8	20.0	19.3	29.7	33.6
600	90.0	89.2	5.7	5.6	1.9	1.9	14.9	4.2	11.4	29.8	30.6	20.0	19.4	29.2	31.8

Appendix E: Matlab codes

E.1. Matlab code for G-LPJ data

```
clearvars
clc

m_ads=18.8815;

A=importdata('D:\G-LPJ\Results\5\1\Data.xlsx');

Leng_des=0;
t_o=A(:,1);
T_1_o=A(:,2);
T_2_o=A(:,3);
T_3_o=A(:,4);
T_4_o=A(:,5);
T_5_o=A(:,6);
p_bed_o=A(:,7);
p_evap_o=A(:,8);
w_o=A(:,9)/m_ads;
T_ch_o=A(:,10);
t(1,1)=0;
T_1(1,1)=0;
T_2(1,1)=0;
T_3(1,1)=0;
T_4(1,1)=0;
T_5(1,1)=0;
p_bed(1,1)=0;
p_evap(1,1)=0;
w(1,1)=0;
w_last_ads=0;
w_last_des=0;

t_c=7200;
t_close=3600;
t_open=7200;
t_co=t_close+t_open;
t_cco=2*t_close+t_open;
No_cycle=1;

for i=1:t_o(end,1)
    q=floor(i/(2*t_co));
    time=rem(i,2*(t_co));
    if i>t_co
        if (time<=t_co && time>t_close)
            %Des
            %%%%%%%%%%%%% Max
            if time==t_close+1
                maxi=-30000;
                for k=i:i+300
                    if maxi<w_o(k,1)
                        maxi=w_o(k,1);
                        z=k;
```

```
                end
            end
        end
        %%%%%%%%%%%%% Max
        if i>=z
            t(end+1,1)=t(end,1)+1;
            T_1(end+1,1)=T_1_o(i,1);
            T_2(end+1,1)=T_2_o(i,1);
            T_3(end+1,1)=T_3_o(i,1);
            T_4(end+1,1)=T_4_o(i,1);
            T_5(end+1,1)=T_5_o(i,1);
            p_bed(end+1,1)=p_bed_o(i,1);
            p_evap(end+1,1)=p_evap_o(i,1);
            w(end+1,1)=w_o(i,1)-maxi+w_last_ads;
        end
    end
    if time==t_co
        w_last_des=w(end,1);
        Leng_des=length(w);
    end
    if ((t_cco<time && time<2*t_co) || time==0)
        %Ads
        %%%%%%%%%%%%% Min
        if time==t_cco+1
            mini=30000;
            for k=i:i+300
                if mini>w_o(k,1)
                    mini=w_o(k,1);
                    j=k;
                end
            end
        end
        %%%%%%%%%%%%% Min

        if i>=j
            t(end+1,1)=t(end,1)+1;
            T_1(end+1,1)=T_1_o(i,1);
            T_2(end+1,1)=T_2_o(i,1);
            T_3(end+1,1)=T_3_o(i,1);
            T_4(end+1,1)=T_4_o(i,1);
            T_5(end+1,1)=T_5_o(i,1);
            p_bed(end+1,1)=p_bed_o(i,1);
            p_evap(end+1,1)=p_evap_o(i,1);
            w(end+1,1)=w_o(i,1)-mini+w_last_des;
        end
    end
    if time==0
        w_last_ads=w(end,1);
        Leng_ads=length(w);
    end
  end
end


for i=1:21300
    t_plot(i,1)=t(i+1,1)/60;
```

```
    T_1_plot(i,1)=T_1(i+1,1);
    T_2_plot(i,1)=T_2(i+1,1);
    T_3_plot(i,1)=T_3(i+1,1);
    T_4_plot(i,1)=T_4(i+1,1);
    T_5_plot(i,1)=T_5(i+1,1);
    p_bed_plot(i,1)=p_bed(i+1,1);
    p_evap_plot(i,1)=p_evap(i+1,1);
    w_plot(i,1)=w(i+1,1);
end



h=figure;
hold on
plot(t_plot,w_plot,'-k','linewidth',1.5);
%%%%%%%%%%%%%%%%%%%%
x = [0.6 0.6];
y = [0.35 0.48];
annotation('textarrow',x,y,'String','Slope of last 10 min=2.5e-6 (1/s)',
'FontName','Arial', 'FontWeight','bold', 'fontsize',16)
set(gca,    'FontName','Arial',    'FontWeight','bold',    'fontsize',16,
'XMinorTick','on','YMinorTick','on',
'LineWidth',1.25,'TickLength',[0.015 0.015]);
xlabel('t (min)', 'FontSize',22,'FontWeight','bold');
ylabel('\omega      (g      H_{2}O/g      Sorbent)','Interpreter','tex',
'FontSize',22,'FontWeight','bold');
hold off
box on
saveas(h,'D:\G-LPJ\Results\5\1\w.jpg')
```

E.2. Matlab code for two-sorber bed sorption test bed data

```
clc
clearvars
format long

t_cycle=600;
t_ads=t_cycle/2;
addrr={'D:\OSHEX_OSHEX_C\Results\T_sorp\40\'};

%%%%%%%%%%%%%%%%%%%%%
h_fg=2498000; % J/kg
h_ads=2777777.77;  % J/kg
%%%%%%%%%%%%%%%%%%%%%
m_sorb_P=0.587; % kg
m_HEX_P=1.722; % kg
m_sorb_F=0.379; % kg
m_HEX_F=1.044; % kg


%%%%%%%%%%%%%%%%%%%%%%%%%%%%%%%%%%%%%%%%%%%%%%%%%%        Thermophysical
properties
%%%% 10 to 90 C
```

```
p_cp=[1.96843994919853e-09,-7.16529701770362e-07,0.000102324609842342,-
0.00713157205841238,0.254630122900774,-
4.45816383273092,4213.23894867659]; % J/kg.K
p_kk=[4.71622852306825e-10,-8.43371971945927e-08,-5.23630481786558e-
06,0.00207966653988023,0.547141870203301]; % (W/mK)
p_mu=[2.60714771095438e-11,-7.28991739599359e-09,8.24662122707676e-07,-
4.98131750834992e-05,0.00172471335857807]; % (kg/ms)
p_rho=[-1.10692269115836e-07,3.62269016299992e-05,-
0.00701607595591988,0.0327309580312716,1000.05965680566]; % (kg/m3)
%%%%%%%%%%%%%%%%%%%%%%%%%%%%%%%%%%%%%%%%%%%%%%%%%%%         Thermophysical
properties

A=importdata([char(addrr) 'New_data.xlsx']);
t_des=t_ads;

t=A(:,1)-A(1,1)+1;
T_P_HEX_in=A(:,2);
T_P_HEX_out=A(:,3);
p_P_HEX=A(:,4);
p_cond=A(:,5);
p_F_HEX=A(:,6);
p_evap=A(:,7);
mdot_evap=A(:,8)/60000; % m^3/s
mdot_cold=A(:,9)/60000; % m^3/s
% mdot_cond=A(:,10);
mdot_hot=A(:,11)/60000; % m^3/s
T_F_HEX_in=A(:,12);
T_F_HEX_out=A(:,13);
T_evap_in=A(:,14);
T_evap_out=A(:,15);
T_bed1=A(:,16);
T_bed2=A(:,17);

Q_ads_P=0;
Q_des_P=0;
Q_evap_P=0;
Q_ads_F=0;
Q_des_F=0;
Q_evap_F=0;

for i=t_ads+1:2*t_ads
    T=(T_evap_in(i,1)+T_evap_out(i,1))/2;
    cp_evap=polyval(p_cp,T);
    rho_evap=polyval(p_rho,T);
    Q_evap_F=Q_evap_F+mdot_evap(i,1)*rho_evap*cp_evap*(T_evap_in(i,1)-
T_evap_out(i,1));
    T=(T_F_HEX_in(i,1)+T_F_HEX_out(i,1))/2;
    cp_bed=polyval(p_cp,T);
    rho_bed=polyval(p_rho,T);
    Q_ads_F=Q_ads_F+mdot_cold(i,1)*rho_bed*cp_bed*(T_F_HEX_out(i,1)-
T_F_HEX_in(i,1));
    T=(T_P_HEX_in(i,1)+T_P_HEX_out(i,1))/2;
    cp_bed=polyval(p_cp,T);
    rho_bed=polyval(p_rho,T);
    Q_des_P=Q_des_P+mdot_hot(i,1)*rho_bed*cp_bed*(T_P_HEX_in(i,1)-
T_P_HEX_out(i,1));
```

```
end


for i=1:t_ads
    T=(T_evap_in(i,1)+T_evap_out(i,1))/2;
    cp_evap=polyval(p_cp,T);
    rho_evap=polyval(p_rho,T);
    Q_evap_P=Q_evap_P+mdot_evap(i,1)*rho_evap*cp_evap*(T_evap_in(i,1)-
T_evap_out(i,1));
    T=(T_F_HEX_in(i,1)+T_F_HEX_out(i,1))/2;
    cp_bed=polyval(p_cp,T);
    rho_bed=polyval(p_rho,T);
    Q_des_F=Q_des_F+mdot_hot(i,1)*rho_bed*cp_bed*(T_F_HEX_in(i,1)-
T_F_HEX_out(i,1));
    T=(T_P_HEX_in(i,1)+T_P_HEX_out(i,1))/2;
    cp_bed=polyval(p_cp,T);
    rho_bed=polyval(p_rho,T);
    Q_ads_P=Q_ads_P+mdot_cold(i,1)*rho_bed*cp_bed*(T_P_HEX_out(i,1)-
T_P_HEX_in(i,1));
end

SCP_F=Q_evap_F/(m_sorb_F*2*t_ads);
COP_F=Q_evap_F/Q_des_F;

SCP_P=Q_evap_P/(m_sorb_P*2*t_ads);
COP_P=Q_evap_P/Q_des_P;

export_s=[SCP_P,COP_P,SCP_F,COP_F];

xlswrite([char(addrr) 'Performance_parameters.xlsx'],export_s);
```

E.3. Matlab code for 2-D analytical model in cartesian coordinate for P-HMX

```
clc
clearvars

format long

global Lambda;

no_gamma=2;

%%%%%%%%%%%%%%%%%%%%%%
% Sorbent:
rho_s=675;
c_p_s=1082;
rho_cp=rho_s*c_p_s;
%%%%%%%%%%%%%%%%%%%%%%
grrr=[0 0.02 0.05 0.1 0.15 0.2];
```

```
   alpha_sss=[2.38175E-07,2.80936E-07,3.45121E-07,5.43E-07,9.86964E-
07,1.3898E-06];
   p_1=polyfit(grrr,alpha_sss,2);
   %%%%%%%%%%%%%%%%%%%%%%
   %%%%%%%%%%%%%%%%%%%%%%
   b=0.01;
   t_f=0.001;
   t_s=0.001;
   gr=0.1;
   time=300;
   t_w=0.004;

   %%%%%%%%%%%%%%%%%%%%%%
   % Aluminum @ 40
   rho_g=2700;
   c_p_g=896;
   k_y=167;
   k_x=167;
   alpha_x=k_x/(rho_g*c_p_g);
   alpha_y=k_y/(rho_g*c_p_g);
   %%%%%%%%%%%%%%%%%%%%%%

   %%%%%%%%%%%%%%%%%%%%%%
   h_fg=2498000; % J/kg
   h_ads=2777777.77;  % J/kg
   c_p_tube=c_p_g;
   c_p_w=4186;
   w_des_0=0.41695;
   %%%%%%%%%%%%%%%%%%%%%%

   l_t=2*t_s+t_f; % tube length
   %%%%%%%%%%%%%%%%%%%%%%%%%%%%%%%%%%%%%%%%%%%%%%%%%%%%%%%%%%%%%%%%%%%%
   %%%%%%%%%%%%%%%%%%% h_dp_RE_Nu
   D_H=2*t_w; % hydraulic diameter
   rho_w=992.2;
   Q_flow=7; %  l/min
   mdot=Q_flow*0.001*rho_w/60;
   t_l=0.013; % Tube width of the cross section
   k_w=0.6178; % water conductivity
   mu_w=0.001002; % water viscosity
   Pr=7.154;
   Re=2*mdot/(mu_w*t_l);
   f_fric=(1.82*log10(Re)-1.64)^-2; % friction factor
   Nu=((f_fric*Re*Pr/8)/(1.07+12.7*(f_fric/8)^0.5*(Pr^(2/3)-
1)))*(0.0006533/0.0005758)^0.11; % only a function of t_l not t_w (Holman
page 282)
   h_f=Nu*k_w/D_H;
   t_t=0.002; %mm Thickness of the tube itself
   R_fluid=(1/h_f)+(t_t/k_x);
   %%%%%%%%%%%%%%%%%%%% h_dp_RE_Nu
   TCR=3;
   A=6.45e-4;
   %%%%%%%%%%%%%%%%%%%%%%%%%%%%%%%%%%%%%%%%%%%%%%%%%%%%%%%%%%%%%%%%%%%%
   T_0=67.5+273.15; %degree C (refer to w_T, start temperature)
   T_f=30+273.15; %degree C
   Theta_0=T_0-T_f;
```

```
%%%%%%%%%%%%%%%%%%%%%%%%%%%%%%%%%%%%%%%%%%%%%%%%%%%%%%%%%%%%%%%%%%%%%%%%%%%%

t_1=sym(linspace(1,time,2));
%%%%%%%%%%%%%%%%%%% Space
eta=linspace(0,1,20);
x_1=t_f/(t_s+t_f);
dxx=x_1/30;
zeta_f=0:dxx:x_1;
zeta_s=x_1:dxx:1+dxx;
zeta_original=[zeta_f(1:end-1),zeta_s(1:end)];
zeta_plot=[zeta_f(1:end),zeta_s(1:end-1)];
%%%%%%%%%%%%%%%%%%% Space

a_ads=-0.007*(1-gr)/0.8;

alpha_s=polyval(p_1,gr);
k_s=rho_cp*alpha_s;

a=a_ads;
alpha_s=k_s/(rho_cp-rho_s*h_ads*a);

k_ave=(k_s+k_x)/2;
Lambda=b/(k_ave*R_fluid);
k=k_s/k_y;
Lambda_c=(t_s+t_f)/(k_y*TCR*A);
Fo=sym(t_1*alpha_x/(b^2));
delta=b/(t_s+t_f);
mu_y=(alpha_y/alpha_x)^0.5;
mu_s=(alpha_s/alpha_x)^0.5;

r_f=k_x/delta^2;
r_s=((rho_cp-rho_s*h_ads*a)*k_x)/(rho_g*c_p_g*delta^2);
p_f=k_y;
p_s=k_s;
%%%%%%%%%%%%%%%%%%%%%%%%%%%%%%%%%%%%%%%%%%%%%%%%%%%%%%%%%%%%%%%%%%%%%%%%%%%%
%%%%%%%%%%% Gamma
xx=0:0.001:10;
roots=zeros(1,length(xx));
my_roots=zeros(1,1);
for i=2:length(xx)
    roots(i)=fzero(@gamma_func,xx(i));
    if (abs(gamma_func(roots(i))))<1e-4
        if roots(i)>0
            my_roots(1,end+1)=roots(i);
        end
    end
end
gamma_temp=zeros(1,length(my_roots)-1);
for i=2:length(my_roots)
    gamma_temp(1,i-1)=my_roots(1,i);
end
gamma_c=[min(gamma_temp)];

for j=1:no_gamma
    min_gamma=1000;
    gamma_temp=gamma_temp-gamma_c(1,end)-0.0001;
```

```
        for i=1:length(gamma_temp)
            if gamma_temp(1,i)>0
               if gamma_temp(1,i)<min_gamma
                   min_gamma=gamma_temp(1,i);
               end
            end
        end
        min_gamma=min_gamma+gamma_c(1,end)+0.0001;
        gamma_temp=gamma_temp+gamma_c(1,end)+0.0001;
        gamma_c(1,end+1)=min_gamma;
    end
    gamma_all=sym(gamma_c);
    %%%%%%%%%%%%%%%%%%%%%%%%%%%%%%%%%%%%%%%%%%%%%%%%%%%%%%%%%%%%%%%%%%%%%%%%%%%%
%%%%%%%%%%%% Gamma
    Theta=zeros(length(eta),length(zeta_original),length(Fo));

    for i_gamma=1:2
        gamma=gamma_all(1,i_gamma);
        q_f=(gamma)^2*r_f; % for each gamma
        q_s=(mu_s*gamma)^2*r_s; % for each gamma
        zeta=zeros(1,1);
        zeta=zeta_original;
        for i_landa=1:1


        for k=1:length(zeta)-1
            if zeta(1,k)<x_1
                l_k(1,k)=zeta(1,k+1)-zeta(1,k);
                p_k(1,k)=p_f;
                r_k(1,k)=r_f;
                q_k(1,k)=q_f;
            elseif zeta(1,k)>x_1
                l_k(1,k)=zeta(1,k+1)-zeta(1,k);
                p_k(1,k)=p_s;
                r_k(1,k)=r_s;
                q_k(1,k)=q_s;
            else
                l_k(1,k)=zeta(1,k+1)-zeta(1,k);
                l_TCR=l_k(1,k);
                p_k(1,k)=l_k(1,k)*(t_s+t_f)/(TCR*A);
                r_k(1,k)=0;
                q_k(1,k)=0;
                w_k(1,k)=0;
            end
        end

%%%%%%%%%%%%%%%%%%%%%%%%%%%%%%%%%%%%%%%%%%%%%%%%%%%%%%%%%%%%%%%%%%%%%%%%%%%%
%%%%%%%%%%%%%%%%%%%%%%%% landa_loop while
        landa_l=0;
        landa_hat_old=0;
        Eps_i=0.01;
        delta_hat=0.001;
        landa_hat=landa_hat_old+delta_hat;
        landa_u=landa_hat;
        while (2>1)
```

```
          %%%%%%%%%%%%%%%%%%%%%%%%%%%%%%%%%%%%%%%%%%%%%%%%%%%%%%%%% N0 &
s_k
          N0(1,i_landa)=0;
          s_k(1,i_landa)=0;

%%%%%%%%%%%%%%%%%%%%%%%%%%%%%%%%%%%%%%%%%%%%%%%%%%%%%%%%%%%%%%%%%%%%%%%%
%%%%%%% k loop

          for k=1:length(zeta)-1
              if zeta(1,k)<x_1
                  w_k(1,k)=((landa_hat*r_f-q_f)/p_f)^0.5;
              elseif zeta(1,k)>x_1
                  w_k(1,k)=((landa_hat*r_s-q_s)/p_s)^0.5;
              end
              N0(1,i_landa)=N0(1,i_landa)+floor(w_k(1,k)*l_k(1,k)/pi);


%%%%%%%%%%%%%%%%%%%%%%%%%%%%%%%%%%%%%%%%%%%%%%%%%%%%%%%%%%%%%%%%% A and B
              if w_k(1,k)^2>0
                  B_k(1,k)=p_k(1,k)*w_k(1,k)/sin(w_k(1,k)*l_k(1,k));
                  A_k(1,k)=B_k(1,k)*cos(w_k(1,k)*l_k(1,k));
              elseif w_k(1,k)^2==0
                  B_k(1,k)=p_k(1,k)/l_k(1,k);
                  A_k(1,k)=B_k(1,k);
              else
                  w_k_star=(abs(w_k(1,k)^2))^0.5;
                  B_k(1,k)=p_k(1,k)*w_k_star/sinh(w_k_star*l_k(1,k));
                  A_k(1,k)=B_k(1,k)*cosh(w_k_star*l_k(1,k));
              end

%%%%%%%%%%%%%%%%%%%%%%%%%%%%%%%%%%%%%%%%%%%%%%%%%%%%%%%%%%%%%%%%% A and B
              D_k(1,1)=1;
              D_k(1,2)=A_k(1,1); % this is correct not A1 bar
              if k>1 && k<length(zeta)-1
                  D_k(1,k+1)=D_k(1,k)*(A_k(1,k)+A_k(1,k-1))-D_k(1,k-
1)*B_k(1,k-1)^2;
              elseif k==length(zeta)-1
                  D_k(1,k+1)=D_k(1,k)*(A_k(1,k))-D_k(1,k-1)*B_k(1,k-
1)^2;
              end

              if (D_k(1,k+1)/D_k(1,k))<0
                  s_k(1,i_landa)=s_k(1,i_landa)+1;
              end
          end

%%%%%%%%%%%%%%%%%%%%%%%%%%%%%%%%%%%%%%%%%%%%%%%%%%%%%%%%%%%%%%%%%%%%%%%%
%%%%%%% k loop

          %%%%%%%%%%%%%%%%%%%%%%%%%%%%%%%%%%%%%%%%%%%%%%%%%%%%%%%%% N0 &
s_k
          N_landa(1,i_landa)=N0(1,i_landa)+s_k(1,i_landa);
          if N_landa(1,i_landa)>=i_landa
              landa_u=landa_hat;
              delta_landa=abs(landa_u-landa_l);
              if delta_landa<=Eps_i
```

```
                Landa(i_gamma,i_landa)=sym((landa_u+landa_l)/2);
                break; % from while loop
            else
                Landa_hat=(landa_u+landa_l)/2;
            end
        else
            landa_l=landa_hat;
            if landa_hat==landa_hat_old+delta_hat
                landa_hat_old=landa_hat;
                landa_hat=landa_hat_old+delta_hat;
                landa_u=landa_hat;
            elseif Landa_hat==(landa_u+landa_l)/2;
                delta_landa=abs(landa_u-landa_l);
                if delta_landa<=Eps_i
                    Landa(i_gamma,i_landa)=sym((landa_u+landa_l)/2);
                    break; % from while loop
                else
                    Landa_hat=(landa_u+landa_l)/2;
                end
            end
        end

    end

%%%%%%%%%%%%%%%%%%%%%%%%%%%%%%%%%%%%%%%%%%%%%%%%%%%%%%%%%%%%%%%%%%%%%%%%%%%%
%%%%%%%%%%%%%%%%%%%%%% landa_loop while


%%%%%%%%%%%%%%%%%%%%%%%%%%%%%%%%%%%%%%%%%%%%%%%%%%%%%%%%%%%%%%%%%%%%%%%%%%%%
%%%%%%%%%%%%%%%%%%%%%% Eigenfunctions


%%%%%%%%%%%%%%%%%%%%%%%%%%%%%%%%%%%%%%%%%%%%%%%%%%%%%%%%%%%%%%%%%%%%%%%%%%%%
%%%%%%%%%%%%%%%%%%%%%%%%%%%%%%%%%%%%%%%%%%%%%%%%%%%%%%%%%%%%%%%%%%%%%%%%%%%%
%%%%%%%%%%%%%% New error after new zeta
    for k=1:length(zeta)-1
        if zeta(1,k)<x_1
            l_k(1,k)=zeta(1,k+1)-zeta(1,k);
            p_k(1,k)=p_f;
            r_k(1,k)=r_f;
            q_k(1,k)=q_f;
        elseif zeta(1,k)>x_1
            l_k(1,k)=zeta(1,k+1)-zeta(1,k);
            p_k(1,k)=p_s;
            r_k(1,k)=r_s;
            q_k(1,k)=q_s;
        else
            l_k(1,k)=zeta(1,k+1)-zeta(1,k);
            l_TCR=l_k(1,k);
            p_k(1,k)=l_k(1,k)*(t_s+t_f)/(TCR*A);
            r_k(1,k)=0;
            q_k(1,k)=0;
            w_k(1,k)=0;
        end
    end
    for k=1:length(zeta)-1
```

```
            if zeta(1,k)<x_1
                w_k(1,k)=((Landa(i_gamma,i_landa)*r_f-q_f)/p_f)^0.5;
%%%%%%%%%%%%%%%%%%%%%%%%%%%%%%%%%%%%%%%%%%%%%%%%%%%%%%%%%%%%%%%%%%%%%%% change to
zeta
            elseif zeta(1,k)>x_1
                w_k(1,k)=((Landa(i_gamma,i_landa)*r_s-q_s)/p_s)^0.5;
            end

            if w_k(1,k)^2>0
                B_k(1,k)=p_k(1,k)*w_k(1,k)/sin(w_k(1,k)*l_k(1,k));
                A_k(1,k)=B_k(1,k)*cos(w_k(1,k)*l_k(1,k));
            elseif w_k(1,k)^2==0
                B_k(1,k)=p_k(1,k)/l_k(1,k);
                A_k(1,k)=B_k(1,k);
            else
                w_k_star=(abs(w_k(1,k)^2))^0.5;
                B_k(1,k)=p_k(1,k)*w_k_star/sinh(w_k_star*l_k(1,k));
                A_k(1,k)=B_k(1,k)*cosh(w_k_star*l_k(1,k));
            end
        end

        psi(i_gamma,i_landa,1)=-1; % eigenfunction at x_0
        psi(i_gamma,i_landa,2)=-A_k(1,1)/B_k(1,1); % eigenfunction at x_1
        for k=1:length(zeta)-2

psi(i_gamma,i_landa,k+2)=((A_k(1,k)+A_k(1,k+1))*psi(i_gamma,i_landa,k+1
)-B_k(1,k)*psi(i_gamma,i_landa,k))/B_k(1,k+1); % eigenfunction at x_k+1
        end
        %                 Err(i_gamma,i_landa)=(Eps_max*length(zeta))-abs(-
B_k(1,length(zeta)-1)*psi(i_gamma,i_landa,length(zeta)-
1)+A_k(1,length(zeta)-1)*psi(i_gamma,i_landa,length(zeta)));  %  Must  be
>=0

%%%%%%%%%%%%%%%%%%%%%%%%%%%%%%%%%%%%%%%%%%%%%%%%%%%%%%%%%%%%%%%%%%%%%%%%%%%%%%%
%%%%%%%%%%%%%%%%%%%%%%%%%%%%%%%%%%%%%%%%%%%%%%%%%%%%%%%%%%%%%%%%%%%%%%%%%%%%%%%
%%%%%%%%%%%%%% New error after new zeta


%%%%%%%%%%%%%%%%%%%%%%%%%%%%%%%%%%%%%%%%%%%%%%%%%%%%%%%%%%%%%%%%%%%%%%%%%%%%%%%
%%%%%%%%%%%%%%%%%%%%%%%% Eigenfunctions


%%%%%%%%%%%%%%%%%%%%%%%%%%%%%%%%%%%%%%%%%%%%%%%%%%%%%%%%%%%%%%%%%%%%%%%%%%%%%%%
%%%%%%%%%%%%%%%%%%%%%%%%% C(i_gamma,i_landa)
        N_gamma(i_gamma,1)=-((tan(gamma)^2-
1)*sin(2*gamma)+2*tan(gamma)*(cos(2*gamma)-1)-
2*gamma*(tan(gamma)^2+1))/(4*gamma);
        num_gamma(i_gamma,1)=tan(gamma)/gamma;
        N_landa(i_gamma,i_landa)=0;
        num_landa(i_gamma,i_landa)=0;
        for k=1:length(zeta)-1
            if w_k(1,k)^2==0

N_landa(i_gamma,i_landa)=N_landa(i_gamma,i_landa)+r_k(1,k)*l_k(1,k)*(ps
i(i_gamma,i_landa,k+1)^3-
```

```
psi(i_gamma,i_landa,k)^3)/(3*(psi(i_gamma,i_landa,k+1)-
psi(i_gamma,i_landa,k)));

num_landa(i_gamma,i_landa)=num_landa(i_gamma,i_landa)+r_k(1,k)*l_k(1,k)
*(psi(i_gamma,i_landa,k+1)+psi(i_gamma,i_landa,k))/2;
          else

N_landa(i_gamma,i_landa)=N_landa(i_gamma,i_landa)+r_k(1,k)*((psi(i_gamm
a,i_landa,k)^2+psi(i_gamma,i_landa,k+1)^2)*(B_k(1,k)^2*l_k(1,k)/p_k(1,k
)-A_k(1,k))+...

2*B_k(1,k)*psi(i_gamma,i_landa,k)*psi(i_gamma,i_landa,k+1)*(1-
A_k(1,k)*l_k(1,k)/p_k(1,k)))/(2*p_k(1,k)*w_k(1,k)^2);

num_landa(i_gamma,i_landa)=num_landa(i_gamma,i_landa)+r_k(1,k)*((psi(i_
gamma,i_landa,k+1)+psi(i_gamma,i_landa,k))*(B_k(1,k)-
A_k(1,k))/(p_k(1,k)*(w_k(1,k)^2)));
          end
      end

C(i_gamma,i_landa)=Theta_0*num_gamma(i_gamma,1)*num_landa(i_gamma,i_lan
da)/(N_gamma(i_gamma,1)*N_landa(i_gamma,i_landa));


%%%%%%%%%%%%%%%%%%%%%%%%%%%%%%%%%%%%%%%%%%%%%%%%%%%%%%%%%%%%%%%%%%%%%%%%
%%%%%%%%%%%%%%%%%%%%%% C(i_gamma,i_landa)


%%%%%%%%%%%%%%%%%%%%%%%%%%%%%%%%%%%%%%%%%%%%%%%%%%%%%%%%%%%%%%%%%%%%%%%%
%%%%%%%%%%%%%%%%%%%%%%%%%%%%%%%%%%%%%%%%%%%%%%%%%%%%%%%%%%%%%%%%%%%%%%%% Theta
      for kk=1:length(zeta_original)
          for k=1:length(zeta)
              if abs(zeta(1,k)-zeta_original(1,kk))<1e-5
                  for i_t=1:length(Fo)
                      for i_eta=1:length(eta)

X=cos(gamma*eta(1,i_eta))+tan(gamma)*sin(gamma*eta(1,i_eta));

Theta(i_eta,kk,i_t)=Theta(i_eta,kk,i_t)+C(i_gamma,i_landa)*X*psi(i_gamm
a,i_landa,k)*exp(-Landa(i_gamma,i_landa)*Fo(1,i_t));
                      end
                  end
              end
          end
      end

%%%%%%%%%%%%%%%%%%%%%%%%%%%%%%%%%%%%%%%%%%%%%%%%%%%%%%%%%%%%%%%%%%%%%%%%
%%%%%%%%%%%%%%%%%%%%%%%%%%%%%%%%%%%%%%%%%%%%%%%%%%%%%%%%%%%%%%%%%%%%%%%% Theta

      end



  end

  for i_t=1:length(t_1)
```

```
T_sorb_ave(i_t,1)=mean(mean(Theta(:,length(zeta_f)+1:length(zeta_plot),
i_t)),2);
   end



   m_sorb=b*t_s*rho_s;
   m_HEX=b*t_f*rho_g;
   m_tube=t_t*(t_f+t_s)*rho_g;
   m_HEX=m_HEX+m_tube;

   dw=a_ads*(T_sorb_ave(2,1)-T_sorb_ave(1,1));
   SCP=zeros(1,2);
   SCP(1,1)=0.5*dw*h_fg/(t_1(1,2)-t_1(1,1));    %%% gr included in a_ads

   %
W_pump=(1/(t_l+0.002))*f_fric*(1_t)^2*Re^3*mu_w^3*time/(4*rho_w^2*D_H^3
);
   Q_evap=m_sorb*dw*h_fg;
   Q_des=m_sorb*dw*h_ads;
   Q_sens=(m_sorb*c_p_s+m_sorb*w_des_0*c_p_w+m_HEX*c_p_g)*(90-30);

   SCP(1,2)=Q_evap/(Q_des+Q_sens); % COP


   xlswrite('D:\2_D model\Results\LTJ\Run one point\SCP_COP.xlsx',SCP);



   function y = gamma_func( x )
   global Lambda;
   y=x*tan(x)-Lambda;
   end
```

E.4. Matlab code for 2-D analytical model in cylindrical coordinate for the F-HMX

```
   clc
   clearvars

   format long
   global Lambda;
   global delta_r;


   %%%%%%%%%%%%%%%%%%%%%%%%%%%%%%%%%%%%%%%%%%%%%%%%%%%%%%%%%%%%%%%%%%%%
   %%%%%%%%%%%%%%%%%%%%%
   h_fg=2498000; % J/kg
   h_ads=2777777.77;  % J/kg
   c_p_w=4186;
```

```
   w_des_0=0.41695;
   %%%%%%%%%%%%%%%%%%%%%
   % Sorbent:
   rho_cp=1.8e6;
   rho_s=655.26;
   c_p_s=rho_cp/rho_s;
   %%%%%%%%%%%%%%%%%%%%%
   grrr=[0 0.02 0.05 0.1 0.15 0.2];
   alpha_sss=[2.38175E-07,2.80936E-07,3.45121E-07,5.43E-07,9.86964E-
07,1.3898E-06];
   p_1=polyfit(grrr,alpha_sss,2);
   %%%%%%%%%%%%%%%%%%%%%
   %%%%%%%%%%%%%%%%%%%%%

   %%%%%%%%%%%%%%%%%%%%%
   % Aluminum @ 40 C
   rho_g=2699;
   c_p_g=909;
   k_y=236.5;
   k_x=236.5;
   alpha_x=k_x/(rho_g*c_p_g);
   alpha_y=k_y/(rho_g*c_p_g);
   %%%%%%%%%%%%%%%%%%%%%

   %%%%%%%%%%%%%%%%%%% h_dp_RE_Nu
   t_w=0.004;
   H_c=t_w;
   D_H=H_c; % hydraulic diameter
   r_1=D_H/2;
   rho_w=992.2;
   Q_flow=7; %  l/min
   mdot=Q_flow*0.001*rho_w/60;
   k_w=0.6178; % water conductivity
   mu_w=0.001002; % water viscosity
   Pr=7.154;
   Re=2*mdot/(mu_w*pi*r_1);
   f_fric=(1.82*log10(Re)-1.64)^-2; % friction factor
   Nu=((f_fric*Re*Pr/8)/(1.07+12.7*(f_fric/8)^0.5*(Pr^(2/3)-
1)))*(0.0006533/0.0005758)^0.11; %  (Holman page 282)
   h_f=Nu*k_w/D_H;
   t_t=0.002; %mm Thickness of the tube itself
   k_tube=385; % copper
   R_fluid=(1/h_f)+(t_t/k_tube);
   %%%%%%%%%%%%%%%%%%% h_dp_RE_Nu
   TCR=3;
   A=6.45e-4;
   %%%%%%%%%%%%%%%%%%%%%%%%%%%%%%%%%%%%%%%%%%%%%%%%%%%%%%%%%%%%%%%%%%%%%%%
   T_0=67.5+273.15; %degree C (refer to w_T, start temperature)
   T_f=30+273.15; %degree C
   Theta_0=T_0-T_f;
   %%%%%%%%%%%%%%%%%%%%%%%%%%%%%%%%%%%%%%%%%%%%%%%%%%%%%%%%%%%%%%%%%%%%%%%

   % x=[bbb,t_ff,t_ss,grr,tt];
   t_1=sym(linspace(1,11.3*60/2,2));

   %%%%%%%%%%%%%%%%%%% Space
```

```
  b=0.01;
  t_f=0.001;
  t_s=0.001;

  %%%%%%%%%%%%%%%%%%% Space
  r_2=r_1+b;
  delta_r=r_1/r_2;
  eta=linspace(delta_r,1,20);
  x_1=t_f/(t_s+t_f);
  dxx=x_1/30;
  zeta_f=0:dxx:x_1;
  zeta_s=x_1:dxx:1+dxx;
  zeta_original=[zeta_f(1:end-1),zeta_s(1:end)];
  zeta_plot=[zeta_f(1:end),zeta_s(1:end-1)];
  %%%%%%%%%%%%%%%%%%% Space

  gr=0.15;

  a_ads=-0.0096*(1-gr)/0.8;

  %%%%%%%%%%%%%%%%%%%%%%%%%%%%%%%%%%%%%%%%%%
  alpha_s=polyval(p_1,gr);
  k_s=rho_cp*alpha_s;

  a=a_ads;
  alpha_s=k_s/(rho_cp-rho_s*h_ads*a);

  k_ave=(k_s+k_x)/2;
  Lambda=r_2/(k_ave*R_fluid);
  k=k_s/k_y;
  Lambda_c=(t_s+t_f)/(k_y*TCR*A);
  delta=r_2/(t_s+t_f);
  mu_y=(alpha_y/alpha_x)^0.5;
  mu_s=(alpha_s/alpha_x)^0.5;

  r_f=k_x/delta^2;
  r_s=((rho_cp-rho_s*h_ads*a)*k_x)/(rho_g*c_p_g*delta^2);
  p_f=k_y;
  p_s=k_s;

  Fo=sym(t_1*alpha_x/(r_2^2));
  %%%%%%%%%%%%%%%%%%%%%%%%%%%%%%%%%%%%%%%%%%

  %%%%%%%%%%%%%%%%%%%%%%%%%%%%%%%%%%%%%%%%%%%%%%%%%%%%%%%%%%%%%%%%%%%%%%
%%%%%%%%%%%%% Gamma
  xx=0:0.001:10;
  roots=zeros(1,length(xx));
  my_roots=zeros(1,1);
  for i=2:length(xx)
  roots(i)=fzero(@gamma_func,xx(i));
  if (abs(gamma_func(roots(i))))<1e-4
      if roots(i)>0
          my_roots(1,end+1)=roots(i);
      end
  end
  end
```

```
   gamma_temp=zeros(1,length(my_roots)-1);
   for i=2:length(my_roots)
       gamma_temp(1,i-1)=my_roots(1,i);
   end
   gamma_c=[min(gamma_temp)];

   gamma_all=sym(gamma_c);
   %%%%%%%%%%%%%%%%%%%%%%%%%%%%%%%%%%%%%%%%%%%%%%%%%%%%%%%%%%%%%%%%%%%%%%%%%%%%
%%%%%%%%%%%% Gamma
   Theta=zeros(length(eta),length(zeta_original),length(Fo));


   for i_gamma=1:1
           gamma=gamma_all(1,i_gamma);
           q_f=(gamma)^2*r_f; % for each gamma
           q_s=(mu_s*gamma)^2*r_s; % for each gamma
           zeta=zeros(1,1);
           zeta=zeta_original;
               for i_landa=1:1


                   for k=1:length(zeta)-1
                       if zeta(1,k)<x_1
                           l_k(1,k)=zeta(1,k+1)-zeta(1,k);
                           p_k(1,k)=p_f;
                           r_k(1,k)=r_f;
                           q_k(1,k)=q_f;
                       elseif zeta(1,k)>x_1
                           l_k(1,k)=zeta(1,k+1)-zeta(1,k);
                           p_k(1,k)=p_s;
                           r_k(1,k)=r_s;
                           q_k(1,k)=q_s;
                       else
                           l_k(1,k)=zeta(1,k+1)-zeta(1,k);
                           l_TCR=l_k(1,k);
                           p_k(1,k)=l_k(1,k)*(t_s+t_f)/(TCR*A);
                           r_k(1,k)=0;
                           q_k(1,k)=0;
                           w_k(1,k)=0;
                       end
                   end

%%%%%%%%%%%%%%%%%%%%%%%%%%%%%%%%%%%%%%%%%%%%%%%%%%%%%%%%%%%%%%%%%%%%%%%%%%%%
%%%%%%%%%%%%%%%%%%%% landa_loop while
                   landa_l=0;
                   landa_hat_old=0;
                   Eps_i=0.01;
                   delta_hat=0.001;
                   landa_hat=landa_hat_old+delta_hat;
                   landa_u=landa_hat;
                   while (2>1)

%%%%%%%%%%%%%%%%%%%%%%%%%%%%%%%%%%%%%%%%%%%%%%%%%%%%%%%%%%%%%%%%%%%%%%%%%%%% N0 & s_k
                       N0(1,i_landa)=0;
                       s_k(1,i_landa)=0;
```

```
%%%%%%%%%%%%%%%%%%%%%%%%%%%%%%%%%%%%%%%%%%%%%%%%%%%%%%%%%%%%%%%%%%%%%%%%%%%%
%%%%%%% k loop

                        for k=1:length(zeta)-1
                            if zeta(1,k)<x_1
                                w_k(1,k)=((landa_hat*r_f-q_f)/p_f)^0.5;
                            elseif zeta(1,k)>x_1
                                w_k(1,k)=((landa_hat*r_s-q_s)/p_s)^0.5;
                            end

N0(1,i_landa)=N0(1,i_landa)+floor(w_k(1,k)*l_k(1,k)/pi);


%%%%%%%%%%%%%%%%%%%%%%%%%%%%%%%%%%%%%%%%%%%%%%%%%%%%%%%%%%%%%%%%%%%%%%%%%%%% A and B
                            if w_k(1,k)^2>0

B_k(1,k)=p_k(1,k)*w_k(1,k)/sin(w_k(1,k)*l_k(1,k));
                                A_k(1,k)=B_k(1,k)*cos(w_k(1,k)*l_k(1,k));
                            elseif w_k(1,k)^2==0
                                B_k(1,k)=p_k(1,k)/l_k(1,k);
                                A_k(1,k)=B_k(1,k);
                            else
                                w_k_star=(abs(w_k(1,k)^2))^0.5;

B_k(1,k)=p_k(1,k)*w_k_star/sinh(w_k_star*l_k(1,k));

A_k(1,k)=B_k(1,k)*cosh(w_k_star*l_k(1,k));
                            end

%%%%%%%%%%%%%%%%%%%%%%%%%%%%%%%%%%%%%%%%%%%%%%%%%%%%%%%%%%%%%%%%%%%%%%%%%%%% A and B
                            D_k(1,1)=1;
                            D_k(1,2)=A_k(1,1); % this is correct not A1 bar
                            if k>1 && k<length(zeta)-1
                                D_k(1,k+1)=D_k(1,k)*(A_k(1,k)+A_k(1,k-
1))-D_k(1,k-1)*B_k(1,k-1)^2;
                            elseif k==length(zeta)-1
                                D_k(1,k+1)=D_k(1,k)*(A_k(1,k))-D_k(1,k-
1)*B_k(1,k-1)^2;
                            end

                            if (D_k(1,k+1)/D_k(1,k))<0
                                s_k(1,i_landa)=s_k(1,i_landa)+1;
                            end
                        end

%%%%%%%%%%%%%%%%%%%%%%%%%%%%%%%%%%%%%%%%%%%%%%%%%%%%%%%%%%%%%%%%%%%%%%%%%%%%
%%%%%%% k loop


%%%%%%%%%%%%%%%%%%%%%%%%%%%%%%%%%%%%%%%%%%%%%%%%%%%%%%%%%%%%%%%%%%%%%%%%%%%% N0 & s_k
                        N_landa(1,i_landa)=N0(1,i_landa)+s_k(1,i_landa);
                        if N_landa(1,i_landa)>=i_landa
                            landa_u=landa_hat;
                            delta_landa=abs(landa_u-landa_l);
                            if delta_landa<=Eps_i
```

```
Landa(i_gamma,i_landa)=sym((landa_u+landa_l)/2);
                                break; % from while loop
                            else
                                Landa_hat=(landa_u+landa_l)/2;
                            end
                        else
                            landa_l=landa_hat;
                            if landa_hat==landa_hat_old+delta_hat
                                landa_hat_old=landa_hat;
                                landa_hat=landa_hat_old+delta_hat;
                                landa_u=landa_hat;
                            elseif Landa_hat==(landa_u+landa_l)/2;
                                delta_landa=abs(landa_u-landa_l);
                                if delta_landa<=Eps_i

Landa(i_gamma,i_landa)=sym((landa_u+landa_l)/2);
                                    break; % from while loop
                                else
                                    Landa_hat=(landa_u+landa_l)/2;
                                end
                            end
                        end

                    end

%%%%%%%%%%%%%%%%%%%%%%%%%%%%%%%%%%%%%%%%%%%%%%%%%%%%%%%%%%%%%%%%%%%%%%%%%%%%%%%
%%%%%%%%%%%%%%%%%%%%%%%% landa_loop while


%%%%%%%%%%%%%%%%%%%%%%%%%%%%%%%%%%%%%%%%%%%%%%%%%%%%%%%%%%%%%%%%%%%%%%%%%%%%%%%
%%%%%%%%%%%%%%%%%%%%%%%% Eigenfunctions


%%%%%%%%%%%%%%%%%%%%%%%%%%%%%%%%%%%%%%%%%%%%%%%%%%%%%%%%%%%%%%%%%%%%%%%%%%%%%%%
%%%%%%%%%%%%%%%%%%%%%%%%%%%%%%%%%%%%%%%%%%%%%%%%%%%%%%%%%%%%%%%%%%%%%%%%%%%%%%%
%%%%%%%%%%%%%% New error after new zeta
                    for k=1:length(zeta)-1
                        % Always for TCR and others :
                        % x_k_1=zeta(1,k);
                        % x_k=zeta(1,k+1);
                        if zeta(1,k)<x_1
                            l_k(1,k)=zeta(1,k+1)-zeta(1,k);
                            p_k(1,k)=p_f;
                            r_k(1,k)=r_f;
                            q_k(1,k)=q_f;
                        elseif zeta(1,k)>x_1
                            l_k(1,k)=zeta(1,k+1)-zeta(1,k);
                            p_k(1,k)=p_s;
                            r_k(1,k)=r_s;
                            q_k(1,k)=q_s;
                        else
                            l_k(1,k)=zeta(1,k+1)-zeta(1,k);
                            l_TCR=l_k(1,k);
                            p_k(1,k)=l_k(1,k)*(t_s+t_f)/(TCR*A);
                            r_k(1,k)=0;
```

```
                        q_k(1,k)=0;
                        w_k(1,k)=0;
                    end
                end
                for k=1:length(zeta)-1
                    if zeta(1,k)<x_1
                        w_k(1,k)=((Landa(i_gamma,i_landa)*r_f-
q_f)/p_f)^0.5;
%%%%%%%%%%%%%%%%%%%%%%%%%%%%%%%%%%%%%%%%%%%%%%%%%%%%%%%%%%%%%%%%%%%% change to
zeta
                    elseif zeta(1,k)>x_1
                        w_k(1,k)=((Landa(i_gamma,i_landa)*r_s-
q_s)/p_s)^0.5;
                    end

                    if w_k(1,k)^2>0

B_k(1,k)=p_k(1,k)*w_k(1,k)/sin(w_k(1,k)*l_k(1,k));
                        A_k(1,k)=B_k(1,k)*cos(w_k(1,k)*l_k(1,k));
                    elseif w_k(1,k)^2==0
                        B_k(1,k)=p_k(1,k)/l_k(1,k);
                        A_k(1,k)=B_k(1,k);
                    else
                        w_k_star=(abs(w_k(1,k)^2))^0.5;

B_k(1,k)=p_k(1,k)*w_k_star/sinh(w_k_star*l_k(1,k));
                        A_k(1,k)=B_k(1,k)*cosh(w_k_star*l_k(1,k));
                    end
                end

                psi(i_gamma,i_landa,1)=-1; % eigenfunction at x_0
                psi(i_gamma,i_landa,2)=-A_k(1,1)/B_k(1,1);           %
eigenfunction at x_1
                for k=1:length(zeta)-2

psi(i_gamma,i_landa,k+2)=((A_k(1,k)+A_k(1,k+1))*psi(i_gamma,i_landa,k+1
)-B_k(1,k)*psi(i_gamma,i_landa,k))/B_k(1,k+1); % eigenfunction at x_k+1
                end
            %             Err(i_gamma,i_landa)=(Eps_max*length(zeta))-
abs(-B_k(1,length(zeta)-1)*psi(i_gamma,i_landa,length(zeta)-
1)+A_k(1,length(zeta)-1)*psi(i_gamma,i_landa,length(zeta)));  %  Must  be
>=0

%%%%%%%%%%%%%%%%%%%%%%%%%%%%%%%%%%%%%%%%%%%%%%%%%%%%%%%%%%%%%%%%%%%%%%%%%%%%
%%%%%%%%%%%%%%%%%%%%%%%%%%%%%%%%%%%%%%%%%%%%%%%%%%%%%%%%%%%%%%%%%%%%%%%%%%%%
%%%%%%%%%%%%%% New error after new zeta


%%%%%%%%%%%%%%%%%%%%%%%%%%%%%%%%%%%%%%%%%%%%%%%%%%%%%%%%%%%%%%%%%%%%%%%%%%%%
%%%%%%%%%%%%%%%%%%%%%%%%%% Eigenfunctions

                syms x_sym;

%%%%%%%%%%%%%%%%%%%%%%%%%%%%%%%%%%%%%%%%%%%%%%%%%%%%%%%%%%%%%%%%%%%%%%%%%%%%
%%%%%%%%%%%%%%%%%%%%%%%%%% C(i_gamma,i_landa)
```

```
                    f_N_gamma=(besselj(0,gamma*x_sym)-
besselj(1,gamma)*bessely(0,gamma*x_sym)/bessely(1,gamma))^2;
                    f_N_int=int(f_N_gamma,delta_r,1);
                    N_gamma(i_gamma,1)=double(f_N_int);

                    f_num_gamma=besselj(0,gamma*x_sym)-
besselj(1,gamma)*bessely(0,gamma*x_sym)/bessely(1,gamma);
                    f_num_int=int(f_num_gamma,delta_r,1);
                    num_gamma(i_gamma,1)=double(f_num_int);

                    N_landa(i_gamma,i_landa)=0;
                    num_landa(i_gamma,i_landa)=0;
                    for k=1:length(zeta)-1
                        if w_k(1,k)^2==0

N_landa(i_gamma,i_landa)=N_landa(i_gamma,i_landa)+r_k(1,k)*l_k(1,k)*(ps
i(i_gamma,i_landa,k+1)^3-
psi(i_gamma,i_landa,k)^3)/(3*(psi(i_gamma,i_landa,k+1)-
psi(i_gamma,i_landa,k)));

num_landa(i_gamma,i_landa)=num_landa(i_gamma,i_landa)+r_k(1,k)*l_k(1,k)
*(psi(i_gamma,i_landa,k+1)+psi(i_gamma,i_landa,k))/2;
                        else

N_landa(i_gamma,i_landa)=N_landa(i_gamma,i_landa)+r_k(1,k)*((psi(i_gamm
a,i_landa,k)^2+psi(i_gamma,i_landa,k+1)^2)*(B_k(1,k)^2*l_k(1,k)/p_k(1,k
)-A_k(1,k))+...

2*B_k(1,k)*psi(i_gamma,i_landa,k)*psi(i_gamma,i_landa,k+1)*(1-
A_k(1,k)*l_k(1,k)/p_k(1,k)))/(2*p_k(1,k)*w_k(1,k)^2);

num_landa(i_gamma,i_landa)=num_landa(i_gamma,i_landa)+r_k(1,k)*((psi(i_
gamma,i_landa,k+1)+psi(i_gamma,i_landa,k))*(B_k(1,k)-
A_k(1,k))/(p_k(1,k)*(w_k(1,k)^2)));
                        end
                    end

C(i_gamma,i_landa)=Theta_0*num_gamma(i_gamma,1)*num_landa(i_gamma,i_lan
da)/(N_gamma(i_gamma,1)*N_landa(i_gamma,i_landa));


%%%%%%%%%%%%%%%%%%%%%%%%%%%%%%%%%%%%%%%%%%%%%%%%%%%%%%%%%%%%%%%%%%%%%%%%
%%%%%%%%%%%%%%%%%%%%%%%% C(i_gamma,i_landa)


%%%%%%%%%%%%%%%%%%%%%%%%%%%%%%%%%%%%%%%%%%%%%%%%%%%%%%%%%%%%%%%%%%%%%%%%
%%%%%%%%%%%%%%%%%%%%%%%%%%%%%%%%%%%%%%%%%%%%%%%%%%%%%%%% Theta
                    for kk=1:length(zeta_original)
                        for k=1:length(zeta)
                            if abs(zeta(1,k)-zeta_original(1,kk))<1e-5
                                for i_t=1:length(Fo)
                                    for i_eta=1:length(eta)

X=besselj(0,gamma*eta(1,i_eta))-
besselj(1,gamma)*bessely(0,gamma*eta(1,i_eta))/bessely(1,gamma);
```

```
Theta(i_eta,kk,i_t)=Theta(i_eta,kk,i_t)+C(i_gamma,i_landa)*X*psi(i_gamm
a,i_landa,k)*exp(-Landa(i_gamma,i_landa)*Fo(1,i_t));
                                    end
                                end
                            end
                        end
                    end

%%%%%%%%%%%%%%%%%%%%%%%%%%%%%%%%%%%%%%%%%%%%%%%%%%%%%%%%%%%%%%%%%%%%%%%
%%%%%%%%%%%%%%%%%%%%%%%%%%%%%%%%%%%%%%%%%%%%%%%%%%%%%%%% Theta

            end
    end


    for i_t=1:length(t_1)

T_sorb_ave(i_t,1)=mean(mean(Theta(:,length(zeta_f)+1:length(zeta_plot),
i_t)),2);
    end

    l_t=2*t_s+t_f; % tube length
    l_rect=pi*(r_1+r_2);
    m_sorb=pi*(r_2^2-r_1^2)*t_s*rho_s/l_rect;
    m_HEX=pi*(r_2^2-r_1^2)*t_f*rho_g/l_rect;
    m_tube=pi*(r_1^2-(r_1-t_t)^2)*(t_f+t_s)*rho_g/l_rect;
    m_HEX=m_HEX+m_tube;

    dw=a_ads*(T_sorb_ave(2,1)-T_sorb_ave(1,1));
    SCP=zeros(2,1);
    time=t_1(1,2)-t_1(1,1);
    SCP(1,1)=0.5*dw*h_fg/time;

    % W_pump=pi*f_fric*l_t*Re^3*mu_w^3*time/(8*rho_w^2*D_H^2);
    Q_evap=m_sorb*dw*h_fg;
    Q_des=m_sorb*dw*h_ads;
    Q_sens=(m_sorb*c_p_s+m_sorb*w_des_0*c_p_w+m_HEX*c_p_g)*(90-30);

    SCP(2,1)=(0.582/0.577)*Q_evap/(Q_des+Q_sens); % COP


    xlswrite('D:\2-D cylindrical\Results\SCP_COP.xlsx',SCP);



    function y = gamma_func( x )
    global Lambda;
    global delta_r;

    y=-
x*besselj(1,x*delta_r)+(x*besselj(1,x)/bessely(1,x))*bessely(1,x*delta_
r)-
Lambda*besselj(0,x*delta_r)+Lambda*(besselj(1,x)/bessely(1,x))*bessely(
0,x*delta_r);
```

```
  end
```

E.5. Matlab code to refine the intervals to increase the accuracy in 2-D analytical models

```
  %%%%%%%%%%%%%%%%%%%%%%%%%%%%%%%%%%%%%%%%%%%%%%%%%%%%%%%%%%%%%%%%%%%%%
%%%%%%%%%%%%%%%%%%%%%%%%%%%%%%%%%%%%%%%%%%%%%%% Step size selection
          Eps_min=0.001;
          Eps_max=0.2;
          l_min=0.00001;
          j=5;
          %step 2
          psi_bar(1,1)=-1; % eigenfunction at x_0
  %         for k=1:n_layer
  %             for i=1:j
  %                 l_j(1,(k-1)*j+i)=l_k(1,k)/j;
  %             end
  %         end

          x_bar(i_landa,1)=zeta(1,1);
          k=1;
          x_bar(i_landa,2)=0;
          l=l_k(1,1);

%%%%%%%%%%%%%%%%%%%%%%%%%%%%%%%%%%%%%%%%%%%%%%%%%%%%%%%%%%%%%%%%%%%%%%%
%%%%%%% while for x
          while (x_bar(i_landa,k)+l<1) %step10

  %             if (x_bar(i_landa,k))<x_1
  %                 l=l_k(1,1);
  %             elseif (x_bar(i_landa,k))>=x_1
  %                 l=l_k(1,end);
  %             end


              %%%%%%%%%%%%%%%%%%%%%%%%%% new w,r,p,q
              if (x_bar(i_landa,k)+l)<x_1
                  p_kk=p_f;
                  r_kk=r_f;
                  q_kk=q_f;
                  w_kk=((Landa(i_gamma,i_landa)*r_f-q_f)/p_f)^0.5;
              elseif (x_bar(i_landa,k)+l)>x_1
                  p_kk=p_s;
                  r_kk=r_s;
                  q_kk=q_s;
                  w_kk=((Landa(i_gamma,i_landa)*r_s-q_s)/p_s)^0.5;
              else
                  p_kk=l/(TCR*A);
                  r_kk=0;
                  q_kk=0;
                  w_kk=0;
              end
              %%%%%%%%%%%%%%%%%%%%%%%%%% new w,r,p,q
```

```
%%%%%%%%%%%%%%%%%%%%%%%%%%%%%%%%%%%%%%%%%%%%%%%%%%%%%%%%%%%%%%%%%%%%%%%%%%%%
%%%%%%%%%%%%%%%%%%%% while for each l_j
                while (2>1)
                    %step3
                    l_j=l/j;
                    %%%%%%%%%%%%%%%%%% new A and B
                    for i=1:j
                        if w_kk^2>0
                            B_j(1,i)=p_kk*w_kk/sin(w_kk*l_j);
                            A_j(1,i)=B_j(1,i)*cos(w_kk*l_j);
                        elseif w_kk^2==0
                            B_j(1,i)=p_kk/l_j;
                            A_j(1,i)=B_j(1,i);
                        else
                            w_k_star=(abs(w_kk^2))^0.5;
                            B_j(1,i)=p_kk*w_k_star/sinh(w_k_star*l_j);
                            A_j(1,i)=B_j(1,i)*cosh(w_k_star*l_j);
                        end
                    end
                    %%%%%%%%%%%%%%%%%% new A and B

                    %%%%%%%%%%%%%%%%%% new A and B
                    if w_kk^2>0
                        B_i(1,k)=p_kk*w_kk/sin(w_kk*l);
                        A_i(1,k)=B_i(1,k)*cos(w_kk*l);
                    elseif w_kk^2==0
                        B_i(1,k)=p_kk/l;
                        A_i(1,k)=B_i(1,k);
                    else
                        w_k_star=(abs(w_kk^2))^0.5;
                        B_i(1,k)=p_kk*w_k_star/sinh(w_k_star*l);
                        A_i(1,k)=B_i(1,k)*cosh(w_k_star*l);
                    end
                    %%%%%%%%%%%%%%%%%% new A and B
                    %step4
                    if k==1
                        psi_bar(1,2)=-A_i(1,1)/B_i(1,1);                %
eigenfunction_bar at x_1
                    else
                        psi_bar(1,k+1)=((A_i(1,k-
1)+A_i(1,k))*psi_bar(1,k)-B_i(1,k-1)*psi_bar(1,k-1))/B_i(1,k);          %
eigenfunction at x_k+1
                    end
                    %step5
                    if k==1
                        psi_j(1,1)=psi_bar(1,1);
                        psi_j(1,2)=psi_bar(1,2);
                    else
                        psi_j(1,1)=psi_j_previous(1,j);  %  psi_j  is  the
psi_j for previous k that we got
                        psi_j(1,2)=psi_j_previous(1,j+1); % psi_j  is  the
psi_j for previous k that we got
                    end
                    for i=1:j-1
```

```
                    psi_j(1,i+2)=((A_j(1,i)+A_j(1,i+1))*psi_j(1,i+1)-
B_j(1,i)*psi_j(1,i))/B_j(1,i+1);
                end
                %step6
                if abs(psi_j(1,j+1)-psi_bar(1,k+1))<Eps_max
                    %step9
  %                   ll_k(1,k)=l;
                    x_bar(i_landa,k+1)=x_bar(i_landa,k)+l;
                    k=k+1;
                    psi_j_previous=psi_j;
                    break; % from while for each l_j
                else
                    %step7
                    if l<l_min
                        %step12
                        error('Inappropriate accuracy requirements');
                    else
                        %step8
                        l=l_j;
  %                       l=l*j; % Or
                    end
                end
            end

%%%%%%%%%%%%%%%%%%%%%%%%%%%%%%%%%%%%%%%%%%%%%%%%%%%%%%%%%%%%%%%%%%%%%%%%%%%%
%%%%%%%%%%%%%%%%%%% while for each l_j
        end

%%%%%%%%%%%%%%%%%%%%%%%%%%%%%%%%%%%%%%%%%%%%%%%%%%%%%%%%%%%%%%%%%%%%%%%%%%%%
%%%%%% while for x
  %         Step11
        x_bar(i_landa,k+1)=1;
  %       ll_k(1,k+1)=1-x_bar(i_landa,k);
        zeta=zeros(1,1);
        l_k=zeros(1,1);
        zeta=x_bar(end,:);

%%%%%%%%%%%%%%%%%%%%%%%%%%%%%%%%%%%%%%%%%%%%%%%%%%%%%%%%%%%%%%%%%%%%%%%%%%%%
%%%%%%%%%%%%%%%%%%%%%%%%%%%%%%%%%%%%%%%% Step size selection
```

Appendix F: Analysis of variance (ANOVA)

Analysis of variance, ANOVA, is a systematic method that can be used to evaluate the impact of design parameters on the performance by calculating the sums of square, level of contribution, F-statistic ratio and p-value [161]–[163]. First, we generate the sample points of variables, e.g. using Box–Behnken design [164] with three levels of design parameters shown in **Table 11**. Since each variable has three levels, the degree of freedom is equal to 2. Based on the sample points generated by Box–Behnken design, the objective functions are evaluated using the analytical models, each objective function is shown by X_j. $\bar{X}_j$ represents the average of objective functions for each variable, and $\bar{X}$ indicates the average of $\bar{X}_j$ for all the variables. With these definitions, the sums of squares, mean squares, F-statistic ratio, and level of contribution (ρ) can be calculated as shown in Table F1. n_j shows the sample size in the jth group (or the number of variables). F-statistic ratio represents the variability between treatment or the ratio of (differences among the sample means) / (an estimate of the variability in the outcome). The greater the F, the more significant effect that parameter has as it can cause more variation.

Table F1. Sums of square, level of contribution and F-statistic ratio in ANOVA

Variable	**Sums of square (SS)**	**Degree of freedom (dof)**	**Mean squares (MS)**	***F***	***ρ* (%)**
b	$SSB = \sum n_j \left(\bar{X}_j - \bar{X} \right)^2$	*k*-1=2	*MSB=SSB*/(*k*-1)	*MSB/MSE*	*SSB/SST*
t_f		2			
t_s		2			
ϕ		2			
τ		2			
r_1, $H_c/2$		2			
Error (residual)	$SSE = \sum \sum \left(X - \bar{X}_j \right)^2$	*N*-*k*=54-12=41	*MSE=SSE*/(*N*-k)		*SSE/SST*
Total	$SST = \sum \sum \left(X - \bar{X} \right)^2$	*N*-1=53			

To examine whether a variable has significant impact on the objective function, Null hypothesis is employed as follows.

H_0: Null hypothesis, which hypothesizes that all the means are equal: $\mu_1 = \mu_2 = \mu_3 \ldots = \mu_k$ (j=1, 2, 3, …, k). If this hypothesis is true, then the variable does not cause significant variation as all the means are equal; thus, the variable has insignificant impact on the objective function.

p-value ≤ α: Reject H0. The differences between some of the means are statistically significant, which means it has significant impact.

p-value > α: The differences between the means are not statistically significant, which means it has negligible impact.

α= significance level (usually 0.05). It means that there is 5% chance that Null hypothesis was wrong and that parameter is significant.

p-value can be calculated based on F-statistic ratio, significance level (α), degree of freedom of the treatment for each variable and degree of freedom of errors, shown by $F_{\alpha, df1, dfE}$. Matlab was used to obtain the p-values for $F_{\alpha, df1, dfE}$. The greater the F, the smaller the p-value.

Appendix G: Drawings of sorber bed heat and mass exchangers

Fig. G.1 and **Fig. G.2** show the CAD drawings used to build the plate-fin sorber bed heat and mass exchanger (P-HMX) and finned-tube sorber bed heat and mass exchanger (F-HMX) discussed in chapter 5.3, **Fig. 56** and **Fig. 57**.

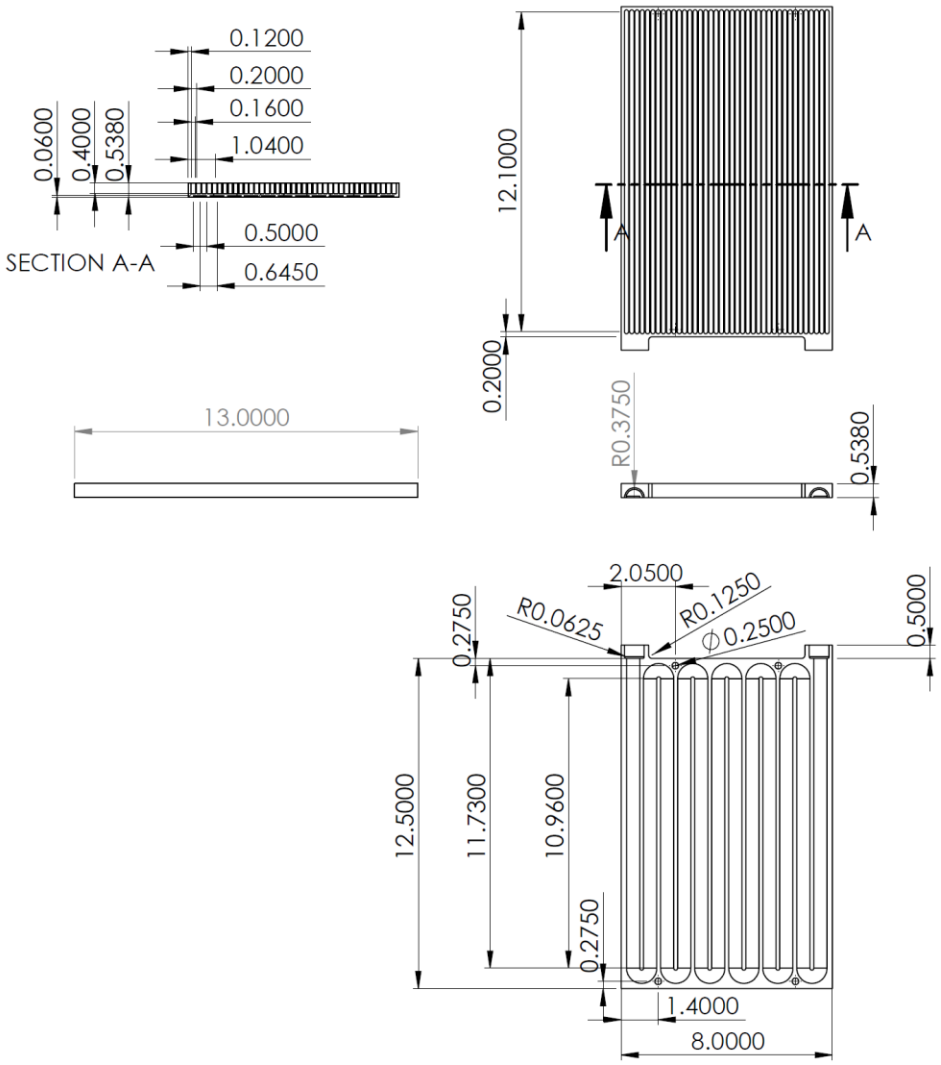

Fig. G.1. CAD drawing of the plate-fin sorber bed heat and mass exchanger (P-HMX), all dimensions are in inches

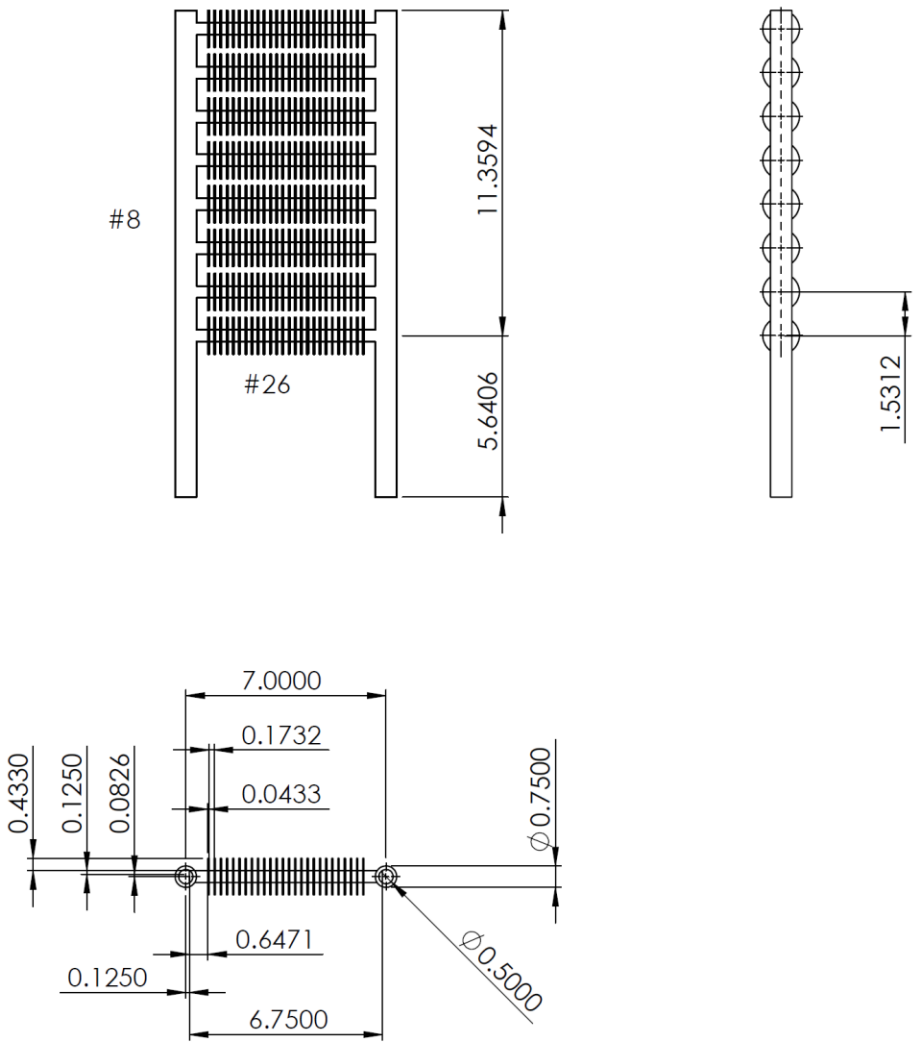

Fig. G.2. CAD drawing of the finned-tube sorber bed heat and mass exchanger (F-HMX), all dimensions are in inches

Appendix H: Integration of sorption cooling systems in PEM fuel cell buses

It was discussed in section 1.2 that the waste heat of fuel cells can be used to run sorption cooling systems (SCS) to generate cooling in automotive applications. **Fig. H.1 (a)** shows the schematic of a NewFlyer 40-foot bus powered by Ballard PEM fuel cells. The PEM fuel cell in the 40-foot bus with 50 kW energy input, generates approximately 25 kW electricity and 25 kW waste heat at the temperature between 60–80 ºC [59]. 44% of the electrical power produced by the PEM fuel cell is consumed to generate 15 kW cooling for the cabin AC using VCR systems, while 56% is left for the bus traction. **Fig. H.1 (b)** shows the integration of SCS in the bus to provide the 15 kW cooling with the 25 kW waste heat from the PEM fuel cell. Therefore, the required COP of a waste-heat driven SCS should be about 0.6. Incorporation of SCS can significantly reduce the AC electrical power consumption. Thus, the hydrogen fuel tanks, fuel cell stacks and the batteries can be reduced in size to provide 14 kW electrical power required for the bus traction, which decreases the cost and weight. Another benefit would be to keep the same size and increase the mileage of the bus.

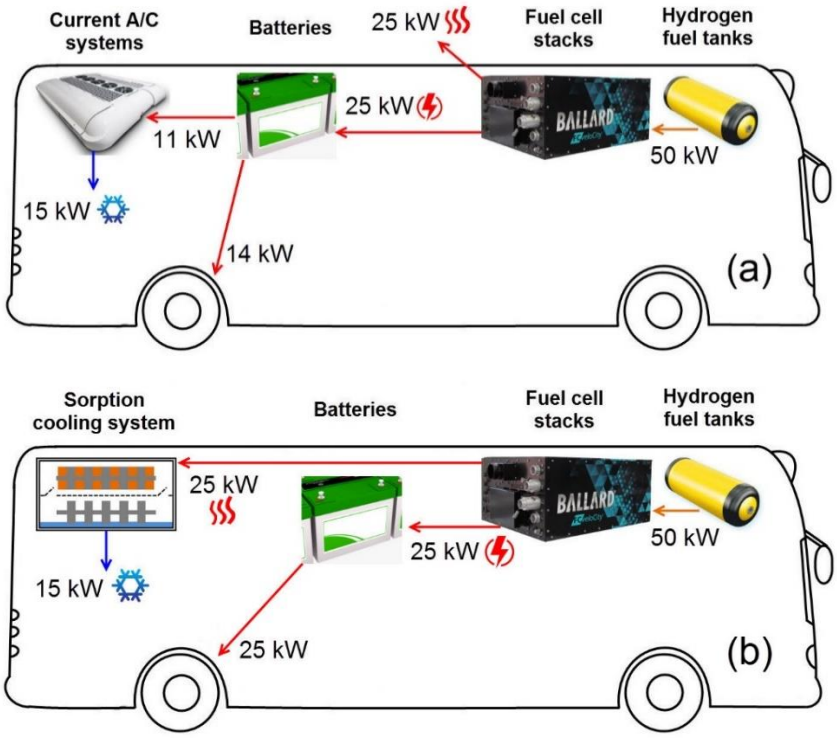

Fig. H.1. Schematic of a NewFlyer 40-foot bus powered by Ballard PEM fuel cells with (a) VCR and (b) SCS as the AC system